

**Interacting Ultracold Gases in Optical Lattices:  
Non-Equilibrium Dynamics  
and Effects of Disorder**

**Dissertation**

zur Erlangung des Doktorgrades  
der Naturwissenschaften

vorgelegt beim Fachbereich Physik  
der Johann Wolfgang Goethe-Universität  
in Frankfurt am Main

von  
Dipl.-Phys. Julia Wernsdorfer  
aus Kremenchug (Ukraine)

Frankfurt am Main 2012

vom Fachbereich Physik  
der Johann Wolfgang Goethe-Universität  
als Dissertation angenommen

Dekan: Prof. Dr. Michael Huth

Gutachter: Prof. Dr. Walter Hofstetter  
Prof. Dr. Maria-Roser Valenti

Datum der Disputation:





# Contents

<b>1</b>	<b>Introduction</b>	<b>1</b>
<b>2</b>	<b>Experiments in a nutshell</b>	<b>5</b>
2.1	Optical dipole potentials . . . . .	6
2.2	Optical dipole trap . . . . .	9
2.3	Optical lattices . . . . .	10
<b>3</b>	<b>Bose-Einstein condensates</b>	<b>13</b>
3.1	The Bose-Hubbard model . . . . .	13
3.1.1	Non-interacting particles in homogeneous systems . . . . .	14
3.1.2	Non-interacting particles in trapped systems . . . . .	24
3.1.3	Two-particle interactions . . . . .	25
3.1.4	Bose-Hubbard Hamiltonian: summary and outlook . . . . .	29
3.2	Quantum phases . . . . .	31
3.2.1	Superfluid . . . . .	31
3.2.2	Mott insulator . . . . .	36
3.2.3	Single particle density matrix . . . . .	38
3.2.4	Quantum phase transition . . . . .	43
3.2.5	Time-of-flight measurements . . . . .	47
3.3	Numerical method: Gutzwiller approximation . . . . .	54
3.3.1	Gutzwiller ansatz . . . . .	55
3.3.2	Mean-field theory . . . . .	56
3.3.3	Range of validity . . . . .	59
3.4	Phase diagram within the mean-field approach . . . . .	61
3.5	Mean-field dynamics . . . . .	65
3.6	Finite temperature . . . . .	69
3.6.1	Density matrix . . . . .	70
3.6.2	Thermalization and adiabaticity . . . . .	73
3.6.3	Mean-field approximations . . . . .	75

<b>4</b>	<b>Lattice ramp dynamics in an interacting Bose-Bose mixture</b>	<b>77</b>
4.1	Model and method . . . . .	78
4.2	Results for $T = 0$ . . . . .	80
4.2.1	Density profiles . . . . .	81
4.2.2	Visibility . . . . .	83
4.3	Results for nonzero $T$ . . . . .	89
4.3.1	Density profiles . . . . .	89
4.3.2	Visibility and oscillations . . . . .	90
4.4	Discussion and conclusion . . . . .	91
<b>5</b>	<b>Expansion of bosonic condensates in optical lattices</b>	<b>93</b>
5.1	Expansion of non-interacting bosons . . . . .	94
5.1.1	Real-space profiles . . . . .	94
5.1.2	Expansion velocities . . . . .	96
5.2	Melting of the Mott insulating cloud . . . . .	98
5.2.1	Setup . . . . .	98
5.2.2	Creation of exotic condensates . . . . .	100
5.2.3	Effect of the SF on the MI expansion . . . . .	104
5.3	Discussion and conclusion . . . . .	109
<b>6</b>	<b>Strongly correlated fermions</b>	<b>111</b>
6.1	The Fermi-Hubbard model . . . . .	111
6.1.1	Non-interacting particles . . . . .	112
6.1.2	Two-particle interactions . . . . .	115
6.1.3	Fermi-Hubbard Hamiltonian: summary and outlook . . . . .	117
6.2	Disorder . . . . .	118
6.2.1	Anderson localization . . . . .	118
6.2.2	Types of disorder . . . . .	122
6.3	Quantum phases . . . . .	126
6.3.1	Insulators: Mott and band . . . . .	127
6.3.2	Spectrum . . . . .	128
6.3.3	Averaging . . . . .	133
6.3.4	Charge gap . . . . .	137
6.3.5	Conductivity . . . . .	137

6.3.6	Compressibility . . . . .	138
6.3.7	Participation ratio and inverse participation number . . . . .	139
6.4	Finite temperatures . . . . .	140
6.5	Numerical method: DMFT . . . . .	141
6.5.1	DMFT . . . . .	142
6.5.2	Impurity solver: NRG and MPT . . . . .	148
6.5.3	RDMFT . . . . .	154
<b>7</b>	<b>Phase diagram of fermionic 1D Hubbard model with box disorder</b>	<b>159</b>
7.1	Peculiarities of 1D fermionic systems . . . . .	159
7.2	Model and methods . . . . .	160
7.3	Results . . . . .	161
7.3.1	Local density of states . . . . .	161
7.3.2	Charge gap . . . . .	165
7.3.3	Inverse participation ratio . . . . .	166
7.4	Discussion and conclusion . . . . .	167
<b>8</b>	<b>Strongly correlated fermions in speckle-disordered lattices</b>	<b>169</b>
8.1	Joint probability distribution functions . . . . .	170
8.2	Phase diagram . . . . .	170
8.3	Comparison with RDMFT . . . . .	173
8.4	Zero-bias anomaly . . . . .	175
<b>9</b>	<b>Summary and outlook</b>	<b>179</b>
<b>10</b>	<b>Zusammenfassung</b>	<b>183</b>
<b>A</b>	<b>Bose-Hubbard parameters</b>	<b>189</b>
<b>B</b>	<b>Particle number violation for parallel updates</b>	<b>193</b>
<b>C</b>	<b>Efficient calculation of time evolution within Gutzwiller</b>	<b>199</b>
<b>D</b>	<b>Temperature estimation in a weak lattice</b>	<b>201</b>
<b>E</b>	<b>Calculation of DMFT effective action</b>	<b>203</b>
<b>F</b>	<b>Derivation of the Weiss Green's function</b>	<b>207</b>

<b>G Properties of a localized state</b>	<b>209</b>
<b>H Sampling of the Hubbard parameter distributions</b>	<b>211</b>
<b>Bibliography</b>	<b>213</b>
<b>Danksagung</b>	<b>236</b>
<b>Curriculum Vitae</b>	<b>238</b>



# 1. Introduction

At sufficiently low temperature the ground state of a bosonic system becomes macroscopically occupied. This phenomenon is known as Bose-Einstein condensation (BEC) in honor of preliminary work by S. Bose in 1920 [1] and the final prediction by A. Einstein in 1925 [2]. However, after its prediction it took a long time before condensed states of bosonic particles could be prepared, controlled and directly observed in experiment. The main obstacle was the extremely low critical temperature crucial for the occurrence of condensation. The first milestone in particle control was set by S. Chu, C. Cohen-Tannoudji and W. D. Phillips. Their invention of atom traps and laser cooling, which yielded a lowering of the temperature down to  $\sim 10^{-5}$  K, was celebrated with a Nobel Prize in 1997. In 1995 the groups of E. A. Cornell, C. E. Wieman [3] and W. Ketterle [4] succeeded in cooling the atoms further down to  $\sim 10^{-8}$  K by applying an additional evaporative cooling technique. For this achievement they were awarded the Nobel Prize in 2001.

Fermionic quantum gases constitute the counterpart to BEC, with a behavior at quantum degeneracy determined by Fermi-Dirac statistics, developed independently by E. Fermi and P. Dirac [5, 6]. In contrast to bosons, the creation of a degenerate Fermi gas is more complicated due to a vanishing scattering cross section at low energies. To compensate for this, sympathetic cooling using the admixture of one further atom species is applied. This technique led to the first realization of a fermionic ultracold gas in 1999 by B. DeMarco *et al.* [7].

Since that time, research on degenerate quantum gases has reached a new level. Creation of condensates in different dimensionalities, trapping in optical lattices of various symmetries and finally the accurate tuning of the interaction strength enable perfect control over system parameters. As a result, ultracold atoms have evolved into a powerful tool for experimental investigations of strongly correlated many-body systems, which until recently were restricted to condensed matter.

Particularly intriguing was the new possibility to access zero-temperature physics predicted by Bose- and Fermi-Hubbard models [8, 9] in an accurately tunable atomic quantum simulator. While thermal fluctuations freeze out at  $T = 0$ , quantum fluctuations persist and can induce phase transitions that lead to macroscopic changes in the many-body ground state. A theoretically predicted transition from the weakly to the strongly correlated regime, the so-called superfluid-Mott insulator phase transition for bosons [9, 10] and the

metal-Mott insulator phase transition for fermions [8, 11], was successfully observed in the experiment by M. Greiner *et al.* [12], R. Jördens *et al.* [13] and U. Schneider *et al.* [14], respectively.

The experimental observation of long-range ordered phases, such as quantum magnetism and supersolidity [15–18], theoretically already predicted in multicomponent mixtures, is now one of the major goals in the field of ultracold gases. Superexchange interactions have been observed and investigated experimentally in two-state mixtures of bosonic  $^{87}\text{Rb}$  [19]. Moreover, a successful creation of a heteronuclear bosonic condensate has been achieved recently [20]. In combination with tunable inter-particle interaction, a mapping of the phase diagram is feasible. However, a most important barrier has not yet been eliminated: the experimental detection of many-body ground states with spin ordering requires even lower temperatures. Quantum magnetism exists at temperature scales of the order  $J^2/U$ , where  $J$  is the tunneling and  $U$  the interaction strength between atoms, which corresponds to temperatures well below 1 nK [21]. This requires additional cooling techniques and control over heating processes induced by three-body recombination or ramping up of the lattice. While the first issue has been extensively investigated both experimentally and theoretically [22–25], the effects on adiabaticity caused by a lattice ramp remain underestimated. Ramping the optical lattice can easily lead to temperature increase, or more precisely raise the entropy. This poses the following questions which will be addressed in this thesis for the case of bosonic atoms: when is the ramping of the optical lattice sufficiently slow, such that the process is adiabatic, and what are the observable non-adiabatic features. In contrast to previous static or single-species investigations [26–28] the effect of a second atomic species on the coherence properties of the first one is investigated considering actual experimental parameters. Particularly, non-equilibrium simulations for different ramping profiles and times prove that the ground state is not reached dynamically in deep lattices. Instead, a *frozen* superfluid and collective excitations are generated. The adiabaticity criterion as is proposed here and published in [29], is based on the experimentally accessible visibility and hence may serve as a guideline for future experiments.

Although equilibration is the goal in most experiments, non-equilibrium can be evoked on purpose. The induced many-body dynamics not only reveals various exciting phenomena but may also establish new experimental probing techniques [30, 31]. In the recent work by L. Hackermüller *et al.* [32] strong correlations have been shown to change the thermodynamics of a quantum many-particle system dramatically even when changes are made in an adiabatic way. Anomalous effects were reported such as expansion of a gas cloud with increasing attractive force between the atoms. Based on these findings, yet unknown effects of interactions on the dynamics raised the interest of theoretical and experimental physicists. In particular, by compensating the confinement potentials, it has been possible to study out-of-equilibrium expansion properties of ultracold fermions in a homogeneous Hubbard model [14]. Surprisingly, the expansion velocity and the shape of the spreading cloud were found to be strongly affected by the interaction strength. The corresponding issues for bosonic species have also been addressed theoretically. Counterintuitively, the coherence was found to be recovered when the initially confined Mott insulating cloud was allowed to expand. Complementary to previous studies on one-dimensional hard-core bosonic [33, 34] and higher-dimensional non-isotropically tunneling systems [35], in this thesis a systematic study of the homogeneous expansion for experimentally relevant setups is presented. Once released from harmonic confinement, the interacting many-body system is observed to develop coherence while simultaneously populating states with finite quasi-momentum. The emerging exotic condensate are found to show unusual effects.

Particularly, parameter regimes are found at which the cloud shape and condensation dynamics are affected by the number of particles in the Mott insulating phase rather than by the particular interaction or tunneling strength. This counterintuitive behavior may be incentive for further studies on non-equilibrium systems.

The high control and tunability of optical lattice potentials allowed another application of ultracold systems: investigations of disorder physics. Impurities, naturally present or artificially introduced into solids, were found to influence strongly the transport properties. The investigations of phenomena in condensed matter induced by impurities started many decades ago. Effects as for instance the unexpected increase of the conductivity were found [36] and explained as a many-body effect induced by a free electron gas interacting with a single localized magnetic impurity moment [37]. Nowadays, this phenomenon is known as the Kondo effect, in honor of the theoretical physicists J. Kondo who first developed the corresponding model and explained the underlying mechanism [38]. Later on, when doping of semiconductors was developed, a series of experiments by G. Feher *et al.* in 1955-56 surprised the community with the effect of localized spin excitations where spin transport was expected instead. This phenomenon is named after the physicist P. W. Anderson, who explained the absence of spin/charge diffusion within a basic model in 1958 [39]. The Anderson model describes a lattice with random energetic on-site offsets where an electron can propagate via nearest-neighbor tunneling. Above a certain concentration/strength of disorder coherent backscattering processes lead to localization of electronic eigenstates, the so-called Anderson localization. The corresponding localized particle wave functions cannot contribute to charge transport, which explains the observed loss of diffusion.

Unfortunately, experimental investigation of disorder effects in solid matter is a difficult task, since even an artificial introduction of impurities via doping techniques is less controllable. A solution to this problem offer ultracold systems. The increasing tunability of optical lattices has enabled implementation of disorder potentials not only of different strength but also of different types. Recently, the groups of J. Billy and G. Roati succeeded in demonstrating Anderson localized states in a non-interacting BEC in speckle-disordered lattices [40, 41]. The additional incorporation of repulsive interactions allowed observation of competing insulating regimes, i.e. Anderson and Mott phases, for speckle and bichromatic disordered bosonic systems [42, 43]. Complementary to already known superfluid and Mott-insulating phases the new insulating, gapless and compressible Bose glass phase was found. On the theoretical side, a non-perturbative description of random potentials requires a sophisticated numerical approach. Exact and approximative methods tailored to low and high dimensional bosonic systems provide corresponding phase diagrams for several disorder types [44-51].

For fermionic systems up to now, only few experiments have been done [52]. However, recent progress in the application of computational methods such as dynamical mean-field theory to disordered systems [53, 54] enabled quantitative theoretical predictions for experimental guidance. The second part of this thesis aims at a description of disorder effects in one- and two-dimensional interacting fermionic systems. Of special interest is the simultaneous presence of disorder and interactions. Although both lead to metal-insulator transitions, their action is competing: the repulsive electron-electron interaction favors a uniform distribution of particles, while disorder localizes the electronic wave function to a few lattice sites. Several investigations, perturbative and non-perturbative, have revealed that the interplay affects the system in a subtle way [44, 50, 51, 55-59]. A metallic phase was found in higher [44, 58] and even two-dimensional systems [55, 60], despite the long-standing belief [61-63] that no phase transition to a delocalized phase

takes place in two dimensions. Also the research presented in this thesis demonstrates that in two-dimensional optical lattices with speckle disorder a metallic phase appears, which continuously separates Anderson- and Mott-insulators. For box-disordered correlated one-dimensional systems a strong indication of delocalization is found. Here, the obtained metal is formed for intermediate interaction and disorder strength only.

This thesis is separated in two parts in which the investigated bosonic and fermionic systems are discussed separately. At the beginning of each of the two sections the underlying Bose- and Fermi-Hubbard models are derived and discussed in detail. The numerical procedures, i.e. the dynamic Gutzwiller method and the real-space extension of dynamical mean-field theory, are introduced as well as the observables important for the characterization of physical effects. And last but not least, the results and discussion of published and unpublished research are given at the end of each section. Specifically, the bosonic result section contains our investigations on lattice-ramp induced dynamics in an interacting bose-bose mixture and on the expansion of bosonic condensates in optical lattices. The fermionic results comprise the analysis of localization of correlated fermions in optical lattices with speckle disorder and investigations of delocalization signatures in the fermionic 1D Hubbard model with box disorder.

## 2. Experiments in a nutshell

In order to perform experiments with cold gases a high degree of control over the position of the investigated particles has to be achieved. In the case of ultracold atoms we are dealing with neutral particles where in contrast to charged particles, there exists no Coulomb interaction which can be used to trap the atoms in an electromagnetic field. For neutral particles alternative methods have been developed based on three different types of interactions [64, 65]:

- **Radiation-pressure traps** operate with near resonant light [66, 67]. The driving forces are the optical excitation and spontaneous emission. In a weak inhomogeneous magnetic field the Zeeman splitting is position dependent. As illustrated in Fig. 2.1 (a), if the laser frequency is slightly below the resonance at  $B = 0$  an atom propagating in positive direction ( $z > 0$ ) will on average absorb more  $\sigma^-$  polarized photons and feel a net time-averaged force toward the trap center. Similarly, atoms propagating in negative direction ( $z < 0$ ) will be slowed down and pushed to the  $B = 0$  center. This setup can be used not only for trapping particles but also for cooling. However, the recoil energy limits the achievable temperature and the resonant absorption/emission processes perturb the internal dynamics.
- **Magnetic traps** are based on the interaction of the magnetic moment of the atoms with an inhomogeneous external magnetic field [68, 69]. The created magnetic potential landscape consists of field gradients towards the trap center and enables trapping of neutral atoms, see Fig. 2.1. However, the trapping efficiency is limited by non-adiabatic or Majorana transitions which reorient the atomic magnetic moment and thus the direction of the magnetic force while the atom moves. Additionally, the trapping effect depends on the spin state of the atom, which limits investigation of spin mixed systems.
- **Optical dipole traps** are based upon the electric dipole interaction between the induced dipole moments of neutral atoms and the electric laser field. The lasers are far-detuned from the atomic resonances such that spontaneous emission effects can be neglected and the resulting dipole potential is purely conservative. No cooling can be achieved with the dipole force, however precooled atoms can be trapped. The depth and the geometry of optical potentials can be easily tuned even during the experiment, which is essential for observation of quantum mechanical phase transitions.

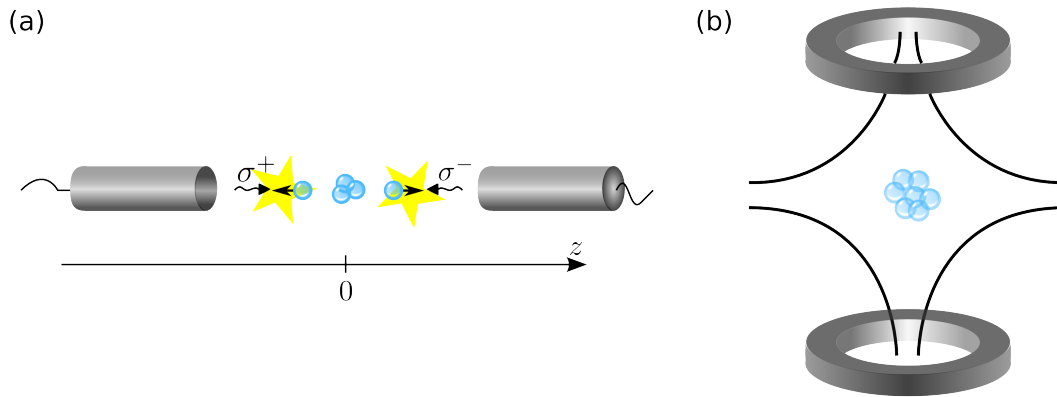


**Figure 2.1:** Illustration of a radiation pressure trap (a) and a magnetic trap (b). (a) In the inhomogeneous magnetic field (not in the figure) the radiation trap lasers are tuned resonant to atomic transition at  $B = 0$ , which is in the center of the device. The left and right moving particles absorb photons  $\sigma^+$  ( $\sigma^-$ ) and experience a kickback as a consequence of the momentum transfer from the photon to the particle. Thus, the atoms collect in the center of the device. Additionally they lose kinetic energy, which leads to a decrease of the temperature of the trapped atomic cloud. (b) In a quadrupole magnetic trap particles are attracted to the minimum of the magnetic field. The black lines visualize the potential gradient created by magnetic coils and the blue bubbles symbolize the atoms trapped in the center.

While for atomic confinement magnetic traps are as common as optical traps, the optical lattices are purely photonic. In order to gain a compact insight into trapping and artificial lattice creation we focus on the interaction between atoms and light only. We first sketch the derivation of the main equations for the dipole interaction between atom and the laser field, which is responsible for trapping of the particles in the optical trap as well as in the optical lattice. Based on that the creation of the lattice is explained.

## 2.1 Optical dipole potentials

The interaction between an atom and laser light can be divided in two processes. After a photon is absorbed by an atom it will either be emitted spontaneously or the emission will be stimulated. The first of the listed processes implicates the absorption of a photon followed by a spontaneous emission and is of dissipative nature because of the momentum transfer between the photon and the atom. Optical cooling and trapping setups are based on this effect. The other process of the interaction refers to a stimulated emission, where the photon is emitted into the same mode however with a phase shift. This atom-light interaction leads to the so-called ac-Stark shift of the potential which lowers the energy of the system. As will be shown next, for laser detuning away from the atomic resonance, the spontaneous emission can be neglected. The remaining laser stimulated interaction can be considered to lead to a conservative potential which can be tuned to create attractive spatially modulated landscapes.

Next, we calculate both interaction contributions respectively.

An oscillating electric field  $\mathbf{E}$  induces an electric dipole  $\mathbf{p}$  in an atom placed in the radiation field. In the complex notation  $\mathbf{E}(\mathbf{r}, t) = \mathbf{e} E(\mathbf{r}) [\exp(i\omega t) + c.c.]$  and  $\mathbf{p}(\mathbf{r}, t) =$

$\mathbf{e} p(\mathbf{r}) [\exp(i\omega t) + c.c.]$ , where  $\mathbf{e}$  denotes a unity polarization vector. The amplitude of the induced dipole moment is proportional to the electric field amplitude, namely  $p(\mathbf{r}) = \alpha E(\mathbf{r})$ , with complex polarizability  $\alpha(\omega)$ .

The interaction potential is given by [70]

$$V_{\text{dip}}(\mathbf{r}) = -\frac{1}{2} \langle \mathbf{p}(\mathbf{r}, t) \mathbf{E}(\mathbf{r}, t) \rangle = -\frac{1}{2\epsilon_0 c} \text{Re}(\alpha) I(\mathbf{r}), \quad (2.1)$$

where  $I(\mathbf{r}) = 2\epsilon_0 c |E(\mathbf{r})|^2$  denotes the intensity of the laser light and the average is taken with respect to time. The constants  $\epsilon_0$  and  $c$  correspond to the permeability and light velocity in vacuum respectively. This potential describes the stimulated part of the interaction where the atomic dipole oscillates in-phase with the driving field.

The out-of-phase part of the dipole interaction is due to absorption. The atom absorbs and re-emits the radiation of the electric field, the absorbed power is [70]

$$P_{\text{abs}} = \langle \dot{\mathbf{p}} \mathbf{E} \rangle = \frac{\omega}{\epsilon_0 c} \text{Im}(\alpha) I(\mathbf{r}). \quad (2.2)$$

The corresponding scattering rate of incoming photons consisting of absorption and re-emission is given by

$$\Gamma_{\text{sc}}(\mathbf{r}) = \frac{P_{\text{abs}}}{\hbar\omega} = \frac{1}{\hbar\epsilon_0 c} \text{Im}(\alpha) I(\mathbf{r}). \quad (2.3)$$

In order to use the above equations we have to calculate the polarizability. This can be directly calculated classically from the equation of motion for a driven damped oscillator  $\ddot{x} + \gamma\dot{x} + \omega_0^2 x = -eE(t)/m_0$  (the Lorentz oscillator model) with complex electric field  $E(t) = E e^{-i\omega t}$ , elementary charge  $e$  and electron mass  $m_0$ . The damping  $\gamma$  is calculated from the Larmor formula  $\gamma = e^2 \omega^2 / 6\pi\epsilon_0 m_0 c^3$ , which gives the energy loss of a non-relativistically accelerated electron [70]. The amplitude of a single induced dipole moment is given by  $p(t) = -ex(t)$ , where

$$x(t) = -\frac{eE}{m_0} \frac{e^{-i\omega t}}{\omega_0^2 - \omega^2 - i\gamma\omega} \quad (2.4)$$

is the solution of the differential equation. With  $p(t) = \alpha E(t)$  the polarizability reads

$$\begin{aligned} \alpha(\omega) &= \frac{e^2}{m_0} \frac{1}{\omega_0^2 - \omega^2 - i\gamma\omega} \\ &= \frac{6\pi\epsilon_0 c^3 \gamma}{\omega^2} \frac{1}{\omega_0^2 - \omega^2 - i\gamma\omega} \\ &= 6\pi\epsilon_0 c^3 \frac{\gamma_0 / \omega_0^2}{\omega_0^2 - \omega^2 - i\gamma_0 \omega^3 / \omega_0^2}. \end{aligned} \quad (2.5)$$

From the first to the second line the prefactor was rewritten using the expression for the classical damping rate. The on-resonance damping rate  $\gamma_0 = \gamma\omega_0^2/\omega^2$  was introduced in the third line.

A semiclassical calculation, which accounts for a two-level quantized nature of electronic excitations but neglects saturation effects<sup>1</sup> yields a similar expression for the polarization

<sup>1</sup>Saturation refers to minimization of the absorption due to a high fraction of already excited electrons. Commonly, when the laser intensity reaches the saturation point, 1/4 of the atoms are in the excited state. With larger detuning from the electronic resonance higher intensities are needed to saturate the system such that for far-detuned lasers the absorption can be assumed constant.

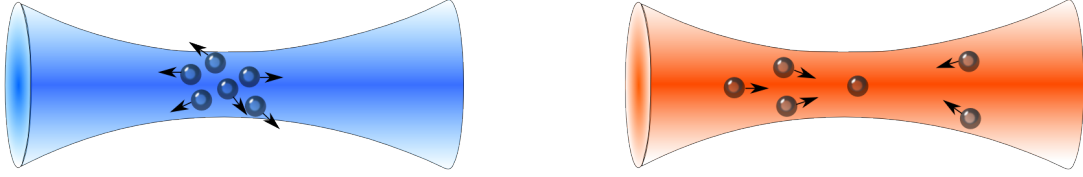


**Figure 2.2:** Effect of the laser detuning on the dipole potential. The Gaussian profiles of blue and red detuned laser beams are illustrated with the atoms inside. A blue detuning leads to a repulsion of particles from the beam center, where the intensity is maximal. In contrast, a red detuning attracts particles to those regions.

Eq. (2.5) with the damping rate  $\gamma_0 = |\langle e|e\mathbf{r}|g\rangle|^2\omega_0^2/3\pi\epsilon_0\hbar c^3$ . Here,  $|e\rangle$  denotes the excited and  $|g\rangle$  the ground state of the atom.

With the estimated polarization the dipole potential Eq. (2.1) and the scattering rate Eq. (2.3) can thus be rewritten

$$V_{\text{dip}}(\mathbf{r}) = -\frac{3\pi c^2}{2\omega_0^3} \left( \frac{\gamma_0}{\omega_0 - \omega} + \frac{\gamma_0}{\omega_0 + \omega} \right) I(\mathbf{r}) \quad (2.6)$$

$$\Gamma_{sc}(\mathbf{r}) = \frac{3\pi c^2}{2\hbar\omega_0^3} \left( \frac{\omega}{\omega_0} \right)^3 \left( \frac{\gamma_0}{\omega_0 - \omega} + \frac{\gamma_0}{\omega_0 + \omega} \right)^2 I(\mathbf{r}). \quad (2.7)$$

For detuning  $\delta \equiv \omega - \omega_0$  with  $|\delta| \ll \omega_0$  the first term dominates and the counter-rotating part with denominator  $\omega_0 + \omega$  can be neglected<sup>2</sup>. Within this so-called *rotating wave approximation* the Eq. (2.6) simplifies to

$$V_{\text{dip}}(\mathbf{r}) = \frac{3\pi c^2}{2\omega_0^3} \frac{\gamma_0}{\delta} I(\mathbf{r}). \quad (2.8)$$

The sign of detuning determines whether the optical dipole potential is attractive (red detuning,  $\delta < 0$ ) or repulsive (blue detuning,  $\delta > 0$ ) as illustrated in Fig. 2.2. In red detuned traps the induced dipole  $\mathbf{p}$  oscillates in phase with the electric field  $\mathbf{E}$  and the atoms are trapped at positions with intensity maxima. Whereas for blue detuned lasers the phase of the oscillating dipole  $\mathbf{p}$  is shifted by  $\pi$  against the phase of the  $\mathbf{E}$ -field and the atoms are trapped at intensity minima. In experiments only the red detuned lasers are used to trap the atoms, while an optical lattice can be generated using red and blue detuned laser light.

Likewise, the rotating wave approximation and  $\omega/\omega_0 \sim 1$  simplification leads to the scattering rate

$$\Gamma_{sc}(\mathbf{r}) = \frac{3\pi c^2}{2\hbar\omega_0^3} \left( \frac{\gamma_0}{\delta} \right)^2 I(\mathbf{r}). \quad (2.9)$$

As absorption leads to a momentum transfer from a photon to an atom, this is an important feature for cooling atoms e.g. in mentioned radiation-pressure traps. However, once the atoms are cooled the absorption of a photon increases the kinetic energy of the atom and thus heats up the atomic sample. Consequently, the scattering rate should be lowered

<sup>2</sup>Otherwise the full equations must be considered in combination with effects of different atomic orbitals [64].



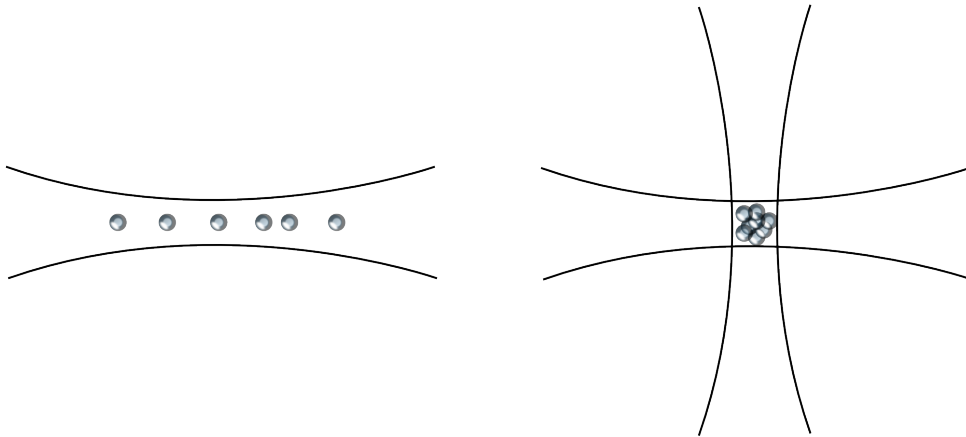


**Figure 2.3:** Illustration of single (left) and crossed (right) red detuned laser beams. Atoms are trapped in the region of the maximal intensity which is axial for a single beam and in the foci of two beams for a crossed beam trap.

once the atoms are trapped. As  $\Gamma_{sc} \sim 1/\delta^2$  large detuning is used in optical dipole traps to reduce the scattering rate responsible for heating of the cooled atoms [71, 72].

In general atoms have multiple electronic transitions which have to be accounted for in the dipole matrix element and lead to a state-dependent polarizability. Consequently, the trapping potentials are unique for each trapped particle species. For a derivation of the trapping with a multi-level ansatz see [64].

## 2.2 Optical dipole trap

As derived in the previous chapter, the dipole potential attracts particles towards the intensity maxima when the laser is red detuned. The spatial intensity of a Gaussian laser beam propagating in  $z$ -direction is described by

$$I(r, z) = I_0 \frac{w_0^2}{w^2(z)} \exp\left(-\frac{2r^2}{w^2(z)}\right), \quad (2.10)$$

where  $r$  denotes the radial distance from the beam axis,  $I_0$  is the peak intensity at  $r = 0$ ,  $z = 0$  and the  $1/e^2$  radius  $w$  depends on the  $z$ -coordinate

$$w(z) = w_0 \sqrt{1 + z^2/z_R^2}. \quad (2.11)$$

The waist  $w_0$  is thereby the minimal radius of the laser beam and  $z_R = \pi w_0^2/\lambda$  is the Rayleigh length. When the laser is tuned below the atomic transition the atoms are trapped axial in a single beam where the intensity is maximal and the dipole potential is minimal (see Eq. 2.8).

Due to the additive character of the intensities, two crossed laser beams attract the particle in their foci. Consequently, Gaussian crossed laser beams represent the easiest way of three-dimensional spatial confinement. The schematic trap types are shown in Fig. 2.3. Because of the ratio between the Rayleigh length and the radial waist  $z_R/w_0 = \pi\lambda w_0$  the

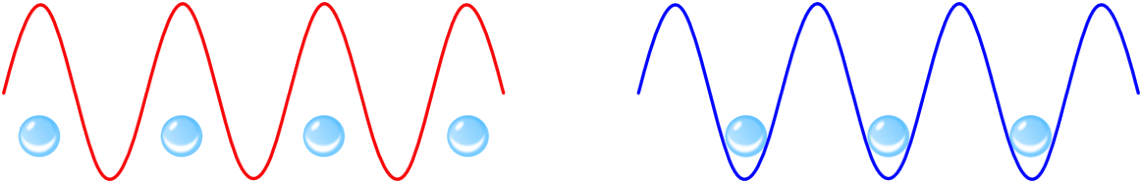


**Figure 2.4:** Trapping of atoms in a periodic 1D lattice potential. Atoms are trapped at anti-nodes when the frequency of the trapping field is red detuned (left) or at nodes for a blue detuning (right).

induced dipole potential in the radial direction is steeper than in the  $z$ -direction. Thus, to stabilize the sample against the gravitational sag, the crossed-beam traps are aligned in the horizontal plane. Tight vertical confinement can additionally minimize the gravity shift. These so-called oblate traps are realized when asymmetric laser beams are used. Their laser profiles have an elliptic instead of a rotational symmetry along the propagation axis and are described by a major and a minor semi-axis  $w_x$  and  $w_y$ , where  $w_x \neq w_y$ .

If the thermal energy  $k_B T$  of the atomic sample is much smaller than the potential depth, the atomic cloud is located around the trap center ( $r = 0, z = 0$ ) where the dipole potential is well approximated by a cylindrically symmetric harmonic potential. Inserting the intensity  $I(r, z)$  from Eq. (2.10) into Eq. (2.8) and expanding the resulting potential to second order in  $r$  and  $z$  around  $r = 0, z = 0$  yields the expression

$$V_{\text{dip}}(r, z) \approx -V_{\text{dip},0} \left( 1 - 2\frac{r^2}{w_0^2} - \frac{z^2}{z_R^2} \right) = -V_{\text{dip},0} + \frac{1}{2}m(\omega_r^2 r^2 + \omega_z^2 z^2), \quad (2.12)$$

where  $V_{\text{dip},0} = |\frac{3\pi c^2}{2w_0^3} \frac{\gamma_0}{\delta} I_0|$ . The harmonic confinement is characterized by radial and axial oscillation frequencies  $\omega_r$  and  $\omega_z$  of a trapped atom of a mass  $m$

$$\omega_r = \sqrt{\frac{4V_{\text{dip},0}}{mw_0^2}}, \quad \omega_z = \sqrt{\frac{2V_{\text{dip},0}}{mz_R^2}}. \quad (2.13)$$

## 2.3 Optical lattices

When two counter propagating laser beams of the same wavelength  $\lambda$  interfere, a 1D standing wave of period  $a = \lambda/2$  is formed<sup>3</sup>, where commonly  $a$  is called the lattice constant. Depending on the detuning of the laser frequency with respect to the atomic resonance, the interaction between the atom and the oscillating electric field attracts the atoms to the anti-nodes or to the nodes of the standing wave, similar to the mechanism leading to dipole trapping. As a result the atoms experience a periodic potential similar to electrons in a crystal as depicted in Fig. 2.4. Due to this analogy, these light potentials are referred to as optical lattices and the nodes/anti-nodes, where the particles are trapped, as lattice sites.

The interference of two identical red-detuned laser beams in  $z$ -direction leads to a potential<sup>4</sup>

$$V(r, z) = -V_{\text{lat},0} \exp\left(-\frac{2r^2}{w^2(z)}\right) \cos^2(kz), \quad (2.14)$$

<sup>3</sup>By changing the angle between two interfering beams away from  $180^\circ$  the periodicity can be increased to values larger than  $\lambda/2$  [73, 74].

<sup>4</sup>In the case of blue-detuning the potential reads  $V(r, z) = V_{\text{lat},0} \exp\left(-\frac{2r^2}{w^2(z)}\right) \sin^2(kz)$ , where a positive sign accounts for detuning  $\delta > 0$  and  $\cos(kz)$  was substituted by  $\sin(kz)$  such that  $z = 0$  still corresponds to a lattice site.

where  $k = 2\pi/\lambda = \pi/a$  is the laser wavelength and  $V_{\text{lat},0}$  is four times larger than the maximal dipole potential of the single laser beam  $V_{\text{dip},0}$  from Eq. (2.12). This is a consequence of the superposition principle, due to which the resulting electric field is a sum of the individual fields, the intensity  $I \sim |E|^2$  is thus four times larger than in the single laser beam. Consequently,  $V_{\text{lat},0} \sim 4I_0$  and hence  $V_{\text{lat},0} = 4V_{\text{dip},0}$ .

Optical lattices are commonly characterized by the maximal potential depth in units of the recoil energy  $E_r = \hbar^2 k^2 / 2m$ , the scale of the thermal energy increase per atom-photon scattering process,

$$s = \frac{V_{\text{lat},0}}{E_r} = \frac{3\pi c^2 \gamma_0}{2w_0^3 |\delta|} 4I_0 \frac{2m}{\hbar^2 k^2}. \quad (2.15)$$

Since the absolute value of the detuning of a laser  $|\delta| = |\omega - \omega_0|$  depends on the atomic resonance frequency, each particle species experiences different potentials for a fixed laser frequency  $\omega$ . Therefore, if a mixture of atoms is loaded into a single lattice each type of bosons experiences a different potential depth  $s$ .

For sufficiently strong optical lattices the periodic cos-potential can be approximated by a parabolic confinement at each lattice site. Close to the trap center the Gaussian beam profile can be neglected and the approximate on-site potential reads

$$V(r=0, z) = -V_{\text{lat},0} \cos^2(kz) \approx V_{\text{lat},0}(-1 + k^2 z^2).$$

Since a global potential is only defined up to an additive constant, we can add  $V_{\text{lat},0}$  and write

$$V(r=0, z) = V_{\text{lat},0} k^2 z^2 = \frac{1}{2} m \omega_{\text{lat},0}^2 z^2, \quad (2.16)$$

with the trapping frequency

$$\omega_{\text{lat},0} = \sqrt{\frac{2V_{\text{lat},0} k^2}{m}} = \sqrt{s} \frac{\hbar k^2}{m}. \quad (2.17)$$

Away from the trap center the Gaussian beam shape leads to an exponential reduction of the potential and to corrections of the on-site lattice frequencies:

$$V(r, z) = -V_{\text{lat},0} \cos^2(kz) \exp\left(-\frac{2r^2}{w^2(z)}\right) \approx V_{\text{lat},0} k^2 z^2 \exp\left(-\frac{2r^2}{w^2(z)}\right) = \frac{1}{2} m \omega_{\text{lat}}^2(r) z^2, \quad (2.18)$$

where

$$\omega_{\text{lat}}(r) = \omega_{\text{lat},0} \exp\left(-\frac{r^2}{w^2(z)}\right). \quad (2.19)$$

For typical experimental parameters, i.e. beam waist  $w_0 = 150$  nm, laser wavelength  $\lambda = 1064$  nm and lattice size of  $(0.2 \times 0.2 \times 0.2)$  mm,  $\frac{r^2}{w^2(z)} = 0.13$  and the corrections  $\exp\left(-\frac{r^2}{w^2(z)}\right) \approx 0.88$  reduce the trapping frequency  $\omega_{\text{lat},0}$  by 12% at the edges of the lattice. Hence, the Gaussian beam shape can be neglected or approximated harmonically and absorbed into an overall harmonic trapping incorporating the magnetic trap present in the most experiments. Therefore we drop for the moment the corrections and assume a homogeneous laser intensity.

Addition of counter propagating laser pairs in  $x$  and  $y$  directions leads to 2 and 3 dimensional lattices (see Fig. 2.5). The resulting 2D potential reads

$$V(x, y) = -V_{\text{lat},0} (\cos^2(kx) + \cos^2(ky) + 2\mathbf{e}_x \mathbf{e}_y \cos(\phi) \cos(kx) \cos(ky)). \quad (2.20)$$

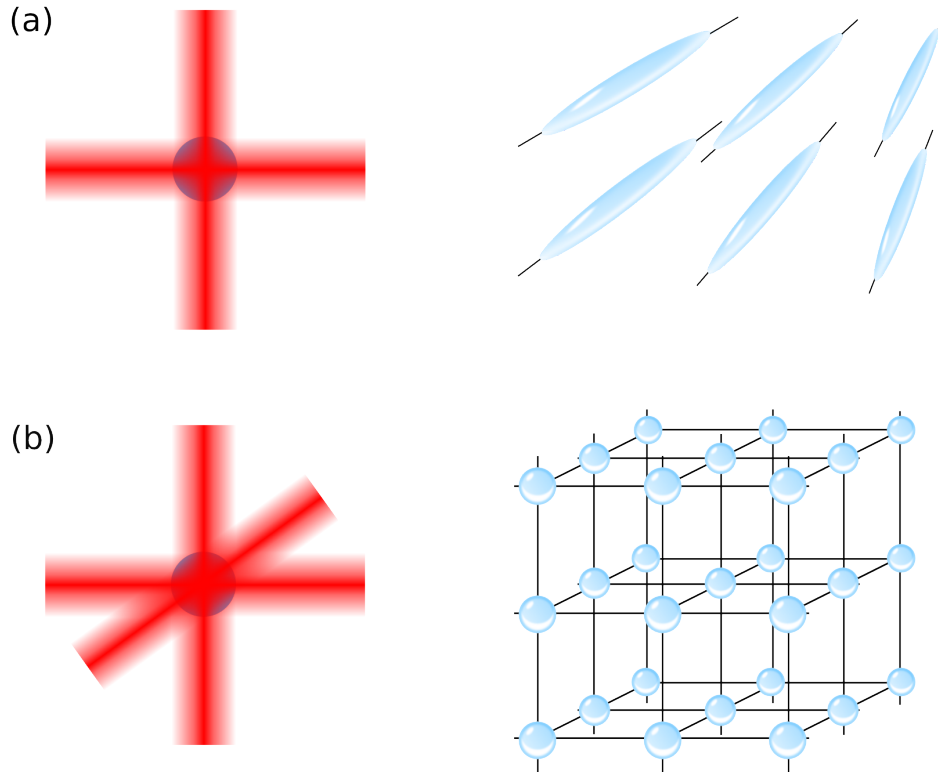


**Figure 2.5:** Cartoon of two (a) and three (b) dimensional optical lattices. (a) A superposition of two pairs of counter-propagating laser beams (red) polarized  $90^\circ$  with respect to each other confines the atoms in the  $x$  and  $y$  directions. The freedom in  $z$  direction gives rise to a final tube structure of atomic clouds (blue). (b) Adding an additional standing wave in  $z$  direction leads to a simple cubic structure in which atoms (blue) are located at nodes.

Here  $k$  is the laser wave vector,  $\mathbf{e}_i$  is the polarization vector in  $i$  direction and  $\phi$  is a time phase between the interfering laser fields. In the case of superposition of lasers with polarization perpendicular to each other the last term of Eq. (2.20) vanishes and the potential yields a simple cubic lattice of period  $\lambda/2$ . Changing the angle between the polarization vectors gives access to hexagonal lattices with a periodicity depending on the angle and the phase [75]. In all 2D setups the particles are allowed to propagate freely in  $z$  direction, which breaks the symmetry and leads to a tube-like structure as shown in Fig. 2.5(a). Analogously, a superposition of three identical<sup>5</sup> standing waves orthogonal to each other with mutually orthogonal polarization leads to a potential

$$V(x, y, z) = -V_{\text{lat},0} (\cos^2(kx) + \cos^2(ky) + \cos^2(kz)) \quad (2.21)$$

for red-detuned lasers when the Gaussian beam profiles are neglected.

<sup>5</sup>In order to minimize the undesirable effect of residual interference in experiments, the standing waves are usually chosen to have slightly different wavelength and the resulting lattice potential is  $V(x, y, z) = -V_{\text{lat},x} \cos^2(kx) - V_{\text{lat},y} \cos^2(ky) - V_{\text{lat},z} \cos^2(kz)$  [76].

# 3. Bose-Einstein condensates

## 3.1 The Bose-Hubbard model

The simplest mathematical description of interacting bosonic particles on a lattice is given by the Bose-Hubbard model [9, 10]. Similar to the Hubbard model for fermionic systems, the Bose-Hubbard Hamiltonian includes short range interactions, kinetic energy and the lattice structure - the ingredients sufficient to describe the insulating and the superfluid regimes and the quantum phase transition between them.

In second quantization the Bose-Hubbard Hamiltonian has the form

$$\hat{\mathcal{H}} = -J \sum_{\langle ij \rangle} (\hat{b}_i^\dagger \hat{b}_j + h.c.) + \frac{U}{2} \sum_i \hat{n}_i (\hat{n}_i - 1) - \sum_i (\mu - V_{i,\text{trap}}) \hat{n}_i, \quad (3.1)$$

where the operator  $\hat{b}_i^\dagger$  ( $\hat{b}_i$ ) creates (annihilates) a boson at site  $i$ . The first term describes the nearest neighbor hopping in a periodic potential, where  $\sum_{\langle ij \rangle}$  represents the sum over the nearest neighbors and  $J$  is the tunneling strength. The second term represents the on-site repulsion between the particles where  $U$  denotes the interaction strength. The last term contains the chemical potential  $\mu$ , which fixes the particle density in the system, and an optional confining potential  $V_{i,\text{trap}}$ , which takes account of inhomogeneities such as additional trapping potentials or modulations due to the Gaussian profile of the laser beams which form the optical lattice. The most common trapping potentials are parabolic:  $V_{i,\text{trap}} = \frac{1}{2} m \omega^2 a^2 |\mathbf{r}_i - \mathbf{r}|^2$ , where  $m$  is the particle mass,  $a$  is the lattice constant,  $\omega$  the trap frequency,  $\mathbf{r}_i$  is the coordinate of the given lattice site  $i$  and  $\mathbf{r}$  is the center of the harmonic potential.

In this section the derivation of the Bose-Hubbard model will be given. The discussion is organized as follows: first the Hamiltonian of non-interacting particles in a periodic potential (the first term of Eq. (3.1)) will be derived and solved. The relevant system parameters are explained and an overview of the approximations and limitations of the model will be given. Subsequently, the homogeneous non-interacting system is extended to a cylindrically symmetric trapping potential (the last term of Eq. (3.1)) and the implications for the phase diagram are discussed. The incorporation of interactions and a brief summary of the results and approximations complete the model and conclude the section.

### 3.1.1 Non-interacting particles in homogeneous systems

We begin our derivation of the Bose-Hubbard model with the simplest problem: non-interacting particles in a periodic potential. We will consider a sinusoidal lattice potential which is created in optical lattices - the system investigated in this thesis. The non-interacting problem does not depend on the particle statistics and the following results can be applied to bosons as well as fermions.

In the field operator representation the single-particle Hamiltonian reads

$$\mathcal{H} = \int d\mathbf{r} \hat{\Psi}^\dagger(\mathbf{r}) \left[ -\frac{\hbar^2}{2m} \nabla^2 + V(\mathbf{r}) \right] \hat{\Psi}(\mathbf{r}), \quad (3.2)$$

where  $V(\mathbf{r})$  denotes the lattice potential and  $\hat{\Psi}(\mathbf{r})$  and  $\hat{\Psi}^\dagger(\mathbf{r})$  are the bosonic field operators that annihilate/create a particle at position  $\mathbf{r}$  and satisfy the canonical commutation relations

$$[\hat{\Psi}(\mathbf{r}), \hat{\Psi}^\dagger(\mathbf{r}')] = \delta(\mathbf{r} - \mathbf{r}') \quad [\hat{\Psi}(\mathbf{r}), \hat{\Psi}(\mathbf{r}')] = 0 = [\hat{\Psi}^\dagger(\mathbf{r}), \hat{\Psi}^\dagger(\mathbf{r}')] . \quad (3.3)$$

The many-body Hamiltonian of  $N$  non-interacting particles is a direct sum of the single-particle Hamiltonians Eq. (3.2)

$$\mathcal{H}_N = \sum_{i=1}^N \mathcal{H}, \quad (3.4)$$

which can be solved exactly. The resulting eigenenergies are direct sums of the single-particle eigenenergies and the corresponding many-body ground state is a symmetrized tensor product of single-particle eigenfunctions. Thus, we can tackle the non-interacting many-body problem by solving the one-body Hamiltonian.

#### Bloch states

A description of a non-interacting particle in a periodic potential was provided by Felix Bloch. The detailed derivations and proofs can be found in every quantum mechanical condensed matter theory book (see e.g. [77–79]). In the following the results will be summarized and applied to a simple cubic optical lattice. Following Sec. 2.3, a homogeneous simple cubic lattice corresponds to a cosinusoidal lattice potential (see Eq. (2.21))

$$V(\mathbf{r}) = -V_0 \sum_{l=x,y,z} \cos^2(kl).$$

where  $k$  denotes the laser momentum corresponding to the laser wavelength  $\lambda$ , namely  $k = 2\pi/\lambda = \pi/a$ , and  $V_0 \equiv V_{\text{lat},0}$ .

The lattice potential is a sum of terms depending on one coordinate each and the Hamiltonian Eq. (3.2) decouples into independent identical differential equations for  $x$ ,  $y$  and  $z$ . The solution of a homogeneous 3D problem is thus reduced to a solution of a 1D Schrödinger equation

$$\left[ -\frac{\hbar^2}{2m} \nabla^2 + V(x) \right] \phi_q^{(n)}(x) = E_q^{(n)} \phi_q^{(n)}(x), \quad (3.5)$$

where  $n \in \mathbb{N}$  labels the eigenstates/eigenenergies in ascending order and  $q$  denotes a quantum number, which we explain next. According to Bloch's theorem, the eigenvectors  $\phi_q^{(n)}(x)$  corresponding to eigenenergies  $E_q^{(n)}$ , called Bloch wave functions, are

$$\phi_q^{(n)}(x) = e^{iqx} \cdot u_q^{(n)}(x), \quad (3.6)$$

where the functions  $u_q^{(n)}(x)$  possess the periodicity of the lattice, i.e.  $u_q^{(n)}(x+a) = u_q^{(n)}(x)$  and  $q$  is a quantum number (quasi-momentum) within the first Brillouin zone (1. BZ). Due to periodic boundary conditions, the Brillouin Zone is a discrete set of quantum numbers  $q$

$$q = \frac{2\pi}{L}m, \quad m \in \mathbb{N} \quad L \text{ is even: } -\frac{L}{2} \leq m \leq \frac{L}{2} \quad L \text{ is odd: } -\frac{L-1}{2} \leq m \leq \frac{L-1}{2} \quad (3.7)$$

Before we proceed with the solution of the Schrödinger equation, some important properties of the Bloch wave functions should be mentioned. The Bloch wave functions are the real space representation of the Bloch states

$$\text{Bloch state: } |q\rangle \quad \text{Bloch function: } \langle x|q\rangle = \phi_q(x) \quad (3.8)$$

The Bloch function is periodic not only in position space but also in momentum space. With  $K'$  being a multiple of the reciprocal lattice vector  $K = 2\pi/a$  the Bloch function can be expanded as

$$\phi_q^{(n)}(x) = \sum_{K'} b_{q-K'}^{(n)} e^{i(q-K')x}. \quad (3.9)$$

Consequently, the Bloch function with a quasi-momentum shifted by  $K$  can be written

$$\phi_{q+K}^{(n)}(x) = \sum_{K'} b_{q+K-K'}^{(n)} e^{i(q+K-K')x} \stackrel{K''=K'+K}{=} \sum_{K''} b_{q-K''}^{(n)} e^{i(q-K'')x} = \phi_q^{(n)}(x) \text{ qed.} \quad (3.10)$$

And last but not least, the Bloch functions form a complete orthonormal basis

$$\int dx \phi_q^{*(n)}(x) \phi_{q'}^{(n')}(x) = \delta_{q,q'} \delta_{n,n'} \quad \sum_q \phi_q^{*(n)}(x) \phi_q^{(n')}(x') = \delta(x-x') \delta_{n,n'}. \quad (3.11)$$

These properties will be used in further calculations.

Inserting ansatz (3.6) into Eq. (3.5) leads to a differential equation for  $u_q^{(n)}(x)$

$$\left[ -\frac{\hbar^2}{2m}(\nabla + iq)^2 + V(x) \right] u_q^{(n)}(x) = E_q^{(n)} u_q^{(n)}(x). \quad (3.12)$$

Every integrable periodic function  $f(x)$  with period  $a$  can be written as a discrete Fourier series  $f(x) = \sum_n f_n e^{2iknx}$ , where  $k = \pi/a$  and  $n \in \mathbb{Z}$ . Using this fact we can express the lattice potential and the function  $u_q^{(n)}(x)$  as follows

$$V(x) = \sum_r V_r e^{2ikrx} \quad \text{and} \quad u_q^{(n)}(x) = \sum_l c_l^{(n,q)} e^{2iklx}. \quad (3.13)$$

The coefficients  $V_r$  can be easily estimated by comparing the expression Eq. (3.13) with the lattice potential

$$V(x) = -V_0 \cos^2(kx) = -\frac{V_0}{4} (e^{ikx} + e^{-ikx})^2 = -\frac{V_0}{4} (e^{2ikx} + e^{-2ikx}) - \frac{V_0}{2}. \quad (3.14)$$

The constant term can be neglected, as it only leads to a constant shift of the energy spectrum, and we are left with  $V_r = -V_0/4$  for  $r = 1$  and  $-1$ . In this representation the potential energy term in Eq. (3.12) becomes

$$\begin{aligned} V(x)u_q^{(n)}(x) &= \sum_{l,r} V_r e^{2i(r+l)kx} c_l^{(n,q)} = -\frac{V_0}{4} \sum_l c_l^{(n,q)} (e^{2i(l+1)kx} + e^{2i(l-1)kx}) \\ &= -\frac{V_0}{4} \sum_l e^{2ilkx} (c_{l-1}^{(n,q)} + c_{l+1}^{(n,q)}). \end{aligned} \quad (3.15)$$

In the last step a shift of indices was performed. Analogously, the kinetic term of Eq. (3.12) reads

$$-\frac{\hbar^2}{2m}(\nabla + iq)^2 u_q^{(n)}(x) = \frac{\hbar^2}{2m} \sum_l (q + 2kl)^2 c_l^{(n,q)} e^{2ilkx}. \quad (3.16)$$

Inserting the transformed kinetic and potential energy terms (Eq. (3.16) and (3.15)) together with the Fourier transform of the function  $u_q^{(n)}(x)$  from Eq. (3.13) into the Schrödinger equation Eq. (3.12) leads to a set of coupled differential equations

$$\begin{aligned} & \sum_l \left[ \frac{\hbar^2}{2m} (q + 2kl)^2 c_l^{(n,q)} - \frac{V_0}{4} (c_{l-1}^{(n,q)} + c_{l+1}^{(n,q)}) \right] e^{2ilkx} = E_q^{(n)} \sum_l c_l^{(n,q)} e^{2ilkx} \\ \Leftrightarrow & \sum_l \left[ \left( \frac{\hbar^2}{2m} (q + 2kl)^2 - E_q^{(n)} \right) c_l^{(n,q)} - \frac{V_0}{4} (c_{l-1}^{(n,q)} + c_{l+1}^{(n,q)}) \right] e^{2ilkx} = 0. \end{aligned} \quad (3.17)$$

Since plane waves form an orthogonal basis, the coefficients within the summation in Eq. (3.17) need to vanish separately for each  $l$ . Thus, the Schrödinger equation decomposes into a set of linear algebraic equations, one for each  $l$

$$\frac{\hbar^2}{2m} (q + 2kl)^2 c_l^{(n,q)} - \frac{V_0}{4} (c_{l-1}^{(n,q)} + c_{l+1}^{(n,q)}) = E_q^{(n)} c_l^{(n,q)}. \quad (3.18)$$

The solution of such a set of equations can be reduced to diagonalization of the tridiagonal matrix

$$\begin{bmatrix} \ddots & & & & 0 \\ \ddots & E_r (q/k - 2)^2 & -V_0/4 & & \\ & -V_0/4 & E_r (q/k)^2 & -V_0/4 & \\ & & -V_0/4 & E_r (q/k + 2)^2 & \ddots \\ 0 & & & & \ddots & \ddots \end{bmatrix} \quad (3.19)$$

where  $E_r = \hbar^2 k^2 / 2m$  denotes the recoil energy. The eigenvalue  $E_q^{(n)}$  for a certain momentum  $q$  represents the eigenenergy of the particle in the  $n^{\text{th}}$  energy band. The corresponding eigenvector defines the coefficient vector  $c^{(n,q)}$  which in turn determines the Bloch wave function through Eq. (3.13) and (3.6). The complete  $n^{\text{th}}$  energy band is formed by the set of eigenvalues corresponding to the quasi-momenta within the 1. BZ.

In practice, a diagonalization of the infinite dimensional matrix is impossible. Truncating the matrix in Eq. (3.19) at an appropriate  $l_{\text{max}}$ , such that  $-l_{\text{max}} \geq l \geq l_{\text{max}}$ , makes the computational effort feasible. Thereby one has to pay attention, that the reduction of the matrix dimension is justified, i.e. the neglected coefficients  $c_l^{(n,q)}$  with  $l \geq |l_{\text{max}}|$  are sufficiently small. This is the case only when the lowest energy bands are considered. The results are presented in Fig. 3.1.

### Wannier states

The Bloch functions are completely delocalized over the lattice. To describe a particle localized at a certain lattice site  $i$  it is more useful to change to an orthonormal basis of Wannier functions. They are real space representations of the Wannier states

$$\text{Wannier state: } |i\rangle \quad \text{Wannier function: } \langle x|i\rangle = \omega(x - x_i). \quad (3.20)$$



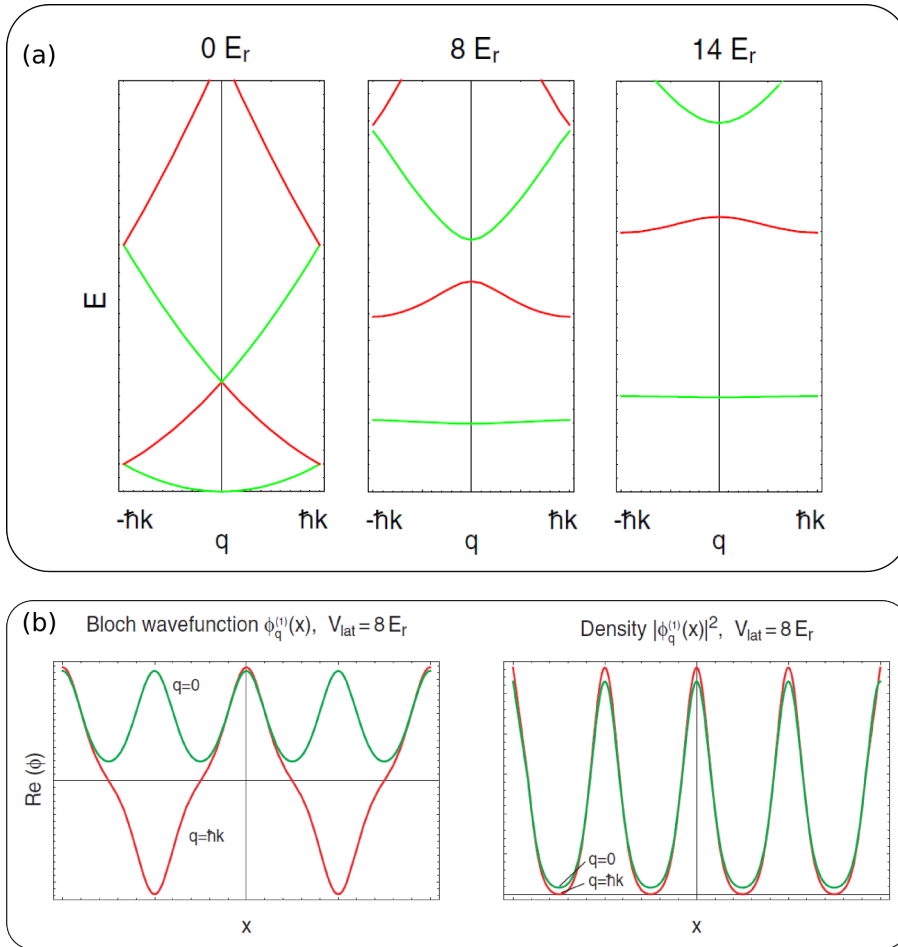


**Figure 3.1:** Band structure and Bloch states of an optical lattice, see [75]. (a) Energy as a function of the quasi-momentum  $q$  within the 1. BZ for different lattice depths in units of the recoil energy. Different colors correspond to different energy bands.  $0 E_r$  represents the free particle quadratic dispersion. With increasing lattice depth the energy gap between different bands appears and increases. The deeper the lattice the better can the cosinusoidal potential be approximated by a parabolic potential at each site, the bands become flatter and the energy gap proportional to  $\hbar\omega_{\text{lat},0}$  - the energy level spacing of harmonic confinement (see Eq. (2.17)). (b) The real part and the probability density of the Bloch states at  $q = 0$  and  $q = \hbar k$  for lattice depth  $8 E_r$ .

Because the Bloch wave functions are periodic in quasi-momentum space with a periodicity of the reciprocal lattice vector, they can be written as a Fourier series

$$\phi_q^{(n)}(x) = \sum_{x_i} \omega^{(n)}(x - x_i) e^{iqx_i}, \quad (3.21)$$

where  $x_i = ai$  with  $a$  being the lattice constant and  $i = 1 \dots L$  the index of a site. The inverse Fourier transform of this equation gives the Wannier function

$$\omega^{(n)}(x - x_i) = \frac{1}{\sqrt{L}} \sum_q^{1.BZ} e^{-iqx_i} \phi_q^{(n)}(x). \quad (3.22)$$

The orthogonality relation of the Wannier functions is a consequence of the orthogonality of the Bloch waves

$$\int dx \omega^{*(n)}(x - x_i) \omega^{(n')}(x - x_j) = \frac{1}{L} \sum_{k,l} e^{i(kx_i - lx_j)} \int dx \phi_k^{*(n)}(x) \phi_l^{(n')}(x) = \delta_{x_i, x_j} \delta_{n, n'}. \quad (3.23)$$

In the last step Eq. (3.11) was used together with the relation  $\frac{1}{L} \sum_k^{1.BZ} e^{ik(x_i - x_j)} = \delta_{x_i, x_j}$ . Thus, the Wannier functions span an orthonormal basis in the subspace of each Bloch energy band  $n$ . Including all bands, the Wannier basis is complete  $\sum_{i,n} |i, n\rangle \langle i, n| = \mathbf{1}$ . In contrast to the Bloch waves, they are not eigenstates of the Hamiltonian in Eq. (3.5). However, due to their strong localization around a certain position, they are commonly used for calculation of on-site interactions and tunneling probabilities between neighboring sites.

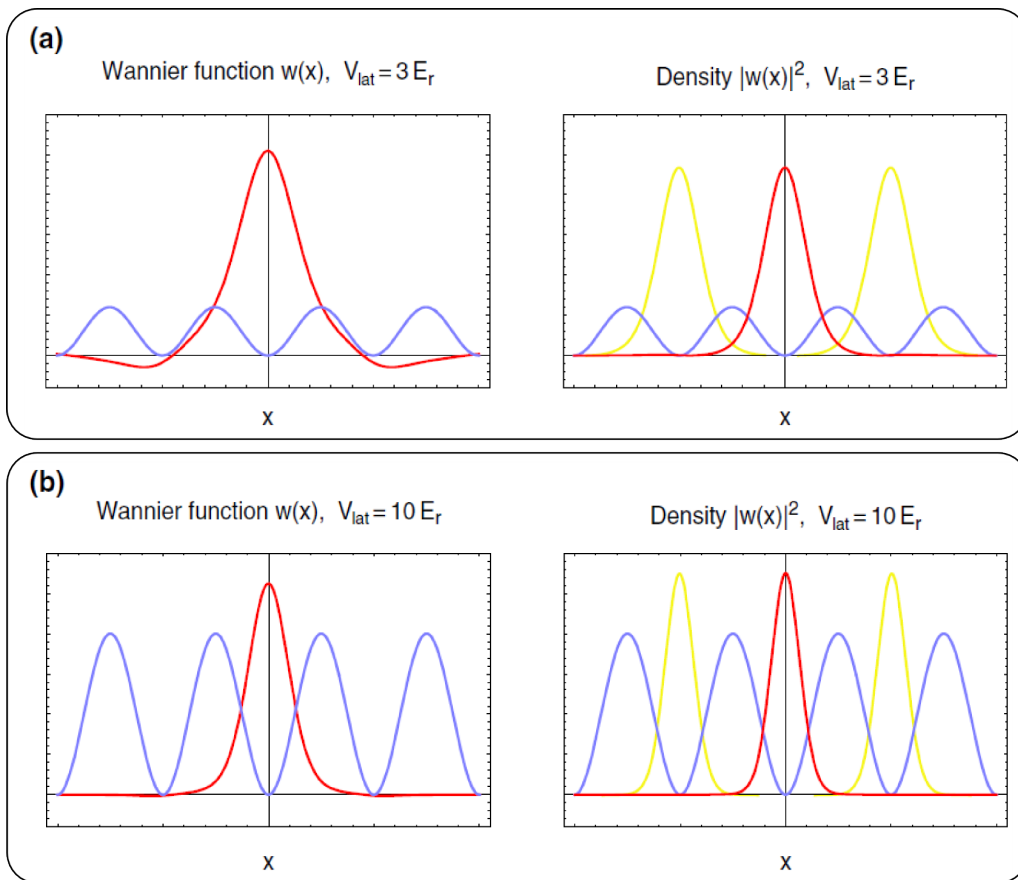


**Figure 3.2:** Wannier states and their probability density for a sinusoidal lattice potential (represented by blue line) of depth  $3 E_r$  (a) and  $10 E_r$  (b), see [75]. With increasing potential depth the side lobes of the Wannier function decrease and the shape is approximately a Gaussian. Due to vanishing side lobes, the overlap between the Wannier states of neighboring sites (yellow functions) decreases.

Fig. 3.2 shows the Wannier functions for different lattice depth  $V_0$ . For shallow lattices the Wannier functions have a finite contribution at neighboring sites. These side lobes indicate a finite probability to find a particle at these sites as well. This probability vanishes with increasing lattice depth, where the Wannier functions becomes approximately Gaussian and decays exponentially away from the localization center.

### Hopping integral

We can expand the field operators in the basis of Wannier functions

$$\hat{\Psi}(x) = \sum_{n,i} \omega^{(n)}(x - x_i) \hat{b}_i, \quad (3.24)$$

where  $i$  denotes a lattice site and the operator  $\hat{b}_i$  annihilates a particle at site  $i$ . Substituting this definition into Eq. (3.2) the Hamiltonian can be rewritten

$$\begin{aligned} \mathcal{H} &= \int dx \hat{\Psi}^\dagger(x) \left[ -\frac{\hbar^2}{2m} \nabla^2 + V(x) \right] \hat{\Psi}(x) = \\ &= \int dx \sum_{i,j,n} \omega^{*(n)}(x - x_i) \hat{b}_i^\dagger \left[ -\frac{\hbar^2}{2m} \nabla^2 + V(x) \right] \omega^{(n)}(x - x_j) \hat{b}_j = \\ &= \sum_{i,j,n} J_{ij}^{(n)} \hat{b}_i^\dagger \hat{b}_j, \end{aligned} \quad (3.25)$$

with the hopping integral

$$J_{ij}^{(n)} = \int dx \omega^{*(n)}(x - x_i) \left[ -\frac{\hbar^2}{2m} \nabla^2 + V(x) \right] \omega^{(n)}(x - x_j). \quad (3.26)$$

The  $\nabla$  operator in the Hamiltonian acts on the Wannier function, leaving the band index unchanged. Thus, due to the orthogonality of the Wannier functions of different bands, only functions from the same band contribute to the integral. For these reasons the band index of the Wannier functions contributing to different field operators is chosen to be the same. The exact values for  $J$  are obtained by diagonalizing numerically Eq. (3.19) for each lattice depth in order to get the Bloch functions, constructing the Wannier functions from the Bloch functions (3.22) and finally carrying out the integration in Eq. (3.26). Until now no approximations have been assumed. In most cases, however, a calculation of the exact integral is not needed. Thus in the next step some common approximations will be introduced. An overview of possible computation of the corresponding  $J$  will be given later in this section.

### Lowest band approximation

We consider a situation in which the lattice potential is so deep that the energy gap between the first and the second Bloch band is much larger than the thermal energy and any other energy scale arising from interactions or tunneling. This implies that the population of higher bands is vanishingly small or even absent, such that the systems is accurately described by the lowest band only. The parameter range for which this approach is valid results from the following consideration: We estimate the energy gap by approximating the cosinusoidal on-site potential harmonically, namely (compare Eq. (2.16))

$$V(x) = -V_{\text{lat},0} \cos^2(kx) \approx V_{\text{lat},0} k^2 x^2 = \frac{1}{2} m \omega_{\text{lat},0} k^2 x^2 \quad (3.27)$$

with  $\omega_{\text{lat},0} = \sqrt{s} \hbar k^2 / m$ , the lattice depth  $s = V_{\text{lat},0} / E_r$  and  $E_r = \hbar^2 k^2 / 2m$ . In this limit the lower Bloch bands nearly correspond to the energy levels of the quantum mechanical oscillator separated by energy gaps  $\hbar \omega_{\text{lat},0}$ . Consequently, the lowest band approximation is valid if kinetic and interaction energy per particle satisfy the relation:  $E_{\text{kin}}, E_{\text{int}} \ll \hbar \omega_{\text{lat},0}$

(we will verify this constraint for common experimental parameters in Sec. 3.1.3). Then the hopping integral is well described by taking only the lowest band into account

$$J_{ij}^{(0)} = \int dx \omega^{*(0)}(x - x_i) \left[ -\frac{\hbar^2}{2m} \nabla^2 + V(x) \right] \omega^{(0)}(x - x_j). \quad (3.28)$$

Restricting the integration to a single band reduces numerical efforts, however it does not circumvent the band structure calculations. In common experiments with  $^{87}\text{Rb}$  and  $^{41}\text{K}$  at laser wavelength 1064 nm (red detuned) or 738 nm (blue detuned) the contribution of higher bands to the hopping integral is at least one order of magnitude smaller and the lowest band approximation is justified for lattice depth  $s \geq 5$ . However, even if small, the virtual bosonic excitations to higher bands are essential to describe e.g. enhanced repulsion among bosons and thus enlarged Mott insulating regions due to presence of fermions in Bose-Fermi mixtures [80, 81]. Nevertheless, for the physics investigated in this work the lowest band approximation is sufficient and we will drop the system parameter's band index.

### Tight-binding approximation

The tight-binding regime refers to an approach in solid-state physics where the many-body wave function is approximated as a superposition of single-particle wave functions of electrons tightly bound to each lattice site. Corrections to the atomic limit are usually treated perturbatively [77]. The similarity between condensed matter theoretical approaches and our calculation lies in the expansion of the field operator, which describes the position of a particle, in the localized Wannier basis.

In deep lattices the overlap between the Wannier functions decays with increasing relative distance between two respective sites. Thus, it is expected that the contribution from the nearest-neighbor hopping represents the dominant hopping matrix element. Neglecting tunneling processes over further distances than between nearest neighbors in Eq. (3.28) constitutes the tight-binding approximation. With this simplification the summation in Eq. (3.25) reduces to  $i = j$  and  $i, j$  being nearest neighbors

$$\begin{aligned} \mathcal{H} &= \sum_{i,j} \left( J_{ij}^{(0)} \delta_{ij} - J_{ij}^{(0)} (1 - \delta_{ij}) \right) \hat{b}_i^\dagger \hat{b}_j \\ &= \varepsilon \sum_i \hat{n}_i - J \sum_{\langle ij \rangle} (\hat{b}_i^\dagger \hat{b}_j + h.c.), \end{aligned}$$

where  $\hat{n}_i = \hat{b}_i^\dagger \hat{b}_i$  denotes the particle number operator and  $\langle ij \rangle$  summation over pairs of neighboring sites. From the first to the second line the indices representing the site dependency of the hopping integrals were dropped. This is true for homogeneous systems and systems with slowly varying potential modulations. Additionally, the hopping integrals were renamed distinguishing the on-site ( $\varepsilon$ ) from the neighboring site ( $J$ ) term. The first term of the upper equation is just a global constant  $\sum_i \varepsilon \hat{n}_i = \varepsilon N$ , where  $N$  is the particle number, which yields only a shift of the total energy of the system and can be neglected. The Hamiltonian of the non-interacting homogeneous system in the tight-binding approximation thus reads

$$\mathcal{H} = -J \sum_{\langle ij \rangle} (\hat{b}_i^\dagger \hat{b}_j + h.c.) \quad (3.29)$$

with the hopping integral  $J \equiv J_{ij}$  Eq. (3.28), assuming only contributions from the lowest band.

### Energy, velocity and tunneling $J$

The Hamiltonian Eq. (3.29) can be easily diagonalized. For this purpose we Fourier transform the creation/annihilation operator

$$\hat{b}_i^\dagger = \frac{1}{\sqrt{L}} \sum_q^{1.BZ} \hat{b}_q^\dagger e^{-iqx_i}. \quad (3.30)$$

Inserting this into the Hamiltonian yields

$$\begin{aligned} \mathcal{H} &= -J \sum_{\langle ij \rangle} \left[ \left( \frac{1}{\sqrt{L}} \sum_q^{1.BZ} \hat{b}_q^\dagger e^{-iqx_i} \right) \left( \frac{1}{\sqrt{L}} \sum_{q'}^{1.BZ} \hat{b}_{q'} e^{iq'x_j} \right) + h.c. \right] \\ &= -J \sum_q^{1.BZ} \hat{b}_q^\dagger \hat{b}_q \frac{1}{L} \sum_{\langle ij \rangle} (e^{iq(x_j-x_i)} + h.c.) - J \sum_{\substack{q, q' \\ q \neq q'}}^{1.BZ} (\hat{b}_q^\dagger \hat{b}_{q'}) \frac{1}{L} \sum_{\langle ij \rangle} e^{i(q'x_j - qx_i)} + h.c.). \end{aligned}$$

The summation over the functions  $\exp\{i(q'x_j - qx_i)\}$  and therefore the entire last term vanishes because  $q \neq q'$  and  $x_i \neq x_j$ . The summation over the pairs  $\langle ij \rangle$  in the first term can be rewritten into the sum over the sites  $i$  and a sum over the corresponding neighbor sites  $j$ :  $\sum_{\langle ij \rangle} = 1/2 \sum_i \sum_{j \text{ n.n. } i}$ .

Thus,

$$\begin{aligned} \mathcal{H} &= -J \sum_q^{1.BZ} \hat{b}_q^\dagger \hat{b}_q \frac{1}{L} \sum_{\langle ij \rangle} (e^{iq(x_j-x_i)} + h.c.) \\ &= -J \sum_q^{1.BZ} \hat{b}_q^\dagger \hat{b}_q \frac{1}{2L} \sum_i \sum_{j \text{ n.n. } i} (e^{iq(x_j-x_i)} + h.c.) \\ &= -J \sum_q^{1.BZ} \hat{b}_q^\dagger \hat{b}_q \frac{1}{2L} \sum_i 2(e^{iqa} + e^{-iqa}) \\ &= -2J \sum_q^{1.BZ} \cos(qa) \hat{b}_q^\dagger \hat{b}_q = \sum_q^{1.BZ} \varepsilon(q) \hat{b}_q^\dagger \hat{b}_q. \end{aligned} \quad (3.31)$$

From the second to the third line we used the relation  $j = i \pm 1$  and thus  $x_j - x_i = x_{i \pm 1} - x_i = \pm a$  with lattice constant  $a = \lambda/2$ . In the last step the function

$$\varepsilon(q) = -2J \cos(qa) \quad (3.32)$$

is introduced which is commonly referred to as the dispersion relation for a 1D lattice.

From the result Eq. (3.31) follows that the non-interacting Hamiltonian is diagonal in quasi-momentum space<sup>1</sup>, namely

$$\mathcal{H}|q\rangle = E(q)|q\rangle, \quad (3.33)$$

with the Bloch states  $|q\rangle$  being the lowest band eigenfunctions,  $E(q) = \varepsilon(q)n_q$  the corresponding eigenenergies and  $n_q = \hat{b}_q^\dagger \hat{b}_q$  the occupation number of the state with quasi-momentum  $q$ .

<sup>1</sup>This agrees with Noether's theorem stating that translational invariance of the lattice corresponds to the momentum conservation, suggesting  $q$  as a good quantum number.

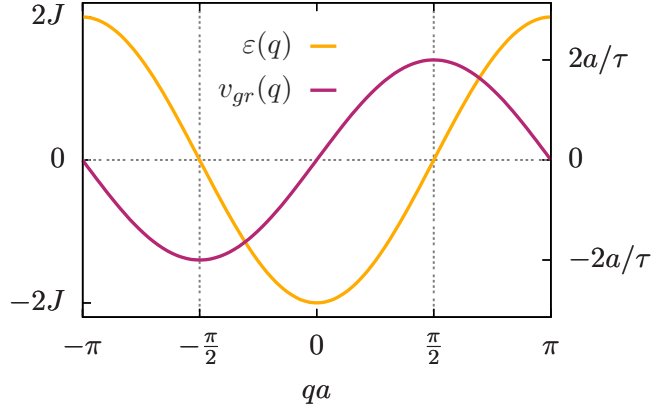


**Figure 3.3:** Dispersion relation  $\varepsilon(q) = -2J \cos(qa)$  and corresponding group velocity  $v_{gr}(q) = \frac{2Ja}{\hbar} \sin(qa)$  in a tight-binding approximation. The left y-axis refers to the dispersion relation and the right axis to the velocity,  $\tau = \frac{\hbar}{J}$  is defined to be the tunneling time.

Due to separability of the lattice potential Eq. (2.21) in  $x, y$  and  $z$  directions, the higher dimensional Hamiltonian can be written as a sum over Hamiltonians for each direction Eq. (3.29), where the pairs  $\langle ij \rangle$  are counted within a corresponding direction. The eigenfunctions are direct products of the 1D eigenfunctions  $|\mathbf{q}\rangle = |q_x, q_y, q_z\rangle$  to the eigenenergies  $E(\mathbf{q}) = E(q_x) + E(q_y) + E(q_z)$ . The 3D dispersion relation is a sum of dispersion relations for each direction:  $\varepsilon(\mathbf{q}) = -2J \sum_{i=x,y,z} \cos(q_i a)$ . This result can be also derived by reconsidering the calculation leading to Eq. (3.31) in higher dimensions.

As for any wave, a group velocity for a single particle possessing momentum  $\mathbf{q}$  can be defined

$$\mathbf{v}_{gr}(\mathbf{q}) = \frac{1}{\hbar} \nabla_{\mathbf{q}} \varepsilon(\mathbf{q}), \quad (3.34)$$

where  $\varepsilon(\mathbf{q})$  represents the dispersion relation. In 1D in the lowest band and the tight-binding approximation  $\varepsilon(q)$  is given by (3.32) and the group velocity becomes

$$v_{gr}(q) = \frac{2Ja}{\hbar} \sin(qa). \quad (3.35)$$

The dispersion relation and the corresponding group velocity are plotted in Fig. 3.3. In contrast to free space, in a lattice within the tight binding approximation the largest energy does not correspond to the maximum velocity. Rather, the maximum group velocity appears at quasi-momenta  $qa = \pm\pi/2$  where the single particle energy is minimal. With  $J$  being the tunneling energy, the corresponding natural time scale for a tunneling process from one site to the neighboring site is  $\sim \frac{\hbar}{J}$ . Defining the tunneling time

$$\tau = \frac{\hbar}{J} \quad (3.36)$$

the possible velocities lie within the range  $[-2a/\tau, 2a/\tau]$ .

The energy difference between the highest and the lowest possible energy within a band is referred to as the bandwidth

$$W = \varepsilon_{\max}(\mathbf{q}) - \varepsilon_{\min}(\mathbf{q}). \quad (3.37)$$

The bandwidth depends on the dimension of the considered system and the tunneling matrix element  $J$ . For the  $d$ -dimensional case  $W = 4Jd$ . Knowing this relation we can calculate  $J$  for a given lattice depth: after having found the Bloch eigenstates Eq. (3.5) the bandwidth is directly obtained from the eigenenergies. An alternative less elegant solution is based on the calculation of the integral Eq. (3.28) via Wannier functions which are gained from the Fourier transformed Bloch functions Eq. (3.22). Both solutions are exact, but they suffer from the numerical efforts of a band calculation to be done for every considered lattice depth, which is time consuming for investigation of lattice depth dynamics. This could be avoided by approximating the Wannier wave functions by a Gaussian. Such approximations, however, lead to an underestimation of the tunneling by almost an order of magnitude as the side lobes contributing to the overlap integral are absent in the latter. A better solution was found by Zwerger. In the publication [82] he presented an analytic expression for the functional dependency of  $J$  on the lattice depth in the limit of deep lattices. In the following section an outline of the derivation is presented.

### Limit of very deep lattices

$J$  as a function of the lattice depth can be calculated from the band structure by relating the Schrödinger equation to the well known Mathieu problem [83]

$$\left[ \frac{\partial^2}{\partial x^2} + (a - 2h \cos(2x)) \right] y(x) = 0. \quad (3.38)$$

For this purpose we rewrite the Schrödinger differential Eq. (3.5) for the optical lattice potential  $V(x) = -V_0 \cos^2(kx)$  in the following way

$$\begin{aligned} & \left[ -\frac{\hbar^2}{2m} \frac{\partial^2}{\partial x^2} + V(x) \right] \phi(x) = E\phi(x) \\ \Leftrightarrow & \left[ -\frac{\hbar^2}{2m} \frac{\partial^2}{\partial x^2} - V_0 \cos^2(kx) - E \right] \phi(x) = 0 \\ \Leftrightarrow & \left[ \frac{\hbar^2}{2m} \frac{\partial^2}{\partial x^2} + \frac{V_0}{2}(1 + \cos(2kx)) + E \right] \phi(x) = 0 \\ \Leftrightarrow & \left[ \frac{1}{k^2} \frac{\partial^2}{\partial x^2} + \frac{s}{2}(1 + \cos(2kx)) + \tilde{\varepsilon} \right] \phi(x) = 0 \end{aligned}$$

with lattice depth and single particle energy in units of the recoil energy  $E_r = \hbar^2 k^2 / 2m$ :  $s = V_0 / E_r$  and  $\tilde{\varepsilon} = E / E_r$  respectively. Transforming the variable  $x$  into  $x' = kx - \pi/2$  leads to

$$\left[ \frac{\partial^2}{\partial x'^2} + \frac{s}{2}(1 - \cos(2x')) + \tilde{\varepsilon} \right] \phi(x') = 0$$

This differential equation corresponds to the Mathieu equation for

$$\frac{s}{2} + \tilde{\varepsilon} = a \quad \text{and} \quad \frac{s}{2} = 2h.$$

Given the lattice depth  $s$  and momentum  $k$  the Mathieu solutions  $y$  correspond to Bloch waves introduced at the beginning of this section [84]. Similar to the calculation of Bloch states, a solution of the full Eq. (3.38) has to be obtained numerically. However, in the limit of very deep lattices  $s = V_0 / E_r \ll 1$ , the band  $E$  becomes an analytic function of

$s$  and from the bandwidth of the lowest band  $W = E_{\max} - E_{\min}$  the hopping integral  $J = W/4$  results [82]

$$J \approx \frac{4}{\sqrt{\pi}} E_r s^{3/4} e^{-2\sqrt{s}}. \quad (3.39)$$

For lattice depth larger than  $15 E_r$  the deep lattice approximation agrees with the exact values within 10%. For shallower lattices the values match less accurately.

### 3.1.2 Non-interacting particles in trapped systems

In the calculations for a homogeneous system any additional potential originating from the intensity profile of the laser beams or from an external confinement is neglected<sup>2</sup>. These, however, are always present in the system. Moreover, they are essential as they prevent particles from escaping the optical lattice. Most common confining potentials are optical dipole traps (see Sec. 2.2). They consist of two laser beams which intersect at right angles and are polarized orthogonal to each other. Due to Gaussian intensity profiles, the lasers form an oblate pancake-shaped trap. In the center, where the particles are located, it is well described by a parabolic potential

$$V_{\text{trap}}(\mathbf{r}) = \frac{m}{2} \sum_{l=x,y,z} \omega_l^2 (r_l - r_{0,l})^2, \quad (3.40)$$

where  $\mathbf{r} = (r_x, r_y, r_z)$ ,  $\mathbf{r}_0$  denotes the center of the trapping,  $\omega_l$  is the trapping frequency in the direction  $l = x, y$  or  $z$  and  $m$  the atomic mass. The corresponding inhomogeneous Hamiltonian reads

$$\mathcal{H} = \mathcal{H}_0 + \int d\mathbf{r} \hat{\Psi}^\dagger(\mathbf{r}) V_{\text{trap}}(\mathbf{r}) \hat{\Psi}(\mathbf{r}), \quad (3.41)$$

where  $\mathcal{H}_0$  equals the Hamiltonian in Eq. (3.2). In the Wannier representation of the field operators Eq. (3.24) within the lowest band the last term can be rewritten

$$\begin{aligned} \int d\mathbf{r} \hat{\Psi}^\dagger(\mathbf{r}) V_{\text{trap}}(\mathbf{r}) \hat{\Psi}(\mathbf{r}) &= \sum_{l=x,y,z} \sum_{i,j} \int d\mathbf{r} \omega^*(\mathbf{r} - \mathbf{r}_i) \hat{b}_i^\dagger \frac{m\omega_l^2 (r_l - r_{0,l})^2}{2} \omega(\mathbf{r} - \mathbf{r}_j) \hat{b}_j \\ &= \sum_{i,j} V_{ij,\text{trap}} \hat{b}_i^\dagger \hat{b}_j, \end{aligned}$$

with

$$V_{ij,\text{trap}} = \sum_{l=x,y,z} \int d\mathbf{r} \omega^*(\mathbf{r} - \mathbf{r}_i) \frac{m\omega_l^2 (r_l - r_{0,l})^2}{2} \omega(\mathbf{r} - \mathbf{r}_j).$$

For a trapping strength small compared to the lattice potential the neighboring sites can be nearly assumed unaffected by inhomogeneity. Correspondingly, the Wannier functions of this small homogeneous subsystem obey an orthogonality relation and the non-local contributions  $i \neq j$  to the integral vanish. Hence,

$$\begin{aligned} V_{ii,\text{trap}} \equiv V_{i,\text{trap}} &= \sum_{l=x,y,z} \int d\mathbf{r} \omega^*(\mathbf{r} - \mathbf{r}_i) \frac{m\omega_l^2 (r_l - r_{0,l})^2}{2} \omega(\mathbf{r} - \mathbf{r}_i) \\ &\approx \frac{m}{2} \sum_{l=x,y,z} \omega_l^2 (r_{i,l} - r_{0,l})^2. \end{aligned} \quad (3.42)$$

<sup>2</sup>Referring to the Hamiltonian Eq. (3.2) this means the following assumption:  $V(r) = -V_{\text{lat},0} \sum_{l=x,y,z} \cos^2(kl) + V_{\text{trap}} \approx -V_{\text{lat},0} \sum_{l=x,y,z} \cos^2(kl)$



The Wannier representation of the first summand  $\mathcal{H}_0$  was derived in the previous section Eq. (3.25)-(3.29), however, for general trapping potential the translational invariance is absent. Thus here for the first time we keep the site dependence of the hopping integral, i.e. use  $J_{ij}$  instead of  $J$ ,

$$\mathcal{H}_0 = - \sum_{\langle ij \rangle} J_{ij} (\hat{b}_i^\dagger \hat{b}_j + h.c.).$$

The confining potential induces a shift of the potential well at each lattice site. If the resulting energy shift  $\Delta E = m\omega^2 a^2/2$  between the neighboring sites is smaller than the depth of the lattice potential  $V_0$ , then the overlap of the neighboring single-particle waves is hardly influenced. In common experiments this assumption is fulfilled, i.e. for  $^{87}\text{Rb}$  and trapping frequencies  $2\pi \times 36$  Hz for lattice constant  $a = \frac{1064}{2}$  nm the lattice potential  $V_0$  exceeds  $\Delta E$  by four orders of magnitude even for shallow lattices of  $V_0 = 5E_r$ . Thus, the effect of the overall trapping potential on hopping integral  $J_{ij}$  Eq. (3.28) can be neglected and the site-dependence can be dropped. The hopping  $J$  is approximately unchanged compared to the homogeneous system. Hence, the Hamiltonian

$$\mathcal{H} = -J \sum_{\langle ij \rangle} (\hat{b}_i^\dagger \hat{b}_j + h.c.) + \sum_i V_{i,\text{trap}} \hat{n}_i \quad (3.43)$$

describes a non-interacting system with an additional weak confining potential in the tight-binding approximation.

In the following we will briefly discuss some consequences of external trapping.

Centering the trap between the lattice sites leads to additional nontrivial effects such as non-periodicity of eigenfunctions for incommensurate displacement of the trap center or oscillating eigenenergies when the displacement is periodically varied [85, 86]. Indeed, the precision of alignment of the trap center is on the order of the lattice constant. Additional thermal fluctuations of the lasers or magneto-optical devices creating the trap lower the quality of the trap. This feature should be kept in mind, as it may lead to a disagreement between theoretical predictions and experimental results.

An external confinement breaks the translational symmetry of the lattice and the quasi-momentum  $q$  is not a good quantum number and the Bloch states are not the eigenstates of the Hamiltonian (3.43). Still, as Bloch states form an orthonormal basis, any state can be expanded in them. Nevertheless, analytical calculations can not be performed in this regime in general.

And last but not least, analysis of the single-particle density of states reveals that the properties of the homogeneous lattice are not obtained in the limit  $\omega \rightarrow 0$  [87]. The density of states for a very weak trapping potential  $\omega \rightarrow 0$  qualitatively differs from the density of states of the homogeneous lattice  $\omega = 0$ . While at low single particle energies  $\varepsilon \sim 0$  the wave functions correspond to the eigenfunctions of the harmonic oscillator, at higher energies modifications due to Bragg reflection take place. For further discussion see [87].

### 3.1.3 Two-particle interactions

Depending on the distance, neutral atoms experience Coulomb or van der Waals interaction. On atomic size scales the Coulomb interaction between the electrons leads to a singular repulsion between the atoms. At larger distances the electronic clouds of the atoms

polarize and the atoms experience an attractive van der Waals force. The combination of both contributions leads to the Lennard-Jones potential

$$V(r) = \frac{C_n}{r^n} - \frac{C}{r^6}, \quad (3.44)$$

$r$  being the distance between two interacting atoms and  $C(C_n)$  particle dependent parameter. The exact calculation of the scattering length for different limits of this potential was provided by Gribakin and Flambaum [88].

It is obvious that an accurate description of the system often does not require the knowledge of the detailed interaction potential. Since in the tight binding regime the particle wave functions in the Wannier representation decay exponentially fast with the distance from the localization site, the on-site interactions are predominant. Therefore we restrict our derivation to the repulsive on-site interactions and neglect the attractive van der Waals force at large distances.

Due to the singularity common perturbative approaches can not be applied. Therefore a perturbative treatment is only possible if the potential can be substituted by an appropriate effective non-singular one which represents the system at characteristic length scales and can be handled in a perturbative way. Thereby, the internal energetic structure of the atoms can be neglected as a typical temperature of a dilute alkali BEC  $T \sim 10^{-8}$  K is well below the typical excitation energies  $T \sim 1$  K of an atom, such that all atoms are in the internal ground state. Next, we will roughly sketch the derivation of an effective interaction potential.

Changing into the basis of center of mass and relative coordinates, the two-particle wave function  $\psi(\tilde{\mathbf{r}})$ , with  $\tilde{r} = |\tilde{\mathbf{r}}|$  being the relative distance between the atoms  $\tilde{r} = |\mathbf{r} - \mathbf{r}'|$ , needs to satisfy the Schrödinger equation

$$\left(-\frac{\hbar^2 \Delta}{2m_{\text{red}}} + V(\tilde{\mathbf{r}})\right)\psi(\tilde{\mathbf{r}}) = E\psi(\tilde{\mathbf{r}}) \quad \text{for } \tilde{r} > a_s, \quad (3.45)$$

where  $m_{\text{red}} = m/2$  is the reduced mass and  $a_s$  denotes the radius of the impenetrable atomic potential - the scattering length<sup>3</sup> - where  $\psi(\tilde{\mathbf{r}}) = 0$  for  $\tilde{r} \leq a_s$ . The physical properties can be estimated from the asymptotic behavior of the particle wave function after a scattering process regardless of the particular short-distance interaction. Considering  $s$ -wave scattering and solutions for  $\tilde{r} > a_s$  the potential  $V(\tilde{\mathbf{r}})$  Eq. (3.44) can be substituted by a pseudo-potential [90, 91]

$$V_p(\tilde{\mathbf{r}})\psi(\tilde{\mathbf{r}}) = \frac{4\pi\hbar^2}{m} \frac{\tan(ka_s)}{k} \delta(\tilde{\mathbf{r}}) \frac{\partial}{\partial \tilde{r}}(\tilde{r}\psi(\tilde{\mathbf{r}})). \quad (3.46)$$

At low temperatures the energy of the system is small and we can approximate  $\frac{\tan(ka_s)}{k} \approx a_s + \mathcal{O}(a_s^3)$  for  $ka_s \ll 1$ . Thus, the Eq. (3.46) reads

$$\begin{aligned} V_p(\tilde{\mathbf{r}})\psi(\tilde{\mathbf{r}}) &= \frac{4\pi\hbar^2 a_s}{m} \delta(\tilde{\mathbf{r}}) \frac{\partial}{\partial \tilde{r}} \tilde{r}\psi(\tilde{\mathbf{r}}) \\ &= \frac{4\pi\hbar^2 a_s}{m} \delta(\tilde{\mathbf{r}}) \left( \psi(\tilde{\mathbf{r}}) + \tilde{r} \frac{\partial \psi(\tilde{\mathbf{r}})}{\partial \tilde{r}} \right). \end{aligned} \quad (3.47)$$

<sup>3</sup>The strength of the atomic potential and thus its extent can be tuned via a Feshbach resonance [89]. In general the scattering length  $a_s$  exceeds the atom radius  $R_0$  mentioned in Eq. (3.44).

We can neglect the last summand as long as it does not lead to divergencies at the origin, which is the case when  $\psi(\tilde{\mathbf{r}}) \sim 1/\tilde{r}^\alpha$  with  $\alpha \leq 1$ . The simplified pseudo-potential reduces to

$$V_p(\tilde{\mathbf{r}}) = g\delta(\tilde{\mathbf{r}}), \quad (3.48)$$

where

$$g = \frac{4\pi\hbar^2 a_s}{m}. \quad (3.49)$$

The two-particle interaction in the field operator representation reads

$$\begin{aligned} \mathcal{H}_{\text{int}} &= \frac{1}{2} \int d\mathbf{r} \int d\mathbf{r}' \hat{\Psi}^\dagger(\mathbf{r}) \hat{\Psi}^\dagger(\mathbf{r}') V_p(\mathbf{r} - \mathbf{r}') \hat{\Psi}(\mathbf{r}') \hat{\Psi}(\mathbf{r}) \\ &= \frac{g}{2} \left( \int dx \int dx' \hat{\Psi}^\dagger(x) \hat{\Psi}^\dagger(x') \delta(x - x') \hat{\Psi}(x') \hat{\Psi}(x) \right)^3. \end{aligned} \quad (3.50)$$

In the last step we replaced the pseudo-potential  $V_p(\mathbf{r} - \mathbf{r}')$  by its approximation from Eq. (3.48) and decomposed the 3D integration into three identical 1D integrals based on the spherical symmetry in a homogeneous system. Assuming that interactions do not significantly change the single particle Wannier states<sup>4</sup>, the localized states of the non-interacting particles in the periodic lattice potential, we can expand the field operators in this basis following Eq. (3.24)  $\hat{\Psi}(x) = \sum_l w(x - x_l) \hat{b}_l$ , whereby we drop the band index<sup>(0)</sup>, and rewrite the integral

$$\begin{aligned} &\sum_{i,j,l,n} \int dx \int dx' w^*(x - x_i) w^*(x' - x_j) \delta(x - x') w(x' - x_l) w(x - x_n) \hat{b}_i^\dagger \hat{b}_j^\dagger \hat{b}_l \hat{b}_n \\ &= \sum_{i,j,l,n} \int dx w^*(x - x_i) w^*(x - x_j) w(x - x_l) w(x - x_n) \hat{b}_i^\dagger \hat{b}_j^\dagger \hat{b}_l \hat{b}_n. \end{aligned} \quad (3.51)$$

Hence for sufficiently deep lattices the overlap of the localized Wannier functions between different lattice sites is negligible, the largest contribution to the integral comes from the case where  $i = j = l = n$ . Restricting to this case means that we only account for the interactions when the interacting particles happen to be on the same site. In this case substituting the result (3.51) into Eq. (3.50) leads to

$$\mathcal{H}_{\text{int}} = \frac{g}{2} \sum_{i,j,l,n} \left[ \int dx |w(x - x_i)|^4 \right]^3 \delta_{ij} \delta_{jl} \delta_{ln} \hat{b}_i^\dagger \hat{b}_j^\dagger \hat{b}_l \hat{b}_n. \quad (3.52)$$

If the system obeys translational invariance the Wannier functions are identical on every site and we can choose without loss of generality  $x_i = 0$ . Additionally, making use of the bosonic commutation relation  $[\hat{b}, \hat{b}^\dagger] = 1$ , the interacting Hamiltonian can be rewritten

$$\begin{aligned} \mathcal{H}_{\text{int}} &= \frac{g}{2} \left[ \int dx |w(x)|^4 \right]^3 \sum_i \hat{n}_i (\hat{n}_i - 1) \\ &= \frac{U}{2} \sum_i \hat{n}_i (\hat{n}_i - 1), \end{aligned} \quad (3.53)$$

<sup>4</sup> When energetically higher lying states get excited via the interparticle interaction, the single particle wave functions do not longer correspond to the unperturbed ground state Wannier functions but become spatially modulated, which leads to corrections in the interaction energy [23].

where in the last step we defined

$$U = g \left[ \int dx |w(x)|^4 \right]^3. \quad (3.54)$$

Finally, the Hamiltonian describing interacting particles in a homogeneous lattice is given by Eq. (3.29) and (3.53):

$$\mathcal{H} = -J \sum_{\langle ij \rangle} (\hat{b}_i^\dagger \hat{b}_j + h.c.) + \frac{U}{2} \sum_i \hat{n}_i (\hat{n}_i - 1). \quad (3.55)$$

To account for an external trapping potential the first summand has to be substituted by Eq. (3.43).

The interaction matrix element  $U$  can be calculated exactly<sup>5</sup> via Eq. (3.54) from a band structure calculation first evaluating Bloch states and afterwards performing a Fourier transformation to get Wannier functions. The obtained  $U$  describes correctly within the assumed approximations the interaction strength in a homogeneous system and constitutes an approximation for slightly inhomogeneous lattices.

As we are solely interested in the on-site integral, in sufficiently deep lattices the Wannier functions can be well approximated by a Gaussian

$$w(x) = \frac{1}{\sqrt{\sigma} \pi^{1/4}} e^{-\frac{x^2}{2\sigma^2}} \quad \text{with} \quad \sigma = \frac{a}{\pi s^{1/4}} \quad (3.56)$$

where  $a = \lambda/2$  is the lattice constant,  $s = V_0/E_r$  the lattice depth in units of the recoil energy  $E_r = \hbar^2 k^2 / 2m$  and  $k = 2\pi/\lambda$  the laser wave number. In this approximation we obtain an analytic expression for the interaction strength  $U$  as a function of the lattice depth  $s$  and scattering length  $a_s$

$$\begin{aligned} U &= g \left[ \int dx |w(x)|^4 \right]^3 \approx g \left[ \frac{1}{\sigma^2 \pi} \int dx e^{-\frac{2x^2}{\sigma^2}} \right]^3 \\ &= g \left[ \frac{1}{\sigma^2 \pi} \frac{\sigma \sqrt{2\pi}}{2} \right]^3 \\ &= \sqrt{\frac{8}{\pi}} k a_s E_r s^{3/4}. \end{aligned} \quad (3.57)$$

Now we can prove the validity of single-band approximation based on the assumption that the energy gained through tunneling or interaction is less than the band gap. Thereby it is sufficient to verify that the interaction energy does not exceed the gap range as the tight-binding approximation and thus the Hubbard model is valid for  $s \geq 5$  where  $U/J \gg 1$  (Eq. (3.57) and (3.39)). The total two-body interaction energy for  $n$  particles per site is given by<sup>6</sup>  $E_{int} = Un(n-1)/2$ . For common laser wave length  $\lambda = 1064$  nm and lattice depth  $s = 5$  holds:  $U/\hbar \approx 5 \cdot 10^3$  Hz<sup>-1</sup> and  $\omega_{lat,0} \approx 58$  kHz, thus the lowest band constraint

<sup>5</sup>The calculations are of course exact only within the assumption of wave functions being single particle Wannier states. Incorporating excited states into the calculation leads to corrections of the interaction integral in Eq. (3.54) which in a three-dimensional optical lattice have been measured to lead to a decrease of the two-body interaction energy by  $\sim 10\%$  compared to the prediction from Eq. (3.53) [92].

<sup>6</sup>This follows from Eq. (3.53) assuming the Fock states being the eigenvectors of the system:  $\mathcal{H}_{int}|n\rangle = E_{int}(n)|n\rangle$ . This is exact for  $J \rightarrow 0$  and gives the upper bound of the interaction energy for finite tunneling regimes.

$E_{int}/n = U(n-1)/2 \ll \hbar\omega_{lat,0}$  is satisfied for  $n \ll 24$ . This condition is usually fulfilled and the influence of higher bands will lead only to small corrections.

When species mixtures are loaded into the lattice, e.g. consisting of atom types  $a$  and  $b$ , additional inter-species interaction occurs

$$\mathcal{H}_{int,ab} = \frac{1}{2} \int d\mathbf{r} \int d\mathbf{r}' \hat{\Psi}_a^\dagger(\mathbf{r}) \hat{\Psi}_b^\dagger(\mathbf{r}') V_p(\mathbf{r} - \mathbf{r}') \hat{\Psi}_b(\mathbf{r}') \hat{\Psi}_a(\mathbf{r}), \quad (3.58)$$

which we can write, in analogy to the intra-species interaction, in the Wannier representation

$$\mathcal{H}_{int,ab} = U_{ab} \sum_i \hat{n}_{ia} \hat{n}_{ib} \quad (3.59)$$

The corresponding interaction matrix element is (details of the derivation are presented in Appendix A)

$$U_{ab} = 4\sqrt{\pi} k a_{ab} E_{r,a} \frac{(1 + m_a/m_b)}{\left(1 + \sqrt{\frac{m_a V_{0,a}}{m_b V_{0,b}}}\right)^{3/2}} s_a^{3/4} \quad (3.60)$$

or equivalently

$$U_{ab} = 4\sqrt{\pi} k a_{ab} E_{r,b} \frac{(1 + m_b/m_a)}{\left(1 + \sqrt{\frac{m_b V_{0,b}}{m_a V_{0,a}}}\right)^{3/2}} s_b^{3/4}. \quad (3.61)$$

Here  $s_{a(b)} = V_{0,a(b)}/E_{r,a(b)}$  denotes the distinct lattice depth,  $E_{r,a(b)} = \hbar^2 k^2 / 2m_{a(b)}$  the species dependent recoil energy and  $k = 2\pi/\lambda$  the laser momentum.

We conclude this section with a small outlook about the many-particle interactions. The inelastic multi-body interactions have been investigated to lead to particle losses in three- and four-body recombinations of atom-atom and atom-molecule collisions [93–95]. However, assuming interaction driven virtual excitations to higher states of the periodic optical potential, the many-body scattering can also lead to renormalization of interaction energies depending on the number of interacting atoms [23, 96]. In this case the two-body interaction accounting for lowest lying band only, i.e.  $Un(n-1)/2$ , has to be extended to the series  $U_2n(n-1)/2 + U_3n(n-1)(n-2)/6 + \dots$ . Even though the  $l$ -body interaction strength  $U_l$  is orders of magnitude smaller compared to  $U_2$ , e.g.  $U_2/U_3 \approx 10$  [23], the many-body effects can influence drastically the non-equilibrium dynamics of the bosonic system e.g. cause large damping and additional time scales in collapse and revival of the matter waves [23, 92, 97].

### 3.1.4 Bose-Hubbard Hamiltonian: summary and outlook

To summarize the results, from the Bose-Hubbard Model

$$\begin{aligned} \mathcal{H} = \int d\mathbf{r} \hat{\Psi}^\dagger(\mathbf{r}) \left[ -\frac{\hbar^2}{2m} \nabla^2 + V(\mathbf{r}) \right] \Psi(\mathbf{r}) + \int d\mathbf{r} \hat{\Psi}^\dagger(\mathbf{r}) V_{\text{trap}}(\mathbf{r}) \Psi(\mathbf{r}) \\ + \frac{1}{2} \int d\mathbf{r} \int d\mathbf{r}' \Psi^\dagger(\mathbf{r}) \Psi^\dagger(\mathbf{r}') V_p(\mathbf{r} - \mathbf{r}') \Psi(\mathbf{r}') \Psi(\mathbf{r}) \end{aligned}$$

accounting for the periodic lattice potential  $V(\mathbf{r})$  Eq. (2.21), an external trapping potential  $V_{\text{trap}}(\mathbf{r})$  Eq. (3.40) and two-particle interaction approximated by a pseudo-potential

$V_p(\mathbf{r} - \mathbf{r}')$  Eq. (3.48) the Bose-Hubbard Hamiltonian in the Wannier representation was derived as

$$\mathcal{H} = -J \sum_{\langle ij \rangle} (\hat{b}_i^\dagger \hat{b}_j + h.c.) + \sum_i V_{i,\text{trap}} \hat{n}_i + \frac{U}{2} \sum_i \hat{n}_i (\hat{n}_i - 1). \quad (3.62)$$

with parameters

$$\begin{aligned} J &= \int dx \omega^*(x - x_i) \left[ -\frac{\hbar^2}{2m} \nabla^2 + V(x) \right] \omega(x - x_j) \approx \frac{4}{\sqrt{\pi}} E_r s^{3/4} e^{-2\sqrt{s}}, \\ V_{i,\text{trap}} &\approx \frac{m}{2} \sum_{l=x,y,z} \omega_l^2 (r_{i,l} - r_{0,l})^2, \\ U &= g \left[ \int dx |w(x)|^4 \right]^3 \approx \sqrt{\frac{8}{\pi}} k a_s E_r s^{3/4}. \end{aligned}$$

Within this thesis rather the Bose-Hubbard Hamiltonian

$$\mathcal{H} = -J \sum_{\langle ij \rangle} (\hat{b}_i^\dagger \hat{b}_j + h.c.) + \sum_i V_{i,\text{trap}} \hat{n}_i - \mu \sum_i \hat{n}_i + \frac{U}{2} \sum_i \hat{n}_i (\hat{n}_i - 1). \quad (3.63)$$

is used. The additional term  $\mu \sum_i \hat{n}_i$  enables the adjustment of a desired particle number via the free parameter  $\mu$  and extends the canonical (Eq. (3.62)) to the grand canonical ensemble (Eq. (3.63)). For  $T = 0$  the expectation value  $\langle \mathcal{H} \rangle$  represents the grand canonical potential instead of the energy and has to be corrected in order to obtain the latter  $E = \langle \mathcal{H} \rangle + \mu N$ .

In the derivation of the Hamiltonian the particle wave functions were assumed to be well described by single-band Wannier functions and tunneling processes on relative distances further than nearest neighbors were neglected. This assumptions are based on the lowest band and the tight-binding approximations in which the Wannier states from the lowest band are considered to be sufficiently localized at lattice sites and contributions from higher bands and other hopping matrix elements are neglected. This means that the single-band Bose-Hubbard model is not suitable for lattices shallower than  $V_0 \approx 5E_r$ . This is the most strict limitation of this model.

In the above formulas only the lowest Bloch band contributes to the parameters  $J$ ,  $U$  and  $V_{i,\text{trap}}$ . Whereas for  $V_{i,\text{trap}}$  this assumption hardly influences the results, the Hamiltonian with approximate  $U$  is not applicable to describe effects based on transitions of atoms to higher orbitals like increased repulsion mediated by fermions in a Bose-Fermi atomic gas mixture. A proper multi-band calculations can be found in [80] for Bose-Fermi mixture and in [23] for multi-body interactions. Also the tunneling  $J$  was found to be affected by particle density and higher-band processes leading to significant changes in the phase diagram [98].

Another approximate assumption is the isotropy and therefore translational invariance in the lattice. Increasing the power of one of interfering lattice lasers to e.g. investigate coupling effects in 1D [99] would violate the first assumption. In this case, however, the model can be easily extended to such more sophisticated lattice structures making  $J$  position-dependent  $J = (J_x, J_y, J_z)$  and calculating  $U$  with respect to  $w(x) \neq w(y) \neq w(z)$ , namely  $U = g \int dx |w(x)|^4 \int dy |w(y)|^4 \int dz |w(z)|^4$ . The translational invariance approach breaks down when a large external potential or disorder are present in the system. Then,

the parameters become site-dependent. An estimation of the hopping  $J_{ij}$  and interaction  $U_i$  depending on the on-site potentials will be given in Sec.6.2. With these upgrades the Bose-Hubbard model can be applied to non-homogeneous systems well.

In the Bose-Hubbard model only on-site two-body interactions are present. For uncharged cold atom systems this model reveals basic phases such as superfluid and Mott insulator, depending on the ratio  $J/U$  (explained in Sec. 3.2). Moreover, the model also includes magnetically ordered phases in bosonic mixtures [100–102]. However, exciting the system to higher bands would naturally lead to next-nearest neighbor interaction requiring extended Bose-Hubbard description via an extra term  $V \sum_{\langle ij \rangle} \hat{n}_i \hat{n}_j$  [103]. Besides in excited systems, the next-nearest neighbor interactions have to be taken into account in dipolar bosonic systems with permanent magnetic or electric dipole moment and consequently long-range dipole-dipole interactions. Theoretical calculations for extended Hubbard model predict besides the superfluid and Mott insulating regimes also mass or charge density waves and supersolid phases (simultaneous presence of superfluidity and modulated particle density) [104–107].

The limitation to two-body scattering processes is only justified as many-body interactions are at least one order of magnitude smaller. But they gain in importance when the particle density is significantly increased over the usual commensurate filling. The corrections, although small, may lead to significant changes in dynamics of the system when excited states are involved. Even though the main physics is captured in the Bose-Hubbard model Eq. (3.62) several effects can be only explained within many-body interaction extension [23, 92, 96].

Finally, we would like to emphasize that the unrestricted use of the analytic expressions  $J(s)$  from Eq. (3.39) and  $U(s)$  Eq. (3.57), which are accurate only in deep lattice regime, leads to inaccuracies [108]. In this thesis both the exact expressions Eq. (3.39) and Eq. (3.57) as well as numerical results for Eq. (3.28) and Eq. (3.54) were applied.

## 3.2 Quantum phases

At zero temperature there exist no thermal fluctuations and the system is dominated by quantum fluctuations. They can lead to a change of the ground state of the system depending on the chosen physical parameter regime. For  $J \gtrsim U$  the total energy is minimized when the kinetic term dominates which means the particle wave functions are spread over the lattice and the system is referred to be superfluid (SF). Increasing the depth of the lattice enhances the interactions and reduces the tunneling at the same time, the atoms minimize their energy by localizing at different sites. Finally, suppression of the tunneling leads to an insulating behavior called Mott insulating phase (MI). The transition between SF and MI phase was theoretically predicted for zero [9, 10] and finite temperature [109, 110] and experimentally investigated [12, 111]. In this section the fundamental properties of both phases are summarized together with the SF-MI phase transition.

### 3.2.1 Superfluid

#### Superfluid vs. Condensate

Depending on the ratio of the interaction to the kinetic energy  $U/J$  the BEC possesses different properties in optical lattices which are classified as superfluid and Mott-insulating

phases. However, referring to the first of two phases as superfluid is rather a matter of convention because the relation between condensation and superfluidity is not unique. The *condensate* is characterized by a macroscopic occupation of a single-particle state. This state may depend on time but, given a total particle number  $N$ , its occupation is finite and of order  $N$  (it is not necessary that all particles condense) at any time, while the number of particles in any other single-particle state is of the order 1 or less. A *superfluid* is defined being irrotational which means  $\nabla \times v_s = 0$ , where  $v_s$  denotes the superfluid velocity, and implies the existence of quantized vortices (L. Onsager 1949). Although superfluidity was believed to be based on BEC [112, 113] both phenomena were proved to exist also independent of each other. While, due to the vortex quantization properties, it is intuitive not to expect superfluidity in BEC it was surprising to observe a 2D superfluid without BEC [114]. Until now superfluidity of optically trapped bosonic gases is not uniquely proven. Further discussion on this topic can be found in [114, 115]. However, following the common agreement, in this manuscript condensate and superfluid will be used as synonyms.

### Ground state

In a homogeneous non-interacting system all bosonic particles occupy the same single-particle ground state, which is the  $|q = 0\rangle$  state (see sec. 3.1.1). Using Fourier transformation Eq. (3.21) together with abstract bra-ket notation Eq. (3.8) and (3.20)

$$|q\rangle = \frac{1}{\sqrt{L}} \sum_m e^{-iqam} |m\rangle, \quad (3.64)$$

where  $m \in \mathbb{N}_0$  is a lattice site index, the single-particle ground state can be written

$$|q = 0\rangle = \frac{1}{\sqrt{L}} \sum_m |m\rangle. \quad (3.65)$$

The many-body state describing  $N$  non-interacting particles being in the same quantum state can be written as a direct product of  $N$  identical single-particle states

$$\begin{aligned} \text{canonical: } |\Psi_{SF}(N)\rangle &= |q = 0\rangle_0 \otimes \cdots \otimes |q = 0\rangle_N \\ &= \left( \frac{1}{\sqrt{L}} \sum_{m=1}^L |m\rangle \right)^N \\ &= \frac{1}{\sqrt{N!}} \left( \frac{1}{\sqrt{L}} \sum_{m=1}^L \hat{b}_m^\dagger \right)^N |0\rangle, \end{aligned} \quad (3.66)$$

where  $|0\rangle$  denotes the vacuum state.

The superfluid phase can also be described by a coherent state which is the eigenstate of the annihilation operator in Fock space and thus the eigenstate of the non-interacting homogeneous system described by the Hamiltonian Eq. (3.29). The single-particle coherent state reads

$$|\phi\rangle \equiv e^{\phi \hat{b}^\dagger} |0\rangle. \quad (3.67)$$



One can prove that the eigenstate relation holds

$$\begin{aligned}
\hat{b}e^{\phi\hat{b}^\dagger}|0\rangle &= \hat{b}\sum_{l=0}^{\infty}\frac{\phi^l\hat{b}^{\dagger l}}{l!}|0\rangle \\
&= \sum_{l=0}^{\infty}\frac{\phi^l}{l!}(l\hat{b}^{\dagger l-1}+\hat{b}^{\dagger l}\hat{b})|0\rangle \\
&= \sum_{l=1}^{\infty}\frac{\phi^l}{l!}l\hat{b}^{\dagger l-1}|0\rangle \\
&= \phi\sum_{l'=0}^{\infty}\frac{\phi^{l'}\hat{b}^{\dagger l'}}{l'!}|0\rangle \\
&= \phi|\phi\rangle \quad \text{qed.}
\end{aligned} \tag{3.68}$$

From the first to the second line we used the relation<sup>7</sup>  $[\hat{b}, \hat{b}^{\dagger l}] = l\hat{b}^{\dagger l-1}$ . The last summand in the second line vanishes as  $\hat{b}|0\rangle = 0$ . Further properties of the coherent states can be found in common quantum optics literature.

Given a total of  $N$  non-interacting particles on average<sup>8</sup> a general form of a coherent many-body ground state is

$$|\alpha, \sqrt{N}\rangle = e^{-\frac{N}{2}} e^{\sqrt{N}\hat{s}_\alpha^\dagger}|0\rangle, \tag{3.69}$$

where  $\hat{s}_\alpha^\dagger$  is a creation operator of a macroscopically occupied single-particle state  $\alpha$ . Compared to Eq. (3.67) an additional phase  $\exp\{-N/2\}$  was introduced, which is useful for later transformations. In case of bosons in a periodic lattice the state  $\alpha$  may correspond to any of the Bloch states (Wannier states) or its linear combination<sup>9</sup>. Hence, the operator reads  $\hat{s}_\alpha^\dagger = \frac{1}{\sqrt{L}}\sum_{l=1}^L a_l^\alpha \hat{b}_l^\dagger$  in real space or  $\hat{s}_\alpha^\dagger = \frac{1}{\sqrt{L}}\sum_{q\in 1.BZ} c_q^\alpha \hat{b}_q^\dagger$  in momentum space, where  $a_l^\alpha, c_q^\alpha \in \mathbb{C}$ . With some effort one can prove that the many-body coherent state satisfies the eigenstate equation for an arbitrary single-particle state  $\alpha$ .

In the superfluid ground state in a homogeneous periodic potential bosons occupy the lowest lying energy level  $|q=0\rangle$  and the general expression Eq. (3.69) reduces in momentum space to

$$\text{coherent: } |\Psi_{SF}(\sqrt{N})\rangle = e^{-\frac{N}{2}} e^{\sqrt{N}\hat{b}_{q=0}^\dagger}|0\rangle. \tag{3.70}$$

The real space representation is given by

$$\begin{aligned}
|\Psi_{SF}(\sqrt{N})\rangle &= e^{-\frac{N}{2}} e^{\sqrt{N}\left(\frac{1}{\sqrt{L}}\sum_{m=1}^L \hat{b}_m^\dagger\right)}|0\rangle \\
&= \prod_{m=1}^L e^{-\frac{n}{2}} e^{\sqrt{n}\hat{b}_m^\dagger}|0\rangle_m \\
&= \prod_{m=1}^L |\Psi_{SF}(\sqrt{n})\rangle_m.
\end{aligned} \tag{3.71}$$

We find that the coherent many-body state with  $N$  particles on average decomposes into a direct product of coherent states on each lattice site with  $n = N/L$  particles on average.

<sup>7</sup>This relation can be easily verified via mathematical induction.

<sup>8</sup>In contrast to the canonical description, the number of particles in the coherent description is fixed only on average  $\langle n_\alpha \rangle = \langle \alpha, \sqrt{N} | \hat{n}_\alpha | \alpha, \sqrt{N} \rangle = N$ .

<sup>9</sup>The  $|q=0\rangle$  momentum state is macroscopically occupied if it is the ground state of the system. This is only the case in homogeneous lattices in equilibrium and does not necessarily apply to trapped or out of equilibrium systems. In the latter a condensate occurs at finite momenta [34].

Canonical and coherent descriptions are equivalent in the thermodynamic limit  $N, L \rightarrow \infty$  at fixed density  $N/L$ . At finite but large particle number the coherent representation can still be used to describe the superfluid ground state to a good approximation [82].

For interacting particles there exists no compact expression for the eigenstates as the Hamiltonian Eq. (3.55) is analytically not exactly solvable. When interactions are finite but small the condensate partially depletes. Although one single-particle state remains macroscopically occupied (the occupation scales proportional to the total particle number but is less than the total particle number) the number of states with occupation  $\sim 1$  grows. In this case the description of the superfluid characteristics of an interacting system has to be based on observables such as number statistics or the superfluid order parameter discussed next.

### Number statistics

Following the definition Eq. (3.67) the coherent state is a superposition of Fock states with different atom numbers. Given that the coherent state factorizes into a product of coherent states of particle density  $n$ , the probability for measuring  $q$  particles at an arbitrary lattice site can be calculated as follows (the site index is dropped for better readability)

$$\begin{aligned}
P_n(q) &= |\langle q | \Psi_{SF}(n) \rangle|^2 \\
&= \left| \langle 0 | \frac{\hat{b}^q}{\sqrt{q!}} e^{-\frac{n}{2}} e^{\sqrt{n}\hat{b}^\dagger} | 0 \rangle \right|^2 \\
&= \left| \frac{1}{\sqrt{q!}} e^{-\frac{n}{2}} \sum_{m=0}^{\infty} \frac{n^{m/2}}{m!} \langle 0 | \hat{b}^q \hat{b}^{\dagger m} | 0 \rangle \right|^2 \\
&= \left| \frac{1}{\sqrt{q!}} e^{-\frac{n}{2}} \sum_{m=0}^{\infty} \frac{n^{m/2}}{m!} \sqrt{q!} \sqrt{m!} \underbrace{\langle q | m \rangle}_{\delta_{qm}} \right|^2 \\
&= \left| \frac{1}{\sqrt{q!}} e^{-\frac{n}{2}} \frac{n^{q/2}}{q!} q! \right|^2 \\
&= \frac{n^q}{q!} e^{-n}. \tag{3.72}
\end{aligned}$$

Hence, it turns out that in the SF phase the probability of finding precisely  $q$  atoms at any given site is Poisson distributed in the thermodynamic limit for  $U = 0$ , see Fig. 3.4. For finite interactions the distribution develops away from pure Poissonian towards number statistics in the MI phase. Both cases have been observed in experiments and can be used to uniquely characterize the quantum phase of the homogeneous and inhomogeneous systems [97, 116–118].

### Superfluid order parameter

The SF phase is defined to correspond to a macroscopic population of a single-particle state. Macroscopic population means that the number of particles in this state  $N_{sf}$  is always finite and of the order of  $N$  (total particle number), thus  $\lim_{N \rightarrow \infty} N_{sf}/N > 0$ . Interactions lead to a reduction of  $N_{sf}$  and although macroscopic  $N_{sf}(U > 0) < N_{sf}(U = 0)$  for finite but small interaction strength. Increasing  $U$  continuously decreases the population until all states become populated and  $N_{sf}/N$  vanishes in the thermodynamic limit. Thus,

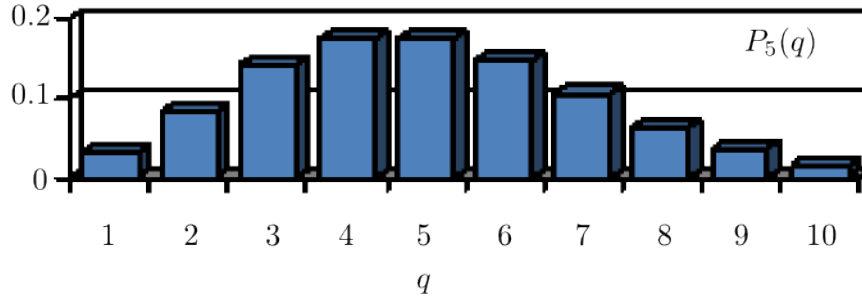


**Figure 3.4:** Probability distribution for observing  $n$  particles at an arbitrary site in a homogeneous superfluid system corresponds to the Poisson statistics  $P_n(q) = \frac{n^q}{q!} e^{-n}$ . Here as an example the distribution  $P_5(q) = \frac{5^q}{q!} e^{-5}$  is shown.

population of the single-particle state serves as an order parameter: it is finite when system is superfluid and zero otherwise.

In a non-interacting homogeneous system all particles occupy the ground state  $|q=0\rangle$ . In the thermodynamic limit this state corresponds to a product of coherent states on each site Eq. (3.71), which are the eigenstates of the annihilation operator at that site and therefore eigenstates of the Hamiltonian Eq. (3.29). Thus, in the non-interacting system for any site  $i$  it is

$$\begin{aligned}
 \langle \hat{b}_i \rangle &= \langle \Psi_{SF}(\sqrt{N}) | \hat{b}_i | \Psi_{SF}(\sqrt{N}) \rangle \\
 &= \prod_{m=1}^L \langle \Psi_{SF}(\sqrt{n}) | \hat{b}_i | \prod_{l=1}^L | \Psi_{SF}(\sqrt{n}) \rangle_l \\
 &= \prod_{m=1}^L \langle \Psi_{SF}(\sqrt{n}) | \sqrt{n}_i | \prod_{l=1}^L | \Psi_{SF}(\sqrt{n}) \rangle_l \\
 &= \sqrt{n}_i.
 \end{aligned}$$

Since in a homogeneous system  $n_i \equiv n$  is the particle density in the coherent on-site state, the total occupation of the coherent state is  $n \cdot L = N$ . The occupation is macroscopic and following the definition the non-interacting homogeneous system is always in a superfluid phase. Hence, it is natural to define the *superfluid order parameter* in the following way:

$$SF\text{-parameter: } \langle \hat{b} \rangle \quad (3.73)$$

Two-particle scattering processes redistribute the particles from the  $|q=0\rangle$  state to other states and lead to a ground state with decreased population of the  $q=0$  momentum and consequently lower SF parameter. In conclusion:

$$\langle b \rangle \begin{cases} = \sqrt{n}, & \text{for } U \rightarrow 0, N \rightarrow \infty, N/L = \text{const.}, \\ < \sqrt{n}, & \text{else.} \end{cases} \quad (3.74)$$

As the Bloch states are not eigenstates of the interacting system anymore, the particular value of the SF parameter has to be calculated numerically in the latter case.

### 3.2.2 Mott insulator

#### Band insulator vs. Mott insulator

The band structure in condensed matter as well as in ultra cold gases originates from the scattering of non-interacting electrons or atoms off the lattice potential. The resulting structure separates the energy scale into bands consisting of energy levels occupied by particles and in band gaps where no states exist. As long as there are free states within a band, particles are expected to scatter into these states and to cause finite conductivity. If all levels are occupied the system is referred to as a *band insulator*. However, some materials and all optical lattice systems show insulating properties for commensurate fillings contrary to the band theory predicting metallic behavior. This property relies on the interparticle interaction which is assumed to lead only to a screened lattice potential within the band theory. This Coulomb interaction localizes the particles individually on lattice sites and leads to the so called *Mott insulator*. The Hubbard model accounts for the interaction-induced localization and, hence the optical lattices are the Hubbard model simulators, the SF-Mott insulator transition can be observed.

#### Ground state

To analyze the features of an insulator we choose the limit where the wave functions of interacting particles are localized and tunneling is completely suppressed. In the limit  $J = 0$  a homogeneous system is dominated by the interaction energy and described by the Hamiltonian (compare to Eq. (3.53))

$$\mathcal{H} = \frac{U}{2} \sum_{i=1}^L \hat{n}_i (\hat{n}_i - 1). \quad (3.75)$$

The Hamiltonian is a direct sum of uncoupled single site Hamiltonians  $\mathcal{H} = \sum_i \mathcal{H}_i$  and consequently the eigensystem  $|\Psi_\alpha\rangle$  of eigenvalue  $E_\alpha$  is spanned by a product of single-site eigenstates  $|\Psi_\alpha\rangle = \prod_i |\psi_{\alpha_i}\rangle_i$ , where the index  $\alpha_i$  labels the energy levels of site  $i$ . In a homogeneous system the sites are equivalent and the eigenstate  $|\Psi_\alpha\rangle$  simplifies to  $|\Psi_\alpha\rangle = (|\psi_\alpha\rangle)^L$ .

Each Hamiltonian  $\mathcal{H}_i$  is diagonal in the Fock basis and hence Fock states correspond to the eigenvectors  $|\psi_{\alpha_i}\rangle_i \equiv |n_i\rangle_i = \frac{1}{\sqrt{n_i}} (\hat{b}_i^\dagger)^{n_i} |0\rangle_i$ , with  $n_i \in \mathbb{N}_0$ . The ground state of an  $N$ -particle system in an homogeneous  $L$ -sites optical lattice can thus be written as

$$|\Psi_{MI}\rangle = \prod_{l=1}^L |n_l\rangle_l \equiv (|n\rangle)^L, \quad (3.76)$$

where  $n_l \equiv n = N/L = 1, 2, \dots$  is the integer particle density in the lattice. This state is often referred to as a number squeezed state similarly to quantum optics. An integer particle density per lattice site indicates localization of particles in real space. Correspondingly, the Fourier transformed MI-state is completely delocalized in momentum space i.e. all quasi-momenta are occupied evenly. Following the definition such a system is insulating. And because the occupation of all available states was induced by interactions only the limit  $J = 0$  corresponds to a Mott insulating regime.

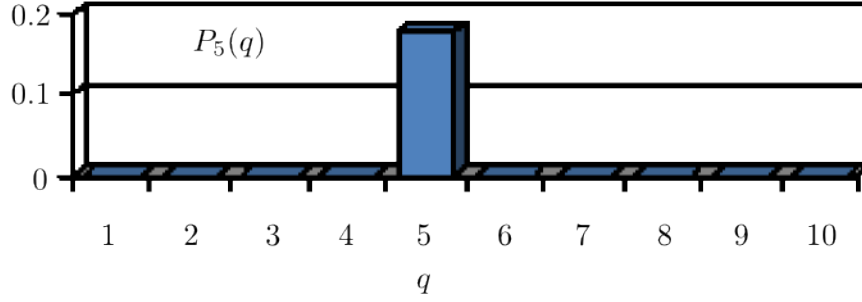


**Figure 3.5:** Probability distribution to find  $n \in \mathbb{N}_0$  particles at any arbitrary site in a homogeneous Mott insulating system. The distribution function is number squeezed  $P_n(q) = \delta_{qn}$ , as an example the distribution  $P_5(q)$  is presented.

### Number statistics

In the MI phase the particles are localized on lattice sites. This is also true when the hopping amplitude  $J$  becomes finite but the gain of kinetic energy remains less than the potential energy  $U$  which has to be paid in case of double occupancy. Thus, at any lattice one observes an integer number of particles  $q$  which corresponds to the filling  $n$ . This leads to a Fock number-statistics

$$\begin{aligned} P_n(q) &= |\langle q | \Psi_{MI} \rangle|^2 \\ &= \delta_{qn}, \quad q \in \mathbb{N}_0. \end{aligned} \quad (3.77)$$

In Fig. 3.5 an example for a system with filling  $n = 5$  is shown. Thus, in an ideal MI phase no particle fluctuations are observed, which is used as an indicator for experimental identification of the phases [117, 118].

### Excitation gap

As already mentioned, in the groundstate of the homogeneous MI phase all momentum states are occupied equally. Scattering of a particle into an already occupied state can only take place at the expense of potential energy gain. This energy barrier is referred to as excitation gap. Equivalently, in real space this energy corresponds to the energy required to add a particle to the lattice or to remove it

$$\tilde{\Delta} = E(N+1) - E(N) = E(N) - E(N-1),$$

where  $E(N)$  is the energy of an  $N$ -particle system:  $\mathcal{H}|\Psi_{MI}\rangle = E(N)|\Psi_{MI}\rangle$ . With  $n_l$  particles per site it is

$$\begin{aligned} \mathcal{H}|\Psi_{MI}\rangle &\stackrel{(3.75),(3.76)}{=} \sum_{i=1}^L \frac{U}{2} \hat{n}_i (\hat{n}_i - 1) \prod_{l=1}^L |n_l\rangle_l \\ &= \sum_{i=1}^L \frac{U}{2} n_i (n_i - 1) \delta_{il} \prod_{l=1}^L |n_l\rangle_l \\ &= \sum_{l=1}^L \frac{U}{2} n_l (n_l - 1) |\Psi_{MI}\rangle \\ &= E(N) |\Psi_{MI}\rangle. \end{aligned}$$

Thus, when to a site  $k$  with  $n_k \equiv n$  a particle is added, the energy difference

$$\begin{aligned} E(N+1) - E(N) &= \sum_{l \neq k}^L \frac{U}{2} n_l (n_l - 1) + \frac{U}{2} (n+1)n - \left[ \sum_{l \neq k}^L \frac{U}{2} n_l (n_l - 1) + \frac{U}{2} n(n-1) \right] \\ &= Un \end{aligned}$$

is obtained. In a homogeneous system with  $n_l \equiv n_k \equiv n$  in the vanishing tunneling limit  $J = 0$  the energy gain per particle is

$$\Delta = \frac{\tilde{\Delta}}{n} = U. \quad (3.78)$$

In the homogeneous MI system with finite  $J$  the scaling of the gap is  $\sim U$  for  $U/J \sim 1$  and only in the strongly interacting limit  $U \gg J$  the gap is  $\Delta = U$ . Consequently, the MI phase can be identified based on the gap appearing in the single particle spectrum. The existence of this gap has been verified in experiments e.g. by Greiner et al. [12].

### Compressibility

While in the SF phase the ground state is macroscopically occupied and the occupation grows with increasing number of particles in the system, in the MI the interactions prevent multiple occupation. As a consequence of the existing energy gap, adding or removing a particle from the ground state requires a finite amount of energy. For the next considerations we have to extend our model as variable particle number requires the grand canonical description Eq. (3.63). Thus, an infinitely small change in the chemical potential does not lead to any change in the particle density as long as  $\delta\mu < \Delta$ . Defining the compressibility as the ratio between the variation of particle density caused by an infinitesimal change in the chemical potential

$$\kappa = \frac{\partial n}{\partial \mu}$$

a new critical observable is obtained. In the MI phase an infinitely small change in the chemical potential does not lead to any change in particle density and the compressibility vanishes whereas in the SF phase  $\kappa > 0$ . As a result the MI is called incompressible and the SF a compressible phase.

### 3.2.3 Single particle density matrix

In fermionic systems the Pauli-principle prohibits multiple occupation of a state, characterized by a set of quantum numbers, by more than one fermion. In contrary, once bosons undergo Bose-Einstein condensation, the ground state becomes macroscopically occupied [119]. The ratio between condensed and non-condensed particles is given by the condensate fraction  $f_c$ . Characterizing condensation based on  $f_c$  is equivalent to the off-diagonal long-range order concept (ODLRO) [82]. But before we define both quantities, we introduce the single particle density matrix.

The single particle density matrix (SPDM) corresponds to the equal time one-particle Green's function  $\mathcal{G}_{lm}(t)$  and is defined as

$$\rho_{lm}(t) = \langle \hat{b}_l^\dagger(t) \hat{b}_m(t) \rangle,$$

where the expectation value is calculated with respect to the many-body state of the particles. In general the SPDM is subject to dynamics of the system, however, in the following discussion we will consider static characteristics and neglect the explicit time dependency:

$$\rho_{lm} = \langle \hat{b}_l^\dagger \hat{b}_m \rangle. \quad (3.79)$$

For  $l \neq m$  the SPDM measures the single-particle correlations in the system. When the atomic sample undergoes Bose-Einstein condensation, the de-Broglie wave length of each boson increases in such a way that any particle is delocalized over several sites. Analogously, the particle tunnels freely within the spatial range of its wave function. In homogeneous non-interacting condensates at  $T = 0$  the creation of an atom at site  $l$  and annihilation at site  $m$ , which corresponds to a tunneling process, does not depend on the distance between the sites and in infinitely large lattices  $\rho_{lm}$  does not vanish for  $|x_l - x_m| \rightarrow \infty$ . Given that all off-diagonal  $l \neq m$  elements of the matrix  $\rho_{lm}$  are finite, the condensate is said to possess ODLRO and to maintain spatial coherence. In interacting systems the correlations  $\langle \hat{b}_l^\dagger \hat{b}_m \rangle$  as well as off-diagonal elements of the SPDM  $\rho_{lm}$  decrease exponentially with increasing  $|x_l - x_m|$ . The ODLRO vanishes.

The equivalence between macroscopic occupation of a quantum state and ODLRO can be demonstrated for a homogeneous system [79]. Applying the Fourier transformation to creation and annihilation operators, Eq. (3.79) reads in momentum space

$$\rho_{lm} = \frac{1}{L} \sum_{k,q}^{1.B.Z} \langle \hat{b}_k^\dagger \hat{b}_q \rangle e^{-i(kx_l - qx_m)}. \quad (3.80)$$

Taking translational invariance into account, the operator  $\hat{b}_k^\dagger \hat{b}_q$  commutes with the momentum operator  $\hat{P} = \sum_p^{1.B.Z} \hbar p \hat{b}_p^\dagger \hat{b}_p$ . This leads to the relation

$$\langle \hat{b}_k^\dagger \hat{b}_q \rangle = \delta_{kq} \langle \hat{b}_q^\dagger \hat{b}_q \rangle = \delta_{kq} \langle \hat{n}_q \rangle. \quad (3.81)$$

Substituting Eq. (3.81) into Eq. (3.80) gives

$$\rho_{lm} = \frac{1}{L} \sum_q^{1.B.Z} \langle \hat{n}_q \rangle e^{-iq(x_l - x_m)} = \frac{\langle \hat{n}_0 \rangle}{L} + \int \frac{dq}{2\pi} \langle \hat{n}_q \rangle e^{-iq(x_l - x_m)}. \quad (3.82)$$

In the limit  $|x_l - x_m| \rightarrow \infty$  the exponential function in the last term oscillates rapidly and the last term vanishes (Riemann-Lebesgue lemma). Thus,

$$\lim_{|x_l - x_m| \rightarrow \infty} \rho_{lm} \rightarrow \frac{\langle \hat{n}_0 \rangle}{L}. \quad (3.83)$$

As in this limit the system size  $L$  becomes infinite as well, the ODLRO is only present when the occupation of the  $q = 0$  state is extensive. Given a constant particle density  $n$ , this criterion corresponds to macroscopic occupation and implicates nothing else but a finite condensate fraction  $f_c$ . Next, we introduce and calculate the  $f_c$  of different systems.

The SPDM is hermitian and can be diagonalized

$$\sum_{m=1}^L \rho_{lm} \phi_m^n = \lambda_n \phi_l^n. \quad (3.84)$$

The eigenvectors of the hermitian matrix  $\phi_m^n$  form an orthonormal basis, the so-called natural orbitals. They can be considered as effective single-particle states in real space. The eigenvalues are real and represent the occupation of each orbital. This can be gathered from the calculation of the trace of the SPDM

$$\text{Tr}[\rho] = \sum_{l=1}^L \rho_{ll} = \sum_l \langle \hat{b}_l^\dagger \hat{b}_l \rangle = \sum_l \langle \hat{n}_l \rangle = N \stackrel{(3.84)}{=} \sum_l \lambda_l. \quad (3.85)$$

The trace corresponds to the total particle number in the system. In the last step we used the fact that the trace is invariant under unitary transformations. As diagonalization is such a transformation, the trace is nothing but summation over the eigenvalues of  $\rho_{lm}$ . From here follows  $0 \leq \lambda_l \leq N$ , in accordance with the picture of the occupation of the natural orbitals. The ratio of particles occupying the lowest orbital, i.e. the maximal eigenvalue, defines the condensate fraction

$$f_c = \frac{\lambda_{max}}{N}. \quad (3.86)$$

If in higher dimensions,  $D \geq 2$ , only the occupation of the lowest natural orbital  $\lambda_{max}$  (highest occupied) scales proportional to the particle number, namely  $\lambda_{max} \sim N$ , it can serve as the BEC order parameter in the thermodynamic limit [120]

$$0 \leq \lim_{N \rightarrow \infty} f_c \leq 1 \quad \text{condensate: } \lim_{N \rightarrow \infty} f_c > 0. \quad (3.87)$$

However, it should be emphasized that the magnitude of the condensate fraction depends on the dimensionality and finite size effects. In 1D there exists no BEC even at zero temperature due to the decay of the one-particle correlations  $\rho_{lm} \sim 1/\sqrt{|x_l - x_m|}$  [121–123]. The occupation of the lowest natural orbital is  $\lambda_{max} \sim \sqrt{N}$ , thus  $\lambda_{max} \rightarrow \infty$  for  $N \rightarrow \infty$ , but  $\lim_{N \rightarrow \infty} \lambda_{max}/N \rightarrow 0$ . Nevertheless, this state is referred to as a quasi-condensate due to the extensive  $\lambda_{max}$ . In contrary, in finite systems with an average particle number  $\langle n_l \rangle = N/L$  the condensate fraction is always finite, namely  $f_c \geq N/L$ , which can be deduced from Eq. (3.85). Thus, a careful finite size scaling has to be performed to characterize the system correctly.

Indeed, the biggest challenge is the diagonalization in Eq. (3.84). For a 2D  $L \times L$  system the dimension of the matrix is  $L^2 \times L^2$ . As the aim of theoretical predictions is to model realistic setups, which implements lattice sizes of the order  $L \sim 100$ , the diagonalization becomes computationally not feasible. However, in the limit of strongly interacting ( $J/U \rightarrow 0$ ) and non-interacting ( $J/U \rightarrow \infty$ ) homogeneous systems the condensate fraction can be calculated exactly.

### Condensate fraction of a homogeneous Mott insulator

In the Mott insulating phase ( $J = 0$ ) the ground state of a homogeneous system Eq. (3.55) is a direct product of the single-site states. In the Fock state representation the many-body ground state reads (compare Eq. (3.76))

$$|\Psi_M\rangle = \prod_{l=1}^L |n_l\rangle_l = \prod_{l=1}^L \frac{\hat{b}_l^{\dagger n_l}}{\sqrt{n_l!}} |0\rangle_l, \quad (3.88)$$



where  $n_l$  denotes the integer occupation number and the state  $|0\rangle$  corresponds to the vacuum state at a site  $l$ . The SPDM can be calculated as follows

$$\begin{aligned}
\rho_{lm} &= \langle \hat{b}_l^\dagger \hat{b}_m \rangle = \prod_{k=1}^L {}_k \langle 0 | \frac{\hat{b}_k^{n_k}}{\sqrt{n_k!}} \hat{b}_l^\dagger \hat{b}_m \prod_{j=1}^L \frac{\hat{b}_j^{\dagger n_j}}{\sqrt{n_j!}} | 0 \rangle_j = \\
&= \prod_{k,j} \frac{1}{\sqrt{n_k! n_j!}} {}_k \langle 0 | \hat{b}_k^{n_k} \hat{b}_l^\dagger \hat{b}_m \hat{b}_j^{\dagger n_j} | 0 \rangle_j = \\
&= \prod_{k,j} \frac{1}{\sqrt{n_k! n_j!}} {}_k \langle n_k | \sqrt{n_k!} \hat{b}_l^\dagger \hat{b}_m \sqrt{n_j!} | n_j \rangle_j = \\
&= \prod_{k,j} {}_k \langle n_k | \hat{b}_l^\dagger \hat{b}_m | n_j \rangle_j = \\
&= \prod_{k,j} \sqrt{n_l n_m} \delta_{kl} \delta_{mj} {}_l \langle n_l - 1 | n_m - 1 \rangle_m = \\
&= \sqrt{n_l n_m} \delta_{lm} = n_l.
\end{aligned} \tag{3.89}$$

In the calculation we have used the orthogonality of Fock states  $\langle \alpha | \beta \rangle = \delta_{\alpha\beta}$  and the relation  $\hat{b}_i^{\dagger \alpha} | 0 \rangle = \sqrt{\alpha!} | \alpha \rangle$ . Thus, the condensate fraction vanishes in the thermodynamic limit

$$\lim_{N \rightarrow \infty} f_c = \lim_{N \rightarrow \infty} \frac{n_l}{N} = 0. \tag{3.90}$$

As expected, there exists no condensate in the Mott insulating phase.

### Condensate fraction of a homogeneous condensate

In a non-interacting homogeneous system (Eq. (3.55) for  $U = 0$ ) the Bloch states  $|q\rangle$ , determined via Eq. (3.6), are the eigenvectors of the Hamiltonian with  $|q = 0\rangle$  being the ground state of the system. As the Bloch states are related to Wannier states by means of the Fourier transformation Eq. (3.22), in the Wannier basis  $|j\rangle$  the Bloch states  $|q\rangle$  can be written

$$|q\rangle = \frac{1}{\sqrt{L}} \sum_{j=1}^L e^{iqx_j} |j\rangle. \tag{3.91}$$

Before we proceed with the actual calculation some words about dimensionality. As mentioned before, true condensation appears in  $D \geq 2$ . In a homogeneous two dimensional  $L_x \times L_y$  system, where WLOG  $L_x = L_y$ , the Bloch states read

$$|q\rangle = |q_x, q_y\rangle = \frac{1}{\sqrt{L}^2} \sum_{j=1}^{L_x} \sum_{k=1}^{L_y} e^{i(q_x x_j + q_y y_k)} |j, k\rangle = \left( \frac{1}{\sqrt{L}} \sum_{j=1}^L e^{iqx_j} |j\rangle \right) \otimes \left( \frac{1}{\sqrt{L}} \sum_{k=1}^L e^{iqy_k} |k\rangle \right).$$

Due to this factorization the calculation of any expectation value simplifies to an effective 1D calculation for  $N$  particles given the total particle number  $N^2$  in 2D system and  $N^3$  in 3D system.

In the ground state all  $N^2$  or  $N^3$  particles occupy the same single particle state  $|\mathbf{q} = 0\rangle$  which consequently is equivalent to the natural orbital  $|\phi_0\rangle \equiv |\mathbf{q} = 0\rangle$  with occupation  $\lambda_{max} = N^2$  or  $N^3$  for 2 or 3 dimensional systems respectively. Thus, the condensate fraction is expected to be  $f_c = 1$ . This can be calculated in the canonical as well as in the

coherent state representation since both descriptions yield the same expectation values for number conserving operators. Next, both calculations will be demonstrated in the effective 1D system, for the sake of readability.

In the canonical description, the macroscopic ground state wave function is (compare Eq. (3.66))

$$|\Psi_{SF}(N)\rangle = \prod_{i=1}^N |q=0\rangle_i = \frac{1}{\sqrt{N!}} \left( \frac{1}{\sqrt{L}} \sum_{j=1}^L \hat{b}_j^\dagger \right)^N |0\rangle, \quad (3.92)$$

where  $|0\rangle$  denotes the many-body vacuum state. The SPDM in this ground state is calculated as follows

$$\begin{aligned} \rho_{lm} &= \langle \hat{b}_l^\dagger \hat{b}_m \rangle = \\ &= \frac{1}{N!} \langle 0 | \left[ \frac{1}{\sqrt{L}} \sum_{j=1}^L \hat{b}_j \right]^N \hat{b}_l^\dagger \hat{b}_m \left[ \frac{1}{\sqrt{L}} \sum_{k=1}^L \hat{b}_k^\dagger \right]^N |0\rangle = \\ &= \frac{1}{N! L^N} \langle 0 | \hat{s}^N \hat{b}_l^\dagger \hat{b}_m \hat{s}^{\dagger N} |0\rangle = \\ &= \frac{1}{N! L^N} \langle 0 | (\hat{b}_l^\dagger \hat{s}^N + N \hat{s}^{N-1}) (N \hat{s}^{\dagger N-1} + \hat{s}^{\dagger N} \hat{b}_m) |0\rangle = \\ &= \frac{N}{(N-1)! L^N} \langle 0 | \hat{s}^{N-1} \hat{s}^{\dagger N-1} |0\rangle = \\ &= \frac{N}{L}. \end{aligned} \quad (3.93)$$

From the second to the third line the abbreviation  $\hat{s} = \sum_{j=1}^L \hat{b}_j$  was used and from the third to the fourth the identity

$$\hat{b}_j \hat{s}^{\dagger N} = N \hat{s}^{\dagger N-1} + \hat{s}^{\dagger N} \hat{b}_j. \quad (3.94)$$

From Eq. (3.93) follows that the SPDM is a  $(L \times L)$  matrix with entries  $N/L$  and can be written as

$$\boldsymbol{\rho} = \frac{N}{L} \begin{bmatrix} 1 & \cdots & 1 \\ \vdots & \ddots & \vdots \\ 1 & \cdots & 1 \end{bmatrix} = \frac{N}{L} \mathbf{1}. \quad (3.95)$$

In a two(three) dimensional system the SPDM reads  $\boldsymbol{\rho} = \frac{N}{L} \mathbf{1}_x \otimes \frac{N}{L} \mathbf{1}_y (\otimes \frac{N}{L} \mathbf{1}_z)$ .

To calculate the condensate fraction we have to find the maximal eigenvalue  $\lambda_{max}$  of the SPDM. Therefore we have to solve the eigenvalue problem of the unity matrix  $\mathbf{1}$ . The characteristic polynomial of the latter is  $\lambda^L - L\lambda^{L-1}$ . Thus, the matrix  $\mathbf{1}$  possesses  $L-1$  eigenvalues 0 and one eigenvalue  $L$ , which is the maximal eigenvalue. Consequently, the maximal eigenvalue of the effective 1D SPDM  $\boldsymbol{\rho}$  is  $\lambda_{max} = N$ . In two and three dimensions it is  $\lambda_{max} = N^2$  and  $N^3$ . Following the definition in Eq. (3.86) the condensate fraction is given by

$$f_c = \frac{\lambda_{max}}{N_{tot}} = \begin{cases} N^2/N^2 = 1 & \text{in 2D,} \\ N^3/N^3 = 1 & \text{in 3D.} \end{cases}$$

as expected for a perfect condensate.

A macroscopically occupied single particle state can always be approximated by a coherent state and thus the same condensate fraction is expected in the coherent state description. Choosing the coherent state  $|\Psi_{SF}(\sqrt{N})\rangle$  with the average particle number  $N$  (see Eq. (3.71))

$$|\Psi_{SF}(\sqrt{N})\rangle = e^{-N/2} e^{\sqrt{N/L} \sum_{m=1}^L \hat{b}_m^\dagger} |0\rangle = e^{-N/2} e^{\sqrt{n} \hat{s}^\dagger} |0\rangle,$$

where we use the abbreviation  $\hat{s}^\dagger = \sum_{m=1}^L \hat{b}_m^\dagger$ , the single particle density matrix is calculated as follows

$$\begin{aligned}
\rho_{lm} &= \langle \Psi_{SF}(\sqrt{N}) | \hat{b}_l^\dagger \hat{b}_m | \Psi_{SF}(\sqrt{N}) \rangle \\
&= \langle 0 | \left( e^{-N/2} \sum_{k=0}^{\infty} \frac{\sqrt{N/L}^k}{k!} \hat{s}^k \right) \hat{b}_l^\dagger \hat{b}_m \left( e^{-N/2} \sum_{n=0}^{\infty} \frac{\sqrt{N/L}^n}{n!} \hat{s}^{\dagger n} \right) | 0 \rangle \\
(3.94) \quad &= \langle 0 | \left( e^{-N/2} \sum_{k=0}^{\infty} \frac{\sqrt{N/L}^k}{k!} (k \hat{s}^{k-1} + \hat{b}_l^\dagger \hat{s}^k) \right) \left( e^{-N/2} \sum_{n=0}^{\infty} \frac{\sqrt{N/L}^n}{n!} (n \hat{s}^{\dagger n-1} + \hat{s}^{\dagger n} \hat{b}_m) \right) | 0 \rangle \\
&= \langle 0 | \left( e^{-N/2} \sum_{k=0}^{\infty} \frac{\sqrt{N/L}^k}{k!} k \hat{s}^{k-1} \right) \left( e^{-N/2} \sum_{n=0}^{\infty} \frac{\sqrt{N/L}^n}{n!} n \hat{s}^{\dagger n-1} \right) | 0 \rangle \\
&= \langle 0 | \left( e^{-N/2} \sum_{k=1}^{\infty} \frac{\sqrt{N/L}^{k-1}}{(k-1)!} \hat{s}^{k-1} \right) \frac{N}{L} \left( e^{-N/2} \sum_{n=1}^{\infty} \frac{\sqrt{N/L}^{n-1}}{(n-1)!} \hat{s}^{\dagger n-1} \right) | 0 \rangle \\
&= \frac{N}{L} \langle 0 | \left( e^{-N/2} \sum_{k'=0}^{\infty} \frac{\sqrt{N/L}^{k'}}{k'!} \hat{s}^{k'} \right) \left( e^{-N/2} \sum_{n'=0}^{\infty} \frac{\sqrt{N/L}^{n'}}{n'!} \hat{s}^{\dagger n'} \right) | 0 \rangle \\
&= \frac{N}{L} \langle \Psi_{SF}(\sqrt{N}) | \Psi_{SF}(\sqrt{N}) \rangle = \frac{N}{L}. \tag{3.96}
\end{aligned}$$

From the fifth to the sixth line the index shift  $k = k' + 1$  and analogously  $n = n' + 1$  was performed. The derivation proved that the SPDM in coherent state representation is identical to the canonical representation Eq. (3.93), which is a necessary condition for equivalence of the representations. Subsequently the condensate fractions are the same.

### 3.2.4 Quantum phase transition

In the previous chapters the individual properties of the system in the cases of purely non-interacting  $U \rightarrow 0$  and purely non-mobile  $J \rightarrow 0$  limits were summarized. However, as already denoted, also for finite interaction or tunneling the SF or MI phases persist. Previous discussions revealed that rather the ratio between kinetic and potential energy than their particular values affects the properties of the ultracold bosonic system. For finite but small hopping amplitude the tunneling happens at the expense of potential energy as the particle number fluctuations lead to a finite repulsion. However, as long as the gain in kinetic energy  $J$  remains smaller than potential energy  $U$  the system remains Mott insulating although the exact ground state can be no longer written as the MI direct product state for  $J = 0$  case in Eq. (3.76). As soon as  $J$  overcomes the energy scale due to interactions the SF-MI transition takes place and particles delocalize. In the limit  $J \gg U, U \rightarrow 0$  the ground state of the system corresponds to the SF ground state Eq. (3.66) or equivalently Eq. (3.71). This quantum phase transition can be experimentally achieved in optical lattices. Following Eq. (3.39) and Eq. (3.57) the hopping amplitude  $J$  can be tuned by changing the lattice depth  $s$  via the laser intensity and the interaction  $U$  by adjusting the scattering length  $a$  via magnetic field.

Predicting the exact ratio  $J/U$  where the transition takes place via theoretical calculations is a challenging mission. As for finite  $J$  and  $U$  the ground state is a many-body state which can't be estimated analytically, advanced numerical methods are needed to calculate the phase diagram. Nevertheless, we can roughly gauge the structure of the phase transition diagram [79].

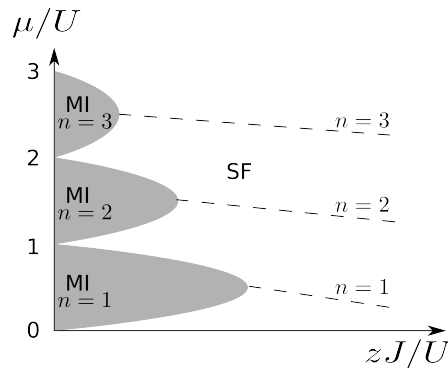


**Figure 3.6:** Illustration of the SF-MI phase transition of the Bose-Hubbard model for a homogeneous system, where  $z$  denotes the number of nearest neighbors. While the particle number per lattice site  $n$  is an integer within a MI, in the SF-region  $n$  can take on all real values. The dotted line indicates the parameter regime for which the particle density is integer in both phases.

### Homogeneous system

For  $J = 0$  the system is in the MI phase with particle density  $n \in \mathbb{N}_0$ . The corresponding ground state minimizes the grand canonical potential (or equivalently the total energy) of the system  $E = \langle \Psi_{MI} | \mathcal{H} - \mu N | \Psi_{MI} \rangle$  with  $\mathcal{H}$  from Eq. (3.75) and ground state  $\Psi_{MI}$  as in Eq. (3.76). As the Hamiltonian is a sum over on-site Hamiltonians, minimization of the total energy  $E$  corresponds to minimization of the on-site energy  $\epsilon = E/L$ . In a homogeneous lattice it is

$$\begin{aligned} \epsilon(n, \mu/U) &= Un(n-1) - \mu n \\ &= \frac{U}{2} \left[ \left( n - \left[ \frac{\mu}{U} + \frac{1}{2} \right] \right)^2 - \left[ \frac{\mu}{U} + \frac{1}{2} \right]^2 \right]. \end{aligned} \quad (3.97)$$

Depending on the chemical potential  $\mu$  or the particle density  $n$  the energy is minimal for

$$\min[\epsilon(n)] \begin{cases} n = 0, & \text{for } \mu < 0, \\ n = \max[\mu/U + 1] \in \mathbb{N}, & \text{else.} \end{cases} \quad (3.98)$$

$$\min[\epsilon(\mu/U)] \quad \text{for } n-1 < \frac{\mu}{U} < n \quad \text{with } n \geq 1. \quad (3.99)$$

At integer values of  $\mu/U$ , e.g.  $\mu/U = n$ , the system is SF even for  $J = 0$  as the energy for  $n$  or  $n+1$  particles per lattice site is the same. Equivalently, the state at  $\mu/U = n-1$  with  $n-1$  particles is degenerate with the  $n$  particle state. Thus, an occupation of a site with  $n$  or  $n+1$  (equivalently  $n-1$  or  $n$ ) particles is equally favorable and no excitation gap exists.

The finite tunneling leads to delocalization and thus to particle number fluctuations<sup>10</sup>. Therefore we expect that for a fixed particle number, finite  $J$  causes a decrease of the  $\mu/U$  range in Eq. (3.99) and thus a reduction of the gap. For large  $J \gg U$  only the SF-phase is possible. This leads to a lobe structure of the MI-phase surrounded by the SF, which is schematically illustrated in Fig. 3.6. The excitation gap of a MI for a given particle density

<sup>10</sup>Particularly, within the MI phase the particle-hole fluctuations exist, whereby the average particle density remains an integer.

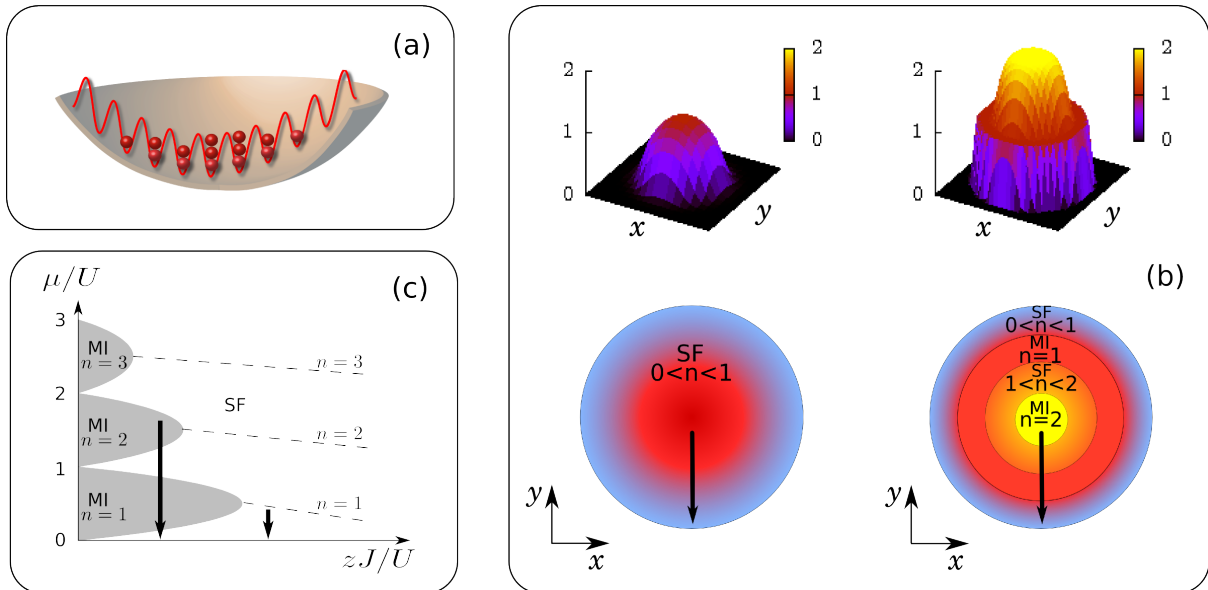


**Figure 3.7:** Illustration of parabolically confined particles in an optical lattice. (a) A cartoon of an optical lattice with an underlying harmonic trap. For better visibility the 2D lattice is indicated by a 1D sinusoidal line. (b) The density profiles in position space mirror the parabolic trapping symmetry. Depending on the filling a pure SF (left) or SF-MI phase mixture (right) appears. The 2D color maps below highlight the respective phases. (c) The arrows in the phase diagram of a homogeneous system indicate the effective local chemical potentials and correspondingly the phases which appear in the trapped system when following the direction according to the arrows in the color maps in (b). The small arrow corresponds to the pure SF and the big one to the wedding-cake structured density profile.

$n$  corresponds to the width of the Mott lobe, which is the distance in the  $\mu/U$  direction at a fixed  $zJ/U$  from the lower to the upper phase border. It is interesting to note that, given a fixed particle density, starting within the MI phase an increase of  $J/U$  leads to a MI-SF phase transition. However, starting from the SF phase, upon decreasing the ratio  $J/U$ , the quantum phase transition can be only achieved when the initial particle density  $n \in \mathbb{N}$ .

The next step is to calculate the exact borders between the SF and MI phases in homogeneous systems. As already mentioned, the Bose Hubbard model is not exactly solvable when interactions are present in the system. Thus, the phase diagram can be only achieved via quantum Monte-Carlo simulations, bosonic dynamical mean-field theory or approximately via Gutzwiller mean-field technique or second order perturbation theory, to name the most frequently used. In Sec. 3.4 the analytic calculations based on Gutzwiller approach are given.

### Inhomogeneous system

When an underlying trapping potential is present in the system the situation changes. The potential landscape constrains the particles around the trap center, as pointed out in Fig. 3.7 (a), which breaks the translational invariance. The additional term in the Hamiltonian  $\sum_i V_{i,\text{trap}} n_i$  (see Eq. (3.63)) can be absorbed in the chemical potential which consequently becomes site dependent

$$-\sum_i (\mu - V_{i,\text{trap}}) n_i = -\sum_i \mu_i^{\text{eff}} n_i. \quad (3.100)$$

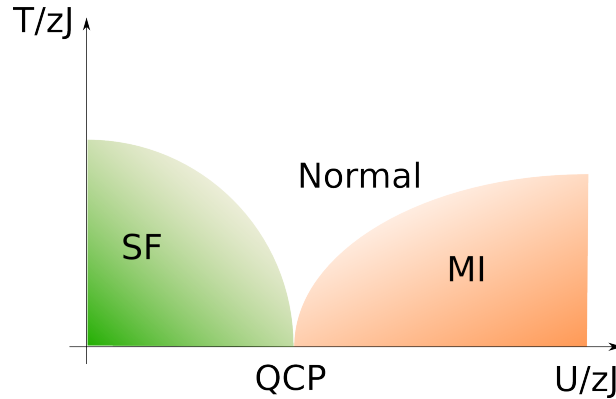


**Figure 3.8:** Qualitative temperature dependent ground state phase diagram for a fixed integer filling  $n$ . QCP denotes the quantum critical point for the SF-MI transition at  $T = 0$ .

Hence, proceeding in the radial direction from the trap center to the trap boundary the effective local chemical potential decreases. This path corresponds to a vertical line in the phase diagram Fig. 3.6 at a fixed  $J/U$  ratio starting at  $\mu_0^{\text{eff}} = \mu$  and ending at zero. The phases crossed along this line are present in the system simultaneously however at different sites.

For large  $J/U$  the entire system is SF. The particle wave functions are delocalized within the area with  $\mu_i^{\text{eff}} > 0$  and the density profile mimics the curvature of the confining potential in contrast to a homogeneous density distribution of a simple periodic lattice, see Fig. 3.7(b) left and the corresponding paths within the homogeneous phase diagram (c). For intermediate  $J/U$  ratios SF as well as MI regions appear. In particular, the axial symmetric MI plateaus are surrounded by SF rings and the density profile resembles a multi-level *wedding cake*, see Fig. 3.7(b) right and the corresponding paths within the homogeneous phase diagram (c). Only for  $J = 0$  the entire system becomes MI and the radial density profile a multi-step function.

### Phase transition at finite temperature

At finite temperatures a new phase emerges - the normal liquid. The thermal fluctuations induce a classical phase transition between condensate and normal phase as they decrease the macroscopic occupation of the SF-state and thus destroy the long range coherence indicating condensation. In addition, temperature causes a crossover between MI and normal phase. We refer to the second as a crossover rather than a phase transition because at finite temperatures the compressibility  $\kappa$  is always finite, which excludes MI by definition. However, the pronounced regions of  $\kappa$  close to zero in the finite  $T$  phase diagram and differences in the density of particle-hole excitations suggest an extension of the glossary. The questions to answer are: what is the critical temperature of SF to normal and MI to normal transitions and how does the temperature affect the SF-MI transition discussed above. A qualitative ground state phase diagram is sketched in Fig. 3.8.

Since for a given integer filling  $n$  the energy gap of the Mott phase depends only on the width of the Mott lobe and thus on the given hopping amplitude  $J$ , at finite temperatures the energy for particle-hole excitations is lowered due to thermally activated particle-hole fluctuations. These fluctuations are exponentially small for temperatures smaller than the gap  $\Delta$  and overcome the excitation energy when  $k_B T > \Delta$ . Consequently, the insulating Mott gap is destroyed for temperatures  $k_B T_c \sim \Delta$ . For increasing temperatures  $T < T_c$  the

Mott plateau (Fig. 3.6) with integer filling shrink, where the Mott lobes with higher particle density persist longer the temperature due to larger interaction strength  $U$  which has to be compensated thermally [109]. Expanding the mean-field approach to finite temperatures (details in Sec. 3.6) the critical  $T_c$  can be calculated. The crossover temperature amounts to  $0.5 \dots 0.7zJ$  around the first Mott lobe and  $1.1 \dots 1.3zJ$  around the second [109]. For  $T > T_c$  particles undergo a crossover to the normal liquid phase. Defining the Mott gap  $\Delta$  as the chemical potential discontinuity random phase approximation calculations revealed  $k_B T_c \approx \Delta$  [124], which was confirmed by numerical investigation of the atomic density profile and on-site number fluctuations via QMC leading to  $k_B T_c = \Delta$  [110]. Moreover, measurements of atomic pair fluctuations allow for temperature estimation at energies of the order  $\mathcal{O}(\Delta)$  in experiments.

Also the size of the SF-region decreases with increasing  $T$ . The temperature leads to a filling of higher momenta and to a depletion of the condensate, defined possessing a macroscopic occupation of the lowest lying natural orbital at  $q = 0$  in thermodynamic limit. Thus, thermal effects amplify the interaction driven reduction of superfluidity. Consequently, with increasing  $U$  the critical temperature needed to destroy SF phase decreases. In the mean-field approximation the non-interacting SF is completely destroyed by thermal fluctuations at  $T_c = 1.45zJ$  and the interacting SF already at  $T < T_c$  [109, 124]. The QMC simulations predict a SF-N phase transition for  $U = 0$  in 3D at  $T_c = 5.6J$  [125].

### 3.2.5 Time-of-flight measurements

The quantum phases - superfluid (SF) and Mott insulator (MI) - are uniquely characterized based on quantum correlations: In the SF phase off-diagonal long range order exists and the macroscopic wave function possesses a phase coherence. In contrast, in the MI phase the long range order is absent, so the one-particle correlations decay exponentially with the distance between sites, i.e.  $\rho_{ij} \sim \exp\{-|i - j|\}$ . Thus, the study of the quantum phases and the quantum phase transition can be based on the investigation of spatial quantum correlations, which are observed in time-of-flight (TOF) and noise correlation measurements [12, 126–130]. In this chapter the theoretical background of the first method will be presented.

The experimental procedure is sketched in Fig. 3.9: the trap and the optical lattice are suddenly switched off and the atomic cloud expands freely in all directions and follows the gravitational sag. The matter waves of single particles interfere with each other and the final density distribution of the atoms can be measured via absorption imaging. The measured particle density is closely related to the initial momentum distribution in the lattice, as will be derived next following the lines of Toth *et al.* [127]. Thus, from the TOF measurements an insight into the coherence properties and spatial correlations of the initial state can be gained.

During the expansion interactions between the atoms take place and lead to scattering into unoccupied modes, which blurs the initial momentum distribution we are interested in. However, since the cross section and with it the scattering probability scales with particle density, these processes become only important in condensates at high density. As during the expansion the particle density decreases and we are interested in large expansion times, we can neglect the effect of interactions in a good approximation through out the derivation for simplicity.

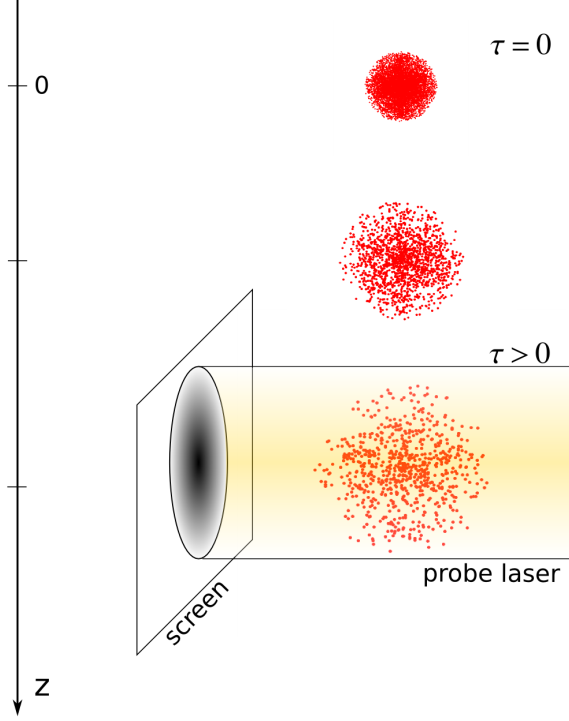


**Figure 3.9:** Schematic representation of the time of flight experiment. The snapshots of the expanding atomic cloud following the gravitational sag in  $z$ -direction are presented simultaneously. After an expansion time  $\tau > 0$  an absorption measurement yields the real space density distribution corresponding to the momentum space density distribution before the expansion.

After the switch-off of all potentials the time evolution of the initial lattice many-body state  $|\Phi\rangle$  is described by the free particle propagator

$$U(t) = e^{-\frac{i\mathcal{H}_0 t}{\hbar}} \quad \text{with} \quad \mathcal{H}_0 = \int d^3r \hat{\Psi}^\dagger(\mathbf{r}) \frac{p^2}{2m} \hat{\Psi}(\mathbf{r}), \quad (3.101)$$

where  $\hat{\Psi}^\dagger(\mathbf{r})$  and  $\hat{\Psi}(\mathbf{r})$  denote the creation and annihilation field operators at position  $\mathbf{r}$  respectively. The particle distribution at time  $t$  is given by

$$\langle \hat{n}(\mathbf{r}, t) \rangle = \langle \hat{\Psi}^\dagger(\mathbf{r}, t) \hat{\Psi}(\mathbf{r}, t) \rangle, \quad (3.102)$$

where the time-dependent field operators in the Heisenberg picture correspond to  $\hat{\Psi}(\mathbf{r}, t) = U^\dagger(t) \hat{\Psi}(\mathbf{r}) U(t)$ , with  $U(t)$  defined in Eq. (3.101). Since the Wannier functions form an orthonormal basis, we can expand the field operators in terms of Wannier states. Thus, in the lowest-band approximation the field operator reads

$$\hat{\Psi}(\mathbf{r}) = \sum_i w_0(\mathbf{r} - \mathbf{R}_i) \hat{b}_i \quad \text{and} \quad \hat{\Psi}(\mathbf{r}, t) = \sum_i w_0(\mathbf{r} - \mathbf{R}_i, t) \hat{b}_i \quad (3.103)$$

where  $w_0(\mathbf{r} - \mathbf{R}_i, t) = U^\dagger(t) w_0(\mathbf{r} - \mathbf{R}_i) U(t)$  is the lowest-band Wannier function localized at lattice site  $i$  and  $\hat{b}_i$  is the bosonic annihilation operator. Using this expression we can rewrite Eq. (3.102) in terms of Wannier states

$$\langle \hat{n}(\mathbf{r}, t) \rangle = \sum_{ij} w_0^*(\mathbf{r} - \mathbf{R}_i, t) w_0(\mathbf{r} - \mathbf{R}_j, t) \langle \hat{b}_i^\dagger \hat{b}_j \rangle. \quad (3.104)$$



Since  $\langle \hat{n}(\mathbf{r}, t) \rangle$  is the observable measured in the TOF experiment, the goal is to calculate this expectation value and to find out how it is related to the distribution in momentum space.

Similar to light interference experiments, the observed pattern depends on the distance between the source of the matter waves and the observation apparatus. Here we differentiate between near-field and far-field diffraction. The *far-field* approximation describes the regime where the initial extent of each interfering wave can be neglected and the dependence on the initial position of each wave can be partially dropped. As will be demonstrated in this chapter, in this limit the observed interference pattern corresponds to the Fourier-transform of the original density distribution in space, i.e. the momentum distribution of interacting particles in the lattice. In the *near-field* approximation the quadratic dependence of the phase on the initial wave positions is taken into account which leads to more complex interference pattern than the pure Fourier-transform.

For lattices of depth  $s > 10E_r$  the Wannier function can be assumed as Gaussian to a good approximation<sup>11</sup>. To derive the right width of the corresponding Gaussian we approximate the lattice potential  $V(\mathbf{r}) = V_0 \sin^2(\mathbf{r})$  around each site  $i$  by a parabolic function and neglect any additional trappings. As the lattice potential is separable in space we restrict ourselves for simplicity to one dimension

$$V(x) = V_0 \sin^2(x) \approx V_0 + V_0(x - x_i)^2 \approx \frac{1}{2}m\omega_l^2(x - x_i)^2, \quad (3.105)$$

where  $\omega_l$  denotes the lattice frequency and the global additive constant  $V_0$  was neglected in the last step. The ground state wave function corresponding to this parabolic potential is a Gaussian  $\phi_0(x) = \frac{1}{\sqrt{\pi x_0}} e^{-\frac{(x-x_i)^2}{x_0^2}}$  of width  $x_0 = \sqrt{\frac{\hbar}{m\omega_l}}$ . In intermediate and deep lattices we can approximate the lowest band Wannier function by this Gaussian, thus, expanding the result to 3D the Wannier function reads

$$w_0(\mathbf{r} - \mathbf{R}_i) \approx \frac{1}{\pi^{3/4} x_0^{3/2}} e^{-(\mathbf{r} - \mathbf{R}_i)^2 / 2x_0^2}. \quad (3.106)$$

The time-dependent approximated Wannier state is calculated via  $w_0(\mathbf{r} - \mathbf{R}_i, t) = U^\dagger(t)w_0(\mathbf{r} - \mathbf{R}_i)U(t)$  with  $U(t)$  defined in Eq. (3.101). The resulting time dependent Wannier function is

$$w_0(\mathbf{r} - \mathbf{R}_i, t) = \frac{1}{\pi^{3/4} W(t)^{3/2}} e^{-\frac{(\mathbf{r} - \mathbf{R}_i)^2}{2W^2(t)}} e^{i\frac{(\mathbf{r} - \mathbf{R}_i)^2}{2W^2(t)} \frac{\hbar t}{mx_0^2}} e^{-i\theta} \quad (3.107)$$

with time dependent Gaussian width

$$W(t) = x_0 \sqrt{1 + (\hbar t / mx_0^2)^2} \quad (3.108)$$

and phase  $\theta = 1/2 \arctan(\hbar t / mx_0^2)$ . Inserting Eq. (3.107) into Eq. (3.104) the time dependent particle density distribution reads

$$\begin{aligned} \langle \hat{n}(\mathbf{r}, t) \rangle &= \frac{1}{\pi^{3/2} W^3(t)} \cdot \sum_{ij} \underbrace{e^{-\frac{(\mathbf{r} - \mathbf{R}_i)^2}{2W^2(t)}} e^{-\frac{(\mathbf{r} - \mathbf{R}_j)^2}{2W^2(t)}}}_A \\ &\cdot \underbrace{e^{-i\frac{(\mathbf{r} - \mathbf{R}_i)^2}{2W^2(t)} \frac{\hbar t}{mx_0^2}} e^{i\frac{(\mathbf{r} - \mathbf{R}_j)^2}{2W^2(t)} \frac{\hbar t}{mx_0^2}}}_B \langle \hat{b}_i^\dagger \hat{b}_j \rangle. \end{aligned} \quad (3.109)$$

<sup>11</sup>For details see Sec. 3.1.1.

Evaluating the upper expression leads to the exact measured density distribution at every time  $t$  when particles were initially in a sufficiently deep lattice ( $s > 10E_r$ ). However, the solution is too complex to recognize the relation to the quantities such as the initial momentum distribution. Thus, based on the fact that the observation point is sufficiently far from the original lattice, we can make approximations and discuss the terms individually.

### Far-field approximation

First, we discuss the situation when the lattice is far from the observation point  $|\mathbf{r}| \gg |\mathbf{R}_i|$  which corresponds to the assumption of large expansion time. In this case the initial extent of each Wannier state is negligible which is equivalent to a point-like particle distribution. Therefore, for large expansion times the constant term under the square root can be neglected. Consequently Eq. (3.108) reads

$$W(t) \approx \frac{\hbar t}{mx_0}. \quad (3.110)$$

Under this approximation the individual terms in Eq. (3.109) can be rewritten:

$$\begin{aligned} A : \quad e^{-\frac{(\mathbf{r}-\mathbf{R}_i)^2}{2W^2(t)}} e^{-\frac{(\mathbf{r}-\mathbf{R}_j)^2}{2W^2(t)}} &= e^{-\left[\frac{\mathbf{r}^2}{W^2(t)} - \frac{\mathbf{r}(\mathbf{R}_i+\mathbf{R}_j)}{W^2(t)} + \frac{\mathbf{R}_i^2+\mathbf{R}_j^2}{2W^2(t)}\right]} \\ &\approx e^{-\frac{\mathbf{r}^2}{W^2(t)}}. \end{aligned} \quad (3.111)$$

Thereby we neglected the last term containing the quadratic dependence on the initial position and the next to last term, as it has only minor effect on the remaining exponentially decaying envelope function. Similarly, the term  $B$  reduces to

$$\begin{aligned} B : \quad e^{-i\frac{(\mathbf{r}-\mathbf{R}_i)^2}{2W^2(t)}\frac{\hbar t}{mx_0}} e^{i\frac{(\mathbf{r}-\mathbf{R}_j)^2}{2W^2(t)}\frac{\hbar t}{mx_0}} &= e^{-i\frac{\hbar t}{mx_0}\left[\frac{-\mathbf{r}(\mathbf{R}_i-\mathbf{R}_j)}{W^2(t)} + \frac{\mathbf{R}_i^2-\mathbf{R}_j^2}{2W^2(t)}\right]} \\ &\approx e^{-i\mathbf{Q}(\mathbf{r})(\mathbf{R}_j-\mathbf{R}_i)}. \end{aligned} \quad (3.112)$$

This time only the term quadratic in  $\mathbf{R}_i$  was dropped. The remaining phase term contains the information about the quasi-momentum and was simplified using the identity  $\mathbf{Q}(\mathbf{r}) = m\mathbf{r}/\hbar t$ . With approximated parts  $A$  and  $B$  the measured density distribution reads

$$\begin{aligned} \langle \hat{n}(\mathbf{r}, t) \rangle_{far} &= \frac{1}{\pi^{3/2}W^3(t)} e^{-\frac{\mathbf{r}^2}{W^2(t)}} \sum_{ij} e^{-i\mathbf{Q}(\mathbf{r})(\mathbf{R}_j-\mathbf{R}_i)} \langle \hat{b}_i^\dagger \hat{b}_j \rangle \\ &= \frac{1}{\pi^{3/2}W^3(t)} e^{-\frac{\mathbf{r}^2}{W^2(t)}} \langle \hat{n}(\mathbf{Q}(\mathbf{r})) \rangle, \end{aligned} \quad (3.113)$$

which is nothing else but the initial quasi-momentum distribution multiplied with an envelope function. Due to the periodicity of the sinusoidal lattice potential the measured distribution is a periodic function in the reciprocal space and we can restrict ourselves to the first Brillouin zone.

The analytic expression in Eq. (3.113) is a good approximation of the TOF measurement result in the *far-field* regime, namely for large expansion times  $t$  and distances  $|\mathbf{r}|$ , and becomes exact in the limit  $t \rightarrow \infty$ . However, as the expansion time becomes shorter the above approximations lose their accuracy and the measured distribution does no longer represent a Fourier transformation.

### Near-field approximation

In the *near-field* approximation, whose range of validity we will discuss next, the neglected quadratic term in the complex phase Eq. (3.112) is taken into account. Hence, the distribution with complete interference term reads

$$\langle \hat{n}(\mathbf{r}, t) \rangle_{near} = \frac{1}{\pi^{3/2} W^3(t)} e^{-\frac{\mathbf{r}^2}{W^2(t)}} \sum_{ij} e^{-i\mathbf{Q}(\mathbf{r})(\mathbf{R}_j - \mathbf{R}_i)} e^{-\frac{im}{\hbar t} \frac{\mathbf{R}_i^2 - \mathbf{R}_j^2}{2}} \langle \hat{b}_i^\dagger \hat{b}_j \rangle. \quad (3.114)$$

When do we have to take the full phase into account? When the correlations are absent in the system, the correlation function  $\langle \hat{b}_i^\dagger \hat{b}_j \rangle$  falls off exponentially with a characteristic length  $l_c$  smaller than the cloud extend  $R_0$  [131]. Thus, the contribution of the sites is suppressed, when the distance between them overcomes the correlation length. This allows an estimate for the largest appearing phase [132]. Near the cloud center the magnitude of the quadratic term is  $\mathbf{R}_i^2 - \mathbf{R}_j^2 \approx l_c$  and the phase is approximately

$$\text{near the cloud center:} \quad \frac{m}{\hbar t} \frac{\mathbf{R}_i^2 - \mathbf{R}_j^2}{2} \approx \frac{ml_c^2}{2\hbar t}. \quad (3.115)$$

Close to the cloud radius  $|\mathbf{R}_i|, |\mathbf{R}_j| \approx R_0$  and  $\mathbf{R}_i^2 - \mathbf{R}_j^2 \approx 2l_c R_0$ . Consequently the magnitude of the phase is

$$\text{near the cloud boundary:} \quad \frac{m}{\hbar t} \frac{\mathbf{R}_i^2 - \mathbf{R}_j^2}{2} \approx \frac{ml_c R_0}{\hbar t}. \quad (3.116)$$

The additional phase can thus be neglected when the expansion time  $t$  overcomes the larger threshold time  $t_F = ml_c R_0 / \hbar$ , which is called the *Fresnel time* in analogy to optics,

$$\text{near-field approx.: } t < \frac{ml_c R_0}{\hbar} \quad \text{far-field approx.: } t \gg \frac{ml_c R_0}{\hbar}. \quad (3.117)$$

As an example, for a typical bosonic experiment with  $^{87}\text{Rb}$  in an optical lattice with lattice constant  $a = 532$  nm and nearly 50 lattice sites [75], within the superfluid phase with  $l_c \approx R_0 \approx 25 \cdot 532$  nm the Fresnel time would be  $t_F \approx 300$  ms while the typical expansion times are of the order of 30 ms. In this case the far-field approximation is a poor approach. On the other hand, in the Mott insulating regime where the correlation length is only few sites large the Fresnel time is  $t_F \approx 20$  ms and the measured distribution indeed corresponds to the Fourier transform of the wave function in the lattice.

It is important to note that, although we approximated the phase in Eq. (3.115) and (3.116) by a constant, this quantity is in general non-local and depends not only on the relative separation of the lattice sites but also on their absolute position due to the inhomogeneities in the lattice induced e.g. by a trapping potential [131, 132]. Hence, deviations between theoretical TOF predictions and measurement are based not only on the finite expansion time but also on specific geometry not taken into account.

### Phase detection via time-of-flight measurements

#### Superfluid

In the non-interacting condensate in a homogeneous lattice we can give an analytic expression for the measured particle density distribution since the single particle density matrix  $\hat{\rho}_{ij} = \langle \hat{b}_i^\dagger \hat{b}_j \rangle$  has been calculated exactly for this case in Sec. 3.2.3. In the homogeneous translational invariant system  $\langle \hat{n}(\mathbf{r}, t) \rangle = \langle \hat{n}(x, t) \rangle \langle \hat{n}(y, t) \rangle \langle \hat{n}(z, t) \rangle = \langle \hat{n}(x, t) \rangle^3$  and the

3D problem is reduced to an effective 1D. In the far-field approximation the distribution  $\langle \hat{n}(x, t) \rangle$  reads

$$\begin{aligned} \langle \hat{n}(x, t) \rangle &= \frac{1}{\pi^{1/2} W(t)} e^{-\frac{x^2}{W^2(t)}} \sum_{ij} e^{-iq(x)(x_j - x_i)} \langle \hat{b}_i^\dagger \hat{b}_j \rangle \\ (3.93) \quad &\stackrel{=}{=} \frac{1}{\pi^{1/2} W(t)} e^{-\frac{x^2}{W^2(t)}} \sum_{ij} e^{-iq(x)(x_j - x_i)} \frac{N}{L} \end{aligned}$$

where  $N$  is the total particle number in a 1D  $L$ -sites lattice. The distance between two sites is discretized in units of lattice spacing  $a$ :  $|x_j - x_i| = la$  with  $l \in \mathbb{N}_0$ . Thus we continue

$$\begin{aligned} &= \frac{1}{\pi^{1/2} W(t)} e^{-\frac{x^2}{W^2(t)}} \frac{N}{L} \sum_{l \in \mathbb{N}_0} e^{\pm iq(x)la} \\ &= A(x) N \delta \left( q(x) = \pm \frac{2\pi m}{a} \right) \\ (3.113) \quad &\stackrel{=}{=} A(x) \langle \hat{n}(q(x)) \rangle, \end{aligned} \tag{3.118}$$

thereby  $A(x) = \frac{1}{\pi^{1/2} W(t)} e^{-\frac{x^2}{W^2(t)}}$  and  $m \in \mathbb{N}_0$ . Following from this result, the homogeneous non-interacting superfluid is indicated by series of delta-peaks at multiples of the reciprocal lattice constant modulated by a Gaussian envelope. The height of the delta peak at  $x = 0$  corresponds to the particle number in the  $q = 0$  mode<sup>12</sup>. As expected, in the non-interacting limit all  $N$  particles coherently populate the lowest energy state.

Interactions lead to a depletion of the condensate at  $q = 0$  and population of other momentum states. Consequently, in a homogeneous system the TOF measurement mirroring the particle distribution in momentum space evolves with increasing interaction strength continuously from the perfect SF delta-peaked structure towards a flat MI distribution [82] discussed next.

In inhomogeneous systems, such as optical lattices with a trapping potential, the correlator  $\langle \hat{b}_i^\dagger \hat{b}_j \rangle$  remains position dependent. Since a broad function in real space becomes a sharp distribution in momentum space and vice versa, the introduction of a spatial confinement leads to broadening of single delta peaks in the momentum distribution, leaving the  $2\pi/a$  periodicity unchanged.

### Mott insulator

The opposite to non-interacting is the  $J/U \rightarrow 0$  ‘‘atomic’’ limit. In homogeneous systems the many body wave function can then be written as a direct product of single site wave functions each being a Fock state  $|n\rangle$  with  $n \in \mathbb{N}$ . Following the calculation in Sec. 3.2.3, due to orthogonality of Fock states the corresponding single particle density matrix is

<sup>12</sup>This delta peak refers to the 1st B.Z.  $q \in [-\pi/a; \pi/a]$ . The delta peaks at other modes reflect the periodicity of higher Brillouin zones and are redundant concerning the degree of condensation.

$\hat{\rho}_{ij} = \langle \hat{b}_i^\dagger \hat{b}_j \rangle = n_i \delta_{ij}$  (see Eq. (3.89)) and the measured TOF distribution in the far-field approximation reads

$$\begin{aligned}
 \langle \hat{n}(x, t) \rangle &= \frac{1}{\pi^{1/2} W(t)} e^{-\frac{x^2}{W^2(t)}} \sum_{ij} e^{-iq(x)(x_j - x_i)} \langle \hat{b}_i^\dagger \hat{b}_j \rangle \\
 &= \frac{1}{\pi^{1/2} W(t)} e^{-\frac{x^2}{W^2(t)}} \sum_{ij} e^{-iq(x)(x_j - x_i)} n_i \delta_{ij} \\
 &= \frac{1}{\pi^{1/2} W(t)} e^{-\frac{x^2}{W^2(t)}} N \\
 &\stackrel{(3.113)}{=} A(x) \langle \hat{n}(q(x)) \rangle, \tag{3.119}
 \end{aligned}$$

where  $A(x) = \frac{1}{\pi^{1/2} W(t)} e^{-\frac{x^2}{W^2(t)}}$ . The measured TOF distribution  $\langle \hat{n}(x, t) \rangle$  is a broad Gaussian which reveals a flat momentum distribution  $\langle \hat{n}(q(x)) \rangle = N$ . Interactions induce population of energetically higher momentum states and lead to a localization of ground state wave function. In accordance with previous discussions in Sec. 3.2.2 sharp on-site localization of particles in real space results in a flat distribution in momentum space.

In inhomogeneous systems the density distribution develops a wedding cake structure i.e. the Mott insulating plateaus become surrounded by superfluid shells (see Sec. 3.2). Scanning the particle density along a radial direction within the trap corresponds to moving parallel to  $\mu$ -axis in the  $(\mu/zJ, U/zJ)$ -phase diagram of a homogeneous system at a fixed  $U/zJ$ . The presence of the superfluid phase inhibits the disappearance of the narrow peak at  $q = 0$  such that the momentum distribution  $\langle \hat{n}(q) \rangle$  does not become flat although a Mott insulating plateau develops. Additionally, the shell structure of the superfluid leads to a fine satellite peak structure at momenta  $q \sim \pi/l$ , where  $l$  is the radius of the shell, following the QMC calculations by [126]. The appearance of such peaks marks the SF-MI transition in the center of the trap. Increasing the interaction  $U$  (or alternatively the lattice depth) decreases the SF shell and raises the occupation in the tail of the distribution, however, the presence of correlations maintains the  $q = 0$  peak with a height proportional to particle number in the SF.

Since in inhomogeneous systems correlations do not vanish completely, the phase transition can not be deduced from the population of the  $q = 0$  peak alone. To characterize the interference pattern the concept of *visibility* was established. This quantity gives the population ratio between the maximally and the minimally occupied momenta

$$\eta = \frac{\langle \hat{n}(\mathbf{Q}_{max}) \rangle - \langle \hat{n}(\mathbf{Q}_{min}) \rangle}{\langle \hat{n}(\mathbf{Q}_{max}) \rangle + \langle \hat{n}(\mathbf{Q}_{min}) \rangle}. \tag{3.120}$$

The visibility is not critical at the phase transition and thus not useful for a precise measurement of the transition point, however, it characterizes the degree of the coherence in the system for a given  $(J/U, V_{latt})$  parameter set. Since extraction of comparable information from direct measurement of correlations or via noise-correlation and particle statistics observation is more complicated experimentally, the visibility is widely used for studies of coherence properties in a broad range of experiments. In a perfect SF phase all particles occupy a single momentum state, thus  $\langle \hat{n}(\mathbf{Q}_{max}) \rangle = N$  and  $\langle \hat{n}(\mathbf{Q}_{min}) \rangle = 0$ , hence  $\eta = 1$ . In the homogeneous MI phase the momentum distribution is flat  $\langle \hat{n}(\mathbf{Q}_{max}) \rangle = \langle \hat{n}(\mathbf{Q}_{min}) \rangle$  and  $\eta = 0$ . In case of inhomogeneities or decreased coherence the visibility takes the values  $\eta \in ]0; 1[$ . Since the main concern was the study of the momentum distribution one has to

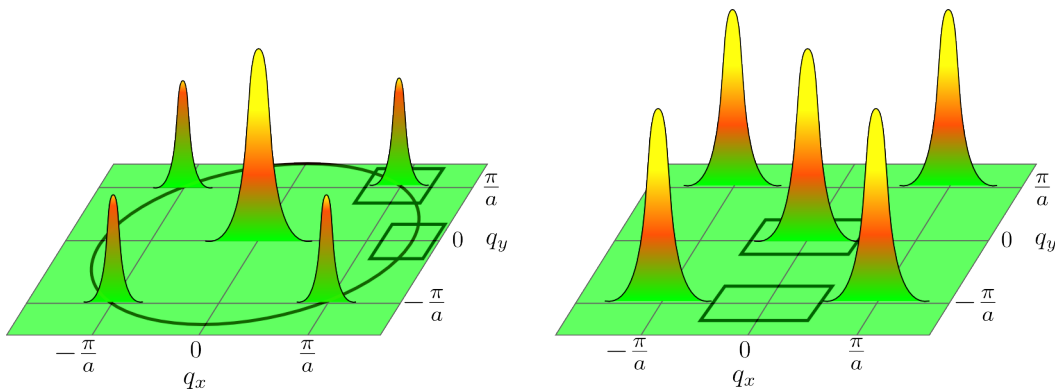


**Figure 3.10:** Sketch of the observed time of flight density distribution (color coded, arbitrary units). In the left figure the delta peaks (here with a finite width for a better visibility) are convolved with a Gaussian envelope. To avoid the contribution of the envelope function in the visibility a peak density is compared with the density in the valley at the same radius (denoted by squares). In the right figure the same peaked structure without the envelope. Since all peaks are of the same height no restrictions exist and the visibility can be calculated e.g. based on values emphasized by squares.

pay attention to the undesired contribution of the superimposed envelope resulting from the shape of the Wannier states, see Fig. 3.10. In the experiment, the distributions along a radius are analyzed such that the contribution of the radially symmetric envelope function does not influence the results. Thus, considered momenta are e.g.  $\mathbf{Q}_{max} = (2\pi/a; 0)$  and  $\mathbf{Q}_{min} = \sqrt{2}(\pi/a; \pi/a)$ . In theoretical calculations the Wannier shape of the initial matter waves is usually not taken into account and a direct relation between the central peak and the background is estimated, i.e. at momenta  $\mathbf{Q}_{max} = (0; 0)$  and  $\mathbf{Q}_{min} = (0; \pi/a)$ .

### 3.3 Numerical method: Gutzwiller approximation

In Sec. 3.2.1 and 3.2.2 we derived the exact ground states for two limits of the homogeneous Bose-Hubbard model: the non-interacting  $U = 0$  and the localized  $J = 0$ . The ground states are direct product states over on-site Fock states within the MI phase Eq. (3.76) and on-site coherent states within the SF phase Eq. (3.71). In the intermediate regime with the finite interaction and tunneling matrix elements no analytic solution exists and the model can be only solved numerically.

Since we are interested in the characterization of the model considering the full range of couplings - both weak and strong - perturbative methods are not applicable. The Hamiltonian in Eq. (3.55) can in principle be analyzed by Quantum Monte Carlo simulations [126, 132] which are exact at finite and in some cases [63, 133] at zero temperatures but suffer from long computational times. Furthermore, these simulations are restricted to equilibrium situations and cannot describe dynamical processes like ramping up of the optical lattice or atomic cloud expansion we are going to investigate in this thesis. Alternatively one can apply the time-evolving block decimation (TEBD) method to simulate the dynamics [28]. This method is exact in 1D but it can not be extended to higher dimensions realized in experiments. Thus, in this thesis we study dynamical as well as static properties of the Bose-Hubbard model by means of a mean-field approximation -

the Gutzwiller method. This technique is exact in both analytic limits,  $J/U \rightarrow 0$  and  $J/U \rightarrow \infty$ , and is assumed to provide good qualitative results in the intermediate parameter regime [124, 134, 135]. It is suitable for ground state calculations as well as for studies of non-equilibrium dynamics requiring a much lower computational effort than exact numerical alternatives. In this section we will derive the approximation for zero and finite temperature, discuss the abilities and restrictions and extend the technique to treat dynamical problems.

### 3.3.1 Gutzwiller ansatz

The Gutzwiller variational method, first developed for the investigation of correlated Fermions [136], was modified in 1991 by Rokhsar and Kotliar for studies of an interacting Bose gas in a lattice [137]. The main idea of the technique is to take a direct product over on-site states, which is exact in the  $J/U \rightarrow 0$  and  $J/U \rightarrow \infty$  limits, as a variational ansatz in the intermediate regime  $0 < J/U < \infty$ . In the Fock basis the many-body Gutzwiller wave function reads

$$|\Psi_{GW}\rangle = \prod_i |\psi_i\rangle_i = \prod_i \left( \sum_{n=0}^{\infty} c_{i,n} |n_i\rangle_i \right). \quad (3.121)$$

In a homogeneous system we have  $n_i \equiv n$  and  $c_{i,n} \equiv c_n$ . The variation of the complex factors  $\{c_{i,n}\}$  is performed with the goal of minimizing the ground state energy

$$\begin{aligned} E_{GW} &= \langle \Psi_{GW} | \mathcal{H} | \Psi_{GW} \rangle \\ (3.63) \quad &= \langle \Psi_{GW} | -J \sum_{\langle ij \rangle} (\hat{b}_i^\dagger \hat{b}_j + c.c.) - \sum_i \mu_{\text{eff},i} \hat{n}_i + \frac{U}{2} \sum_i \hat{n}_i (\hat{n}_i - 1) | \Psi_{GW} \rangle \\ &= -J \sum_{\langle ij \rangle} (\langle \hat{b}_i^\dagger \rangle \langle \hat{b}_j \rangle + h.c.) - \sum_i \mu_{\text{eff},i} \langle \hat{n}_i \rangle + \frac{U}{2} \sum_i \langle \hat{n}_i \rangle (\langle \hat{n}_i \rangle - 1), \end{aligned}$$

where the expectation values are calculated with respect to the variational Gutzwiller state and  $\mu_{\text{eff},i} = \mu - V_{i,\text{trap}}$  accounts for possible lattice inhomogeneities such as a trapping potential. Relying on the decomposition of the many-body state into a direct product of on-site states in the Gutzwiller ansatz, the coupling of the nearest neighbors factorizes:  $\langle \hat{b}_i^\dagger \hat{b}_j \rangle = \langle \hat{b}_i^\dagger \rangle \langle \hat{b}_j \rangle$ . This leads to the following simplification

$$\begin{aligned} \sum_{\langle ij \rangle} (\langle \hat{b}_i^\dagger \rangle \langle \hat{b}_j \rangle + c.c.) &= \frac{1}{2} \sum_i \sum_{j \text{ n.n. } i} (\langle \hat{b}_i^\dagger \rangle \langle \hat{b}_j \rangle + \langle \hat{b}_i \rangle \langle \hat{b}_j^\dagger \rangle) \\ &= \frac{1}{2} \left( \sum_i \langle \hat{b}_i^\dagger \rangle \sum_{j \text{ n.n. } i} \langle \hat{b}_j \rangle + \sum_i \langle \hat{b}_i \rangle \sum_{j \text{ n.n. } i} \langle \hat{b}_j^\dagger \rangle \right) \end{aligned}$$

In the first line the sum over the neighboring pairs was rewritten where  $\sum_{j \text{ n.n. } i}$  indicates a sum over the lattice sites  $j$  being nearest neighbors to the site  $i$ , the factor  $1/2$  corrects the double counting (see Fig. 3.11). Introducing the abbreviation  $\eta_i = \sum_{j \text{ n.n. } i} \langle \hat{b}_j \rangle$  the energy decomposes into a sum of on-site terms

$$E_{GW} = \sum_i \left( -\frac{J}{2} (\langle \hat{b}_i^\dagger \rangle \eta_i + c.c.) - \mu_{\text{eff},i} \langle \hat{n}_i \rangle + \frac{U}{2} \langle \hat{n}_i \rangle (\langle \hat{n}_i \rangle - 1) \right).$$

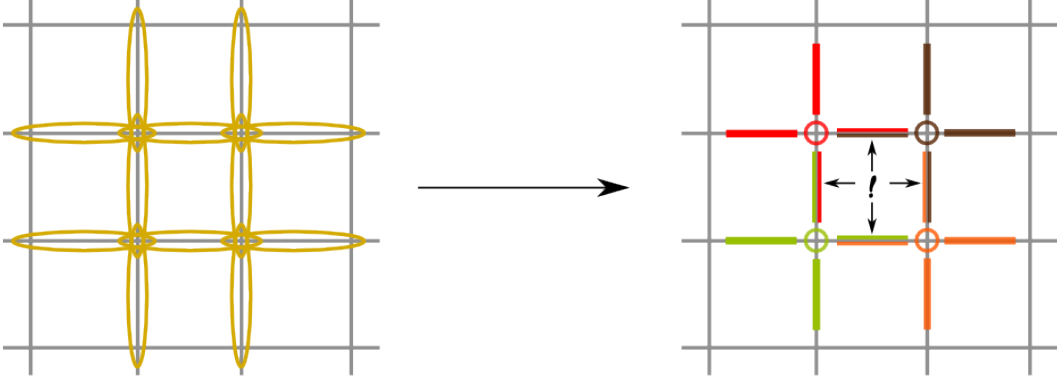


**Figure 3.11:** Summation over the nearest neighbors. Left the coupling of nearest neighbors in  $\sum_{\langle ij \rangle}$  is indicated. Thereby only pairs of neighbors are connected to each other. This summation is replaced by the summation over the lattice sites with subsequent summation over the respective neighbors  $\sum_i \sum_{j \text{ n.n. } i}$  (indicated by colored lines). The arising double counting of lattice connections has to be corrected by factor  $1/2$ .

To make the notation easier we proceed with a homogeneous system where  $V_{i,trap} = 0 \forall i$  and consequently  $\mu_{\text{eff},i} \equiv \mu$ ,  $\langle \hat{b}_i \rangle \equiv \langle \hat{b}_j \rangle$  and  $\eta_i = z \langle \hat{b}_i \rangle$ , where  $z = 2D$  is the number of next neighbors in  $D$  dimensions. Hence the energy reads

$$\begin{aligned}
 E_{GW}(\{c_n\}) &= \sum_i \left( -Jz |\langle \hat{b}_i^\dagger \rangle|^2 - \mu \langle \hat{n}_i \rangle + \frac{U}{2} \langle \hat{n}_i \rangle (\langle \hat{n}_i \rangle - 1) \right) \\
 &= L \left[ \frac{U}{2} \sum_n^{n_{\max}} |c_n|^2 n(n-1) - \mu \sum_n^{n_{\max}} n |c_n|^2 - Jz \left| \sum_n^{n_{\max}} c_n^* c_{n+1} \sqrt{n+1} \right|^2 \right],
 \end{aligned} \tag{3.122}$$

where the expectation values were evaluated based on the Gutzwiller ground state in the Fock representation Eq. (3.121). The variation with respect to an infinite number of Fock states is of course not feasible, thus, a cut-off  $n_{\max}$  was introduced. This cut-off has to be chosen much larger than the average particle number in the system, i.e.  $n_{\max} \gg \langle n \rangle$ . Additionally, the results must be independent of the choice of  $n_{\max}$  indicating that important Fock states are untouched by truncation. Finally, minimization of the  $n_{\max}$ -dimensional function  $E_{GW}(\{c_n\})$  with respect to the complex parameters  $\{c_n\}$  provides the mean field solution of the Schrödinger equation: the ground state and the corresponding energy.

### 3.3.2 Mean-field theory

One can show that the Gutzwiller technique is a mean-field method. For this purpose we first introduce the mean-field concept. We rewrite the annihilation operator in the following way

$$\hat{b}_i = \langle \hat{b}_i \rangle + (\hat{b}_i - \langle \hat{b}_i \rangle).$$

And correspondingly

$$\begin{aligned}
 \hat{b}_i^\dagger \hat{b}_j &= \hat{b}_i^\dagger \langle \hat{b}_j \rangle + \hat{b}_j \langle \hat{b}_i^\dagger \rangle - \langle \hat{b}_i^\dagger \rangle \langle \hat{b}_j \rangle + (\hat{b}_i^\dagger - \langle \hat{b}_i^\dagger \rangle) (\hat{b}_j - \langle \hat{b}_j \rangle) \\
 &\approx \hat{b}_i^\dagger \langle \hat{b}_j \rangle + \hat{b}_j \langle \hat{b}_i^\dagger \rangle - \langle \hat{b}_i^\dagger \rangle \langle \hat{b}_j \rangle + \mathcal{O}((\hat{b}_j - \langle \hat{b}_j \rangle)^2).
 \end{aligned}$$



Neglecting the second order particle density fluctuations in the last line is called the *mean-field decoupling*. Inserting this expression into the hopping term of the Hamiltonian leads to

$$\begin{aligned}
\sum_{\langle ij \rangle} (\hat{b}_i^\dagger \hat{b}_j + h.c.) &\approx \sum_{\langle ij \rangle} (\hat{b}_i^\dagger \langle \hat{b}_j \rangle + \hat{b}_j \langle \hat{b}_i^\dagger \rangle - \langle \hat{b}_i^\dagger \rangle \langle \hat{b}_j \rangle + h.c.) \\
&= \sum_{\langle ij \rangle} (2\hat{b}_i^\dagger \langle \hat{b}_j \rangle + 2\hat{b}_j \langle \hat{b}_i^\dagger \rangle - \langle \hat{b}_i^\dagger \rangle \langle \hat{b}_j \rangle - \langle \hat{b}_j^\dagger \rangle \langle \hat{b}_i \rangle) \\
&= \sum_i \sum_{j \text{ n.n. } i} (\hat{b}_i^\dagger \langle \hat{b}_j \rangle + \hat{b}_j \langle \hat{b}_i^\dagger \rangle - \frac{1}{2} \langle \hat{b}_i^\dagger \rangle \langle \hat{b}_j \rangle - \frac{1}{2} \langle \hat{b}_j^\dagger \rangle \langle \hat{b}_i \rangle) \\
&= \sum_i \left[ (\hat{b}_i^\dagger \eta_i + h.c.) - \frac{1}{2} (\langle \hat{b}_i^\dagger \rangle \eta_i + c.c.) \right]
\end{aligned}$$

In the derivation the abbreviation  $\eta_i = \sum_{j \text{ n.n. } i} \langle \hat{b}_j \rangle$  was used and the summation over nearest neighbors was rewritten as  $\sum_{\langle ij \rangle} \rightarrow 1/2 \sum_i \sum_{j \text{ n.n. } i}$ . When the approximated tunneling term is implemented in the Bose-Hubbard model Eq. (3.63) a new mean-field Hamiltonian is obtained

$$\mathcal{H}_{MF} = \sum_i \left( -J(\hat{b}_i^\dagger \eta_i + h.c.) - \mu_{\text{eff},i} \hat{n}_i + \frac{U}{2} \hat{n}_i (\hat{n}_i - 1) + c_i \right) = \sum_i \mathcal{H}_{MF,i}, \quad (3.123)$$

with the constant  $c_i = \frac{J}{2} (\langle \hat{b}_i^\dagger \rangle \eta_i + c.c.)$ . In contrast to the original Bose-Hubbard model, the mean-field Hamiltonian decomposes into single-site Hamiltonians. This reduces the solution of a differential Schrödinger equation coupling  $L$  unknown wave functions  $|\psi_i\rangle_i$  to  $L$  independent on-site differentials for each  $|\psi_i\rangle_i$  in an  $L$ -site system. However, the decoupling is not complete. The tunneling matrix element  $J$  couples the site  $i$  to the neighboring sites described by a scalar  $\eta_i = \sum_{j \text{ n.n. } i} \langle \hat{b}_j \rangle$ . Due to the introduction of an effective field  $\eta$  the method owes its name - the mean field technique.

The parameter  $\langle \hat{b}_i \rangle$  is often referred to as *mean-field* or *SF parameter* as it shows critical behavior at the SF-MI phase transition. One can understand it easily considering both possible limits of the model. In the non-interacting case, where the ground state corresponds to a coherent state which is the eigenstate of the annihilation operator, the mean-field parameter is nothing but the appropriate eigenvalue. In the MI phase at  $J = 0$  with a fixed integer particle density  $n_i$  the SF-parameter vanishes:  $\langle \hat{b}_i \rangle = \langle n_i | \hat{b}_i | n_i \rangle = \sqrt{n_i} \langle n_i | n_i - 1 \rangle = 0$ . At finite tunneling and interaction strength  $\langle \hat{b}_i \rangle$  remains finite as long as a condensate is present in the system and particle fluctuations exist.

### Selfconsistent solution

From quantum mechanics it is well known that the eigenstates of an operator, which decomposes into a direct sum, can be written as a direct product of eigenstates of each operator summand. Hence, the ground state solution of the decoupled mean-field Hamiltonian is

$$\begin{aligned}
|\Psi_{MF}\rangle &= \prod_i |\psi_{MF}\rangle_i \\
\text{with } \mathcal{H}_{MF,i} |\psi_{MF}\rangle_i &= E_{MF,i} |\psi_{MF}\rangle_i.
\end{aligned}$$

Each on-site eigenvalue equation can be solved separately. In the Fock basis each equation reads (for the sake of readability we drop the site index  $i$  for the moment)

$$\sum_n (\mathcal{H}_{MF})_{mn} (\psi_{MF})_n = E_{MF}^{(m)} (\psi_{MF})_m$$

with

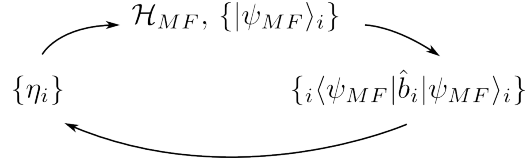
$$(\mathcal{H}_{MF})_{mn} = \delta_{mn} \left( \frac{U}{2} n(n-1) - \mu_{\text{eff}} n \right) - \frac{J}{2} (\eta \sqrt{n+1} \delta_{m,n+1} + \eta^* \sqrt{n} \delta_{m,n-1}). \quad (3.124)$$

Equivalently in the matrix notation with a cut-off Fock number  $n_{\text{max}}$ , each single-site mean-field Hamiltonian corresponds to a tridiagonal matrix form

$$\mathcal{H}_{MF,i} = \begin{bmatrix} \tilde{c}_i & -\frac{J}{2} \eta_i \sqrt{1} & 0 & 0 & 0 \\ -\frac{J}{2} \eta_i^* \sqrt{1} & -\mu_{\text{eff},i} & -\frac{J}{2} \eta_i \sqrt{2} & 0 & 0 \\ 0 & -\frac{J}{2} \eta_i^* \sqrt{2} & 2\frac{U}{2} - 2\mu_{\text{eff},i} & \ddots & 0 \\ 0 & 0 & \ddots & \ddots & -\frac{J}{2} \eta_i \sqrt{n_{\text{max}}} \\ 0 & 0 & 0 & -\frac{J}{2} \eta_i^* \sqrt{n_{\text{max}}} & \frac{U}{2} n_{\text{max}}(n_{\text{max}} - 1) - \mu_{\text{eff},i} n_{\text{max}} \end{bmatrix}$$

The lowest eigenvalue and the corresponding eigenstate are the ground state energy and the ground state of the lattice site respectively.

Since the study of the on-site mean-field Hamiltonians Eq. (3.124) requires the knowledge of the fields  $\eta_i$ , we deal with a set of implicit equations which have to be solved selfconsistently. Starting with an initial guess of SF-parameters the on-site Hamiltonians are diagonalized and subsequent set of parameters  $\langle \hat{b}_i \rangle$  is calculated based on obtained on-site ground states



The selfconsistency is reached when each SF-parameter  $\langle \hat{b}_i \rangle$  inserted into the on-site Hamiltonian is equivalent to the expectation value of the annihilation operator calculated with respect to the on-site ground state of this Hamiltonian  $|\psi_{MF}\rangle_i$ . Alternatively, the self-consistency loop can be substituted by a root-finding algorithm e.g. Newton-Raphson or bisection method [138], however, it has been proved to improve the computational time only for a certain range of parameters and to be slower for others.

### Equivalence to the Gutzwiller ansatz

In order to compare the mean-field with the Gutzwiller ansatz we calculate the energy of a homogeneous mean-field system and compare it with the known result Eq. (3.122). It is

$$\begin{aligned} E_{MF}(\{\langle \hat{b} \rangle\}) &= \langle \Psi_{MF} | \mathcal{H}_{MF} | \Psi_{MF} \rangle = \sum_i \langle \psi_{MF} | \mathcal{H}_{MF,i} | \psi_{MF} \rangle_i \\ (3.123) \quad &= L \left[ -\frac{J}{2} (\langle \hat{b}^\dagger \rangle \eta + \langle \hat{b} \rangle \eta^*) - \mu \langle \hat{n} \rangle + \frac{U}{2} \langle \hat{n} \rangle (\langle \hat{n} \rangle - 1) \right] \\ &= L \left[ -Jz |\langle \hat{b}^\dagger \rangle|^2 - \mu \langle \hat{n} \rangle + \frac{U}{2} \langle \hat{n} \rangle (\langle \hat{n} \rangle - 1) \right], \end{aligned}$$

with  $z$  being the number of nearest neighbors,  $\mu_{\text{eff},i} \equiv \mu$  and  $\eta = \sum_i \langle \hat{b} \rangle = z \langle \hat{b} \rangle$ . We immediately see that the ground state energies of the mean-field Hamiltonian Eq. (3.123) and the Bose-Hubbard Hamiltonian Eq. (3.63) calculated with respect to the Gutzwiller ansatz Eq. (3.122) are identical. Since the Gutzwiller ansatz is a product state similar to the mean-field state, which is a product state due to the decomposition of the lattice Hamiltonian into a sum of on-site Hamiltonians, both methods are equivalent. However, calculation of the ground state energy of the Bose-Hubbard Hamiltonian with the Gutzwiller ansatz requires minimization of the Gutzwiller energy with respect to the complex variables  $\{c_n\}$ , which is computationally more demanding than the convergence of the selfconsistency loop of the SF-parameter of the mean-field method. This fact advocates the use of the mean-field approach. Although both routines are technically distinct we use the names Gutzwiller and mean-field as synonyms, according to common use.

### 3.3.3 Range of validity

The benefits of a site-decoupled Hamiltonian come at the costs of a mean-field treatment of the neighboring sites, namely through the effective scalar fields  $\eta_i$ . The description by means of an expectation value rather than via a true observable neglects fluctuations. As the latter decrease with increasing number of sites the field is averaged over, the mean-field method becomes exact in infinite dimensions or equivalently for a fully connected lattice, i.e. for infinite configuration number. Particularly, the mean-field approximation is exact in the limits  $J/U \rightarrow 0$  and  $J/U \rightarrow \infty$  where the ground states are analytically proven to be product states. At the same time, the incorporation of neighboring sites, even on a mean-field level, enables studies of inhomogeneous lattices - lattices with external trapping potential or disorder to name the most common. The real-space resolution provides a description of phase separation, particle density waves and a manifold of spatially coexisting quantum states like in the case of the so called wedding cake structure. Corrections to the mean-field results scale like  $1/z$ , where  $z$  is the number of neighbors [17, 139]. Consequently, on the cubic lattice where  $z = 6$  the mean-field theory is well-controlled and provides still qualitatively good results in two dimensions ( $z = 4$ ).

The description of a many-body state via a product state has an additional effect on the single particle density matrix or equivalently the long range correlations. The SPDM defined in Eq. (3.79) reads in the mean-field approximation

$$\rho_{lm} = \langle \hat{b}_l^\dagger \hat{b}_m \rangle = \langle \hat{b}_l^\dagger \rangle \langle \hat{b}_m \rangle - \delta_{lm} \left( \langle \hat{n}_l \rangle - \langle \hat{b}_l^\dagger \rangle \langle \hat{b}_l \rangle \right).$$

The factorization of the expectation values is an artifact of the method. The off-diagonal elements of the matrix  $\langle \hat{b}_l^\dagger \rangle \langle \hat{b}_m \rangle$  become even independent of the distance  $|l - m|$  in a homogeneous system which emphasizes that the correlations are not correctly described<sup>13</sup>. However, a closer look puts the results into perspective. The coherence length  $\zeta$  gives a distance over which, as the name says, the coherence is maintained. The exact correlator  $\langle \hat{b}_l^\dagger \hat{b}_m \rangle$  is finite and distance dependent for  $|l - m| \lesssim \zeta$  and vanishes for  $|l - m| \gg \zeta$ . In a homogeneous SF at  $T = 0$  the coherence length diverges in the limit  $U \rightarrow 0$ , consequently, in the range of the lattice size  $\langle \hat{b}_l^\dagger \hat{b}_m \rangle \approx \text{const.}$  and distance independent<sup>14</sup>. In this case

<sup>13</sup>In a non-homogeneous system  $\rho_{lm}$  remains a function of the cite separation  $|l - m|$  however its value does not correspond to the exact correlations due to the mean-field factorization.

<sup>14</sup>This result was already derived in Eq. (3.93) based on the fact that in the perfect SF for  $U \rightarrow 0$  all particles occupy the  $\mathbf{k} = 0$  state which is homogeneously delocalized in the lattice.

the factorization is justified and Gutzwiller provides correct results. In a homogeneous MI phase in the limit  $J \rightarrow 0$  the correlation length is of the order of the lattice constant  $\zeta \sim a$  and  $\langle \hat{b}_l^\dagger \hat{b}_m \rangle \rightarrow 0$  for  $|l - m| > a$ , trivially it is distance independent. Hence, also in this regime mean-field technique characterizes the system correctly. Thus, for finite  $U$  only correlations in the range of  $|l - m| \lesssim \zeta$  - the so called *short range* correlations - are not reproduced within Gutzwiller. This will be important in the later discussions concerning the momentum distribution calculated within our approach.

Another important feature of the mean-field approximation concerns certain symmetries which affect the conservation laws of the system. The exact Bose-Hubbard model Eq. (3.63) is invariant under a global phase shift of operators which corresponds to a conservation of the total particle number  $\hat{N} = \sum_i \hat{n}_i$

$$\begin{aligned}
[\mathcal{H}, \hat{N}] &= \left[ -\frac{J}{2} \sum_i \sum_{j \text{ n.n. } i} (\hat{b}_i^\dagger \hat{b}_j + h.c.), \sum_l \hat{n}_l \right] \\
&= -\frac{J}{2} \sum_{i,l} \sum_{j \text{ n.n. } i} \left( \hat{b}_i^\dagger [\hat{b}_j, \hat{n}_l] + [\hat{b}_i^\dagger, \hat{n}_l] \hat{b}_j + \hat{b}_j^\dagger [\hat{b}_i, \hat{n}_l] + [\hat{b}_j^\dagger, \hat{n}_l] \hat{b}_i \right) \\
&= -\frac{J}{2} \sum_i \sum_{j \text{ n.n. } i} (\hat{b}_i^\dagger \hat{b}_j - \hat{b}_i^\dagger \hat{b}_j + \hat{b}_j^\dagger \hat{b}_i - \hat{b}_j^\dagger \hat{b}_i) \\
&= 0.
\end{aligned}$$

In the derivation we dropped the terms in the Hamiltonian including  $\hat{n}_j$  in the first line, since  $[\hat{n}_i, \hat{n}_j] = 0$ , and used the commutation relation  $[\hat{b}_j, \hat{n}_i] = \delta_{ij} \hat{b}_i$ . In contrary, the mean-field Hamiltonian Eq. (3.123) does not possess this symmetry, since

$$\begin{aligned}
[\mathcal{H}_{MF}, \hat{N}] &= \left[ \sum_j -J(\hat{b}_j^\dagger \eta_j + h.c.), \hat{N} \right] \\
&= -J \sum_{ij} \left( \eta_j [\hat{b}_j^\dagger, \hat{n}_i] + \eta_j^* [\hat{b}_j, \hat{n}_i] \right) \\
&= J \sum_{ij} \left( \eta_j \delta_{ij} \hat{b}_i^\dagger - \eta_j^* \delta_{ij} \hat{b}_i \right) \\
&= J \sum_i \left( \eta_i \hat{b}_i^\dagger - \eta_i^* \hat{b}_i \right) \neq 0. \tag{3.125}
\end{aligned}$$

Thus, the mean-field Hamiltonian is not particle number conserving in general. An exception is the Mott insulating regime with  $\langle \hat{b}_i \rangle = 0 \Leftrightarrow \eta_i = 0$ , as in this case the eigenbasis of the Hamiltonian is equivalent to the Fock basis  $\{|n\rangle\}$ ,  $n \in \mathbb{N}$ , which is the eigenbasis of the particle density operator  $\hat{n}_i$  and correspondingly of the operator  $\hat{N}$ . Operators possessing a set of common eigenstates commute. Otherwise, finite SF-parameters indicate that the on-site eigenstates are a coherent superposition of states with different atom numbers

and thus by definition can not be eigenstates of  $\hat{n}_i$ . Nevertheless, on average the particle number is conserved

$$\begin{aligned}
\langle [\mathcal{H}_{MF}, \hat{N}] \rangle &= \langle J \sum_i (\eta_i \hat{b}_i^\dagger - \eta_i^* \hat{b}_i) \rangle \\
&= J \left( \sum_i \sum_{j \text{ n.n. } i} \langle \hat{b}_j \rangle \langle \hat{b}_i^\dagger \rangle - \sum_i \sum_{j \text{ n.n. } i} \langle \hat{b}_j^\dagger \rangle \langle \hat{b}_i \rangle \right) \\
&= J \left( \sum_i \sum_{j \text{ n.n. } i} \langle \hat{b}_j \rangle \langle \hat{b}_i^\dagger \rangle - \sum_j \sum_{i \text{ n.n. } j} \langle \hat{b}_j^\dagger \rangle \langle \hat{b}_i \rangle \right) \\
&= 0.
\end{aligned}$$

The validity of this conservation law is required in time dependent Gutzwiller simulations, see Sec. 3.5.

Further peculiarities of the mean-field approximation will be discussed in the results sections.

### 3.4 Phase diagram within the mean-field approach

Combining the mean-field approximation and perturbative calculations, we can estimate the MI and SF regions and the positions of the phase borders in a homogeneous system analytically [79]. For this purpose we write the mean-field Hamiltonian Eq. (3.123) as a sum

$$\mathcal{H} = \mathcal{H}_0 + \mathcal{H}_1,$$

with

$$\begin{aligned}
\mathcal{H}_0 &= \sum_i -\mu_{\text{eff},i} \hat{n}_i + \frac{U}{2} \hat{n}_i (\hat{n}_i - 1) + \frac{J}{2} (\langle \hat{b}_i^\dagger \rangle \eta_i + c.c.) \\
\mathcal{H}_1 &= \sum_i -J (\hat{b}_i^\dagger \eta_i + h.c.).
\end{aligned}$$

In a homogeneous system the site dependence can be dropped since the effective chemical potential becomes constant  $\mu_{\text{eff},i} \equiv \mu$  and  $\eta_i = \sum_{j \text{ n.n. } i} \langle \hat{b}_i \rangle = z \langle \hat{b} \rangle$ . Although the SF-parameter  $\langle \hat{b} \rangle$  can be chosen real<sup>15</sup>, for the sake of generality we proceed with  $\langle \hat{b} \rangle \in \mathbb{C}$ . The Hamiltonians  $\mathcal{H}_0$  and  $\mathcal{H}_1$  read

$$\mathcal{H}_0 = \sum_i \left( \frac{U}{2} \hat{n} (\hat{n} - 1) - \mu \hat{n} + zJ |\langle \hat{b} \rangle|^2 \right) = \sum_i h_0, \quad (3.126)$$

$$\mathcal{H}_1 = \sum_i \left( -zJ (\hat{b}^\dagger \langle \hat{b} \rangle + \langle \hat{b}^\dagger \rangle \hat{b}) \right) = \sum_i h_1. \quad (3.127)$$

We can approximately solve the Schrödinger equation  $(\mathcal{H}_0 + \mathcal{H}_1) |\Psi_n\rangle = E_n |\Psi_n\rangle$  considering  $\mathcal{H}_1$  as a small perturbation. We assume that the eigenvalue problem is solved  $\mathcal{H}_0 |\Phi_n\rangle =$

<sup>15</sup>The many-body ground state is given by Eq. (3.71) up to a global phase, which can be chosen at will. In particular, this phase can be adjusted such that  $\langle \hat{b} \rangle = \langle \Psi_{SF}(\sqrt{N}) | \hat{b} | \Psi_{SF}(\sqrt{N}) \rangle \in \mathbb{R}$ .

$E_n^0|\Phi_n\rangle$  and the eigenstates  $|\Phi_n\rangle$  are not degenerate. For a small perturbation we can express the energy  $E_n = \langle \mathcal{H}_0 + \mathcal{H}_1 \rangle$  in terms of the energy levels and eigenstates of the  $\mathcal{H}_0$  Hamiltonian<sup>16</sup>, in particular the ground state energy is

$$E_0 = E_0^0 + E^{(1)} + E^{(2)} + \dots$$

with

$$\begin{aligned} E^{(1)} &= \langle \Phi_0 | \mathcal{H}_1 | \Phi_0 \rangle \\ E^{(2)} &= \sum_{\substack{n \\ n \neq 0}} \frac{|\langle \Phi_0 | \mathcal{H}_1 | \Phi_n \rangle|^2}{E_0^0 - E_n^0}. \end{aligned}$$

Since the eigensystem of  $\mathcal{H}_0$  and particularly the ground state  $|\Phi_0\rangle$  is a direct product of identical on-site Fock states with a fixed particle number according to the given chemical potential, the first non-vanishing correction is the second order perturbation  $E^{(2)}$  which we calculate next.

The unperturbed Hamiltonian  $\mathcal{H}_0$  describes a system with fixed homogeneous particle density per lattice site  $n$  with MI ground state  $|\Phi_0\rangle = \prod_i |\phi_0\rangle_i$ , where single-site eigenstates correspond to a Fock state  $|\phi_0\rangle_i \equiv |n\rangle_i$  (see Sec. 3.2.2). The total ground state energy thus reads

$$E_0^0 = L\epsilon_0^0 \tag{3.128}$$

with

$$\epsilon_0^0(n) = \langle \phi_0 | h_0 | \phi_0 \rangle = \begin{cases} zJ|\langle \hat{b} \rangle|^2, & \text{if } \mu < 0 \Rightarrow n = 0, \\ \frac{U}{2}n(n-1) - \mu n + zJ|\langle \hat{b} \rangle|^2 & \text{if } n-1 < \mu < n, n \in \mathbb{N}. \end{cases}$$

In the following we would like to estimate the extent of the Mott insulating regions, the so called Mott lobes, thus for the further calculations the chemical potential is assumed to be  $\mu > 0$  and accordingly the single-site ground state energy  $\epsilon_0^0(n) = \frac{U}{2}n(n-1) - \mu n + zJ|\langle \hat{b} \rangle|^2$ .

The excitation corresponds to adding or removing one particle at an arbitrary site, leading to an increase or decrease of a total particle number  $N \rightarrow N+1$  or  $N \rightarrow N-1$ . Thus, there exist two excited states  $|\Phi_1\rangle \equiv |\Phi_+\rangle = (|n\rangle)^{L-1}|n+1\rangle$  and  $|\Phi_2\rangle \equiv |\Phi_-\rangle = (|n\rangle)^{L-1}|n-1\rangle$  in the former and in the latter case respectively. Making use of the site decomposition of the Hamiltonian, the total energy of the excited system  $E_{1/2}^0 \equiv E_{\pm}^0 = \langle \Phi_{\pm} | \mathcal{H}_0 | \Phi_{\pm} \rangle$  is

$$E_{\pm}^0 = \begin{cases} (L-1)\epsilon_0^0(n) + \epsilon_0^0(n+1), & \text{if } N \rightarrow N+1, \\ (L-1)\epsilon_0^0(n) + \epsilon_0^0(n-1), & \text{if } N \rightarrow N-1, \end{cases}$$

with

$$\begin{aligned} \epsilon_0^0(n) &= \frac{U}{2}n(n-1) - \mu n + zJ|\langle \hat{b} \rangle|^2, \\ \epsilon_0^0(n+1) &= \frac{U}{2}n(n+1) - \mu(n+1) + zJ|\langle \hat{b} \rangle|^2, \\ \epsilon_0^0(n-1) &= \frac{U}{2}(n-1)(n-2) - \mu(n-1) + zJ|\langle \hat{b} \rangle|^2. \end{aligned}$$

Altogether this gives

$$E_{\pm}^0 = \begin{cases} \frac{Un(n+1)}{2} - \mu(n+1) + (L-1) \left[ \frac{U}{2}n(n-1) - \mu n \right] + zJL|\langle \hat{b} \rangle|^2, & \text{if } N \rightarrow N+1, \\ \frac{U(n-2)(n-1)}{2} - \mu(n-1) + (L-1) \left[ \frac{U}{2}n(n-1) - \mu n \right] + zJL|\langle \hat{b} \rangle|^2, & \text{if } N \rightarrow N-1. \end{cases} \tag{3.129}$$

<sup>16</sup>A more detailed derivation of perturbation theory can be found in a conventional quantum mechanical literature, e.g. [78, 140].

And the energy difference between the ground and excited states reads

$$E_0^0 - E_{\pm}^0 \stackrel{(3.128)}{=} \stackrel{(3.129)}{=} \begin{cases} -(Un - \mu), & \text{if } N \rightarrow N + 1, \\ U(n - 1) - \mu, & \text{if } N \rightarrow N - 1. \end{cases} \quad (3.130)$$

Next, we calculate the matrix elements  $\langle \Phi_0 | \mathcal{H}_1 | \Phi_{\pm} \rangle$ . Given the ground state  $|\Phi_0\rangle = \prod_j |n\rangle_j$  and two excited states  $|\Phi_{\pm}\rangle = \prod_k |n_k\rangle_k$ , where  $n_k = n$  for  $k \neq l$  and  $n_k = n \pm 1$  for  $k = l$ , the matrix elements read

$$\begin{aligned} \langle \Phi_0 | \mathcal{H}_1 | \Phi_{\pm} \rangle &= \prod_j \langle n | \sum_i \left( -zJ \langle \hat{b} \rangle (b_i + b_i^\dagger) \right) \prod_k |n_k\rangle_k \\ &= \sum_i -zJ \langle \hat{b} \rangle \prod_j \prod_k \left\{ {}_j \langle n | b_i | n_k \rangle_k + {}_j \langle n | b_i^\dagger | n_k \rangle_k \right\} \\ &= \sum_i -zJ \langle \hat{b} \rangle \prod_j \prod_k \delta_{ik} \left\{ \sqrt{n_k} {}_j \langle n | n_k - 1 \rangle_k + \sqrt{n_k + 1} {}_j \langle n | n_k + 1 \rangle_k \right\} \\ &= \sum_i -zJ \langle \hat{b} \rangle \prod_j \prod_k \delta_{ik} \left\{ \sqrt{n_k} \delta_{jk} \delta_{n_k, n+1} + \sqrt{n_k + 1} \delta_{jk} \delta_{n_k, n-1} \right\} \\ &= \sum_i -zJ \langle \hat{b} \rangle \left\{ \sqrt{n_i} \delta_{n_i, n+1} + \sqrt{n_i + 1} \delta_{n_i, n-1} \right\} \\ &= -zJ \langle \hat{b} \rangle \left\{ \sqrt{n+1} \delta_{n_l, n+1} + \sqrt{n} \delta_{n_l, n-1} \right\} \end{aligned}$$

In the last step the sum reduces to one summand because in the excited state the particle density  $n_i$  differs from  $n$  only on one site  $l$ . Thus,

$$|\langle \Phi_0 | \mathcal{H}_1 | \Phi_{\pm} \rangle|^2 = \begin{cases} z^2 J^2 |\langle \hat{b} \rangle|^2 (n+1), & \text{if } N \rightarrow N + 1, \\ z^2 J^2 |\langle \hat{b} \rangle|^2 n, & \text{if } N \rightarrow N - 1. \end{cases} \quad (3.131)$$

Now, combining the results from Eq. (3.130) and Eq. (3.131) the second order perturbation theory leads to corrections of the non-interacting ground state energy

$$\begin{aligned} E^{(2)} &= \sum_n \frac{|\langle \Phi_n | \mathcal{H}_1 | \Phi_0 \rangle|^2}{E_0^0 - E_n^0} \\ &= \frac{|\langle \Phi_+ | \mathcal{H}_1 | \Phi_0 \rangle|^2}{E_0^0 - E_+^0} + \frac{|\langle \Phi_- | \mathcal{H}_1 | \Phi_0 \rangle|^2}{E_0^0 - E_-^0} \\ &= \left( -\frac{n+1}{Un - \mu} + \frac{n}{U(n-1) - \mu} \right) z^2 J^2 |\langle \hat{b} \rangle|^2 \end{aligned} \quad (3.132)$$

Following the Ginzburg-Landau theory for the second order phase transitions in superconductors [141] we write the ground state energy of the full system  $E_0 = E_0^0 + E^{(2)}$  as a function of the complex parameter  $\langle \hat{b} \rangle$

$$\begin{aligned} E_0(\langle \hat{b} \rangle) &\stackrel{(3.128)}{=} \stackrel{(3.132)}{=} \frac{U}{2} n(n-1) - \mu n + zJ |\langle \hat{b} \rangle|^2 + E^{(2)} \\ &= A + B \cdot |\langle \hat{b} \rangle|^2, \end{aligned}$$

where  $A = \frac{U}{2} n(n-1) - \mu n$  and  $B = zJ + E^{(2)} / |\langle \hat{b} \rangle|^2$ . The energy is minimal for  $|\langle \hat{b} \rangle| = 0$  when  $B > 0$  or for any finite  $|\langle \hat{b} \rangle|$  when  $B < 0$ . That is, the phase transition occurs when

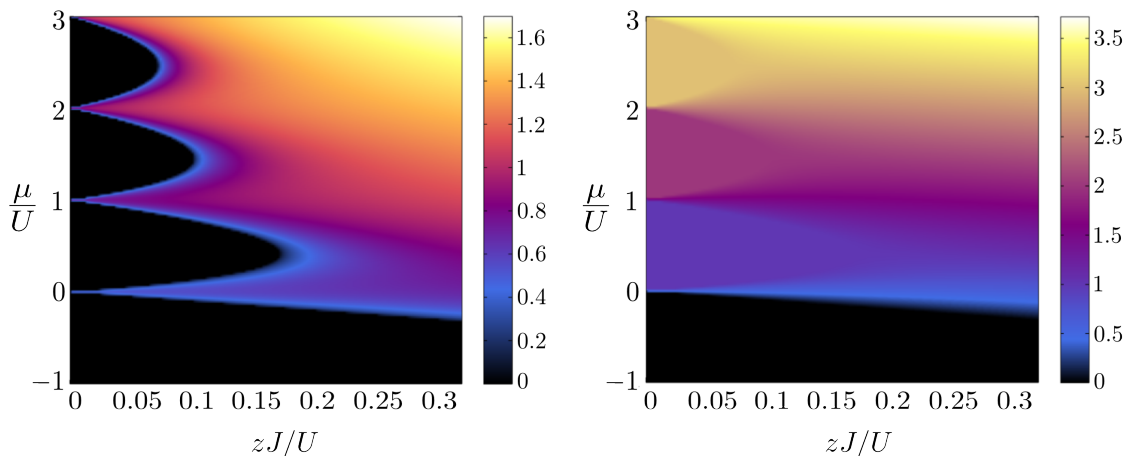


**Figure 3.12:** Mean-field phase diagram (numerical results). (Left) SF-parameter  $\langle \hat{b} \rangle$  as a function of  $\mu/U$  and  $zJ/U$ . The vanishing SF-parameter indicates Mott insulating regions - the Mott lobes. The SF-MI phase transition happens at  $(zJ/U)_c$  as predicted in Eq. (3.133). (Right) The particle density for the same parameter region. Within each Mott lobe  $\langle \hat{n} \rangle$  is fixed at an integer number independent of  $\mu$ . For further details see text below.

$B = 0$ . This condition leads to the upper  $\mu_+/U$  and the lower  $\mu_-/U$  borders of the Mott lobes for a given  $zJ/U$

$$\frac{\mu_{\pm}}{U} = \frac{1}{2} \left( 2n - 1 - \frac{zJ}{U} \pm \sqrt{\left(\frac{zJ}{U}\right)^2 - (2n+1)\frac{zJ}{U} + \frac{1}{4}} \right).$$

The critical  $(zJ/U)_c$  at which the tip of the Mott lobe vanishes, i.e.  $\mu_+/U - \mu_-/U = 0$ , is

$$\left(\frac{zJ}{U}\right)_c = 2n + 1 + 2\sqrt{n(n+1)}. \quad (3.133)$$

The numerically calculated  $\mu/U$ - $zJ/U$ -phase diagram is shown in Fig. 3.12. The numerical phase diagrams confirm the results of the perturbation theory. The SF-parameter in Fig. 3.12 (left) shows critical behavior at the SF-MI phase transition and remains zero within the MI phase. The tips of the Mott lobes are situated at  $(zJ/U)_c$  in accordance with Eq. (3.133). At integer  $\mu/U$  values the Mott regions with different particle number intersect. This degeneracy leads to particle-hole fluctuations at  $\langle \hat{b} \rangle = 0$ . With increasing tunneling the superfluidity monotonously enhances. In Fig. 3.12 (right) the particle density is presented. The Mott-lobes correspond to plateaus with integer particle number. Within each MI region particle the number does not change when the chemical potential is varied in agreement with the incompressibility of the phase. In the SF-regime  $\langle \hat{n} \rangle$  increases monotonously as a function of the chemical potential and in the limit  $zJ/U \rightarrow \infty$  becomes  $|\langle \hat{b} \rangle|^2$ . The latter is a consequence of the ground state becoming a coherent state<sup>17</sup>. A complementary discussion of the bosonic ground state phase diagram in the mean-field approximation in a homogeneous system can be found in [9].

<sup>17</sup>Since in a homogeneous system the coherent many-body state is a product of single-site coherent states  $|\Psi_{coh}(\sqrt{N})\rangle = \prod_i |\Psi_{coh}(\sqrt{n})\rangle_i$  (see Sec. 3.2.3) it is  $|\langle \hat{b}_i \rangle| = |\langle \Psi_{coh}(\sqrt{n}) | \hat{b}_i | \Psi_{coh}(\sqrt{n}) \rangle_i| = \sqrt{n}$  and from here  $n = \langle \hat{n}_i \rangle = |\langle \hat{b}_i \rangle|^2$ .



MI-SF phase transition for $n = 1$		
Method	$(J/U)_c$	Dimension
MF [9]	$0.172/z$	
SCE [135]	0.429	1
SCE[135]	0.122	2
QMC [143]	0.429	1
QMC [144]	0.118	2
QMC [125]	0.034	3

**Table 3.1:** Critical interaction strength for the SF-MI transition at the first Mott lobe (particle density  $n = 1$ ) calculated via different methods. The Quantum Monte Carlo results are for finite temperature, whereas the mean-field predictions and strong coupling expansion (SCE) are for  $T = 0$ . The mean-field results are exact in infinite spatial dimensions and provide a qualitative description in lower dimensions, with  $z$  being the number of nearest neighbors.

Calculations of the phase diagram have been also performed with other methods. Shezhadri *et al.* provided a quantitative comparison between approximate mean-field results and numerically exact Quantum Monte Carlo simulations which revealed good agreement between both methods [124]. In the strong-coupling expansion the energy of the Mott insulating state is compared with the energy of the so called defect state, both calculated perturbatively. The defect state contains one additional particle (hole), which moves coherently through the lattice. The point where the energies of the MI and the defect state are degenerate indicates finite compressibility and thus the MI-SF transition. The ground state phase diagram calculated in this way provides qualitatively better results in lower dimensions  $D \leq 2$  than the corresponding mean-field approach, which becomes exact in infinite dimensions [135]. Results of the higher order perturbative corrections are investigated in [142]. In table 3.1 some numerically calculated critical values  $(J/U)_c$  for the SF-MI phase transition at  $n = 1$  are summarized.

Although the Gutzwiller method is expected to give qualitatively good results in 3D the deviation from the exact QMC critical point amounts e.g. to 19% for  $n = 1$ . The reason is the description of the phase transition by means of the mean-field approximation. In the Gutzwiller method the phase transition is indicated by a vanishing SF-parameter. For  $\langle \hat{b} \rangle = 0$  the kinetic part of the mean-field Hamiltonian Eq. (3.63) becomes zero and the particle fluctuations disappear even for finite  $J$ . This is an artifact of the method since in the exact Bose-Hubbard Hamiltonian the variance of on-site particle number  $n$  persists until  $J \rightarrow 0$  [82]. From this argument it follows that the Gutzwiller ansatz overestimates the range of the MI phase and is also not capable of capturing magnetic phases within the MI, which are arising from  $J^2/U$  processes in spin-mixtures.

### 3.5 Mean-field dynamics

Until now the calculations have been purely static: the parameters did not change and the system was in the ground state. Although already this problem was challenging and not analytically exactly solvable we would now like to proceed with an additional exciting question: non-equilibrium dynamics. Such processes are either present due to the experimental realization, e.g. lattice ramping [20], or induced externally. The latter serves as

an experimental spectroscopy technique [30, 31] or for investigations of interaction effects [34, 92, 97, 134].

Different techniques have been developed to study time dependent processes such as the time-dependent density matrix renormalization group in 1D or Gross-Pitaevskii equations for weakly interacting Bose gases in any dimension, to name a few. However, a deep understanding of dynamical many-body effects requires a rigorous study of different interaction regimes and dimensionality. This is possible by the dynamical Gutzwiller method [145]. It has been argued and recently proved to have the same validity range as the static method [146]. Due to its efficiency this technique is the most widely used, in particular in this thesis. Therefore we are going to derive it next.

In terms of a general formalism the time evolution of a many-body state  $|\Psi\rangle$  is controlled via the unitary time evolution operator<sup>18</sup>  $U(t, 0) = U(t)$ :

$$|\Psi(t)\rangle = U(t)|\Psi(0)\rangle. \quad (3.134)$$

Implementing this definition into the Schrödinger equation

$$\begin{aligned} i\hbar\partial_t|\Psi(t)\rangle &= \mathcal{H}|\Psi(t)\rangle \\ \Leftrightarrow i\hbar\partial_tU(t)|\Psi(0)\rangle &= \mathcal{H}U(t)|\Psi(0)\rangle \end{aligned}$$

the differential equation

$$\partial_tU(t) = -\frac{i}{\hbar}\mathcal{H}U(t) \quad (3.135)$$

is found to determine the time evolution operator with  $\mathcal{H}$  being the Hamiltonian of the system investigated, which in case of the exact Bose-Hubbard model is given by Eq. (3.63) and for the Gutzwiller approximation by Eq. (3.123). Hence, in order to obtain an explicit expression for  $U(t)$  the differential equation (3.135) has to be solved.

For a time independent Hamiltonian, separation of variables and subsequent integration of Eq. (3.135) leads

$$U(t) = \exp\left\{-\frac{i}{\hbar}\mathcal{H}t\right\} \quad (\mathcal{H} \neq \mathcal{H}(t)). \quad (3.136)$$

In particular, in the mean-field approximation the operator reads  $U_{MF}(t) = \exp\{-\frac{i}{\hbar}\mathcal{H}_{MF}t\}$ , where  $\mathcal{H}_{MF}$  is given by Eq. (3.123). Since the Gutzwiller ansatz is a product state Eq. (3.121) and the mean-field Hamiltonian factorizes over the lattice sites Eq. (3.123) the many-body dynamics factorizes as well

$$\begin{aligned} |\Psi_{MF}(t)\rangle &= U_{MF}(t) \prod_{i=1}^L |\psi_{MF}(0)\rangle_i \\ &= \prod_{j=1}^L e^{-\frac{i}{\hbar}\mathcal{H}_{MF,j}t} \prod_{i=1}^L |\psi_{MF}(0)\rangle_i \\ &= \prod_{i=1}^L e^{-\frac{i}{\hbar}\mathcal{H}_{MF,i}t} |\psi_{MF}(0)\rangle_i \\ &= \prod_{i=1}^L |\psi_{MF}(t)\rangle_i, \end{aligned} \quad (3.137)$$

---

<sup>18</sup>A more detailed discussion about characteristics of a time evolution operator can be found in common quantum mechanics literature, e.g. [78]

with  $|\psi_{MF}(t)\rangle_i = e^{-\frac{i}{\hbar}\mathcal{H}_{MF,i}t}|\psi_{MF}(0)\rangle_i$ .

In case of a time dependent Hamilton operator the integration of the Eq. (3.135) leads to a recursive relation

$$\begin{aligned} U(t) &= 1 - \frac{i}{\hbar} \int_0^t dt' \mathcal{H}(t') U(t') \\ &= 1 - \frac{i}{\hbar} \int_0^t dt' \mathcal{H}(t') \left( 1 - \frac{i}{\hbar} \int_0^{t'} dt'' \mathcal{H}(t'') U(t'') \right) \\ &= \dots \\ &= T \left[ \exp\left\{-\frac{i}{\hbar} \int_0^t \mathcal{H}(t') dt'\right\} \right] \quad (\mathcal{H} = \mathcal{H}(t)), \end{aligned} \quad (3.138)$$

where  $T$  denotes the time ordering operator (step-by-step derivation can be found in common quantum mechanics literature like [78]). The upper equation is a formal solution of the differential equation valid in case of a Hamiltonian not commuting with itself at different times, i.e.  $[\mathcal{H}(t), \mathcal{H}(t')] \neq 0$ . In special cases of time dependent Hamiltonians where the commutator vanishes, e.g. the Ising model with a time-dependent spin coupling or magnetic field, the time ordering operator can be dropped and the solution reads  $U(t) = \exp\{-\frac{i}{\hbar} \int_0^t \mathcal{H}(t') dt'\}$ .

The Hamiltonians describing systems of interest for us are time dependent. During a lattice ramp-up, for example, the lattice depth changes, i.e.  $s = s(t)$ , which causes time dependence of the parameters  $J(s(t))$  and  $U(s(t))$ . Subsequently  $\langle \hat{b}_i \rangle$  becomes a dynamic quantity. But even for a sudden creation of a non-equilibrium state (like switching-off of the trapping potential) and subsequent evolution of the system with constant system parameters, the SF-parameters remain time-dependent since they are calculated based on the evolving states  $\langle \hat{b}_i \rangle(t) = {}_i\langle \psi(t) | \hat{b}_i | \psi(t) \rangle_i$ . Particularly, in the mean-field approach the Eq. (3.138) factorizes over the lattice sites

$$\begin{aligned} U(t) &= T \left[ \exp\left\{-\frac{i}{\hbar} \int_0^t \mathcal{H}_{MF}(t') dt'\right\} \right] \\ &= T \left[ \exp\left\{-\frac{i}{\hbar} \int_0^t \sum_i \mathcal{H}_{MF,i}(t') dt'\right\} \right] \\ &= \prod_i T \left[ \exp\left\{-\frac{i}{\hbar} \int_0^t \mathcal{H}_{MF,i}(t') dt'\right\} \right] \end{aligned}$$

with

$$\mathcal{H}_{MF,i}(t') = -J(t') \left( \hat{b}_i^\dagger \eta_i(t') + h.c. \right) - \mu_{\text{eff},i}(t') \hat{n}_i + \frac{U(t')}{2} \hat{n}_i (\hat{n}_i - 1) + c_i(t').$$

In the above derivation the commutator of the Hamiltonians at equal and different times was used:  $[\mathcal{H}_{MF,i}(t'), \mathcal{H}_{MF,j}(t'')] = 0$  for  $i \neq j$ . Equivalently to the derivation of Eq. (3.137), the time evolution of the many-body system decomposes into single-site problems also for a time-dependent Hamiltonian

$$|\psi_{MF}(t)\rangle_i = T e^{-\frac{i}{\hbar} \int_0^t \mathcal{H}_{MF,i}(t') dt'} |\psi_{MF}(0)\rangle_i. \quad (3.139)$$

Although the upper equation describes formally the dynamics of an on-site wave function, the particular calculation can not be performed straightforwardly. The reason is the indirect dependence of the on-site Hamiltonian  $\mathcal{H}_{MF,i}(t')$  on the neighboring sites by means

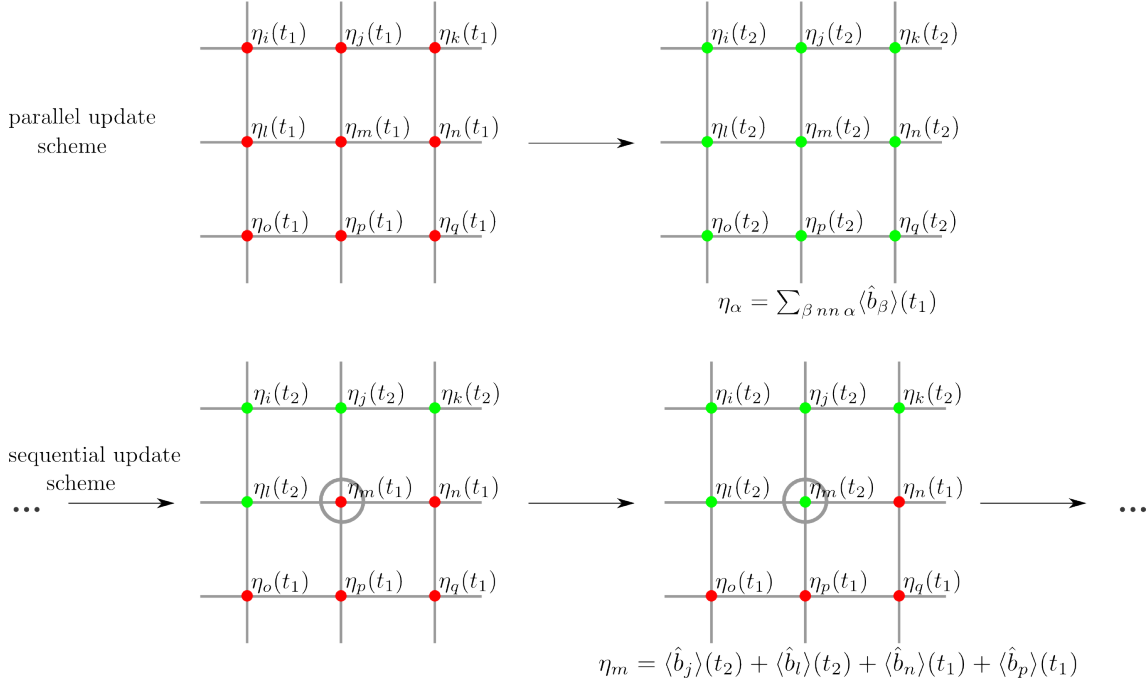


**Figure 3.13:** Parallel and sequential update schemes. In the parallel update the sites are updated independently within one time step based on the results of the previous update. In the sequential update each site is updated after another. Hereby the already updated SF-parameters are involved as pointed out for the calculation at site  $m$ .

of the scalar field  $\eta_i(t')$ , whose calculation requires the wave functions of the neighbors:  $\eta_i(t') = \sum_{j \text{ n.n. } i} \langle \hat{b}_j \rangle(t') = \sum_{j \text{ n.n. } i} \langle \psi_{MF}(t') | \hat{b}_j | \psi_{MF}(t') \rangle_j$ . However, those are coupled vice versa to the site  $i$ . At this point an appropriate approximation to Eq. (3.139) has to be found, which we achieve in two steps.

First, we express the time integral, conform with numerical integration and the mean value theory, in the following way

$$\int_{t_1}^{t_2} \mathcal{H}_{MF,i}(t') dt' = \mathcal{H}_{MF,i}(\tilde{t})(t_2 - t_1) \approx \mathcal{H}_{MF,i}(t_1)(t_2 - t_1), \quad \text{for } \tilde{t} \in [t_1, t_2]. \quad (3.140)$$

The approximation performed in the last step is valid for sufficiently small time intervals  $\Delta t = t_2 - t_1$ . In principle, the time evolution of a state  $|\psi_{MF}(t)\rangle_i$  can be now calculated iteratively

$$\begin{aligned} |\psi_{MF}(t)\rangle_i &= e^{-\frac{i}{\hbar} \mathcal{H}_{MF,i}(t_1)(t-t_1)} |\psi_{MF}(t_1)\rangle_i \\ &= e^{-\frac{i}{\hbar} \mathcal{H}_{MF,i}(t_1)(t-t_1)} \cdot e^{-\frac{i}{\hbar} \mathcal{H}_{MF,i}(t_2)(t_1-t_2)} |\psi_{MF}(t_2)\rangle_i \\ &= e^{-\frac{i}{\hbar} \mathcal{H}_{MF,i}(t_1)(t-t_1)} \cdot e^{-\frac{i}{\hbar} \mathcal{H}_{MF,i}(t_2)(t_1-t_2)} \dots e^{-\frac{i}{\hbar} \mathcal{H}_{MF,i}(t_n)(t_{n-1}-t_n)} |\psi_{MF}(t_n)\rangle_i \end{aligned}$$

with  $0 < \dots < t_n < t_{n-1} < \dots < t_2 < t_1 < t$ . However, doing so regardless of the updating order of the sites may violate the particle number conservation. It is useful to differentiate between parallel and sequential updates. In a *parallel scheme* the calculation of a time step is based on an "old" set of SF-parameters, whereas in the *sequential scheme* the already updated sites are accounted for if present, see Fig. 3.13. The latter method is more costly computationally since it is not suitable for parallelization of single-site diagonalizations, nonetheless, it conserves the particle number to a very high accuracy in contrary to the first scheme (see Appendix. B), which is an essential requirement.

Even with the right updating scheme, the choice of the time steps must be carried out with caution. Too large time steps can still lead to particle or energy losses and other unphysical effects when the approximation in Eq. (3.140) is not justified anymore. Thereby, the conserved observables must be under control during the entire dynamical calculation since small deviations could diverge, thus identifying an inappropriate choice of  $\Delta t$ . Possible symmetry breaks due to updating procedure from left top to right bottom of the lattice are corrected by subsequent reverse processing from right bottom to left top. Since we are not interested in boundary effects, periodic boundary conditions were implemented. However, they lead to particle losses or gains when bosons touch the boundary. This situation is easily avoided by choosing the lattice sufficiently large.

Last but not least, the updating routine can be accelerated by the following trick: On every site the diagonalization of the respective on-site Hamiltonian in the Fock basis  $\{|n\rangle\} = (|0\rangle, \dots, |n_{\max}\rangle)$  is performed  $\mathcal{H}_i|\psi_l\rangle_i = E_{l,i}|\psi_l\rangle_i$  (for a better readability the mean-field indication was dropped). Afterwards, the full eigenbasis is used to construct an operator  $A_i$ :

$$A_i = \begin{pmatrix} \psi_i^{(0)}(0) & \dots & \psi_i^{(n_{\max})}(0) \\ \vdots & \dots & \vdots \\ \psi_i^{(0)}(n_{\max}) & \dots & \psi_i^{(n_{\max})}(n_{\max}) \end{pmatrix}$$

where  $\psi_i^{(l)}(n) = \langle n|\psi_l\rangle_i$  is the projection of an  $l$ -th eigenstate on a Fock state  $|n\rangle$  (alternatively: each state builds a row) at site  $i$ . Since the eigenstates are normalized and orthogonal the operator  $A_i$  is unitary. Thus, with  $\Delta t = t_2 - t_1$  we can write

$$\begin{aligned} |\psi_{MF}(t_2)\rangle_i &= e^{-\frac{i}{\hbar}\mathcal{H}_i(t_1)\Delta t}|\psi_{MF}(t_1)\rangle_i \\ \Leftrightarrow A|\psi_{MF}(t_2)\rangle_i &= Ae^{-\frac{i}{\hbar}\mathcal{H}_i(t_1)\Delta t}A^\dagger A|\psi_{MF}(t_1)\rangle_i \\ \Leftrightarrow A|\psi_{MF}(t_2)\rangle_i &= e^{-\frac{i}{\hbar}\mathbf{E}_i(t_1)\Delta t}A|\psi_{MF}(t_1)\rangle_i \\ \Leftrightarrow |\psi_{MF}(t_2)\rangle_i &= A^\dagger\mathbf{D}A|\psi_{MF}(t_1)\rangle_i, \end{aligned} \tag{3.141}$$

with

$$\mathbf{D} = \begin{pmatrix} e^{-\frac{i}{\hbar}E_{0,i}(t_1)\Delta t} & 0 & \dots \\ 0 & e^{-\frac{i}{\hbar}E_{1,i}(t_1)\Delta t} & \dots \\ \vdots & \vdots & \ddots \end{pmatrix}.$$

A detailed explanation of the individual steps can be found in Appendix C. The benefit of the time evolution based on Eq. (3.141) is the speed of matrix multiplications compared to a calculation of a function.

## 3.6 Finite temperature

Temperature plays an important role, not only for the superfluid-normal transition, but also due to the impact of thermal fluctuations which redistribute the occupation of energy levels and in this way directly influence the long range order, number statistics and cause symmetry breaking in magnetic phases or superfluid samples [109–111, 124, 147, 148]. On the other hand, perturbed systems after being isolated from the environment may not thermalize. Once driven out of thermal equilibrium, the relaxation into a new non-equilibrium steady state may happen [149, 150].

The investigation of the  $T = 0$  regime in previous chapters is an artificial yet very common constraint of many theoretical calculations which successfully predict physics in low-temperature experiments. Certainly, since temperature may lead to excitations and decoherence of the collective many-body excitations studied in this thesis, an extension of these calculations to the finite temperature regime is essential to additionally capture the full range of thermal effects. Luckily, the Gutzwiller method is also readily generalized to nonzero temperature. However, before starting with the finite temperature extension of the mean-field concepts we would like to briefly introduce some basics of quantum statistics needed for further derivations.

### 3.6.1 Density matrix

Finite temperature leads to thermal population of excited states, thus the state of the system is rather described by a statistical ensemble than by a single lowest lying orbital. The validation of a statistical description is based on ergodicity of the system which postulates that the system reaches every possible state in the phase space at sufficiently large times and consequently the time average (the measurement of an observable) can be substituted by an average over the states in an ensemble. For this reason we would like to introduce briefly the concept of *density matrices*<sup>19</sup>. A system being in a statistical superposition of different orthonormal states  $\{|\psi^{(l)}\rangle\}$  with corresponding probabilities  $\{p_l\}$ , where

$$\sum_l p_l = 1,$$

is represented by a density matrix

$$\hat{\rho} = \sum_l p_l |\psi^{(l)}\rangle \langle \psi^{(l)}|. \quad (3.142)$$

Including all possible states of the system, the representation of the system by means of the density matrix is also valid out of equilibrium. The expectation value of an operator  $\hat{O}$  can be obtained by means of the density matrix as

$$\begin{aligned} \langle \hat{O} \rangle &= \sum_l p_l \langle \psi^{(l)} | \hat{O} | \psi^{(l)} \rangle = \sum_l p_l \langle \psi^{(l)} | \sum_i |\phi^{(i)}\rangle \langle \phi^{(i)} | \hat{O} | \psi^{(l)} \rangle \\ &= \sum_i \langle \phi^{(i)} | \hat{O} \sum_l p_l |\psi^{(l)}\rangle \langle \psi^{(l)} | \phi^{(i)} \rangle \\ &= \text{Tr}[\hat{\rho} \hat{O}]. \end{aligned}$$

Here we introduced a complete orthonormal basis  $\{|\phi^{(i)}\rangle\}$  which we do not have to specify further because the trace is independent of the basis used. Since no further constraints were applied, the density matrix describes the system in equilibrium as well as out of equilibrium.

In the Schrödinger representation the full time dependency of the states is passed on to the density matrix. However, apart from this it is conceivable that the probabilities change in time too. We will show via a proof by contradiction, that this is not the case and derive

<sup>19</sup>For complementary explanations see common literature on quantum statistical mechanics e.g. [151].

that the initial probabilities remain constant during a unitary time evolution. Based on the unitary time transformation of the states Eq. (3.134) and assuming  $p_l = p_l(t)$  it is

$$\hat{\rho}(t) = \sum_l p_l(t) |\psi^{(l)}(t)\rangle \langle \psi^{(l)}(t)| \quad (3.143)$$

$$= \sum_l p_l(t) U(t) |\psi^{(l)}(0)\rangle \langle \psi^{(l)}(0)| U^\dagger(t) \quad (3.144)$$

$$= U(t) \left( \sum_l p_l(t) |\psi^{(l)}(0)\rangle \langle \psi^{(l)}(0)| \right) U^\dagger(t) \quad (3.145)$$

Since the projectors  $\{|\psi^{(l)}(0)\rangle \langle \psi^{(l)}(0)|\}$  together with the probabilities  $p_l(0)$  describe the initial statistical ensemble, it naturally follows that

$$\hat{\rho}(t) = U(t) \left( \sum_l p_l(0) |\psi^{(l)}(0)\rangle \langle \psi^{(l)}(0)| \right) U^\dagger(t) \quad (3.146)$$

However, given that the vectors  $\{|\psi^{(l)}\rangle\}$  are the eigenstates of the density matrix<sup>20</sup> the unitary transformation  $U(t)$  preserves the corresponding eigenvalues, such that  $p_l \equiv p_l(0) \equiv p_l(t)$  and the time evolution of the density operator reads

$$\hat{\rho}(t) = \sum_l p_l |\psi^{(l)}(t)\rangle \langle \psi^{(l)}(t)| = U(t) \hat{\rho}(0) U^\dagger(t). \quad (3.147)$$

It is worth pointing out that the eigenstates of the density matrix at any time are not necessarily the eigenstates of the Hamilton operator of the system, depending on whether the system is in equilibrium or not. We will come to this point later in this section.

Alternatively, the differential notation of time evolution in Eq. (3.147) can be derived. Starting with the Schrödinger equation

$$i\hbar \partial_t |\psi^{(l)}(t)\rangle = \hat{\mathcal{H}}(t) |\psi^{(l)}(t)\rangle$$

the time evolution of the density matrix is

$$\begin{aligned} i\hbar \partial_t \hat{\rho}(t) &= i\hbar \partial_t \left[ \sum_l p_l |\psi^{(l)}(t)\rangle \langle \psi^{(l)}(t)| \right] \\ &= \sum_l p_l \left[ (i\hbar \partial_t |\psi^{(l)}(t)\rangle) \langle \psi^{(l)}(t)| + |\psi^{(l)}(t)\rangle (i\hbar \partial_t \langle \psi^{(l)}(t)|) \right] \\ &= \sum_l p_l \left[ \hat{\mathcal{H}}(t) |\psi^{(l)}(t)\rangle \langle \psi^{(l)}(t)| - |\psi^{(l)}(t)\rangle \langle \psi^{(l)}(t)| \hat{\mathcal{H}} \right] \\ &= [\hat{\mathcal{H}}(t), \hat{\rho}(t)] \quad . \end{aligned} \quad (3.148)$$

This relation is known as the von Neumann equation for which Eq. (3.147) represents the general solution. It should be pointed out that Eq. (3.148) based on the Schrödinger picture of states doesn't correspond to the equation of motion of an operator in the Heisenberg picture, which differs in the sign  $i\hbar \partial_t \hat{O}(t) = -[\hat{\mathcal{H}}(t), \hat{O}(t)]$ . The density matrix, build from states, behaves differently from "normal" operators, since it is not an observable, and does not depend on time in Heisenberg representation.

<sup>20</sup>  $\hat{\rho} |\psi^{(m)}\rangle = \sum_l p_l |\psi^{(l)}\rangle \langle \psi^{(l)} | \psi^{(m)}\rangle = \sum_l p_l |\psi^{(l)}\rangle \delta_{lm} = p_m |\psi^{(m)}\rangle$

In equilibrium the states occupied by particles do not evolve dynamically and the density matrix becomes time independent. Nevertheless, stationary dynamics may be encountered where the particles change the states they occupy without influencing the total occupation of this particular state and correspondingly the probabilities  $\{p_l\}$ . In this case the density matrix  $\hat{\rho}(t) \equiv \hat{\rho}$  commutes with the Hamiltonian

$$\text{(equilibrium)} \quad i\hbar\partial_t\hat{\rho} = 0 = [\hat{\mathcal{H}}, \hat{\rho}]. \quad (3.149)$$

Commuting operators have a common basis, thus, the system is in the statistic superposition of the eigenstates of the Hamiltonian which simultaneously form the eigenbasis of the density operator.

As we already introduced the density matrix and its characteristics we can proceed with the specification for a grand canonical ensemble described by the Bose-Hubbard Hamiltonian Eq. (3.63). For this we need to specify the eigenstates and the corresponding eigenvalues of the density operator. In a mixed state in equilibrium the system is in a statistical superposition of ground and excited eigenstates with appropriate eigenenergies:

$$\begin{aligned} \hat{\mathcal{H}}|\Psi^{(l)}\rangle &= E^{(l)}|\Psi^{(l)}\rangle \\ \text{and} \\ \hat{\rho} &= \sum_l p_l |\Psi^{(l)}\rangle\langle\Psi^{(l)}| \end{aligned}$$

The normalized probabilities  $\{p_l\}$  are calculated based on their classical counterpart leaning on the analogy between classical and quantum mechanical representations, the so called *correspondence principle*<sup>21</sup>. Although at fundamental level the correspondence is restricted, it is intuitive to assume that the general form of the probability to find the system in a state  $|\Psi^{(l)}\rangle$  with energy  $E^{(l)}$  corresponds to the Gibbs factor<sup>22</sup>

$$p_l \sim e^{-\beta E^{(l)}},$$

with inverse temperature  $\beta = 1/k_B T$ . The proportionality constant is obtained from the normalization condition

$$\begin{aligned} 1 &\stackrel{!}{=} \frac{1}{Z} \sum_l e^{-\beta E^{(l)}} = \frac{1}{Z} \sum_l \langle\Psi^{(l)}|e^{-\beta\hat{\mathcal{H}}}| \Psi^{(l)}\rangle = \frac{1}{Z} \text{Tr}[e^{-\beta\hat{\mathcal{H}}}] \\ &\Leftrightarrow Z = \text{Tr}[e^{-\beta\hat{\mathcal{H}}}]. \end{aligned} \quad (3.150)$$

The proportionality constant  $Z$  is often referred to as the *partition function*. The normalized probabilities are

$$p_l = \frac{e^{-\beta E^{(l)}}}{Z} = \frac{e^{-\beta E^{(l)}}}{\text{Tr}[e^{-\beta\hat{\mathcal{H}}}]}$$

<sup>21</sup>After having investigated the correspondence between the Poisson bracket in the classical Hamiltonian formalism and the quantum mechanical commutators, Dirac formulated the transformation theory [152], where classical mechanics is obtained as a special case of quantum mechanics. The background of the theory was the attempt to use canonical transformations in analogy to classical procedure.

<sup>22</sup>Since the addition of the chemical potential differs the canonical from the grand canonical ensemble, it is convenient to write out the part with the chemical potential explicitly  $p_l \sim \exp[-\beta(\tilde{E}^{(l)} - \mu N^{(l)})]$  where the eigenvalues  $\tilde{E}^{(l)}$  refer rather to the canonical Hamiltonian Eq. (3.62). When calculating the trace of this density matrix the summation has to be done with respect to the energy levels and contained particle number which is implicated in the summation over the levels in our notation.



and the normalization relation holds

$$\sum_l p_l = \sum_l \frac{e^{-\beta E^{(l)}}}{\text{Tr}[e^{-\beta \hat{H}}]} \stackrel{(3.150)}{=} \frac{\text{Tr}[e^{-\beta \hat{H}}]}{\text{Tr}[e^{-\beta \hat{H}}]} = 1.$$

The partition function contains the complete information about the system. Therefore it is often used for derivation of thermodynamic quantities such as

grand potential	$\Phi = -\frac{\ln[Z]}{\beta}$
von Neumann entropy	$S = -\frac{\partial \Phi}{\partial T} = -k_B \text{Tr}[\hat{\rho} \ln \hat{\rho}]$
internal energy	$E = \frac{\partial(\Phi\beta)}{\partial \beta}$
average particle number	$N = \frac{\partial \Phi}{\partial \mu}$

Having specified the ensemble, we can turn back to the characterization of time-dependent processes. When the dynamically evolving eigenstates of the density matrix remain eigenstates of the system we are dealing with a stationary equilibrium process described by Eq. (3.149) obeying the postulates of thermodynamics. The microscopic situation is not of importance anymore since the total system is well described by a few macroscopic parameters such as volume, total particle number and temperature. Not so in a non-equilibrium case. The diversity of phenomena and complexity of theoretical description attracted the attention of many physicists to a new field of investigations: thermal non-equilibrium dynamics. But before we proceed with studies of specific systems we will briefly introduce some useful terminology concerning this topic.

### 3.6.2 Thermalization and adiabaticity

When the system is in thermal, mechanical and radiational equilibrium no net transport processes or fluctuations exist - the system is in thermodynamic equilibrium. The entropy of the system becomes maximal and the temperature of the sample is well defined. Such a system obeys Boltzmann statistics and the time average corresponds to the ensemble average. Based on the averaged internal energy the temperature of the system can be defined [151].

In local thermal equilibrium the thermodynamic quantities such as density fulfill local thermodynamic relations in each arbitrarily small volume, however, not globally. In this sense the local thermal equilibrium, which still allows spatial and temporal variance of thermodynamic observables, is a special case of non-equilibrium thermodynamics. However, the variation in time must be sufficiently slow such that the local Maxwell-Boltzmann distributions are sustained. In such locally equilibrated system local temperatures, which vary spatially, still can be defined.

Thus, after an initial perturbation the global thermal equilibrium is approached when the system undergoes collisional relaxation processes, with mass and energy flows leading to local and finally to global thermal equilibria.

Whereas scattering happens on a characteristic time scale  $\tau$  the flow is controlled by the mean free path and leads to equilibration in space on a larger time scale [151]. Therefore in

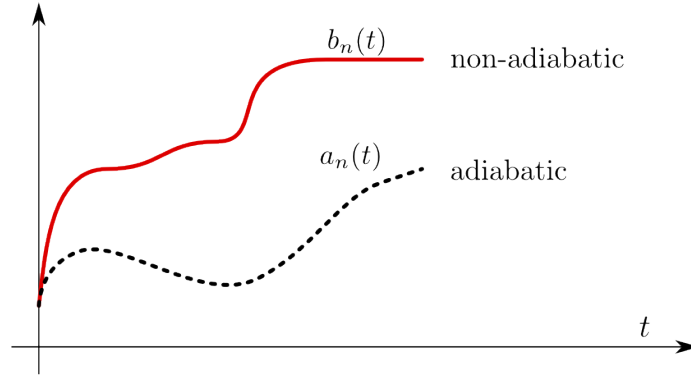


**Figure 3.14:** Difference between an adiabatic and a non-adiabatic process. In case of adiabaticity the time-evolving state  $|\Phi(t)\rangle = \sum_n b_n(t)|n\rangle$  must follow the evolution of the eigenstate of the system  $|\Psi^{(0)}\rangle = \sum_n a_n(t)|n\rangle$ , thus  $a_n(t) \equiv b_n(t)$  for  $\forall t$  otherwise the dynamics is not adiabatic.

this thesis we distinguish between thermalization and adiabaticity. A system is considered to be thermalized when the temperatures of subsystems assimilate leading to a global temperature. Adiabaticity refers to the many-body state of the system. Here, the evolution is considered adiabatic when the system remains in the ground state at every time step. Whereas thermalization corresponds to global thermal equilibrium and requires longer time scales to be reached, adiabaticity reflects the local equilibration on shorter time steps.

To get familiar with both concepts we make a gedankenexperiment in which a system is exposed to a perturbation at  $t = 0$  or during it evolves in time. Hereby we concentrate on an infinitesimally small part of an isolated system, such that the coupling to the rest of the system can be considered as a coupling to a thermal bath, with a composite Hilbert space  $\mathcal{H}_s \otimes \mathcal{H}_{\text{bath}}$ .

We start with a simple example: a subsystem being in its ground state  $|\Psi^{(0)}\rangle$  coupled to a thermal bath, both at temperature  $T = 0$ . Hence, the initial reduced density matrix of a pure subsystem reads in the Fock basis  $\{|n\rangle\}$

$$\hat{\rho}_s(t=0) = \text{Tr}_{\text{bath}} \hat{\rho}(t=0) = |\Psi^{(0)}\rangle\langle\Psi^{(0)}| = \sum_n |a_n(t=0)|^2 |n\rangle\langle n|.$$

If no heat is transferred to the system the initial temperature is preserved and the described ensemble is trivially in the thermal equilibrium. At  $T = 0$  no thermal excitations can occur and the density matrix of the reduced system  $\hat{\rho}_s$  remains in a pure state. However, depending on the dynamics, the time evolved state of the subsystem can differ from the ground state at time  $t$ . Hence, in general the density matrix reads

$$\hat{\rho}_s(t) = |\Phi(t)\rangle\langle\Phi(t)| = \sum_n |b_n(t)|^2 |n\rangle\langle n|$$

and describes a thermal non-adiabatic process. The time evolution is only adiabatic when  $|\Phi(t)\rangle \equiv |\Psi^{(0)}(t)\rangle$  with  $|\Psi^{(0)}(t)\rangle$  being the ground state of the subsystem at any time:  $\mathcal{H}_s(t)|\Psi^{(0)}(t)\rangle = E_s^{(0)}(t)|\Psi^{(0)}(t)\rangle$ . The Fig. 3.14 demonstrates the difference between both time evolutions. We will characterize adiabatic and non-adiabatic processes in more detail in Sec. 4.

The situation becomes more complicated, when the bath and the system are at finite but not necessarily equal temperature. The particles are thermally excited to energetically higher levels and the total as well as the subsystem are in a mixed state respectively. Given the eigenvalue equation  $\mathcal{H}_s|\Psi^{(l)}\rangle = E_s^{(l)}|\Psi^{(l)}\rangle$ , the initial reduced density matrix of the subsystem reads

$$\hat{\rho}_s(t=0) = \frac{1}{Z} \sum_l e^{-\beta_s E_s^{(l)}} |\Psi^{(l)}\rangle \langle \Psi^{(l)}|.$$

The particular form of the density matrix during a dynamic evolution depends on the processes happening. Different to the  $T = 0$  case, at finite temperature the characterization of the subsystem is based on  $\beta_s$ ,  $E_s^{(l)}$ ,  $|\Psi^{(l)}\rangle$  and on their development in time. The latter can be unitary and non-unitary.

If the time evolution is unitary the Gibb's factors are time independent (see the derivation Eq. (3.143)-(3.146)). In the subsystem, once prepared with thermal weights  $e^{-\beta_s E_s^{(l)}}(t=0) \equiv e^{-\beta_s E_s^{(l)}}$ , only the states may change and the reduced density matrix is

$$\text{non-thermalized, non-adiabatic: } \hat{\rho}_s(t) = \frac{1}{Z} \sum_l e^{-\beta_s E_s^{(l)}} |\Phi^{(l)}(t)\rangle \langle \Phi^{(l)}(t)| \quad (3.151)$$

where  $|\Phi^{(l)}(t)\rangle$  describe unitarily evolved states different from the eigenstates indicating a non-adiabatic time evolution. Through the coupling to the neighbors directly or indirectly a local thermalization may take place. However, since it is not obligatory, for the sake of generality the subsystem described by Eq. (3.151) is titled non-thermalized.

If the dynamical processes during the time evolution are adiabatic, such an ensemble is represented by

$$\text{non-thermalized, adiabatic: } \hat{\rho}_s(t) = \frac{1}{Z} \sum_l e^{-\beta_s E_s^{(l)}} |\Psi^{(l)}(t)\rangle \langle \Psi^{(l)}(t)|,$$

where  $|\Psi^{(l)}(t)\rangle$  are the eigenstates of the subsystem at any time. Hence, the Hamiltonian of the subsystem and  $\hat{\rho}_s(t)$  have a common eigenbasis. However, the inverse temperature  $\beta_s$  may not correspond to the temperature in the bath. Consequently, the ensemble may remain unthermalized.

In a perturbed, completely isolated system trivially a global thermalization is not possible without dissipation processes. The most prominent mechanisms reducing the Helmholtz free energy of the system are various forms of dephasing, vibrational relaxation and three-body losses. Since in the Bose-Hubbard model such processes are not included, in order to account for dissipations one has to apply the Lindblad equation [153]. The Kossakowski-Lindblad equation is a quantum mechanical generalization of a *master equation* continuous in time. It incorporates Markov processes, where the system changes its state stochastically, describing non-unitary evolution of the density matrix  $\hat{\rho}(t)$ . Since we are not going to investigate processes like that in this thesis, we refer to detailed explanations in general statistics books.

### 3.6.3 Mean-field approximations

Since a thermally excited system is no longer described by the energetically lowest lying state alone, the mean-field ansatz must be extended, whereby the excited states are as-

sumed to factorize over the lattice sites corresponding to the ground state (compare with Sec. 3.3.2)

$$|\Psi_{MF}^{(n)}\rangle = \prod_i |\psi_{MF}^{(n)}\rangle_i$$

where  $\hat{\mathcal{H}}_{MF,i} |\psi_{MF}^{(n)}\rangle_i = E_{MF,i}^{(n)} |\psi_{MF}^{(n)}\rangle_i$ .

Hence, the tuple of probabilities characterizing the statistics of the total  $L$ -site system  $\{p_n\}$  turns into a multiplet of on-site statistics  $\{\{p_{n,1}\}, \dots, \{p_{n,L}\}\}$ . Consequently, the density matrix in this approximation becomes a product

$$\begin{aligned} \hat{\rho} &= \sum_n p_n |\Psi_{MF}^{(n)}\rangle \langle \Psi_{MF}^{(n)}| \\ &= \sum_n \prod_i \left( p_{n,i} |\psi_{MF}^{(n)}\rangle_{ii} \langle \psi_{MF}^{(n)}| \right) \\ &= \prod_i \hat{\rho}_i \end{aligned} \quad (3.152)$$

of single-site density matrices

$$\hat{\rho}_i = \sum_n p_{n,i} |\psi_{MF}^{(n)}\rangle_{ii} \langle \psi_{MF}^{(n)}|.$$

The normalized on-site probabilities are calculated with respect to the on-site spectrum

$$p_{n,i} = \frac{1}{Z_i} e^{-\beta E_{MF,i}^{(n)}} \quad , \quad Z_i = \text{Tr}[e^{-\beta \hat{\mathcal{H}}_{MF,i}}].$$

The system evolving in time is described by a time dependent density matrix  $\hat{\rho}(t) = \sum_l p_l |\Psi_{MF}^{(l)}(t)\rangle \langle \Psi_{MF}^{(l)}(t)|$ . Since the time-dependent many-body state in the mean-field approximation is a product state over the on-site states (see Eq. (3.137) and Eq. (3.139)), the time dependent density matrix decomposes analogously to Eq. (3.152)

$$\hat{\rho}(t) = \prod_i \hat{\rho}_i(t) \quad , \quad \text{with} \quad \hat{\rho}_i(t) = \sum_n p_{n,i} |\psi_{MF}^{(n)}(t)\rangle_{ii} \langle \psi_{MF}^{(n)}(t)| \quad (3.153)$$

where  $|\psi_{MF}^{(n)}(t)\rangle_i$  obey the Schrödinger dynamics induced by time dependence in local Hamiltonians  $\hat{\mathcal{H}}_{MF,i}(t)$  (see Sec. 3.5). As a matter of fact each on-site density matrix obeys the von Neumann relation

$$i\hbar \partial_t \hat{\rho}_i(t) = [\hat{\mathcal{H}}_{MF,i}(t), \hat{\rho}_i(t)].$$

The von Neumann time evolution is unitary and hence preserves the weights in the density matrix. Thus, the thermal weights  $e^{-\beta E_n^i}/Z_i$  remain time-independent during a simulation, where  $E_n$  are the initial eigenvalues of the system and  $Z_i$  is the initial partition function.

## 4. Lattice ramp dynamics in an interacting Bose-Bose mixture

Up to now we have characterized degenerate quantum gas consisting of one bosonic species in the strongly and weakly correlated regimes and discussed properties of SF and MI phases as well as possible phase transitions between them. This topics were already investigated theoretically [9, 10] and realized experimentally [12]. Adding a second atomic species results in a wealth of new quantum phases, clearly demonstrating the complexity of correlated ensembles. Currently, several experimental groups are working on Fermi-Bose [24, 154, 155], Fermi-Fermi [14, 156–158] and Bose-Bose [19, 20, 159] mixtures in optical lattices which are promising devices for studies of disorder [160], dipolar molecule formation [161], and spin arrays [162]. In Bose-Fermi mixtures [15, 16] and Bose-Bose mixtures [17, 18], a supersolid phase has been predicted to exist.

Recently the Florence group has realized a Bose-Bose mixture of  $^{87}\text{Rb}$  and  $^{41}\text{K}$  trapped in a 3D optical lattice [20]. They showed that the SF-MI transition of Rubidium is shifted towards shallower optical lattices when Potassium is present in the system. The same reduction of the visibility was seen in experiments where fermions were added to bosons in optical lattices [24, 154, 155].

These experiments are important steps towards the study of low-temperature properties of atomic mixtures. The experimental investigation of quantum many-body ground-states, for instance with spin ordering, requires the achievement of rather low temperatures in the lattice. For fermions this already poses problems before ramping up the optical lattice, since evaporative cooling becomes inefficient in the degenerate limit. Bosons, on the other hand, can be cooled to very low temperatures [4]. However, ramping up the optical lattice can easily increase the temperature, or more precisely the entropy, again. Thus, the conditions for adiabatic lattice ramp need to be clarified, which is one of the aims of our research discussed in the following sections.

The timescale for ramping the optical lattice in the experiment is usually determined such that the system ends up in the lowest band of the optical lattice, i.e. the ramping time is chosen large with respect to the inverse band gap. Since the band gap is small for shallow optical lattices, sometimes an exponential ramp-up profile is chosen. However, this does not guarantee that the ramping process is also adiabatic with respect to the many-body

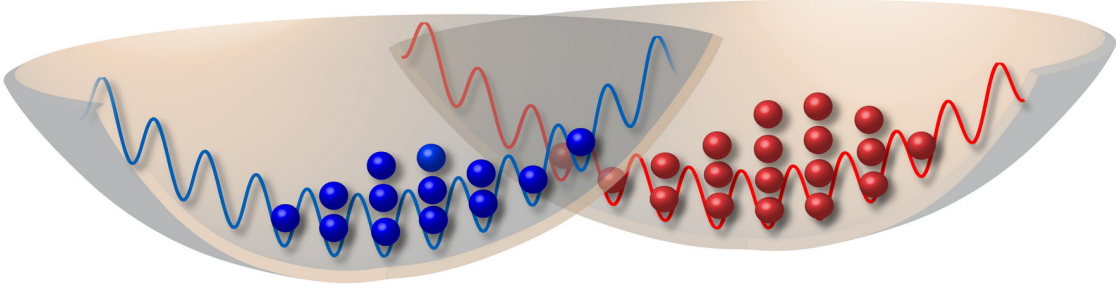


**Figure 4.1:** Modeling of the gravitational sag by two spatially separated parabolic trapping potentials. The lattice potential with the superimposed harmonic trapping potential (here drawn in one dimension only) is represented by a sinusoidal blue and red line. Different colors represent the two different bosonic species.

states in the lowest band [26, 28]. This is indeed not true and can be easily seen from the fact that the tunneling time for the atoms  $t_{\text{hop}}(s) = \frac{\pi}{2} \frac{\hbar}{J_{Rb}(s)}$  is of the same order as the ramp-up time in most experiments.

We address this questions here by systematically mapping out the visibility of a Bose-Bose mixture as a function of ramp-up time, focusing on the experiment by Catani *et al.* [20]. Specifically, the results are discussed with respect to the issue of adiabaticity. We consider a two-dimensional system. In this way we keep the numerical effect manageable, and yet avoid the peculiarities associated with a one-dimensional system, like the absence of long range order even at zero temperature, which makes the extrapolation of one-dimensional results to higher dimensions problematic.

## 4.1 Model and method

The two-species bosonic system we consider is described by the Bose-Hubbard Hamiltonian:

$$\hat{\mathcal{H}} = \sum_{\alpha=a,b} \left[ \sum_{\langle ij \rangle} J_{\alpha} (\hat{b}_{i\alpha}^{\dagger} \hat{b}_{j\alpha} + h.c.) + \sum_i \frac{U_{\alpha}}{2} \hat{n}_{i\alpha} (\hat{n}_{i\alpha} - 1) - \sum_i (\mu_{\alpha} - V_{i\alpha}^{\text{trap}}) \hat{n}_{i\alpha} \right] + \sum_i U_{ab} \hat{n}_{ia} \hat{n}_{ib} \quad , \quad (4.1)$$

where the operator  $\hat{b}_{i\alpha}^{\dagger}$  ( $\hat{b}_{i\alpha}$ ) creates (annihilates) a boson of flavor  $\alpha$ ,  $\alpha = a, b$  at site  $i$ . Since our goal is to model the experiment [20], we choose the two species as  $^{87}\text{Rb}$  and  $^{41}\text{K}$ . The separation of the center of mass of the two clouds due to the gravitational sag is modeled by two spatially separated parabolic traps  $V_{i\alpha}^{\text{trap}} = \frac{1}{2} m_{\alpha} \omega_{\alpha}^2 d^2 |\mathbf{r}_i - \mathbf{r}_{\alpha}|^2$ , where  $d$  is the lattice constant,  $\omega_{\alpha}$  the trap frequency,  $\mathbf{r}_i$  are the coordinates of the given lattice site  $i$  and  $\mathbf{r}_{\alpha}$  are the centers of the harmonic potentials, see Fig. 4.1. The frequencies of the parabolic trap are  $\omega_{Rb} = 2\pi \times 36\text{Hz}$  and  $\omega_K = 2\pi \times 53\text{Hz}$ . The distance between the two trap centers was chosen in such a way that the atomic clouds overlap only on a few lattice sites, as in the experiment [20]. The chemical potentials  $\mu_{\alpha}$  are adjusted such that the resulting particle numbers correspond to the particle number ratio of the experiment  $N_K/N_{Rb} \approx 0.1$  [20] ( $N_K \approx 30, N_{Rb} \approx 300$ ). The parameters  $U_{\alpha}, U_{ab}, J_{\alpha}$  indicate the intra-/interspecies Coulomb repulsion and the hopping amplitude. As input we use the experimental values

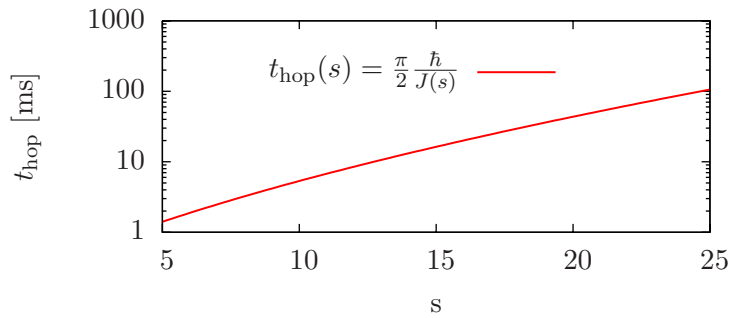


**Figure 4.2:** The tunneling time as a function of the lattice depth.

of the Florence experiments [20]: lattice laser wavelength  $\lambda_L = 1064$  nm, scattering length  $a_{Rb-K} = 163a_0$ ,  $a_{Rb} = 99a_0$ ,  $a_K = 65a_0$ , with  $a_0$  the Bohr radius. The hopping constants  $J_\alpha$  and the interaction parameters  $U_\alpha$ ,  $U_{ab}$  are calculated according to [108]:

$$J_\alpha = \frac{4}{\sqrt{\pi}} \frac{\hbar^2}{2m_\alpha} \left( \frac{2\pi}{\lambda_L} \right)^2 s_\alpha^{3/4} e^{-2\sqrt{s_\alpha}}, \quad (4.2)$$

$$U_\alpha = \sqrt{\frac{8}{\pi}} \frac{2\pi}{\lambda_L} a_\alpha E_r^\alpha s_\alpha^{3/4}, \quad (4.3)$$

$$U_{Rb-K} = \frac{4}{\sqrt{\pi}} k a_{Rb-K} E_r^\alpha \frac{1 + \frac{m_{Rb}}{m_K}}{\left(1 + \sqrt{\frac{m_{Rb} V_L^{Rb}}{m_K V_L^K}}\right)^{3/2}} s_{Rb}^{3/4} \quad (4.4)$$

with the dimensionless lattice depth  $s_\alpha = V_L^\alpha / E_r^\alpha$ , where  $V_L^\alpha$  is the depth of the laser-induced potential and  $E_r^\alpha$  the recoil energy of species  $\alpha$ . From the hopping constant we directly obtain the tunneling time of Rb-atoms  $t_{\text{hop}}(s) = \frac{\pi}{2} \frac{\hbar}{J_{Rb}(s)}$ , which we plot as a function of lattice depth in Fig. 4.2. For the given wavelength the depth of the laser induced lattice potential is species-specific:  $V_L^{Rb} = 1.1V_L^K$  and  $E_r^K = 2.1E_r^{Rb}$ . This results in  $s_{Rb} = 2.3s_K$ . In the following we use the short-hand notation  $s = s_{Rb}$ . Here we neglect the influence of the parabolic confinement on the parameters. This is justified because experimentally the potential energy difference between neighboring lattice wells is much smaller than the barrier height [87].

Here we simulate the experimental ramp-up dynamics within a mean-field approximation. In the Gutzwiller method a mean-field approximation is applied to the operators  $\hat{b}_{i\alpha}^\dagger$  ( $\hat{b}_{i\alpha}$ ) in the hopping part of the Hamiltonian Eq. (4.1). This leads to a decomposition of the lattice Hamiltonian into a sum over decoupled single-site Hamiltonians, which can be solved numerically:

$$\begin{aligned} \hat{\mathcal{H}}_i^{MF} = & \sum_{\alpha=a,b} [J_\alpha (\phi_{i\alpha}^* \hat{b}_{i\alpha} + h.c.) + \frac{U_\alpha}{2} \hat{n}_{i\alpha} (\hat{n}_{i\alpha} - 1) \\ & - (\mu_\alpha - V_{i\alpha}^{\text{trap}}) \hat{n}_{i\alpha}] + U_{ab} \hat{n}_{ia} \hat{n}_{ib} \quad , \end{aligned} \quad (4.5)$$

with  $\eta_{i\alpha} = \sum_{j \text{ n.n. } i} \langle \hat{b}_{j\alpha} \rangle$ , where the mean-field parameters  $\langle \hat{b}_{j\alpha} \rangle$  (superfluid order parameters) have to be found selfconsistently. Since the Hamiltonian is a sum over on-site Hamiltonians, the many-body wave function is a product wave function over the lattice sites. However, the different sites are coupled by the superfluid order parameter  $\eta_{i\alpha}$ . When the bosons are superfluid, the superfluid order parameter is nonzero and the phase is constant in space. This establishes superfluid long range order in the system.

Similarly to the single-species Gutzwiller dynamics, at zero temperature the total wave function is assumed to be a product wave function over the lattice sites:  $|\Psi(t)\rangle = \prod_i |\psi(t)\rangle_i$ . The single-site states are tensor products of two Hilbert spaces, one per species:

$$|\psi(t)\rangle_i = \sum_{n_a, n_b} \beta_{i, n_a, n_b}(t) (\hat{b}_{i_a}^\dagger)^{n_a} (\hat{b}_{i_b}^\dagger)^{n_b} |0\rangle. \quad (4.6)$$

Each of the on-site wave-functions is evolved in time according to the local Schrödinger equation

$$i\hbar\partial_t |\psi(t)\rangle_i = \hat{\mathcal{H}}_i^{MF}(t) |\psi(t)\rangle_i \quad .$$

This constitutes a set of coupled non-linear differential equations for the  $\beta_{i, n_a, n_b}(t)$ , which have to be solved.

In order to study possible thermal effects, the applied method is extended to finite temperatures. The corresponding theoretical concepts are discussed in Sec. 3.6. Similarly to the single-species case, the total density matrix for Bose-Bose mixed system factorizes over the lattice sites as  $\hat{\rho}(t) = \prod_i \hat{\rho}_i(t)$ , with  $\hat{\rho}_i(t) = \sum_n \frac{e^{-\beta E_n^i}}{Z_i} |\psi_n(t)\rangle_{ii} \langle\psi_n(t)|$ , where  $|\psi_n(t)\rangle_i$  are the local eigenstates defined in Eq. (4.6) of the Hamiltonian  $\hat{\mathcal{H}}_i^{MF}(t)$  and  $Z_i$  the on-site partition functions. The dynamics is simulated via the von Neumann equation (see Eq. (3.148))

$$i\hbar\partial_t \hat{\rho}_i(t) = [\hat{\mathcal{H}}_i^{MF}(t), \hat{\rho}_i(t)] \quad . \quad (4.7)$$

Due to unitarity of the time evolution the thermal weights in the density matrix  $\frac{e^{-\beta E_n^i}}{Z_i}$  in the ramp simulation are time-independent. Thus,  $E_n$  are the initial eigenvalues of the system and  $Z_i$  is the initial partition function. The initial inverse temperature  $\beta = 1/k_B T$  is set to an experimentally reasonable value.

## 4.2 Results for $T = 0$

At low lattice depth the system does not fulfill the single-band tight-binding approximation required for the Bose-Hubbard Hamiltonian in Eq. (4.1) to be valid. We therefore start our calculations at  $s = 5$  where  $^{87}\text{Rb}$  is already far in the tight-binding and the lowest band regime. The corresponding lattice depth for  $^{41}\text{K}$  is  $s_K = 2.17$ . Since the ratio between the bandwidth  $4J_K$  and the band gap  $E_{gap} = 2\sqrt{s_k}E_r$  is small for the initial  $s_K$  ( $4J_K/E_{gap} \approx 0.03$ ), the single-band approximation is also satisfied for  $^{41}\text{K}$ . We assume that the wave function still corresponds to ground state when the ramp in the experiment reaches this initial lattice depth. This is a valid assumption, since interactions are still weak for  $s = 5$  and the ramping time in the experiments is chosen adiabatic with respect to the band gap, which guarantees that the particles remain in the lowest band. Starting with  $s = 4$  and  $s = 6$  indeed did not change our results.

Although the ramp of the lattice affects both species, only effects of the ramp-up dynamics on the  $^{87}\text{Rb}$ -atoms are discussed in the following, as in the experiments [20].

To investigate the adiabaticity of the lattice-ramp, we now first present results for the density distribution in real-space as well as in momentum space. Later on we focus on the visibility.



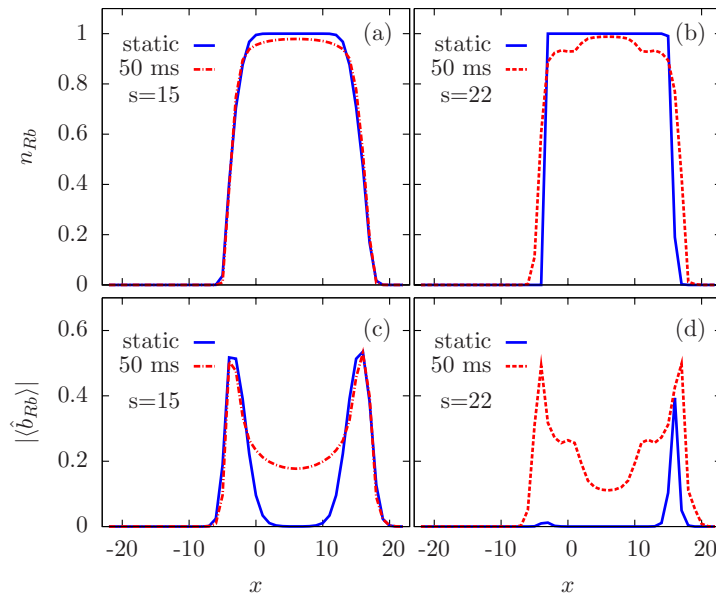


**Figure 4.3:** Particle density and superfluid order parameter of  $^{87}\text{Rb}$  along a cut in  $x$ -direction through the center of the trap ( $y = 0$ ). (a) For  $s = 15$  and ramp duration  $t = 50$  ms (red dashed line) the particles in the center of the trap are in the “frozen phase” in contrast to the ground state profile (blue solid line), where a Mott-plateau is present. This is indicated by the non-integer density  $n_{Rb}$  and nonzero local superfluid order parameter  $|\langle \hat{b}_{Rb} \rangle|$  (c). (b) For  $s = 22$  and  $t = 50$  ms (red dashed line) a density wave is induced due to the fast ramp and high non-adiabaticity. Global parameters:  $L = 45$ ,  $N_{Rb} = 303$ ,  $N_K = 30$ ,  $U_{Rb-K} = 1.93U_{Rb}$ . Parameters for (a) and (c):  $J_{Rb} = 0.02U_{Rb}$ , Parameters for (b) and (d):  $J_{Rb} = 0.004U_{Rb}$ .

### 4.2.1 Density profiles

#### Real space

To investigate the effect of the ramping dynamics we first compare the density distributions in real-space after the lattice ramp-up with static density profiles at the corresponding final lattice depth. The static profiles originate from the ground state at  $T = 0$  for a given  $s$ .

For small final  $s$  ( $s < 10$ ) the density profiles agree perfectly with the static ones independently of the ramping time. For larger  $s$ , longer ramping times are needed to achieve good agreement between the profiles. In particular, for  $s \geq 15$  in equilibrium a Mott plateau appears in the center of the trap. However the dynamically evolved wave function remains a superposition of various Fock states for fast ramps. This can be understood by the following argument. In the limit of an instantaneous increase of the lattice depth the superfluid wave function consisting of local superpositions of various Fock states remains unchanged. Since the hopping  $J$  decreases exponentially with increasing lattice depth, after this sudden step to a deep lattice the time-evolution operator consists mainly out of the interaction part  $U\hat{n}(\hat{n}-1)/2$  which rotates the phase of each Fock state independently, but leaves the local wave function in a superposition of multiple Fock states. The situation is similar for a fast ramp and leads to non-integer particle density (see Fig. 4.3 (a)(b)) and nonzero local superfluid order parameter (see Fig. 4.3 (c)(d)). Although the absolute value of the superfluid parameter is non-vanishing, long-range order is destroyed as the complex phases of  $\langle \hat{b}_i \rangle$  are not constant over the lattice anymore. Correlations between the phases, however, can be partially recovered for certain ramp-up times. This corresponds

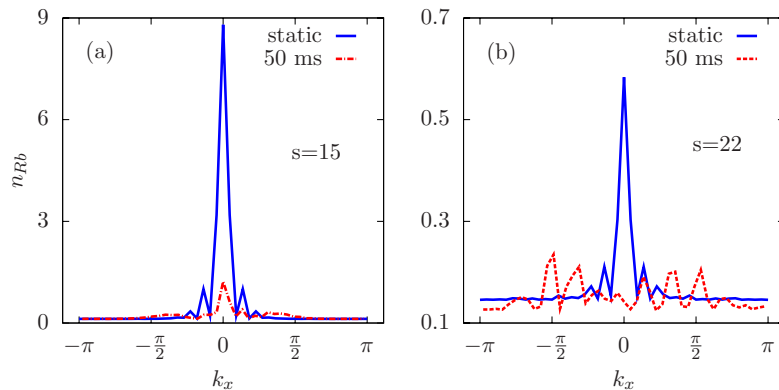


**Figure 4.4:** Particle density in momentum space along a cut in (1,0)-direction for  $k_y = 0$ . (a) In the static calculations (blue solid line) the central peak at  $\mathbf{k} = (0,0)$  is present, due to the SF shell, and small side peaks at nonzero  $\mathbf{k}$  due to the MI-core in the middle of the trap. Fast ramps with  $t = 50$  ms (red dashed line) drive the particles into a frozen phase with lowered phase coherence, which is mirrored in a decreased central peak. (b) Ramping within the same time to a deeper lattice is highly non-adiabatic. The central peak becomes smaller than the side peaks or even the background value  $n(\mathbf{k} = (\pi, \pi))$  and the  $\pm\mathbf{k}$  symmetry disappears.

to the collapse-and-revival dynamics [163]: after time intervals of length  $2\pi\hbar/U$  all the individual phases are back in phase and global phase coherence is restored. Away from the revival times, due to the vanishing coherence this phase is not a SF-phase, we refer to it as a “frozen” phase.

Ramping the lattice to higher  $s$  with the same ramp-up time means effectively faster increase of the lattice depth per time unit. This causes not only significant deviations from the static density profiles but also the formation of density waves (Fig. 4.3 (b)). This behavior is observed for ramp-up times below 100 ms. The density waves are a further evidence that the final state reached after the lattice ramp is not necessarily the ground state.

We finally examine the rotational symmetry of the density profile of the Rb atoms. Due to the presence of the K species (and hence additional repulsive interactions), the rotational symmetry of the Rb cloud is always broken. However, this effect is only very pronounced for large  $s$ . Deep in the MI regime the compressible superfluid boundary layer, adjacent to the cloud of K-atoms, disappears because of the strong repulsive force experienced by the K atoms. The corresponding superfluid order parameter vanishes in the ground state. This is different in the case of the time-evolved profiles: as the  $^{87}\text{Rb}$  atoms for  $t = 50$  s = 22 ms are in the “frozen” phase, the breaking of circular symmetry is far less pronounced than in the static case, where the system is already Mott-insulating.

### Momentum space

More information regarding superfluid long-range order is available in momentum space. Besides, in contrast to the real-space particle distribution, information on the momentum distribution is experimentally well accessible by time-of-flight measurements. The non-adiabaticity and oscillations in the density profile are mirrored in the momentum distribution. To accentuate the global behavior as a function of the ramp-up time and the final lattice depth we show only the values averaged over an equilibration time of 16 ms.

As already pointed out in Sec. 3.3.3 the site decoupling within the mean-field approximation which we employ leads to approximate results for the momentum distribution. In the homogeneous interacting case it yields a coherent peak at strictly zero momentum on top of a flat background arising from the non-condensed atoms. It thus neglects short-range correlations at distances of the order of the coherence length, which turn this flat background into a Gaussian with finite width. Since this width is large for the parameters of interest, the approximation by a flat background is well justified and the Gutzwiller approximation still gives a faithful representation of the momentum distribution. Because we investigate trapped systems, the momentum distribution is additionally broadened by the trap which makes the neglected short range correlations even less important. Moreover, in most of the following results we deal with the visibility, which involves the weight of the coherent peak, but does not depend on the exact shape of the distribution. Altogether, this justifies the study of the momentum distribution via the Gutzwiller method.

As denoted in the previous subsection, for short ramp-up times and deep lattices the local superfluid order parameter remains finite in the region where the static calculation predicts a MI-plateau. Particles stay “frozen” in a superfluid-like phase indicated by non-integer particle densities and finite local superfluid order parameter. Although in the dynamic case all Rb atoms seem to be superfluid, the phase coherence is lost. This is shown in Fig. 4.4. The reduced central peak in the  $n(\mathbf{k})$ -profile compared to the static data clearly indicates destroyed long-range order in the system (Fig. 4.4 (a)). In extremely non-adiabatic cases the central peak becomes smaller than the side peaks or even the background value  $n(\mathbf{k} = (\pi, \pi))$ . This leads to a significant broadening of the momentum distribution. Additionally the  $\pm\mathbf{k}$  symmetry breaks down (Fig. 4.4 (b)).

### 4.2.2 Visibility

The most convenient way to compare the experimental momentum distribution with our theoretical results is to calculate the visibility  $\eta$  (see Sec. 3.2.5) for the  $^{87}\text{Rb}$  atoms as a function of lattice depth  $s$

$$\eta(s) = \frac{n_s(\mathbf{k} = (0, 0)) - n_s(\mathbf{k} = (\pi, \pi))}{n_s(\mathbf{k} = (0, 0)) + n_s(\mathbf{k} = (\pi, \pi))} . \quad (4.8)$$

Here  $n_s(\mathbf{k})$  corresponds to the spatial Fourier transform of  $\langle \hat{b}_i^\dagger \hat{b}_j \rangle(s)$ . In the experimental procedure [20] the height of the first order peaks is compared with the minimum in  $n(\mathbf{k})$  at the same distance from the central zero order peak, to divide out the contribution of the Wannier function. Our calculations are performed within the tight-binding model Eq. (4.1) and do not include the shape of the Wannier function. We therefore calculate the visibility by comparing the central peak with the minimum at the edge of the Brillouin-zone, see Fig. 3.10.

The  $n(\mathbf{k})$  values are extracted in the experiment [20] by integrating finite square areas around the peaks instead of taking single values. Application of this method to our theoretical data shifts the visibility for all ramp-up times. This is a small quantitative effect and depends on the extent of the integration area. It has no effect on the conclusions drawn in this thesis.

In order to investigate the reduction of the visibility in a systematic way, we now subsequently analyze the role of the second species, the ramp-up profile of the lattice and the ramp-up time.

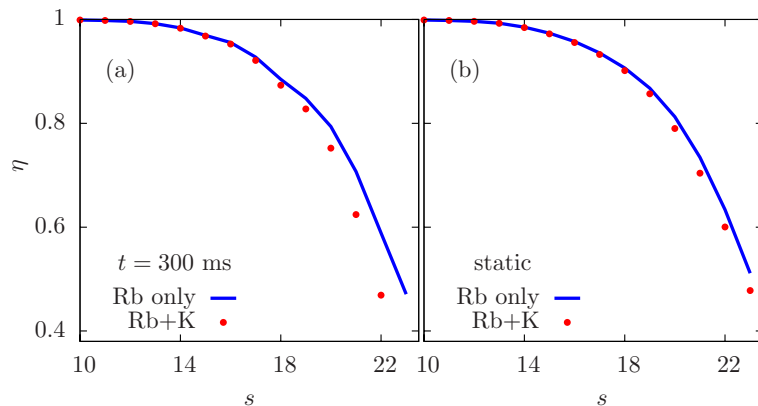


**Figure 4.5:** Visibility for pure  $^{87}\text{Rb}$  (blue solid line) and in the presence of  $^{41}\text{K}$  (red dots) after a  $t = 300$  ms ramp (a) and in the static case (b). In both cases the visibility of pure  $^{87}\text{Rb}$  is higher.

### Effect of the second species

It is observed experimentally that addition of  $^{41}\text{K}$  to a system of  $^{87}\text{Rb}$ -particles reduces the phase coherence and the visibility [20]. Our simulations reproduce this behavior for similar parameters and particle number ratios as in the experiment, i.e.  $N_{\text{Rb}} \approx 303$  and  $N_{\text{K}} \approx 30$ . We observed this effect for all simulated ramping times (from 50 to 300 ms with a linear ramp-up profile) as well as in the static case (Fig. 4.5 (a),(b)). In particular, the destructive effect of the  $^{41}\text{K}$  on the phase correlations of the superfluid order parameter of  $^{87}\text{Rb}$  is more pronounced in the dynamic case than in the static one. This indicates that the second species enhances the non-equilibrium induced by the lattice ramp.

The reason for the lower  $^{87}\text{Rb}$  visibility in the presence of  $^{41}\text{K}$  in the static case is the following. The repulsive interaction between the species pushes the  $^{87}\text{Rb}$  atoms out of the overlap region and enhances the  $^{87}\text{Rb}$  density in the trap center. This increases the interaction energy of  $^{87}\text{Rb}$  and brings the particles closer to the SF-MI transition, thus decreasing the coherence of the system in the static case [27].

The dynamic lattice ramp to deep lattices leads even to a lower visibility than in the static case. This can be explained by the following argument. As we will show below, one of the reasons for the non-adiabaticity of the ramp-up is the excitation of collective modes. This effect results from the interplay between the intraspecies repulsion and the increase of the lattice depth, which squeezes the atomic cloud. When  $^{41}\text{K}$  is present, the clouds exert a repulsive force on each other, even though the overlap region is small. This leads to additional collective modes in the system, which reduce the phase coherence and hence the visibility. Below we will quantify this statement. This mechanism could explain why in experiments always a reduced visibility is seen when a second species is added.

### Effect of the ramp-up profile

In this subsection we investigate the effect of the time profile of the lattice ramp on adiabaticity. Our motivation is that in experiments the ramping profiles are usually of exponential shape to keep particles in the lowest band at the beginning of the ramp. For

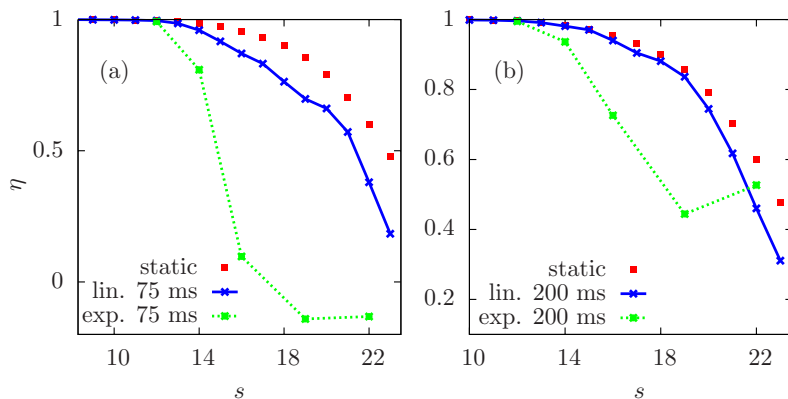


**Figure 4.6:** Effect of the ramping profile on the visibility of  $^{87}\text{Rb}$  in the presence of  $^{41}\text{K}$ . (a) The resulting visibility after a  $t = 75$  ms ramp with the linear profile (blue solid line) lies closer to the adiabatic static visibility (red solid line) than the visibility after a ramp with the exponential profile (green dashed line). (b) Results with the same profiles but for  $t = 200$  ms ramp.

a better comparison between the simulated linear profile and the one used in experiment we also used the same shape as in [20]

$$s'(t') = (e^{\frac{t'}{0.4t}} - 1) \frac{s}{e^{\frac{1}{0.4}} - 1}, \quad (4.9)$$

where  $s$  is the final lattice depth and  $t$  the ramping time. We performed calculations for 50 to 300 ms ramp-up times. These simulations demonstrate that the exponential ramp leads to a lower visibility than the linear profile (Fig. 4.6). The highly non-adiabatic ramp-up time of 75 ms with exponential profile leads even to negative visibilities (Fig. 4.6 (a)). This indicates that the system displays collapse-and-revival physics for these short ramping times. Extending the ramping time to  $t = 200$  ms results in an almost adiabatic linear ramp for  $s \leq 15$  as the calculated visibility corresponds very well to the static (Fig. 4.6 (a)). The visibility of  $^{87}\text{Rb}$  after 200 ms exponential ramp is higher than after 75 ms but still lower than the linear results. For deep lattices with  $s = 22$  the exponential ramp-up profile leads to a higher visibility than the linear ramp. However, this is due to the fact that the exponential ramp-up is still highly non-adiabatic for this ramping time, leading to a large SF-fraction, whereas the linear ramp is closer to being adiabatic.

The observation that the exponential ramp-up profile leads to less adiabatic behavior is explained by the fact that this profile has a low ramp-up velocity for the smaller lattice-depths, where the interaction only plays a minor role, whereas for the higher lattice depths, where many-body effects become important, the ramping velocity is very high. For this reason further investigations were performed exclusively with a linear ramp-up shape.

### Effect of the ramp-up time

Finally we investigate the effect of the ramp-up time on the visibility. Whereas one would expect that a slower ramp automatically enhances the adiabaticity and the visibility, in the simulations we observe that only the dynamic real-space particle distributions become similar to the static ones. The visibility, and therefore the phase coherence, remains different from the ground state one. Especially for intermediate ramping times the behavior

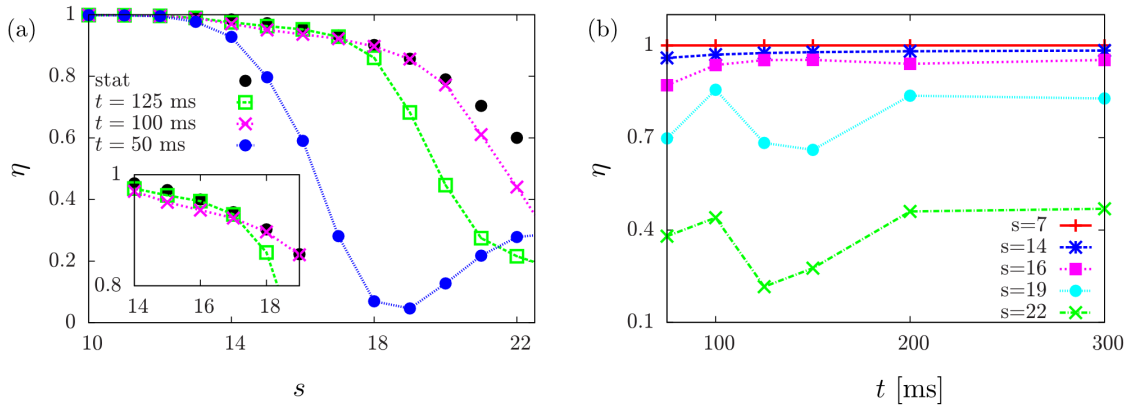


**Figure 4.7:** (a) Calculated visibilities for 125 ms (green squares) 100 ms (pink crosses) and 50 ms (blue dots) ramp times compared to the static visibility (black dots, not connected by line). The inset demonstrates that for  $s < 17$  the visibility after a 125 ms ramp lies closer to the static visibility than after a 100 ms and vice versa for deeper lattices. The increase of the visibility for deep lattices for  $t = 50$  ms is due to the highly non-adiabatic revival of the coherence. (b) Visibility as a function of ramp-up time. For  $s = 7$  (red solid line) all considered ramping times are adiabatic and the visibility is independent of the ramp-up time. For  $s = 14$  (blue asterisks) longer ramp leads to the ground state visibility, indicating 300 ms as the appropriate ramp-up time. For  $s \geq 17$  oscillations are induced, as explained in the text below.

is counterintuitive (Fig. 4.7 (a)). While for lattice depth  $s < 15$  the visibility increases monotonically with the ramp-up time (Fig. 4.7 (a) inset), deeper in the MI-regime this tendency is washed out. This is surprising as the longer ramp is expected to be more adiabatic. Plotting the visibility as a function of ramp-up time for a fixed  $s$  demonstrates that the effect of the ramping time is not the same for all  $s$  (Fig. 4.7 (b)). We distinguish two different regimes. Ramping up to shallow lattices  $s \leq 12$  ( $\hbar/J(s = 12) \approx 5.4$  ms) is adiabatic on all time scales and thus not affected by the ramp duration. In the regime of final lattice depth around the SF-MI transition and in MI-phase, oscillations in the visibility occur.

These oscillations were also observed experimentally [20, 163] but not yet explained. In the next subsection we give an explanation in terms of coupling to the collective modes of the system. Before this we add some remarks on the figures. The oscillating behavior depends on the ramp-up profile (Fig. 4.8 (a)(b)). The exponential shape shifts the oscillations to longer ramp-up times. The presence of  $^{41}\text{K}$  has only a minor effect on the oscillations: the second species only leads to a global shift in the visibility without changing the position of maxima and minima (Fig. 4.8 (c)(d)). This is consistent with the experimental findings [20].

### Explanation of visibility oscillations

We now turn to the explanation of the oscillations in the visibility. A closer look at the simulations shows that the only component contributing to the visibility which oscillates in time at a fixed  $s$  is  $n(\mathbf{k} = (0, 0))$ . The particle density in momentum space is given by

$$n(\mathbf{k} = (0, 0)) = \frac{1}{L^2} \sum_{i=1}^{L^2} \left( \langle \hat{n}_i \rangle - r_i^2 \right) + \frac{1}{L^2} \left| \sum_{i=1}^{L^2} r_i e^{-i\phi_i} \right|^2, \quad (4.10)$$

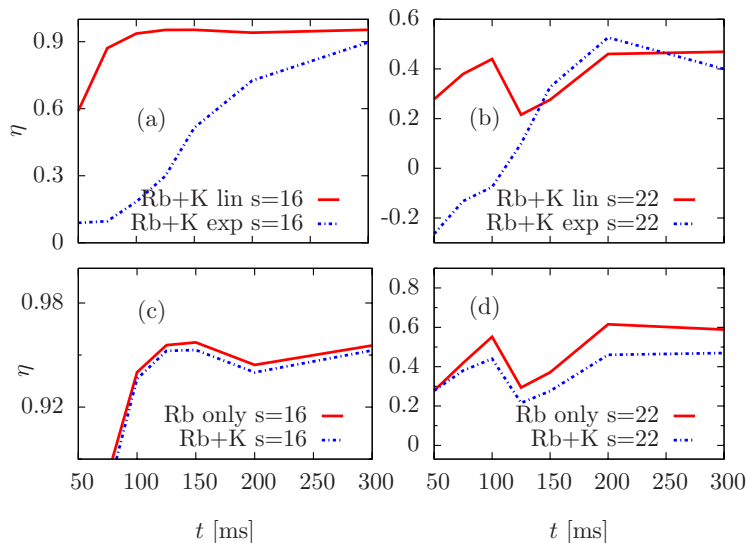


**Figure 4.8:** Effect of the ramping profile on the visibility oscillations (a), (b) and effect of the second species (c), (d). For intermediate lattices, e.g.  $s = 16$ , the exponential ramp-up profile (blue dashed line) damps the oscillations, which are present for the linear profile (red solid line) (a). For  $s = 22$  and exponential ramp (b) a non-adiabatic maximum appears. The presence of a second species (blue dashed line) (c), (d) only induces a global shift of the visibility.

where  $L^2$  is the total number of lattice sites,  $r_i(r_j)$  and  $\phi_i(\phi_j)$  are the absolute value and the phase of the local superfluid order parameter on a site  $i$  ( $j$ ) respectively:  $\langle b_i^\dagger \rangle = r_i e^{-i\phi_i}$ . We can separate the contribution of the absolute value and the phase to the visibility. The absolute value  $r_i$  shows monotonic behavior and is continuously decreasing if the ramp-up time is reduced. This is measured by the Gutzwiller SF-fraction  $f_c = \sum_i |\langle b_i \rangle|^2 / N$ . In Fig. 4.9 (d) the SF-fraction is continuously decreasing and always higher than the equilibrium value. Only for long ramping times ( $t = 300$  ms), the dynamical and static SF-fraction approach each other. This means that for the short ramping times the visibility is dominated by this anomalously large SF-fraction. However, for very fast ramping times the SF-fraction is high, but the phases are uncorrelated, leading to a low visibility. With increasing ramping time the phase coherence builds up and compensates the decay of the SF-fraction leading to an increasingly higher visibility.

For even longer ramping times the visibility decreases again. We explain this by an enhanced coupling to the collective breathing mode of the system induced by the lattice ramp. Increasing the lattice depth results in an increased ratio of the strength of the harmonic trapping potential and the hopping constant  $J$ . This forces the particles to move towards the center of the parabolic trap and leads to a higher occupancy in the middle of the trap. At the same time the particles experience a higher repulsion as  $U(s)$  grows with the lattice depth (see Eq. (4.3)). This repulsion acts against the increasing population and induces a reverse flow. The interplay between these two mechanisms yields the collective modes.

We indeed find numerical evidence for these collective oscillations by observing the cloud size  $R^2 = \langle \mathbf{r}^2 \rangle - \langle \mathbf{r} \rangle^2$  during the waiting time after the ramp. The sinusoidal oscillations of  $R^2$  indicate the collective movement of particles within the breathing mode in Fig. 4.9 (a). The data for other ramp-up times can also be fitted similarly. This leads to the conclusion that only the breathing mode is excited. Depending on the ramping time the amplitude of

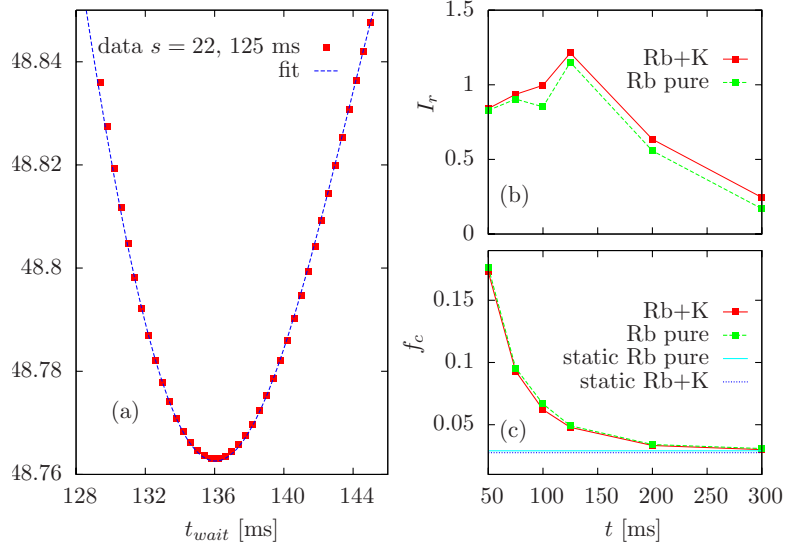


**Figure 4.9:** (a) Oscillations of the radius of the Rb-cloud during the waiting time of 16 ms after a  $t_0 = 125$  ms ramp to  $s = 22$ . The data is fitted by  $f(t) = 0.135 \sin(0.18t + 5.19) \exp^{-0.031(t-t_0)} + 48.857$  (blue line). The sinusoidal form corresponds to the excitation of the breathing mode. (b) The current at  $s = 22$ , averaged over the waiting time and renormalized with respect to SF-fraction, induced after different ramp-up times. The maximum of the renormalized current indicates the regime with the maximal coupling to the collective modes. The second species leads to an enhanced coupling for all ramp-up times. (c) The SF-fraction averaged over the waiting time as a function of ramping time at  $s = 22$ . The “freezing” in the SF-phase is dominant for fast ramps. For longer ramp-up the system approaches the ground state (static) value and the ramp is getting more adiabatic. The  $^{41}\text{K}$  slightly reduces the SF-fraction.

the oscillation changes. In particular, the amplitude is continuously decreasing when the ramping time is made longer. However, this is mainly due to the decreasing SF-fraction, which reduces the number of mobile particles. Renormalizing the amplitude by the SF-fraction leads to a peak at the position of the visibility minimum, which evidences that the coupling to the modes is responsible for this minimum.

Analysis of the total current in the system  $I = \sum_{\langle ij \rangle} |\langle \hat{b}_i^\dagger \hat{b}_j - \hat{b}_j^\dagger \hat{b}_i \rangle|^2$  further clarifies this. The total current is decaying because of the decaying SF-fraction. To investigate the relative motion of the mobile particles we therefore renormalize the total current by  $f_c^2$ :  $I_r = I/Nf_c^2$ . This function again shows a clear maximum at the position of the visibility minimum (see Fig. 4.9 (c)). As the coupling to collective modes destroys the phase coherence, this fully agrees with the minimum in visibility for a 125 ms ramp, see Fig. 4.8 (d).

For  $t > 150$  ms the SF-fraction approximates the static value and the collective modes are less excited. This is the most adiabatic ramping regime.

For the exponential ramp-up profile, the oscillations are shifted (Fig. 4.8 (a)(b)). This is because the SF-fraction remains anomalously high even for long ramping times and the visibility is dominated by this effect. In particular the maximum at  $t_{\text{ramp}} = 200$  ms for  $s = 22$  is explained by the high SF-fraction and is thus a highly non-adiabatic point. The decrease of the visibility at  $t = 300$  ms for  $s = 22$  is explained by an enhanced coupling to collective excitations.



The fact that the presence of a second species leads only to a small shift in the visibility is explained by the observation that the overlap of the atomic clouds is very small and the modes are mainly excited by the increased repulsion between the  $^{87}\text{Rb}$  particles when the optical lattice is ramped up. However, the second species induces additional modes, which lower the visibility. This is seen in the higher renormalized current in Fig. 4.9 (b) for the mixture compared to the single-species system.

The additional induced modes in the system due to the presence of  $^{41}\text{K}$  not only explain the lower visibility, but also offer an explanation for the experimental observation that adding a second species leads to a broadening of the momentum profile beyond a certain lattice depth [20]. The presence of collective modes leads to macroscopic occupation of single particle states with nonzero momentum and hence broadens the momentum distribution. It is worth noting that for this explanation the amount of spatial overlap of the two species is less important: as long as the two clouds touch, they can exert a force on each other. This explains why this effect was already found for widely separated components.

### 4.3 Results for nonzero $T$

In order to understand the effect of finite temperature in the experiments we also perform simulations for this case. We perform simulations for initial temperatures of 19 nK ( $k_B T_2 = 2.2 J_{Rb, s=5}$ ) and 12.6 nK ( $k_B T_1 = 1.5 J_{Rb, s=5}$ ). This is in the range of typical experimental temperatures, which can be estimated as detailed in Appendix D. To investigate the adiabaticity of the ramp at finite temperature we again compare time-dependent ramp-up simulations with static results. The latter correspond to the ensemble in thermal equilibrium at a final lattice depth with effective inverse temperature  $\tilde{\beta} = 1/k_B \tilde{T}$ . The effective temperature is chosen such that the entropy of the static system equals the initial entropy of the ramped system. The static results thus represent an adiabatically ramped and completely thermalized ensemble. Accordingly, the static density matrix is  $\rho = \sum_n \frac{e^{-\tilde{\beta} E_n^i}}{Z_i} |E_n\rangle_i \langle E_n|$ , where  $E_n$ ,  $|E_n\rangle_i$  are the eigenvalues and eigenstates of the Hamiltonian at site  $i$  respectively.

#### 4.3.1 Density profiles

We first investigate the density profiles in real-space at  $k_B T_1 = 1.5 J_{Rb, s=5}$ . Ramping in 50 ms to  $s = 12$  provides a density profile similar to the static thermalized result with effective temperature  $k_B \tilde{T}_1 = 0.95 J_{Rb, s=5}$  (see Fig. 4.10 (a)). The local superfluid order parameter, however, differs from the value in thermal equilibrium (see Fig. 4.10 (c)). In the center of the  $^{87}\text{Rb}$  cloud the local superfluid order parameter is reduced. Hence the system after the ramp does not correspond to an adiabatically ramped and thermalized ensemble. At deeper lattices the dynamic density profiles do not fit the thermal static distribution. Fig. 4.10 (b) demonstrates the squeezing of the dynamic profile for  $s = 16$  compared to the static one with effective temperature  $k_B \tilde{T}_2 = 0.42 J_{Rb, s=5}$ . Similar as in the  $T = 0$  case, the fast 50 ms ramp is non-adiabatic and induces density waves around the plateau (see Fig. 4.10 (b)). The peaked local superfluid order parameter in Fig. 4.10 (d) corresponds to the region where the density waves appear. For  $t = 300$  ms in Fig. 4.10 (b) a plateau is formed at non-integer density in the center of the trap. At the same time the corresponding local superfluid order parameters vanish which indicates a formation of a normal phase instead of a MI-plateau as found previously in the  $T = 0$  case.

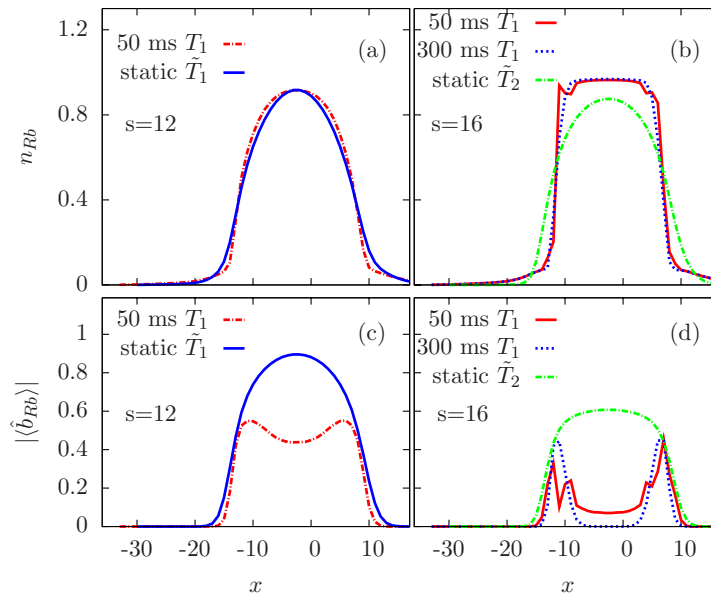


**Figure 4.10:** Finite temperature results for the particle density and superfluid order parameter of  $^{87}\text{Rb}$  at final lattice depth  $s = 12, 16$  along a cut in  $x$ -direction through the center of the trap ( $y = 0$ ). All dynamic profiles are calculated for the initial temperature  $k_B T_1 = 1.5 J_{Rb, s=5}$ . (a) For a 50 ms ramp (red dashed line) the results correspond well to the static thermalized ensemble (blue solid line) with effective temperature  $k_B \tilde{T}_1 = 0.95 J_{Rb, s=5}$ . However, the local superfluid order parameter is reduced in the center of the atomic cloud (c). (b) After the ramp to  $s = 16$  the dynamic profiles differ from the static ones with corresponding effective temperature  $k_B \tilde{T}_2 = 0.42 J_{Rb, s=5}$ . A density plateau is formed in the center of the trap at a non-integer density. For 50 ms ramp (red solid line) density waves appear around this plateau. (d) The superfluid order parameter (red solid line) is peaked in the region where the density waves appear. Parameters:  $L = 60$ ,  $N_{Rb} = 303$ ,  $N_K = 30$ ,  $U_{Rb-K} = 1.93 U_{Rb}$ , Parameters for (a) and (c):  $J_{Rb} = 0.24 U_{Rb}$ , Parameters for (b) and (d):  $J_{Rb} = 0.02 U_{Rb}$ .

### 4.3.2 Visibility and oscillations

As shown in the previous subsection, with increasing temperature and lattice depth the condensate depletes. This also lowers the visibility. In Fig. 4.11 this behavior is exemplified for a 300 ms ramp. For low temperature  $k_B T_1 = 1.5 J_{Rb, s=5}$  and shallow lattices  $s \leq 12$  the visibility is hardly changed compared to  $T = 0$ . With increasing lattice depth, however, the superfluid order parameter vanishes in the trap center, leading to a decreased visibility. For higher temperature ( $k_B T_2 = 2.2 J_{Rb, s=5}$ ) the fraction of the atoms in the normal phase increases, thus lowering the visibility further.

The visibility oscillations are affected as well. When temperature and final lattice depth are sufficiently small, the only effect of the temperature is to reduce the visibility (Fig. 4.12 (a)  $k_B T_1 = 1.5 J_{Rb, s=5}$ ). Although the absolute value of the local superfluid parameter is reduced in the center of the trap for slow lattice ramp compared to fast ramp (Fig. 4.10 (d)), the phase coherence in the latter case is almost completely destroyed. This leads to a higher visibility for a 300 ms ramp than for a 50 ms. For  $k_B T_2 = 2.2 J_{Rb, s=5}$  the visibility oscillations are suppressed and the minimum at  $t = 200$  ms disappears. We can understand the disappearance of the minimum in the visibility in a qualitative way by comparing the excitation energy of the breathing mode with the temperature. We indeed find that the

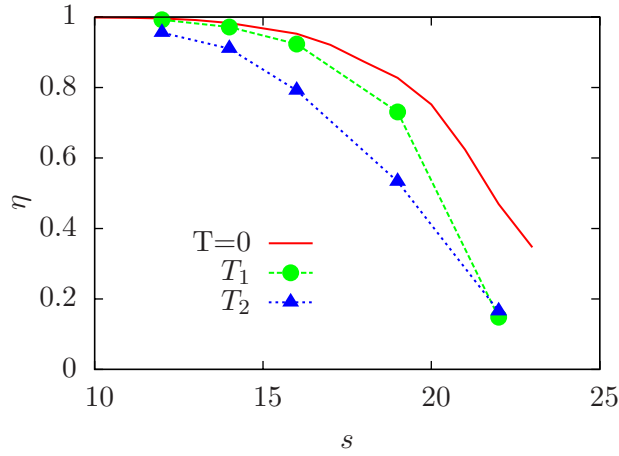


**Figure 4.11:** Visibility after 300 ms ramp-up for  $k_B T_1 = 1.5 J_{Rb, s=5}$  (green dots) and  $k_B T_2 = 2.2 J_{Rb, s=5}$  (blue triangles) compared with  $T = 0$  (red solid line). The visibility decreases with increasing temperature.

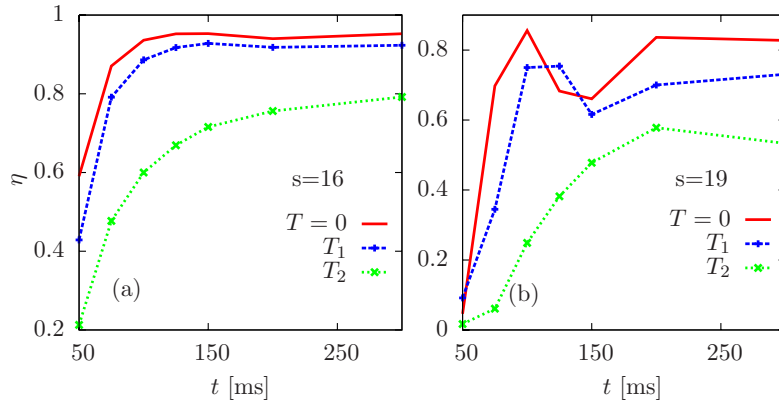


**Figure 4.12:** Visibility as a function of ramp-up time for different temperatures and final lattice depths. (a) At shallow lattices for  $T = 0$  (red solid line) oscillations appear with a visibility minimum at  $t = 200$  ms. For  $k_B T_1 = 1.5 J_{Rb, s=5}$  (blue dashed line) the global visibility and the oscillation amplitude is reduced. Higher temperature ( $k_B T_2 = 2.2 J_{Rb, s=5}$ , green dotted line) blurs the oscillations. (b) For  $s = 19$  the shape of the oscillations at  $T = 0$  is mainly conserved for  $k_B T_1 = 1.5 J_{Rb, s=5}$ . The graph is shifted to lower visibility and longer ramp-up times. At  $k_B T_2 = 2.2 J_{Rb, s=5}$  only one maximum at  $t = 200$  ms is present.

temperature here is higher than the excitation energy, meaning that the mode is already thermally occupied and that the ramp of the lattice has less effect.

## 4.4 Discussion and conclusion

Using a time-dependent Gutzwiller model for an interacting Bose-Bose mixture we investigated the ramp-up of the optical lattice for zero and finite temperatures.

The non-adiabaticity of the lattice ramp was analyzed by comparing density profiles in real and momentum space and by studying the visibility. The adiabatic regime is reached when the density profiles as well as visibility agree with the equilibrium results. We observed

that in the regime of deep optical lattices the ramp-up dynamics generally does not lead to the ground state of the system.

We have shown that a ramp-up of the optical lattice carried out on a time scale comparable to the tunneling time does not necessarily provide the ground state of the system. Depending on the ramp-up time, ramping the lattice at  $T = 0$  leads to trapping of the particles in a "frozen" phase with non-integer particle number and nonzero local superfluid order parameter but vanishing global phase coherence. The exponential ramping profile was found to be even less adiabatic than a linear increase of the depth of the optical lattice. Ramping the lattice at finite temperature additionally causes a depletion of the condensate. The latter grows with increasing temperature. Both ramp effects lead to decreased visibility.

The ground state visibility was only reached for shallow lattices within the investigated ramping times. The fact that one needs rather long times to be completely adiabatic for deep lattices, is rooted in the critical slowing down of the hopping at the SF-MI-phase boundary at  $T = 0$  or the SF-normal-phase at finite temperature. At the same time we found that a longer ramp-up time does not naturally lead to a better visibility. In fact, depending on the final lattice depth oscillations may occur for  $T = 0$  and low temperatures, which also have been observed in experiments with a single bosonic species [163] and a two-component bosonic mixture [20]. The fact that we reproduce these oscillations within the mean-field dynamics, where heating due to three-body collisions is not included, indicates that they are part of the real many-body dynamics.

We explain these oscillations by a coupling of the ramp-up process to the collective excitations of the systems, in particular the breathing mode. This is consistent with the appearance of density waves in the system. Lowered superfluidity and a larger normal phase prevents collective excitations at higher temperatures.

One of our main results is that the maximum in the visibility is not a good indication of adiabaticity, although sometimes used as an experimental criterion. This regime is in fact highly non-adiabatic, since the maximum is caused by an anomalously large SF-fraction induced by the short ramping time. The region where the visibility saturates is the most adiabatic. However in our approach three-body collisions and heating is not included. These processes become relevant at long time scales and also lead to non-adiabaticity.

In experiments, the presence of a second species destroys the phase coherence of the majority species, leading to a decreased visibility. In contrast, previous static calculations predict either enhanced or decreased long range order, depending on the actual particle ratio [27]. Here we observed that for  $T = 0$  the dynamical ramp induces additional non-equilibrium and leads to a more pronounced visibility decay in the region where static calculation also predicts lowering. We explained this in terms of an enhanced current in the system. This stronger visibility reduction could be the reason for the experimental findings.

## 5. Expansion of bosonic condensates in optical lattices

The unprecedented control and tunability of parameters in ultracold atomic systems enables experimental insight into static as well as dynamical properties of the Hubbard model. After developing a basic understanding of the equilibrium features such as quantum phases and transitions [9, 10, 12, 109–111] the new field of non-equilibrium dynamics has started gaining attention.

Despite the multitude of novel physical phenomena such as center-of-mass dynamics of atomic clouds consisting of fermions or bosons [164–166] and the role of interaction in fermionic mass transport [167], the studies of non-equilibrium revealed new aspects like bosonic collapse and revival effect. The latter shows effects of virtual transitions to higher bands induced by interaction. The admixture of Wannier states of other bands modifies the shape of the ground-state wave function. This change in turn makes the Hubbard repulsion  $U$  filling dependent [92, 97]. Thus, the experimental and theoretical efforts revealed hand in hand the importance of non-equilibrium physics for understanding the fundamentals of many-body concepts [32, 99, 168].

More recently, it has been discovered that an initially confined MI cloud, which has finite short-range correlations only, develops long-range coherence when the atoms are allowed to expand in an optical lattice after the switch-off of the trap. Initially studied in 1D hard-core systems ( $U \rightarrow \infty$ ) [33, 34] the same effect was observed in higher dimensions for non-homogeneous tunneling [35]. In this thesis we address the homogeneous expansion of a bosonic quantum gas originally prepared in the Mott insulating ground state and surrounded by a SF ring in an optical 2D lattice. Once released from the harmonic confinement, the interacting many-body system is observed to develop coherence while simultaneously populating finite quasi-momentum states. We demonstrate that in the strong and intermediate coupling regimes the emerging condensate fraction depends on the number of particles in the MI phase rather than on the particular interaction or tunneling strength. While expanding, the condensate that is formed was observed to develop a spiked structure breaking the initial spherical symmetry, where the expanding spikes exhibit the maximal lattice velocity independent of system parameter. The dynamical properties of this system are obtained by means of Gutzwiller theory and confirmed by an analytic analysis for large expansion times.

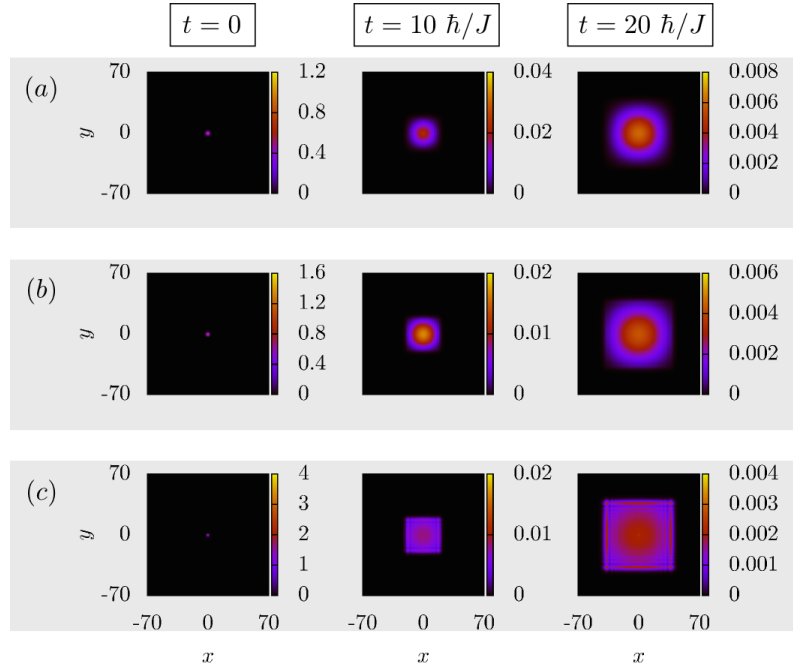


**Figure 5.1:** Density distribution of a non-interacting expanding cloud. Three clouds confined in a parabolic potential at  $t = 0$  of the strength  $V^{\text{trap}} = 0.05 \cdot 10^3 \hbar/s$  are expanding in the homogeneous lattice with different tunneling strength (a)  $J/V^{\text{trap}} = 10.1$  (b)  $J/V^{\text{trap}} = 5$  (c)  $J/V^{\text{trap}} = 1.27$ . The colormap shows snapshots of the time evolution at  $t = 10 \hbar/J$  and  $20 \hbar/J$ . Depending on the tunneling strength  $J$  the final symmetry of the cloud can be spheric or quadratic.

## 5.1 Expansion of non-interacting bosons

### 5.1.1 Real-space profiles

We start our investigations of the cloud expansion with the simplest case of non-interacting particles described by the Bose-Hubbard Hamiltonian

$$\hat{\mathcal{H}} = \sum_{\langle ij \rangle} J(\hat{b}_i^\dagger \hat{b}_j + h.c.) - \sum_i (\mu - V_i^{\text{trap}}) \hat{n}_i,$$

with  $J$  being the tunneling strength,  $\mu$  the chemical potential and the parabolic trapping potential  $V^{\text{trap}} = \frac{1}{2} m \omega^2 d^2 |\mathbf{r}_i - \mathbf{r}|^2$ , where  $d$  is the lattice constant,  $\omega$  the trap frequency and  $\mathbf{r}_i$  are the coordinates of the given lattice site  $i$ . After the switch-off of the trapping, the particles are allowed to expand freely in a homogeneous 2D optical lattice and the Hamiltonian reads (for derivation of the quasi-momentum representation see Sec. 3.1.1)

$$(t > 0) \quad \hat{\mathcal{H}} = \sum_{\langle ij \rangle} J(\hat{b}_i^\dagger \hat{b}_j + h.c.) - \mu \sum_i \hat{n}_i = \sum_{\mathbf{k}} (\varepsilon(\mathbf{k}) - \mu) \hat{n}_{\mathbf{k}} \quad (5.1)$$

with  $\varepsilon(\mathbf{k}) = -2J[\cos(k_x a) + \cos(k_y a)]$  being the non-interacting dispersion relation. In this case  $[\hat{\mathcal{H}}, \hat{n}_{\mathbf{k}}] = 0$  and the momentum space and velocity distributions are conserved during the time evolution. Each initially confined particle expands with constant velocity, the expansion is ballistic and is equivalent to a continuous quantum walk [169, 170].

At the beginning of the expansion the density distribution reflects the spherical symmetry of the trapping potential and changes its shape for long expansion time, see Fig. 5.1. In

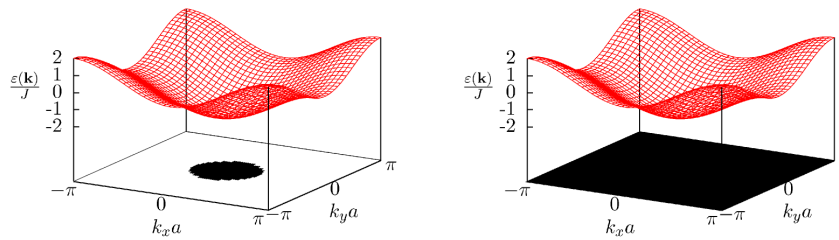


**Figure 5.2:** Occupation of momentum states depending on the initial particle localization. For sufficiently delocalized particles, i.e. large tunneling strength  $J$ , the occupied momenta are located spherically symmetric around  $\mathbf{k} = (0, 0)$  (left). A high localization of particle wave functions for a small tunneling matrix element  $J$  corresponds to a delocalization in momentum space and a population of all states within the 1. BZ (right).

systems with larger tunneling, see Fig. 5.1 (a), the cloud remains spherically symmetric, for small  $J$ , however, the shape of the cloud develops square-shaped  $C_4$  symmetry Fig. 5.1 (c). An understanding of this behavior can be gained from the following consideration. The smaller the tunneling matrix element, the stronger is the confinement of each single-particle wave function within the lattice. The corresponding momentum space distribution continuously fills the first Brillouin zone (1. BZ), which is quadratic in case of a square lattice, see Fig. 5.2. When momenta  $(k_x a, k_y a) \approx (0, 0)$  are occupied, which is the case for large  $J$ , the Taylor series of the dispersion relation can be truncated after the expansion up to second order

$$\varepsilon(\mathbf{k}) = -2J [\cos(k_x a) + \cos(k_y a)] \approx -4J + J((k_x a)^2 + (k_y a)^2).$$

Taking the Taylor expanded dispersion into account the non-interacting velocity profile is

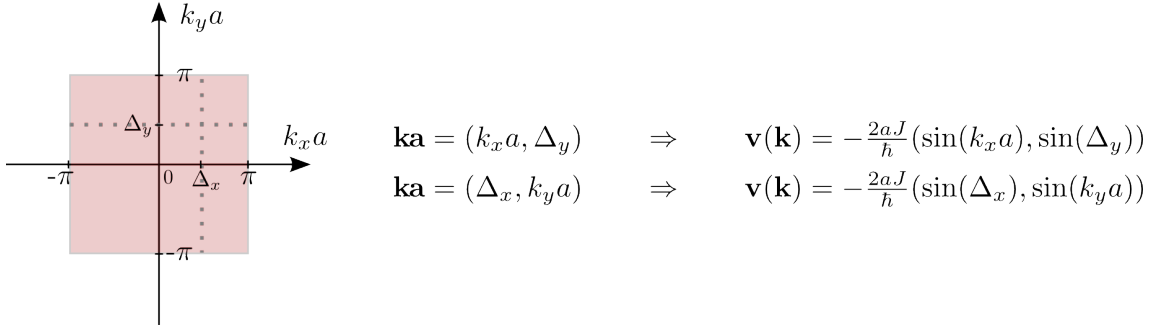
$$\begin{aligned} \mathbf{v}(\mathbf{k}) &= \frac{1}{\hbar} \partial_{\mathbf{k}} \varepsilon(\mathbf{k}) \approx \frac{2Ja^2}{\hbar} (k_x, k_y) \\ |\mathbf{v}(\mathbf{k})| &\approx \frac{2Ja^2}{\hbar} \sqrt{k_x^2 + k_y^2} \quad \text{for } \mathbf{k} \approx (0, 0). \end{aligned}$$

That is, all velocity vectors point in the radial direction and all appearing absolute values fill a spherical symmetric surface. Since for long expansion times the density distribution approximates the velocity distribution, the cloud remains round for systems with sufficiently large tunneling  $J$ , see Fig. 5.1 top row.

A cloud of initially completely (or sufficiently) localized particles corresponds to a fully occupied first Brillouin zone. In this case the exact dispersion leads to

$$\mathbf{v}(\mathbf{k}) = \frac{1}{\hbar} \partial_{\mathbf{k}} \varepsilon(\mathbf{k}) = -\frac{2aJ}{\hbar} (\sin(k_x a), \sin(k_y a)). \quad (5.2)$$

However, for all momentum states parallel to any side of the square Brillouin zone, i.e. for a fixed  $k_x$  or  $k_y$  component, the corresponding velocities have the same absolute values in  $x$  or  $y$  directions. For fixed  $k_x a \equiv \Delta_x$  and arbitrary  $k_y a$  (or vice versa arbitrary  $k_x a$  and fixed  $k_y a \equiv \Delta_y$ ) the velocity profiles are



Particles possessing identical velocity components in one direction build a straight front. Thus, for sufficiently small tunneling matrix element  $J$  the cloud approaches the square shape during the expansion, see Fig. 5.1 bottom row. For other lattice structures the symmetry of the corresponding Brillouin zone will control the density distribution of the cloud.

### 5.1.2 Expansion velocities

A comparison of the expansion dynamics of different clouds is performed using the cloud radius  $R$ , which is defined as

$$R^2 = \frac{1}{N} \sum_i^{L \cdot L} n_i r_i^2 \quad (5.3)$$

where  $N$  is the total particle number,  $n_i$  denotes the particle density and  $r_i$  the coordinate of site  $i$  in a  $L \times L$  2D lattice.

In Fig. 5.3 the cloud radius for each density profile presented in Fig. 5.1 is shown. For better comparability a renormalization with respect to the initial cloud extent  $R_0$  was performed. The results show that in systems with larger  $J$  the cloud radius increases slower in time. It may appear counterintuitive at the first glance, since the tunneling time scales proportional to the inverse tunneling strength, i.e. with decreasing  $J$  more milliseconds are needed for a particle to move. However, since we compare dynamics on the time scale of tunneling process, we rather investigate the distance covered within a given amount of hoppings. From our results it follows, that within a fixed number of tunneling steps stronger initial localization augments expansion. This can be understood in analogy to a potential gradient being the driving force of dynamics, i.e. a homogeneous density distribution resulting from a flat potential and localization of particle wave function from a potential gradient: in the same way as the steepness of the potential gradient influences the force, stronger localization enhances the expansion dynamics.

It is interesting to note that the single particle width of a particle localized at one lattice site increases linearly in time<sup>1</sup>, i.e.  $R_{\text{sp}} = v_{\text{exp}} t$ . This is a consequence of a coherent superposition of states corresponding to a particle being in one of the neighboring sites [170]. The total density distribution of the cloud results from a convolution of the initial density distribution with the delocalized probability distribution of the individual atoms

<sup>1</sup>In classical physics a particle jumps randomly to one of the neighboring sites, the particle density width obeys a binomial (for discrete number of steps) or normal (for continuous time) distribution and correspondingly  $R_{\text{sp}} \sim \sqrt{t}$ .



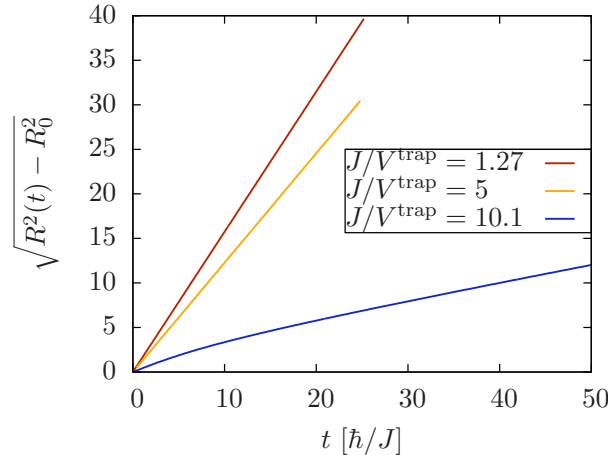


**Figure 5.3:** Renormalized radii of non-interacting clouds expanding with different tunneling strength  $J$ . Initially stronger localized particles (smaller  $J$ ) expand further than more delocalized particles (larger  $J$ ) within the same number of tunneling processes.

and  $R_{\text{sp}}$  [171]. This leads to the cloud radius  $R(t) = \sqrt{R_0^2 + v_{\text{exp}}^2 t^2}$ . From here the expansion velocity is

$$v_{\text{exp}} t = \sqrt{R^2(t) - R_0^2}. \quad (5.4)$$

Although in our system the particles are not localized at single sites initially, plotting the calculated  $R(t)$  as in Fig. 5.3 results in a straight line and the expansion velocity can be extracted from the slope. The functional dependence of expansion velocities on the tunneling strength  $J$  is shown in Fig. 5.4 (left). In agreement with previous discussions, the expansion velocities decrease with increasing  $J$ . Additionally, the effect of the initial trapping strength is shown. Steeper confinement leads to further localization of particle wave functions, thus with increasing potential  $V^{\text{trap}}$  the expansion velocities are shifted to higher values. Due to the equivalence of localizing a particle by augmenting the trapping frequency or by decreasing the tunneling strength<sup>2</sup>, plotting velocities as a functions of  $J/V^{\text{trap}}$  shows a universal dependency, see Fig. 5.4 (right).

For a non-interacting particle the expansion velocity corresponds to the expectation value of the velocity distribution given in Eq. (5.2)

$$v_{\text{exp}}^2 = \langle \mathbf{v}^2(\mathbf{k}) \rangle = \sum_i \langle v_i^2(k_i) \rangle = \frac{1}{\hbar^2} \sum_i \langle (\partial_{k_i} \varepsilon(k_i))^2 \rangle, \quad (5.5)$$

where the decomposition into a sum over components  $i = x, y, z$  (depending on the dimensionality of the system) is based on the dimensional separability of a homogeneous system. In the limit of a particle localized at one lattice site the corresponding Wannier wave function is a delta function in real space. The corresponding momentum distribution is a constant in  $k$ -space. Thus, the velocity expectation value yields an average over the first Brillouin zone

$$\langle v_i^2(k_i) \rangle = \frac{a}{2\pi} \int_{-\pi/a}^{\pi/a} dk_i \left( \frac{2aJ}{\hbar} \right)^2 \sin^2(k_i a) = 2 \left( \frac{aJ}{\hbar} \right)^2.$$

<sup>2</sup>This is of course true from a physical point of view, however, when the confining potential leads to significant potential differences on the neighboring sites the tunneling  $J$  becomes site dependent.

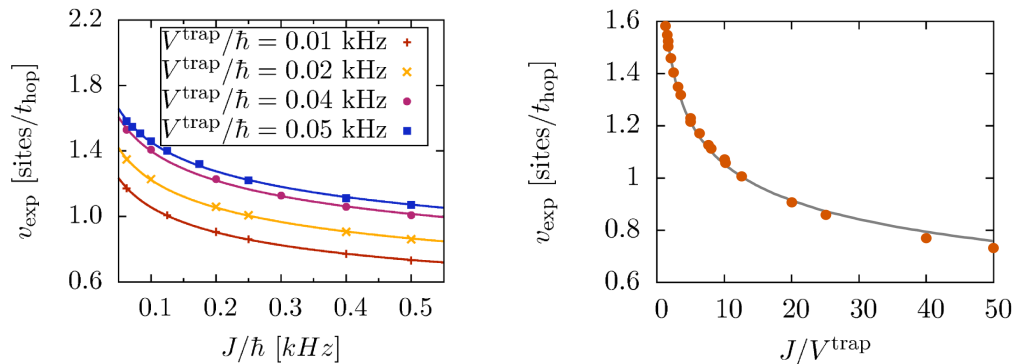


**Figure 5.4:** Expansion velocities corresponding to the slopes of renormalized radii as defined in Eq. (5.4). (left) Decreasing localization due to increasing  $J$  leads to a reduction of expansion velocities. An additional shift towards smaller velocities is provided when the localization of the cloud controlled by the initial trapping potential is reduced, i.e. when the strength of the confinement is diminished. The data was fitted with  $v_{\text{fit}}(J/\hbar) = \alpha(J/\hbar)^\beta$ , see text. (right) Since the localization of a wave function by decreasing the tunneling  $J$  is equivalent to the localization triggered by the strength of the confining potential, the velocities plotted in left figure show a universal dependence when plotted against  $J/V^{\text{trap}}$ . The line is a guide to the eye.

Inserting this result in Eq. (5.5) leads to the expansion velocity of an initially localized particle in a homogeneous  $D$ -dimensional system

$$v_{\text{exp}} = \sqrt{\sum_i \langle v_i^2(k_i) \rangle} = \sqrt{2D} \left( \frac{aJ}{\hbar} \right). \quad (5.6)$$

However, when an additional confinement is present and the particles are delocalized the momentum distribution depends on  $J$  and  $V^{\text{trap}}$ . The exact calculation of  $n(\mathbf{k})$  requires band structure calculations, see Sec. 3.1.1. Nevertheless, fitting data with a function resulting from Eq. (5.6) varying the dependence on  $J$  and the prefactor

$$v_{\text{fit}} = \alpha \left( \frac{J}{\hbar} \right)^\beta$$

leads to excellent agreement with the simulated results, see Fig. 5.4 (left).

We continue with the case of interacting atoms and the expansion including diffusive scattering effects due to Hubbard repulsion.

## 5.2 Melting of the Mott insulating cloud

### 5.2.1 Setup

Similarly to the non-interacting case, we consider a setup in which a bosonic cloud loaded into a 2D optical lattice is confined by an additional harmonic potential. Such a system is described by the Bose-Hubbard Hamilton discussed in Sec. 3.1:

$$\mathcal{H} = -J \sum_{\langle ij \rangle} (\hat{b}_i^\dagger \hat{b}_j + h.c.) - \sum_i (\mu - V_i^{\text{trap}}) \hat{n}_i + \frac{U}{2} \sum_i \hat{n}_i (\hat{n}_i - 1), \quad (5.7)$$

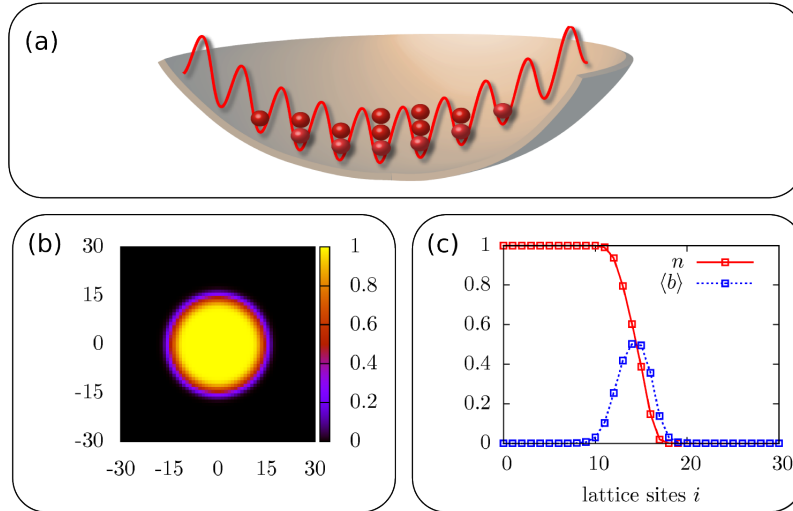


**Figure 5.5:** The initial setup. (a) An illustration of particles loaded into an optical lattice and additionally confined by a parabolic trapping potential. (b) Colormap of the initial particle density shows a MI-core surrounded by a SF ring. (c) Particle density and SF order parameter profiles in radial direction from the center. MI core is indicated by  $n = 1$  and  $\langle b \rangle = 0$ . The area with  $\langle b \rangle \neq 0$  denotes the extent of the SF ring. In (b) and (c) the parameters are  $U/\hbar = 30$  kHz,  $V^{\text{trap}}/\hbar = 0.01$  kHz,  $J/\hbar = 0.17$  kHz and total particle number  $N = 660$ , whereas the number of particle in the MI phase is  $N_{MI} = 97$ .

where the operator  $\hat{b}_i^\dagger(\hat{b}_i)$  creates (annihilates) a boson,  $\mu$  is the chemical potential,  $U$  and  $J$  indicate the Coulomb repulsion and the hopping amplitude. The localization of the atomic cloud is provided by a parabolic trap  $V_i^{\text{trap}}$  defined as in the case of non-interacting particles. The chemical potential and the trapping strength are adjusted to achieve the desired particle number in the cloud and especially that within the MI phase. To solve this problem numerically we use the Gutzwiller approximation of the model, see Eq. (3.123).

Although we model the expansion of the entire cloud, we are particularly interested in the expansion of particles that originate in the MI phase. Since the superposition of a trapping potential and chemical potential leads to a non-homogeneous effective chemical potential landscape,  $\mu_{\text{eff},i} = \mu - V_i^{\text{trap}}$ , the resulting particle density profile is no longer homogeneous but rather possesses a “wedding cake” structure, see Fig. 3.7. Thus, despite the trivial case  $J/U = 0$ , the MI plateaus are surrounded by SF shells. The effective chemical potential in the center of the cloud and the  $J/U$  ratio determine the extent of each domain, given a trapping frequency  $\omega$ . Thus, the desired total particle number corresponding to a specified number of particles in the MI phase is achieved by adjusting the global chemical potential  $\mu$  and the trapping strength  $\omega$  respectively. The systems investigated in this section consist of a single MI plateau surrounded by a SF ring. In order to study the effect of the SF on the expansion dynamics of the inner MI core, the total number of particle was kept constant at  $N = 660$  in all parameter sets while the number of particles in the insulator  $N_{MI}$  was varied.

It is worth mentioning that the identification of the quantum phases, which is essential for the particle counting, is limited in the numerical simulation. The definition of a SF or MI phase by means of an integer or non-integer particle density as well as vanishing SF-parameter are fulfilled only within a certain tolerance from the numerical point of view. Hence, in this thesis a SF order parameter  $\langle \hat{b} \rangle \geq 1 \cdot 10^{-5}$  is assumed to define the SF phase.

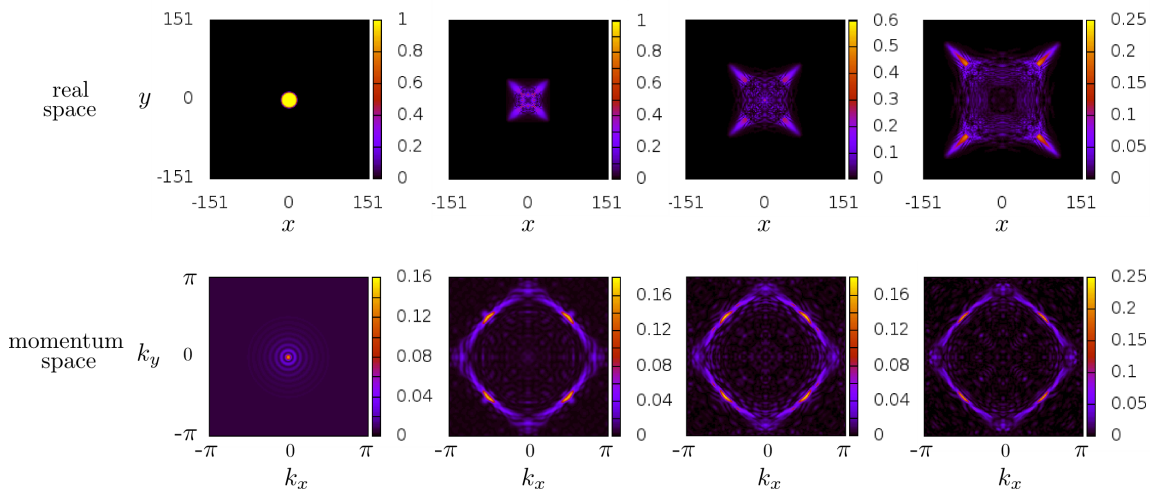


**Figure 5.6:** Expansion of the cloud: density distribution in the real space (top row) and momentum distribution (bottom row) of the system at  $U/J = 459.77$  and  $t = 0, 15, 30$  and  $50 \hbar/J$  (from left to right) initially trapped in a periodic potential of strength  $V/J = 0.11$  and containing a Mott insulating particle fraction  $N_{MI}/N = 225/660$ . The expansion of the cloud takes place mostly along the diagonals and the corresponding momentum distribution function has a rhombic symmetry.

It is important to note that the mean-field treatment of the nearest-neighbor coupling excludes any dynamics in a purely MI system since vanishing SF-parameters lead to a vanishing kinetic term:

$$\eta_i = \sum_{j \text{ n.n. } i} \langle \hat{b}_i \rangle = 0 \quad \text{if} \quad \langle \hat{b}_i \rangle = 0 \quad \forall i$$

and

$$\mathcal{H}_{MF,kin} = -J \sum_i (\hat{b}_i^\dagger \eta_i + h.c.) = 0,$$

in contrast to the kinetic part in the exact Bose-Hubbard model Eq. (5.7). Thus, the SF ring surrounding the MI plateau is not only of interest due to its effect on the inner insulating core but is a required “seed” for expansion dynamics. Due to this “artificial” generation of initial dynamics, simulations via the Gutzwiller method are not a priori justified for this parameter regime. Hence, the justification of the application of the mean-field approximation via investigation of the SF-ring effects on the expansion process is one of the goals of this study.

## 5.2.2 Creation of exotic condensates

### Real- and momentum-space results

The system is initially prepared in the Gutzwiller ground-state in the optical lattice with an additional parabolic trapping. The expansion of the atomic cloud is triggered by switching off the parabolic trapping potential at time  $t = 0$ . In Fig. 5.6 the time evolution of a cloud at  $U/J = 459.77$  and Mott insulating fraction  $N_{MI}/N = 225/660$  is shown. The initial rotationally symmetric cloud consisting of a MI core in the center surrounded by a small SF ring starts expanding once the trapping potential is switched off. For  $t > 0$  the expansion of the outer SF particles leads to the expansion of the inner insulating core, i.e. the

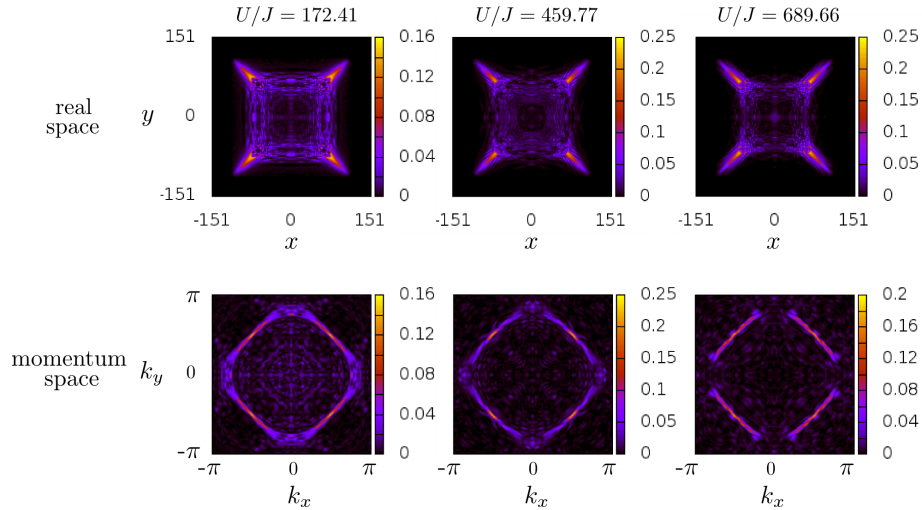


**Figure 5.7:** Expansion profiles at  $t = 50 \hbar/J$  for different  $U/J$  ratios in real space (top row) and momentum space (bottom row). All samples contained in total  $N = 660$  particles and different  $N_{MI}$ , i.e.  $N_{MI} = 97, 225$  and  $325$  (from left to right). The expansion on spikes in diagonal directions as well as the occupation of momenta on the rhombus becomes more pronounced with increasing  $U/J$ .

Mott insulator “melts”. It is interesting to note that the initial rotational symmetry of the system is broken and a new  $C_4$  symmetry is established: we observe a structure that exhibits pronounced population along the diagonals of the lattice, which we then term “spikes” or a “spiked” structure.

The bottom row in Fig. 5.6 shows the occupation in momentum space corresponding to the density profiles depicted in the top row of the same figure. At  $t = 0$  the peak at  $\mathbf{k} = (0, 0)$  indicates the presence of long-range coherence due to the SF ring. In contrast, the MI phase results in a constant occupation of all momentum states within the first BZ. Unexpectedly, for  $t > 0$ , the melting of the MI core leads to a redistribution of  $n(\mathbf{k})$ : The central peak disappears and the occupation is reallocated to the edges of a rhombus. The additional structure within the rhombus decreases during the expansion, but persists even to very large time scales.

A comparison between the density and momentum distributions of systems with different values of  $U/J$  at expansion time  $50 \hbar/J$  is given in Fig. 5.7. With increasing  $U/J$  the spiked structure becomes more pronounced. It is interesting to note that whereas the spikes reach the same distance from the cloud center at  $t = 50 \hbar/J$  the remaining square shaped part spreads more slowly as the system approaches the hard core regime  $U/J \rightarrow \infty$ .

An understanding of the expansion behavior can be gained analytically from consideration of a limiting case. For large expansion times the density of the cloud reaches the limit where  $n(\mathbf{r}) \ll 1$ . Assuming the hard-core interaction regime, the Fock states  $n \geq 2$  are almost unoccupied and the potential term in the Hamiltonian becomes negligible since it scales  $\sim n_i^2$ . Thus, the dynamics is dominated by the kinetic term only and we can consider our system for  $t \gg 0$  to a good approximation as non-interacting. From here, in the limit of large expansion times, the energy of the system is

$$E_{\text{fin}} = \sum_{\mathbf{k}} \varepsilon(\mathbf{k}) n_{\mathbf{k}} \quad (5.8)$$

where  $\varepsilon(\mathbf{k}) = -2J [\cos(k_x a) + \cos(k_y a)]$  is the dispersion relation and  $n_{\mathbf{k}}$  the momentum distribution function. The initial energy of the system is estimated by a similar argument. As the interaction energy vanishes for a SF in the hard-core limit and for a MI with filling  $n = 1$ , and because the kinetic energy within the MI phase is zero due to  $\langle \hat{b}_i \rangle = 0$ , after the trap has been switched off, the energy of the system must consist of only the kinetic energy of the SF. We simplify our system further assuming that the initial SF-ring is negligibly small, such that

$$E_{\text{init}} = \langle -J \sum_i (\hat{b}_i^\dagger \eta_i + h.c.) \rangle \approx 0, \quad (5.9)$$

with  $\eta_i = \sum_{j \text{ n.n. } i} \langle \hat{b}_j \rangle$ . Since in a non-interacting system no energy transfer can take place, the final energy of each single particle has to vanish to guarantee energy conservation, i.e.  $E_{\text{fin}} = E_{\text{init}}$ . Under the above assumptions, the occupied momenta must satisfy the relation

$$\varepsilon(\mathbf{k}) = -2J(\cos(k_x a) + \cos(k_y a)) = 0. \quad (5.10)$$

The solutions of this equation are given by momenta  $\mathbf{k} = (k_x, k_y)$  which obey the relations

$$k_y = \frac{\pi}{a} \pm k_x \quad (5.11)$$

$$k_y = -\frac{\pi}{a} \pm k_x \quad (5.12)$$

and describe a rhombus within the first BZ, see Fig. 5.8. This prediction is in very good agreement with the outcome of our simulations: the occupation of momenta for all simulated parameter regimes, in particular of those in Fig. 5.7, occurs along this square structure. The deviations from the analytic results may be rooted in the approximations within the derivation, namely, the neglect of the SF-ring contribution in the initial kinetic energy and the dropping of the interaction effects. As clearly seen in Fig. 5.7 the momentum distribution approaches the rhombus predicted by Eq. (5.11)-(5.12) for increasing  $U/J$  and decreasing number of SF particles. We proceed with the discussion of effects caused by the presence of a SF in Sec. (5.2.3).

The analytic derivations give additional insights into the real-space density profiles shown in Fig. 5.6 and 5.7. The density spreading is determined by the velocity distribution in the system. For  $t \gg 0$  and assuming the system is in a non-interacting regime to a good approximation, the group velocities are given by

$$\mathbf{v}(\mathbf{k}) = \frac{1}{\hbar} \partial_{\mathbf{k}} \varepsilon(\mathbf{k}) = \frac{2aJ}{\hbar} (\sin(k_x a) \mathbf{x} + \sin(k_y a) \mathbf{y}), \quad (5.13)$$

where  $\mathbf{x}$  and  $\mathbf{y}$  denote the unit basis vectors in the real space. The occupation of momenta indicated in Eq. (5.11)-(5.12) leads to a velocity distribution pointing in diagonal directions, see Fig. 5.8

$$\mathbf{v} = 2a \frac{J}{\hbar} \sin(k_x a) (\pm 1, 1) \quad (5.14)$$

$$\mathbf{v} = 2a \frac{J}{\hbar} \sin(k_x a) (\pm 1, -1). \quad (5.15)$$

The preferred expansion along the diagonals of the lattice is clearly visible in our results in Fig. 5.6 and 5.7 which indicates the high occupation of momentum states corresponding to  $\varepsilon(\mathbf{k}) = 0$ . It is interesting to note that the momenta  $(\pm\pi; 0)$  and  $(0; \pm\pi)$  in the corners of the rhombus are hardly populated in our system. These momenta correspond to  $|\mathbf{v}(\mathbf{k})| \approx 0$

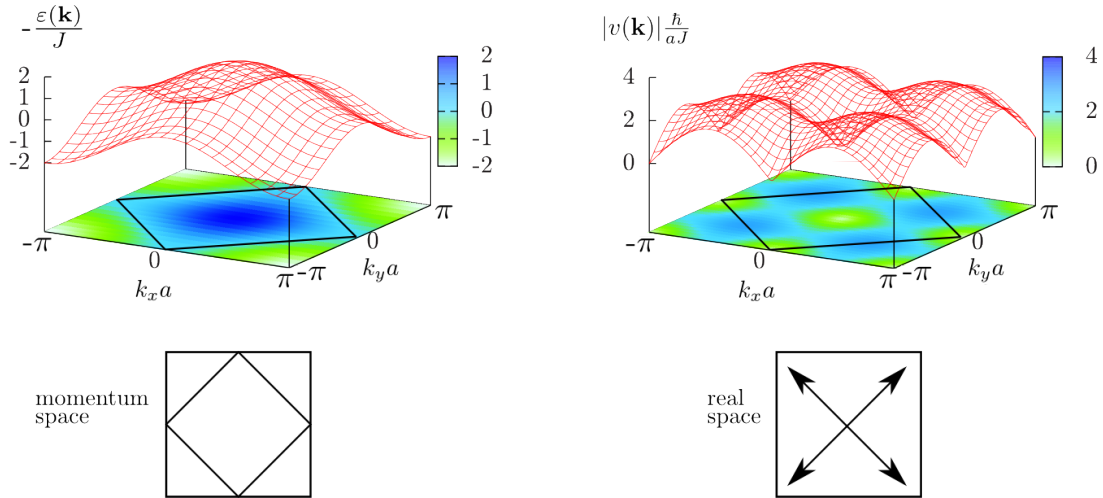


**Figure 5.8:** Square momentum density distribution and the corresponding velocity. (left) Dispersion relation  $\varepsilon(\mathbf{k}) = -2J(\cos(k_x a) + \cos(k_y a))$  within the 1. BZ as a color map and a 3d plot. Each momentum state  $\mathbf{k} = (k_x, k_y)$  on the rhombus (highlighted by a black line) corresponds to a vanishing single particle energy  $\varepsilon(\mathbf{k})$  leading to a total energy  $E_{\text{fin}} = 0$ . (right) Absolute velocities  $|\mathbf{v}(\mathbf{k})| = 2\frac{aJ}{\hbar}\sqrt{\sin^2(k_x a) + \sin^2(k_y a)}$  within the 1. BZ as a colormap and a 3d plot. Particles occupying momenta on the rhombus (highlighted by a black line) all possess velocities in the range  $[0; 4]$ . Thereby, the corresponding velocity vectors point all along the diagonals in the real space leading to a cross shaped density distribution for long times, as sketched below.

and hence the majority of particles have appreciable velocity. This results in a spiked real space density profile rather than a continuously connected cross-like profile, as is the case in the analytic consideration in Fig. 5.8. On the other hand, the expansion of the spikes happens with a velocity  $|\mathbf{v}| = 2\sqrt{2}a\frac{J}{\hbar}$  for all simulated  $U/J$ , which is in agreement with the maximal possible velocity within the non-interacting predictions Eq. (5.14)-(5.15). With increasing ratio  $U/J$  the spiked distribution becomes more pronounced, although, a convergence towards the analytic prediction was not observed. The reason could be the presence of the SF ring with finite kinetic energy affecting the relation Eq. (5.10).

### Formation of long-range order

Another remarkable result concerns the long-range order of the bosonic cloud. In interacting systems the eigenstates of the density matrix define the natural orbitals, also known as effective single-particle states, see Sec. 3.2.3. The corresponding eigenvalues indicate their population. If the occupation of the lowest natural orbital, which is the most highly occupied one, is proportional to the total particle number, the system is known to possess long-range order in higher dimensional systems. In periodic homogeneous lattices in equilibrium the natural orbitals are momentum states where macroscopic occupation of the  $\mathbf{k} = (0, 0)$  state indicates the coherence. Since the melting of the MI leads to the occupation of the momenta on the rhombus, one could infer that the system loses the long range order during the expansion. However this is surprisingly not the case in our out-of-equilibrium system. This is measured by the Gutzwiller SF-fraction  $f_c = \sum_i |\langle \hat{b}_i \rangle|^2 / N$  and presented in Fig. 5.9. Starting with low condensate fraction due to the thin SF-ring initially surrounding the MI core, the melting of the insulating cloud center and the subsequent expansion continuously lead to an enhancement of coherence, see Fig. 5.9 (left).

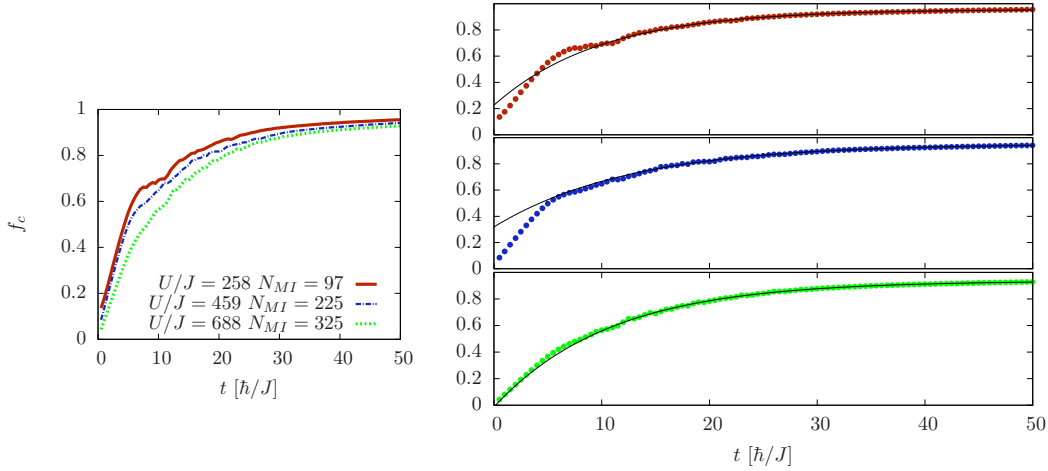


**Figure 5.9:** Time evolution of the condensate fraction for  $U/J = 258, 459$  and  $688$ . (left) The condensate fraction continuously increases during the melting and expansion processes, and tends to  $f_c = 1$  for large expansion times. The coherent population of the lowest lying natural orbital reduces with increasing number of initially MI particles providing a global shift of the  $f_c$  graph to the lower values. (right) The growth of coherence can be divided into two processes: a rapid increase during the melting of the MI core for  $t < 10 \hbar/J$  and the exponential approach of the perfect long range coherence during the following expansion of the cloud. The data is fitted by  $f(t) = a - be^{-cx}$  (see text for values of fitting parameter).

We notice that  $f_c(t)$  is shifted to lower fractions with increasing number of particles in the initial MI phase without substantial changes in the functional dependence. The shift can be traced back to the reduction of initial coherence as enhanced  $N_{MI}$  corresponds to a thinner SF-ring and thus lower condensate fraction. The persistence of global long-range order indicates that the processes leading to the creation of the coherence do not depend on  $N_{MI}$ . Additionally, the condensate fraction is found to increase dramatically during the melting of the MI for  $t < 10 \hbar/J$  and to approach exponentially the perfect condensation  $f_c = 1$ , as shown in Fig. 5.9 (right). The data has been fitted by:  $f(t) = 0.94 - 0.95e^{-0.09t}$  for  $U/J = 688$ ;  $f(t) = 0.95 - 0.63e^{-0.08t}$  for  $U/J = 459$  and  $f(t) = 0.96 - 0.73e^{-0.1t}$  for  $U/J = 258$ .

Thus, the remarkable result of this analysis is that long-range order can develop as a consequence of non-equilibrium dynamics. Different to equilibrium condensates in homogeneous lattices, expanding MI-SF particles populate momenta on a rhombus which, based on analysis of the condensate fraction, all form a single coherent state. The population of certain modes together with appropriate expansion in the real space were explained based on analytic considerations.

However, some questions remain to be answered. What is the role of the SF ring in the MI expansion? Does the mobility of the SF particles influence the evolution of the inner insulating core? How well does the system fulfill the analytic predictions when the system parameters approach the corresponding limiting assumptions?

### 5.2.3 Effect of the SF on the MI expansion

The SF shell can influence the inner MI core in two ways. Since for large  $U/J$  values double and higher occupancies are energetically not favorable, the expansion of the inner  $n_i = 1$  part of the cloud depends on the expansion velocity of the outer regions. Thus,



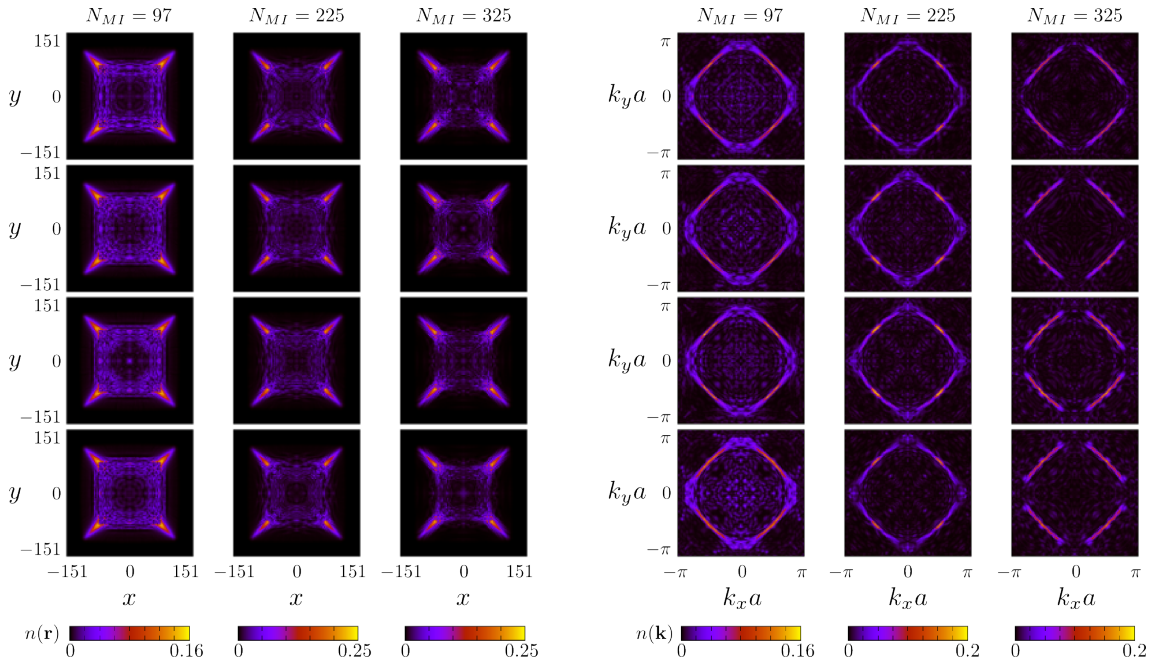


**Figure 5.10:** Density distribution in real (left) and momentum (right) space after  $t = 50\hbar/J$  expansion time. Each column represents the results for a fixed  $N_{MI}$  but varying  $U/J$  values:  $N_{MI} = 97$  and  $U/J = 172 - 259$ ;  $N_{MI} = 225$  and  $U/J = 374 - 460$ ;  $N_{MI} = 325$  and  $U/J = 517 - 690$ . It is obvious that keeping the number of particles in each phase constant and modifying the initial dynamics of the SF shell leads to no essential changes even when the ratio  $U/J$  is increased up to 1.5 times.

intuitively we would expect that the dynamics of the SF shell would significantly modify the melting process of the MI. On the other hand, the presence of a finite SF-ring is needed for the dynamical Gutzwiller in order to initiate expansion. From this one could infer that artifacts are present in the observations. Hence, the application of the mean-field approach needs to be justified.

### Influence on expansion dynamics

The feedback of the SF on the expansion of the inner MI can be investigated by modifying the initial configuration of the SF shell. Since the mean-field on-site Hamiltonians within the MI core consist of the interaction part only, solely the kinetic parts driving the dynamics of the SF particles are influenced by the variation of the ratio  $U/J$ . With increasing  $U/J$  the Wannier states, the most appropriate basis to describe the system, become more localized. Additionally, the occupation of higher Fock states becomes energetically more unfavorable. Since the evolution of the cloud and in particular the melting of the MI proceeds from the outside inwards, this change affects the SF shell first. Thus, we investigate the effect of the SF on the MI expansion modifying  $U/J$  and keeping the number of MI and SF particles constant to control any possible scattering processes leading to a population of other modes than predicted analytically.

A comparison between the density and momentum distributions of systems with  $N_{MI} = 97, 225$  and  $325$  for varying  $U/J$  values are presented in Fig. 5.10. The results are organized as follows: the number of MI particles is kept constant in each column while the ratio  $U/J$  increases from top to bottom within the range given in the caption. The real space density

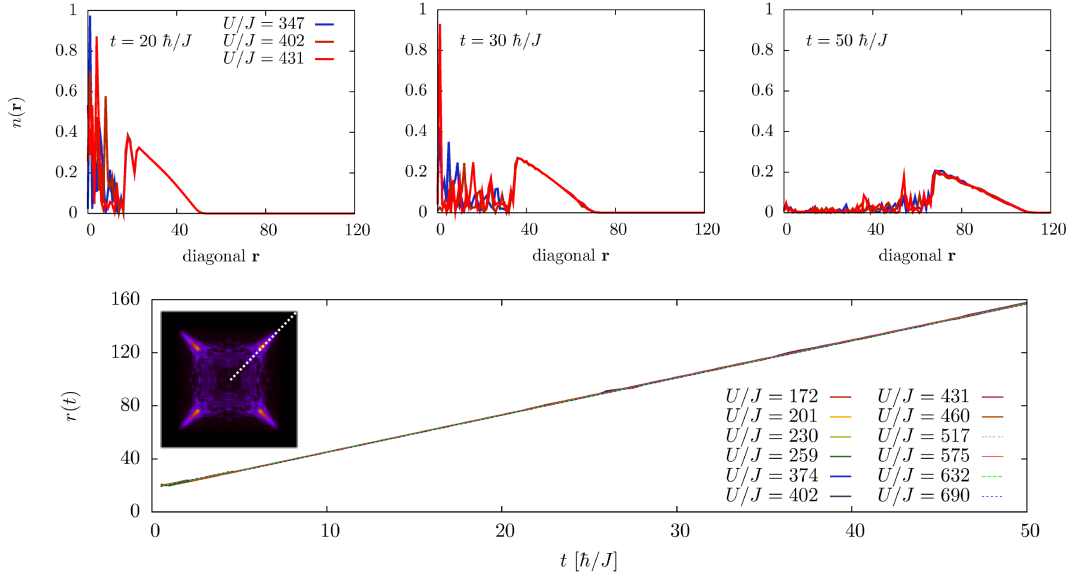


**Figure 5.11:** (top row) Comparison of the expanding density profiles for  $N_{MI} = 225$  along a diagonal (indicated by a white line in the color map inset). At every time step the occupation of the spike coincides. This indicates that the feedback of the SF shell on the melting MI core has a vanishing effect. Solely the density waves in the center of the evolving cloud are affected by the varying  $U/J$  ratio. (bottom row) The position of the outermost part of the cloud as a function of time. According to the analytic results, the occupation of rhombic modes especially of  $\mathbf{k} = (\pi/2; \pi/2)$  leads to the maximal diagonal velocity  $|\mathbf{v}_{\max}| = 2a \frac{J}{\hbar} \sqrt{2}$ . This prediction is confirmed by our observations for all  $N_{MI}$  and  $U/J$  parameter sets, i.e.  $\Delta r(t)/\Delta t \equiv |\mathbf{v}_{\max}|$ .

profiles of the cloud after  $50 \hbar/J$  expansion time feature the same distributions for a fixed  $N_{MI}$ : the formation and population of the spikes accompanied by a weak population of a remaining square shaped structure of the same extent. It is surprising that the time evolution in a system with smaller  $U/J$  proceeds in a similar way as in a system with  $U/J$  nearly 1.5 times larger. Thus, complementary to the findings of the previous chapter, not only the  $U/J$  value determines the density profiles but rather the initial number of MI particles. Hence, with increasing  $N_{MI}$  and  $U/J$  the spiked structure becomes more pronounced and the shape of the cloud approximates the analytically predicted diagonal expansion – the magnitude of the interaction ratio alone is not a sufficient criteria. In any case, the momentum distributions categorize corresponding to  $N_{MI}$ , whereupon each group shows a similar occupation of modes. Hereby, the population of momenta other than on the rhombic structure decreases with increasing  $N_{MI}$ .

Although in absolute terms the time of each hopping process increases proportional to  $\hbar/J$ , the distance covered within each tunneling step is independent of the system parameters for a given fixed  $N_{MI}$ . In Fig. 5.11 (upper plots) the overlap of the real space density profiles is shown for  $N_{MI} = 225$  and  $U/J = 347 - 431$  during the time evolution. Despite the differences in  $U/J$  values and their effect on the initial SF expansion, the density profiles agree perfectly at every  $t$  in the outer region where the structure which we refer to as “spikes” is predominant. Since the population of spikes is due to the melting process, this indicates that the effect of SF on the melting of the MI core is negligible.

A closer look at Fig. 5.10 reveals that not only for a constant initial  $N_{MI}$  the spikes of all sampled  $N_{MI}$  and  $U/J$  seem to have reached the same distance from the cloud center at  $t = 50 \hbar/J$ . This feature is captured more quantitatively in Fig. 5.11 (lower plot) where

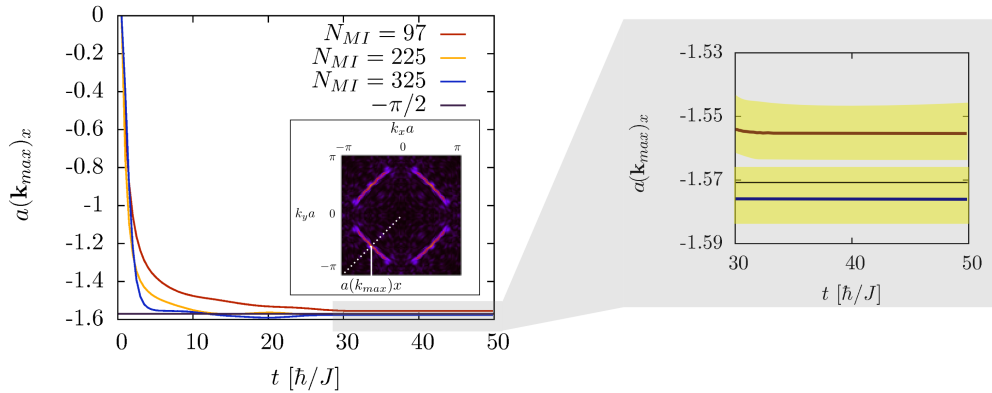


**Figure 5.12:** Maximally occupied mode along the diagonal at different time steps. Due to the symmetry only the  $x$ -coordinate is shown, as pointed out in the inset. (left) In equilibrium before the expansion the population of the  $\mathbf{k} = (0, 0)$  mode is maximal as a result of the SF shell surrounding the MI core. During the expansion the maximally occupied momenta approach the analytically estimated position of the rhombus  $\mathbf{k} = (-\pi/2, -\pi/2)$ . (right) At the end of the cloud expansion the position of the most populated mode saturates. The yellow shaded area highlights the resolution due to discretization of the  $k$ -space. The condensation for  $N_{MI} = 225$  and  $325$  corresponds best to the analytic results.

the distance from the cloud center to the outermost part (particle density  $n_i = 5 \cdot 10^{-4}$ ) on the diagonal is shown for every time step during the evolution. It is interesting to note that the slope  $\Delta r(t)/\Delta t = 2a \frac{J}{\hbar} \sqrt{2}$  is consistent with the maximal diagonal velocity predicted in Eq. (5.14)-(5.15) even at the early stage of the expansion where the assumption that the particles are non-interacting is barely fulfilled. Thus, the expansion velocity of the MI follows the analytic assumptions regardless of the properties of the surrounding SF.

### Impact on occupation of momentum states

In order to analyze the agreement between the analytical predictions for the expansion of a pure MI and the numerical results, which treat the neighbor coupling in the mean field manner and need a SF seed to initiate dynamics, we would like to point out the key analytic features of the pure MI melting: all MI particles are expected to condense in momentum space on a rhombic structure leading to a cross shaped expansion in the real space. Thus, to prove the accuracy of the Gutzwiller method and exclude possible artifacts due to the presence of SF shells we need to analyze the location and the magnitude of the momenta and spikes population.

It is important to note that the energy of the system within Gutzwiller is completely due to the presence of SF shells since no energy is stored in the MI core<sup>3</sup>. The finite total energy, however, modifies the relation the populated modes which are derived from in Eq. (5.10). Additionally, the dispersion relation for finite  $U/J$  values differs from the presumed non-interacting dispersion. While the latter deviation from the analytic limit decreases during the cloud expansion, the first one remains and modifies the population of modes. Fig. 5.12 shows at which mode the maximal population appears during the cloud spreading. In order to investigate the momentum evolution of the system the maximum position  $a\mathbf{k}_{\max}$  of the distribution function  $n(\mathbf{k})$  along the diagonal was captured

<sup>3</sup>The vanishing SF parameter  $\langle \hat{b}_i \rangle$  cancels the kinetic part of the mean-field Hamiltonian and for particle densities  $n_i = 1$  the interaction term becomes zero as well. Thus, the on-site Hamiltonians and with it their expectation values vanish within the MI.

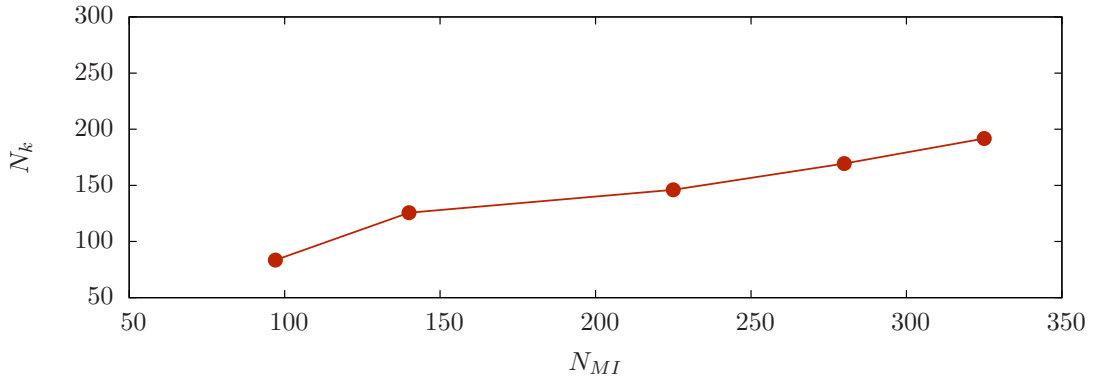


**Figure 5.13:** The number of particles occupying the rhombic modes after  $50 \hbar/J$  expansion. The calculation of the population was performed regarding the finite width of the rhombi. In all simulations the occupation was found to increase proportionally to the initial number of the MI particles.

at every time step, as pointed out in the inset, see Fig. 5.12 (left). In the equilibrium before the expansion sets in, the presence of the SF shell leads to an enhanced occupation of the  $\mathbf{k} = (0, 0)$  momentum. During evolution, the system converges towards the non-interacting limit and with it the dispersion of the interacting system approaches the non-interacting dispersion relation. Hence, the momentum distribution rather develops towards the anticipated value by subsequently occupying all intermediate momenta than immediately appears at the final  $\mathbf{k}$ . The saturation at the rhombus for all  $N_{MI}$  at  $t \sim 30 \hbar/J$  indicates that the non-interacting regime has been reached. Nonetheless, a closer look at the finally occupied mode in Fig. 5.12 (right) reveals small differences: due to finite total system energies, the maximally occupied momentum is slightly shifted compared to predictions in Eq. (5.10). Here, because of the larger initial SF shell and consequently an enhanced total energy per particle  $E_{\text{fin}}/N \approx -0.08$ , the cloud with  $N_{MI} = 97$  condenses further away from the predicted value  $\mathbf{k} = (-\pi/2, -\pi/2)$  than  $N_{MI} = 225$  and  $325$  which both possess approximately  $E_{\text{fin}}/N \approx -1 \cdot 10^{-5}$ .

At this point, however, we should put the analytic results into perspective. The population of a rhombus in momentum space through the points  $\mathbf{k} = (\pm\pi/2; \pm\pi/2)$  is based on a simplified analytic assumption of evanescent total energy. Since in the Bose-Hubbard model in the MI phase the particle-hole excitations vanish only in the limit  $U/J \rightarrow \infty$  the kinetic energy remains finite for finite  $U/J$  and the Eq. 5.10 has to be corrected, namely  $\varepsilon(\mathbf{k}) = -2J(\cos(k_x a) + \cos(k_y a)) = \delta$ . This fact does not change the square symmetry of estimated occupied modes but shifts the edges of the rhombus according to the conserved energy per particle  $\delta$ . Nevertheless, although this is observed within the Gutzwiller calculations, the finite energy originates from the SF rather than from the MI. However, increasing the ratio  $U/J$  and reducing the SF shell leads to an approximation of the analytic estimate for the melting of a fluctuation free insulator. The improvement of the mean-field accuracy suggests that our numerical approach provides qualitatively correct results.

Up to now we have demonstrated that the redistribution of momentum occupation saturates at well defined momentum states. Moreover, the condensate fraction starting at a minimal value due to initial coherence in SF shells was shown to increase during the MI melting and to approach the long-range coherence limit  $f_c \sim 1$ , see Fig. 5.9. These results are evidence for the formation of a non-equilibrium condensate at finite momenta in accor-

dance with analytic predictions. The remaining question to answer is, whether all particles initially in the MI core occupy the rhombic structure similarly to the pure MI expansion. Fig. 5.13 presents the number of particles  $N_k$  populating the appropriate  $k$ -modes after  $50 \hbar/J$  expansion for initial number of MI particles  $N_{MI} = 97, 140, 225, 280, 325$ . Here, the summation took into account the finite width of the rhombi sides. For all systems studied in this work we find that the occupation of square momentum states increases with the MI particle fraction. At the same time,  $N_k$  is found to be slightly less than  $N_{MI}$ . The deviations can be due to an exponentially slow rate of condensation that only develops complete long-range coherence in the limit  $t \rightarrow \infty$  and to inaccuracies in the description of the short range correlations within the mean-field approach.

### 5.3 Discussion and conclusion

In this chapter we have presented detailed investigations of the non-equilibrium expansion dynamics of a bosonic Mott insulator surrounded by a SF shell in a 2D optical lattice. Once released from the harmonic confinement, the interacting many-body system is observed to develop coherence while simultaneously populating finite quasi-momenta states. While expanding, the created condensate was observed to develop a spiked structure breaking the initial spherical symmetry. The expanding spikes were found to exhibit maximal lattice velocity independent of the system parameters. These observations were explained analytically based on energy conservation during the evolution. Additionally the influence of the SF shell on the expansion process was studied. We demonstrated that in the strong and intermediate interaction regimes the emerging condensate fraction depends on the number of particles in the MI phase rather than on the particular interaction or tunneling strength. In particular the melting dynamics of the MI was found to be independent of the  $U/J$  ratio when the particle fractions  $N_{MI}/N$  and  $N_{SF}/N$  are kept constant. This is a remarkable result since it suggests that although the SF is required to initiate MI melting within the Gutzwiller method, this has no impact on the core expansion. This fact, together with the agreement of numerical results extrapolated to the limits  $U/J \rightarrow \infty$  and  $N_{MI} \rightarrow N$  with the analytical analysis, justifies the use of the Gutzwiller theory for studies of non-equilibrium MI dynamics. The accuracy of the mean-field method and the validity of the analytic assumptions were discussed, but as both were analyzed to be valid only in a certain limit or within a certain range of parameters, an experimental realization would provide the definitive validation.



## 6. Strongly correlated fermions

### 6.1 The Fermi-Hubbard model

The Fermi-Hubbard model, similar to Bose-Hubbard model introduced in Sec. (3.1), is one of the frequently used simplified models describing interacting fermions in a periodic potential. In fact, the original development of the formalism by John Hubbard 1963 was set up for fermionic particles [8]. In particular, the model was proposed to characterize  $d$ -electrons in solids and has since been used to address various condensed matter questions and, more recently, ultracold atoms in optical lattices. Within this thesis the model is applied to investigate questions in both fields, therefore, we account for peculiarities of each system in the following sections.

The model implements tunneling of particles, on-site interactions, allows different lattice symmetries and additional external potentials. However, despite the fact that it is powerful, the original formulation does not cover long-range interaction effects such as Coulomb interaction<sup>1</sup>. Nevertheless, this model successfully describes the Mott transition by means of correlations [8] and was used as a prototype for other models like e.g. the  $t - J$  model [176]. For ultracold fermions interacting only via the short-range van der Waals force this approach is more accurate.

In second quantization the Fermi-Hubbard model reads

$$\hat{\mathcal{H}} = -t \sum_{\langle ij \rangle, \sigma} (\hat{c}_{i, \sigma}^\dagger \hat{c}_{j, \sigma} + h.c.) + \frac{U}{2} \sum_i \hat{n}_{i, \uparrow} \hat{n}_{i, \downarrow} - \sum_{i, \sigma} (\mu_\sigma - V_{i, \sigma}) \hat{n}_{i, \sigma}. \quad (6.1)$$

The index  $\sigma = \uparrow, \downarrow$  denotes the spin of the particle, which in the case of ultracold fermions is an abbreviation for different hyperfine states of the atoms. The operators  $\hat{c}_{i, \sigma}^\dagger$  and  $\hat{c}_{i, \sigma}$  are fermionic creation and annihilation operators at site  $i$ , respectively, and the summation  $\sum_{\langle ij \rangle}$  concerns only nearest neighbors. The parameters  $t$  and  $U$  denote the tunneling and the on-site interaction strength. The chemical potential  $\mu_\sigma$  can be chosen to depend on the spin direction to create spin-imbalanced systems or to be equal for both spin species  $\mu \equiv \mu_\uparrow = \mu_\downarrow$  otherwise. The last term in Eq. (6.1) accounts for an optional external potential  $V_{i, \sigma}$ . This can be an additional harmonic trapping, which we discussed in Sec. (3.1) for

---

<sup>1</sup>To study long-range interactions a generalization of the Fermi-Hubbard model has been developed, the so-called *extended Hubbard model* which incorporates e.g. nearest-neighbor interactions [172–175].

bosonic species in optical lattices, or a disorder potential. In the fermionic part of this thesis we mostly concentrate on disordered lattices and introduce the corresponding potentials in Sec. 6.2.

The difference to the Bose-Hubbard model lies in the interaction term of the Hamiltonian accounting for the *Pauli exclusion principle*, which states that no two fermions may occupy the same quantum state simultaneously [177, 178].

In this section we give a brief derivation of the Fermi-Hubbard model. We start with the discussion of non-interacting fermions, pointing out the parallels to non-interacting bosons and using the already known results from Sec. (3.1.1). Subsequently, the on-site interaction term will be derived. The end of the section provides a summary and a discussion of limitations of the Fermi-Hubbard model.

### 6.1.1 Non-interacting particles

#### Statistics

In quantum mechanical description of many-particle systems, contrary to classical statistics, particles in the same quantum state are indistinguishable. This condition leads to two possible effects on the many-body wave function. Interchanging the order of particles via a permutation operator  $\hat{P}$  in a  $N$ -particle state corresponding to the wave function  $\Psi(1, \dots, i, \dots, j, \dots, N)$  leads<sup>2</sup>

$$\hat{P}\Psi(1, \dots, i, \dots, j, \dots, N) = \begin{cases} (-1)^l \Psi(1, \dots, i, \dots, j, \dots, N) & \text{if } \Psi \text{ antisymmetric,} \\ \Psi(1, \dots, i, \dots, j, \dots, N) & \text{if } \Psi \text{ symmetric,} \end{cases}$$

where  $l$  denotes the number of transpositions. Particles described by a symmetric wave function fulfilling the upper condition are called *bosons* and those possessing antisymmetric properties are referred to as *fermions*.

The differences in wave-functions lead to fundamentally different statistics of quantum states occupation: *Bose-Einstein statistics* and *Fermi-Dirac statistics*. As discussed in the previous chapter, below a critical temperature non-interacting bosons macroscopically occupy the lowest single-particle energy state without an upper limit on the particle number [1, 2, 180] as depicted in Fig. 6.1. The average occupation of a non-degenerate state  $i$  in thermal equilibrium is given by

$$\text{Bose-Einstein distribution:} \quad f(\varepsilon_i) = \frac{1}{e^{(\varepsilon_i - \mu)/k_B T} - 1},$$

where  $\mu$  is the chemical potential,  $\varepsilon_i$  is the energy of the state  $i$  whereby  $\varepsilon_i > \mu$ ,  $k_B$  is the Boltzmann constant and  $T$  the absolute temperature. The situation is different when atoms obey the Pauli exclusion principle. In thermal equilibrium, the distribution of particles on different energy states, accounting for the condition that no two particles can occupy the same state, reads

$$\text{Fermi-Dirac distribution:} \quad f(\varepsilon_i) = \frac{1}{e^{(\varepsilon_i - \mu)/k_B T} + 1},$$

where  $\varepsilon_i$  and  $\mu$  are independent. At  $T = 0$  all energy states  $\varepsilon_i$  below the chemical potential are fully occupied, i.e.  $f(\varepsilon_i) = 1$ , and those above remain empty, see Fig. 6.1. In this case the chemical potential is equal to the *Fermi energy*  $\varepsilon_F$  and the *Fermi temperature* is consequently defined  $T_F = \varepsilon_F/k_B$ . At finite temperatures according to the Pauli principle the occupation is  $0 \leq f(\varepsilon_i) \leq 1$ .

<sup>2</sup>It can be shown that an arbitrary permutation of  $N$  particles can be decomposed into a product of two-particle transpositions of fixed parity  $+1$  or  $-1$  [179].



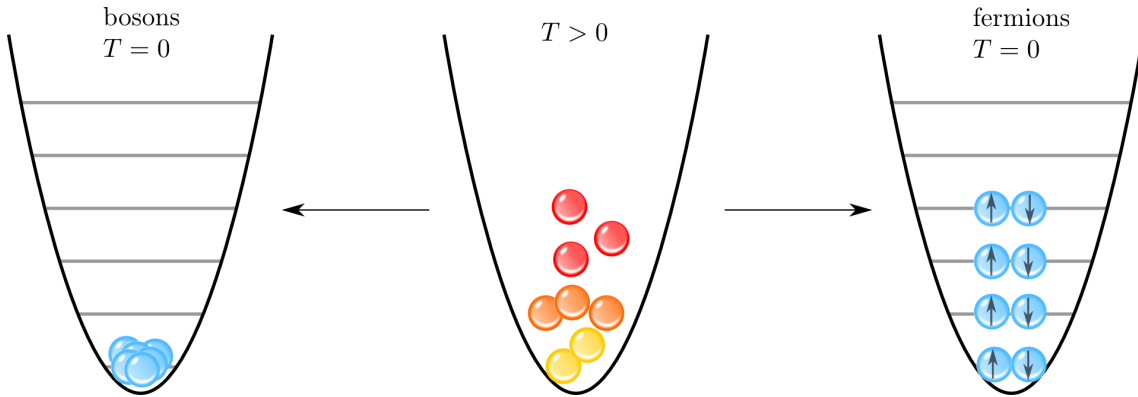


**Figure 6.1:** Illustration of the difference in the energy eigenstate occupation statistics between bosons and fermions at  $T = 0$ . When the particles are cooled down the intrinsically distinct quantum nature becomes evident: if particles are bosons they all occupy the lowest energy state, if particles are fermions each level and spin state becomes singly occupied. For experimental results on bosonic and fermionic cloud cooling see [181].

### Periodic potential

Non-interacting fermions are described by the single-particle Hamiltonian, which in the field operator representation reads

$$\mathcal{H} = \int d\mathbf{r} \hat{\Psi}_\sigma^\dagger(\mathbf{r}) \left[ -\frac{\hbar^2}{2m} \nabla^2 + V(\mathbf{r}) \right] \Psi_\sigma(\mathbf{r}), \quad (6.2)$$

with  $\Psi_\sigma(\mathbf{r})$  and  $\Psi_\sigma^\dagger(\mathbf{r})$  being the annihilation and creation fermionic field operators, and  $V(\mathbf{r})$  the periodic lattice potential. Contrary to the bosonic field operators, the fermionic field operators satisfy anticommutation relations

$$\{\Psi_{\sigma'}(\mathbf{r}), \Psi_\sigma^\dagger(\mathbf{r}')\} = \delta(\mathbf{r} - \mathbf{r}') \delta_{\sigma, \sigma'} \quad \{\hat{\Psi}_\sigma(\mathbf{r}), \hat{\Psi}_\sigma(\mathbf{r}')\} = 0 = \{\hat{\Psi}_\sigma^\dagger(\mathbf{r}), \hat{\Psi}_\sigma^\dagger(\mathbf{r}')\}.$$

The solution of the differential equation (6.2) does not differ from the solution of the non-interacting bosonic Hamiltonian Eq. (3.2). The eigenstates are the Bloch wave functions Eq. (3.6) and the eigenenergies are the corresponding energy bands in momentum space  $q \in 1$  BZ. Details of the calculation can be found in Sec. 3.1.1. The difference to the bosons lies in the occupation of the energy levels: beginning with the lowest, the energy-spin states are subsequently singly populated, each by one fermion.

Using the Wannier function representation, which can be derived from the Bloch functions by the inverse Fourier transformation, see Eq. (3.22), we can expand our field operators in the following way:

$$\hat{\Psi}_\sigma(\mathbf{r}) = \sum_{n,i} \hat{c}_{\mathbf{r}_i, \sigma} \omega_x^{(n)}(x - x_i) \omega_y^{(n)}(y - y_i) \omega_z^{(n)}(z - z_i). \quad (6.3)$$

Here  $n$  denotes the energy band index,  $\hat{c}_{\mathbf{r}_i, \sigma}$  annihilates a fermion with the spin  $\sigma$  at position  $\mathbf{r}_i = (x_i, y_i, z_i)$ , and  $\omega_x^{(n)}(x - x_i)$  denotes a Wannier function corresponding to the periodic potential in  $x$ -direction localized around  $\mathbf{r}_i$ . In homogeneous lattices the Hamiltonian given in Eq. (6.2) decomposes into a product of identical differential equations for the  $x$ ,  $y$  and

$z$  variables. The solution of a homogeneous 3D problem is thus reduced to a solution of the 1D equation

$$\begin{aligned}\mathcal{H} &= \int dx \hat{\Psi}_\sigma^\dagger(x) \left[ -\frac{\hbar^2}{2m} \nabla^2 + V(x) \right] \hat{\Psi}_\sigma(x) = \\ &= \int dx \sum_{i,j,n} \omega^{*(n)}(x-x_i) \hat{c}_{i,\sigma}^\dagger \left[ -\frac{\hbar^2}{2m} \nabla^2 + V(x) \right] \omega^{(n)}(x-x_j) \hat{c}_{j,\sigma} = \\ &= - \sum_{i,j,n} t_{ij}^{(n)} \hat{c}_{i,\sigma}^\dagger \hat{c}_{j,\sigma},\end{aligned}\tag{6.4}$$

with the hopping amplitude integral

$$t_{ij}^{(n)} = \int dx \omega^{*(n)}(x-x_i) \left[ -\frac{\hbar^2}{2m} \nabla^2 + V(x) \right] \omega^{(n)}(x-x_j).\tag{6.5}$$

This result is mathematically exact and similar to the bosonic Eq. (3.26).

In order to simplify the expression (6.5), we apply the most common approximations, which were already introduced and discussed in detail in Sec. 3.1.1. If the thermal- and interaction-induced excitations do not exceed the band gap energy, the *lowest-band approach* is justified and we can neglect all bands except the lowest one with  $n = 0$ . Dropping the band index for better readability, the hopping integral is

$$t_{ij} = \int dx \omega(x-x_i) \left[ -\frac{\hbar^2}{2m} \nabla^2 + V(x) \right] \omega(x-x_j).$$

Within this approach the low-energy and low-temperature properties are well described since mostly only few or even just one band crosses the Fermi energy.

Further approximations can be made if the lattice potential is sufficiently strong, such that the many-body wave function is approximated by a sum over site-localized Wannier functions. In case of electrons in condensed matter this is a very drastic simplification since it reduces the degenerated  $d$ -orbitals, required for metal–Mott insulator transition, to simple  $s$ -wave orbitals. The latter neglects various degrees of freedom like degeneracy, spin fluctuations, orbital fluctuations and orbital-symmetry breaking which, e.g., occur in perovskite structures [182]. In contrast, in ultracold fermionic systems this approach is less drastic since atoms in an optical lattice correspond to electrons in non-degenerate orbitals.

Despite the mentioned drawbacks, the lowest-band approach makes the theoretical effort feasible. Exponentially decaying Wannier functions overlap only between nearest neighbor sites. Consequently, the tunneling matrix element is finite only for the site  $j$  being the nearest neighbor of the site  $i$  and the summation in Eq. (6.4) reduces to

$$\mathcal{H} = - \sum_{\langle ij \rangle, \sigma} t_{ij} (\hat{c}_{i,\sigma}^\dagger \hat{c}_{j,\sigma} + h.c.)\tag{6.6}$$

with the tunneling matrix element  $t_{ij} \equiv t$  in case of homogeneous lattices. Since the calculation of  $t$  is based on Wannier functions, which are independent of particle statistics, in deep lattices the same approximations are applied as in the derivation of bosonic hopping integral  $J$ . This leads to the same analytic expression (see Eq. (3.39))

$$t \approx \frac{4}{\sqrt{\pi}} E_r s^{3/4} e^{-2\sqrt{s}},$$

where  $E_r = \hbar^2 k^2 / 2m$  is the recoil energy, the particle mass is denoted by  $m$ ,  $k = 2\pi/\lambda$  with the laser wavelength  $\lambda$  and the lattice depth  $s = V_0/E_r$  indicating the lattice potential in units of the recoil energy. Exact values for any lattice depth are obtained via band calculations of Bloch states which are Fourier transforms of Wannier states. For details of the calculation and possible approximations in deep lattices see Sec. 3.1.1.

The result (6.6) corresponds to the first term in the Fermi-Hubbard Hamiltonian (6.1). To obtain the second term we have to include interactions between particles.

### 6.1.2 Two-particle interactions

Before we start with the derivation of the interaction part of the Fermi-Hubbard Hamiltonian, we would first like to point out which type of interactions are meant below. When the model is used to describe electrons in condensed matter, the Coulomb interactions of electrons among each other and with nuclei have to be implemented. However, an explicit consideration of such a complex many-body problem is theoretically not feasible. Indeed, the particular form of interactions between all electrons inside an atom is not needed since the electric properties of condensed matter are determined by valence electrons. Together with nuclei the inner electrons produce an effective lattice potential experienced by valence electrons. This physics is governed in the first summand of the model in Eq. (6.4) derived in the foregoing section. Thus, the remaining interaction we need to account for is the long-range Coulomb force between the valence electrons of different atoms. These correlations are essential to explain the metal-Mott insulator transition [183]. In the Fermi-Hubbard model the long-range interactions are approximated by on-site interactions. This simplification is validated due to the screening of Coulomb repulsion among valence electrons by electrons in other orbitals. Thus, the long-range interactions within a valence band reduce to effective short-range interactions [184].

Neutral ultracold atoms interact via the van der Waals force. If the spin-orbit and hyperfine coupling are neglected, the potential describing interacting fermions is identical to the potential of the interacting bosons given in Eq. (3.44):

$$V(r) \begin{cases} = \infty & \text{if } r < R_0, \\ \propto -\frac{1}{r^6} & \text{else,} \end{cases} \quad (6.7)$$

$R_0$  being the radius of an atom and  $r$  is the distance between two interacting atoms. Following the arguments given in Sec. 3.1.3, this potential can be substituted by an effective non-singular one which enables a perturbative treatment, the so-called contact interaction potential,

$$V_p(\mathbf{r} - \mathbf{r}') = \frac{4\pi\hbar^2 a_s}{m} \delta(\mathbf{r} - \mathbf{r}'). \quad (6.8)$$

Here  $|\mathbf{r} - \mathbf{r}'|$  denotes the relative distance between interacting atoms,  $a_s$  is the scattering length and  $m$  is the mass of an atom<sup>3</sup>.

Therefore, the two-particle interaction Hamiltonian in a homogeneous lattice in the field-operator representation is

$$\begin{aligned} \mathcal{H}_{\text{int}} &= \frac{1}{2} \int d\mathbf{r} \int d\mathbf{r}' \hat{\Psi}_{\sigma}^{\dagger}(\mathbf{r}) \hat{\Psi}_{\sigma'}^{\dagger}(\mathbf{r}') V_p(\mathbf{r} - \mathbf{r}') \hat{\Psi}_{\sigma'}(\mathbf{r}') \hat{\Psi}_{\sigma}(\mathbf{r}) \\ \stackrel{\text{Eq. (6.8)}}{=} & \frac{1}{2} \frac{4\pi\hbar^2 a_s}{m} \left( \int dx \int dx' \hat{\Psi}_{\sigma}^{\dagger}(x) \hat{\Psi}_{\sigma'}^{\dagger}(x') \delta(x - x') \hat{\Psi}_{\sigma'}(x') \hat{\Psi}_{\sigma}(x) \right)^2. \end{aligned} \quad (6.9)$$

<sup>3</sup>In case of a heteronuclear fermionic mixture the reduced mass has to be used instead:  $m_{\text{red}} = m_1 m_2 / (m_1 + m_2)$ .

Writing the field operators in the lowest-band Wannier representation,  $\hat{\Psi}_\sigma(x) = \sum_k \omega(x - x_k) \hat{b}_{k,\sigma}$  (see Eq. (3.24)), the integral reads

$$\begin{aligned} & \sum_{\substack{i,k,l,m \\ \sigma,\sigma'}} \int dx \int dx' w^*(x - x_i) w^*(x' - x_k) \delta(x - x') w(x' - x_l) w(x - x_m) \hat{b}_{i,\sigma}^\dagger \hat{b}_{k,\sigma'}^\dagger \hat{b}_{l,\sigma'} \hat{b}_{m,\sigma} \\ &= \sum_{\substack{i,k,l,m \\ \sigma,\sigma'}} \int dx w^*(x - x_i) w^*(x - x_k) w(x - x_l) w(x - x_m) \hat{b}_{i,\sigma}^\dagger \hat{b}_{k,\sigma'}^\dagger \hat{b}_{l,\sigma'} \hat{b}_{m,\sigma}. \end{aligned}$$

Accounting for on-site interactions only, i.e.  $i = k = l = m$ , the integral can be further simplified such that after this approximation the interaction Hamiltonian (6.9) becomes

$$\mathcal{H}_{\text{int}} = \frac{1}{2} \frac{4\pi\hbar^2 a_s}{m} \sum_{\substack{i,k,l,m \\ \sigma,\sigma'}} \left[ \int dx |\omega(x - x_i)|^4 \right]^3 \delta_{ik} \delta_{kl} \delta_{lm} \hat{b}_{i,\sigma}^\dagger \hat{b}_{k,\sigma'}^\dagger \hat{b}_{l,\sigma'} \hat{b}_{m,\sigma}. \quad (6.10)$$

In homogeneous systems, due to translational invariance, the sites and corresponding Wannier functions are identical, thus without loss of generality we can drop the site index. Using the fermionic anticommutation relation  $\{\hat{b}_{i,\sigma}, \hat{b}_{i,\sigma'}^\dagger\} = \delta_{\sigma,\sigma'}$  we get

$$\begin{aligned} \mathcal{H}_{\text{int}} &= \frac{1}{2} \frac{4\pi\hbar^2 a_s}{m} \left[ \int dx |w(x)|^4 \right]^3 \sum_{i,\sigma,\sigma'} \hat{n}_{i\sigma} \hat{n}_{i\sigma'} \\ &= U \sum_i \hat{n}_{i\uparrow} \hat{n}_{i\downarrow}. \end{aligned} \quad (6.11)$$

In the last step we defined

$$U = \frac{4\pi\hbar^2 a_s}{m} \left[ \int dx |w(x)|^4 \right]^3.$$

The interaction strength  $U$  is calculated with respect to Wannier functions which depend on the lattice potential only. Thus, similarly to bosons, exact value of  $U$  can be obtained via band calculations leading to Wannier functions (see Sec. 3.1.1) or in the deep-lattice limit approximated by (see Eq. (3.57))

$$U \approx \sqrt{\frac{8}{\pi}} k a_s E_r s^{3/4},$$

with  $k = 2\pi/\lambda$ , where  $\lambda$  is the laser wavelength,  $a_s$  the scattering length,  $E_r = \hbar^2 k^2 / 2m$  is the recoil energy,  $m$  the particle mass and  $s = V_0 / E_r$  is the lattice depth corresponding to the lattice potential in units of the recoil energy.

The expression (6.11) corresponds to the second summand in the Fermi-Hubbard model Eq. (6.1). Combining the Hamiltonian of the non-interacting fermions Eq. (6.6) with the interaction part (6.11) leads to the complete interacting Fermi-Hubbard model for homogeneous systems

$$\mathcal{H} = -t \sum_{\langle ij \rangle, \sigma} (\hat{c}_{i,\sigma}^\dagger \hat{c}_{j,\sigma} + h.c.) + U \sum_i \hat{n}_{i\uparrow} \hat{n}_{i\downarrow}. \quad (6.12)$$

### 6.1.3 Fermi-Hubbard Hamiltonian: summary and outlook

As already mentioned in Sec. 6.1.1, simplifying the degenerate multi-orbital structure of the conduction band by a single non-degenerate  $s$ -band lacks some aspects of metal-Mott insulator transitions in condensed matter. For example, orbital correlations cause double-exchange processes in Mn oxides that lead to a transition from antiferromagnetic Mott insulator to a ferromagnetic metal. Note also that the *colossal negative magnetoresistance* was observed near this transition [185]. A model not accounting for these effects would give an incomplete prediction, but luckily, an extension of the theoretical description is possible and was developed in [186, 187]. Another property missing in a single-orbital description is the overlap of degenerate orbitals, which results in a modification of the charge gap between the singly-occupied and doubly-occupied conduction band leading to a so-called *charge-transfer insulator* [188]. Further details on Mott insulator transitions in condensed matter can be found in [184]. Despite the existing obstacles, the single-band model was found to successfully predict the low-energy physics near the Fermi level and is promising to contribute to an understanding of high- $T_c$  superconductivity, where prominent aspects are correlation-induced quantum fluctuations and orbital non-degeneracy [189].

In contrast, due to tunability of the lattice potential, the tight binding regime is reached in every experiment on ultracold gases with lattice depths  $s > 5$  [171] comparable to the bosonic case (see Sec. 3.1.1). This lattice depth sets the lower limit for applicability of the Fermi-Hubbard model in optical lattices. The representation of a conduction band based on atomic non-degenerate  $s$ -orbitals incorporated in the fermionic Hubbard model perfectly corresponds to the cosine-shaped band of the optical lattice. Nevertheless, although it is not yet explicitly investigated for purely fermionic systems, for Bose-Fermi mixtures the interactions were shown to modify the shape of the non-interacting Wannier functions [24, 80]. Thus, the calculation of the tunneling matrix element  $t$  and interaction strength  $U$  with non-perturbed Wannier states is an approximation. In the limit of strong interactions additional effects like density-assisted hopping need to be included [190].

Substitution of the long-range Coulomb interaction by short-range on-site interaction is justified when electrons from other orbitals screen the repulsion between the conduction-band carriers. Nevertheless, ignoring the inter-site interaction is a simplification that is not capable of reproducing charge-ordering effects. Including next-nearest neighbor interactions at certain commensurate fillings results in a formation of charge-density and spin-density waves, which correspond to new ordered phases observed in addition to the metal and Mott insulating phases [191]. Referring to Mott [192], who assumed that with increasing  $U/t$  the carrier density decreases and the screening effect vanishes, the long-range Coulomb interaction leads to formation of an electron-hole bound pair at finite  $U$  and, thus, to a first-order phase transition. This interpretation, however, has been discussed controversially since not only carrier-number reduction but also a mass increment was found near the phase border depending on the type of the transition.

In ultracold gases the interactions between neutral atoms are caused by the van der Waals force. Neglecting spin-orbit and hyperfine coupling, each atom induces a dipole moment in every other atom in an optical lattice which leads to effective dipole-dipole interactions between atoms independent of fermionic or bosonic statistics (see Sec. 6.1.2). In the region where the potential is attractive its strength decays as  $r^{-6}$  with  $r$  indicating interatomic distance. The characteristic van der Waals length  $l = 0.5 \sqrt[4]{mC_6/\hbar^2}$  corresponds to the range of the potential and is  $\approx 3.4$  nm for  $^{40}\text{K}$  which is far below the usual separation given by the lattice constant  $a = 1064$  nm. Here  $C_6$  denotes the van der Waals coefficient [193]. Thus, neglecting next-neighbor interactions is valid for ultracold systems. At the

same time, at very short distances, where the electronic clouds of atoms overlap, the spin gives rise to a splitting into singlet and triplet that leads to a subdivision of the interaction-induced potential landscape. The situation becomes even more complicated if the hyperfine atomic structure is taken into account [194, 195]. In this case, it becomes necessary to specify the *scattering channel* which determines an effective  $U$  for a given hyperfine structure.

Nevertheless, one can address the question about additional effects that are induced by long-range interactions e.g. investigating dipolar gases. Due to the Pauli principle, in order to observe long-range effects the strength of the dipolar interaction has to be comparable with the Fermi energy. Such systems have been realized experimentally [196] and studied theoretically [197–202]. At  $T = 0$  phases such as singlet-superfluid, charge density wave and supersolid were found to appear at zero temperature [203].

## 6.2 Disorder

In the Fermi-Hubbard model given in Eq. (6.1) an additional term accounting for an external potential is included. In the chapter 3.1.1 on the Bose-Hubbard model this external potential we considered a parabolic trap, which is commonly applied in experimental setups to confine particles within an optical lattice. Such traps are also present in ultracold fermionic experiments and lead to a spatially varying local density, analogous to bosonic case. The questions to address are, whether ordered phases still form in confined systems and what their influence on long-range order is. Those topics have been studied theoretically [204–208] and experimentally [209–211]. It was found that antiferromagnetic order is stabilized in the regions where the system is approximately half-filled but although for particle densities away from half-filling [208].

Potentials additional to the homogeneous lattice structure, on which we focus in the fermionic part of this thesis, are disorder potentials. Disorder is naturally present or can be artificially introduced in condensed matter as well as in ultracold systems. The known disorder sources in condensed matter are position displacements, vacant lattice positions and defect atoms. The latter substitute the native lattice atoms and lead to local disturbances of the homogeneous potential. Sometimes disorder is implemented in a controlled way such as doping of semi-conductors. Here, the so called *impurities* lead to additional charge-carriers and states within the band gap and enhance the transport properties. Optical lattices are artificially pure systems whose potentials can be distorted e.g. by a superposition with an external laser field. In Sec. 6.2.2 possible disorder types and their realization in optical systems are explained.

In this chapter we will introduce features of disordered systems such as the concept of Anderson localization, an insulating quantum phase caused by disorder, its identification, and last but not least the implementation of disorder in ultracold gases.

### 6.2.1 Anderson localization

#### Non-interacting Fermions

In his paper 1958 [39] Anderson suggested that localization of non-interacting electrons may appear as a consequence of elastic scattering of quantum particles on impurities although classical physics predicts no confinement. This work stimulated later investigations

on disordered electronic systems. Anderson's primary interest was the transport of non-interacting electrons and spin diffusion. The Anderson model describes a lattice with nearest-neighbor hopping and random on-site energies. By solving the Hamiltonian by means of a perturbation expansion in powers of the tunneling strength, he demonstrated that electronic eigenstates become localized for sufficiently strong disorder or near band edges. The corresponding electronic wave functions were found to decay exponentially with distance from the localization site [39], which is the site with the maximal amplitude. The corresponding characteristic length scale is called localization length  $\xi$ . If all states are localized the system becomes an insulator which is called *Anderson insulator* in honor of Anderson.

The effect of disorder depends strongly on the dimensionality of the system. In their review paper in 1961 [212] Mott and Twose gave a first proof that in one dimension every finite disorder strength leads to global localization<sup>4</sup>. A similar effect was recognized by means of linear response theory and scaling theory later in 2D systems. In contrast, in 3D lattices a critical disorder strength was found, which has to be exceeded to drive a system from the metallic into an insulating phase [61, 215]. For weak disorder in 3D away from the band edges, the physics is, however, well described by common theories of metals and strongly doped semiconductors in which disorder induces transitions within Bloch waves in an energy band [216].

The fundamental reason for the localization of particles, as pointed out by Anderson in [39], is the coherent scattering of wave functions on impurities. The resulting interference effects induce spatial confinement of wave functions. In 1D there exist only 2 types of scattering processes: the forward scattering, if the chirality of the fermion is conserved and the particle continues its tunneling process in the same direction, and the backward scattering, if the particle is reflected from the impurity potential contrary to the original direction of motion. One can show [213, 214] that forward scattering has no effect on the conductivity at all and only backward scattering gives rise to localization. Fig. 6.2 illustrates the density distribution of a wave function in a disordered 1D system. In higher dimensions by varying the scattering angles, different momenta exchanges and scattering directions can be realized such that no comparable classification can be done. Still, the interference of the wave function with itself as a result of scattering processes affects the transport and, depending on the disorder strength and dimensionality, induces localization.

The concept of wave function localization originates in early considerations of *return probability* by Anderson. This return probability indicates the likelihood of a particle to return to the initial site when propagating in an infinitely large disordered lattice. Being in a localized state, a particle initially situated at site 0 has a finite probability to return to its original place, while for an extended state the probability vanishes

$$\lim_{t \rightarrow \infty} \mathcal{P}_{0 \rightarrow 0}(t) \begin{cases} > 0 & \text{localization,} \\ = 0 & \text{delocalization.} \end{cases} \quad (6.13)$$

Intuitively this behavior can be explained based on scattering arguments. As mentioned above, scattering processes induce the pinning of the wave function. If the pinning leads to a density distribution confined to a certain finite area, there is a finite probability of a particle to be at a site  $i$  corresponding to the absolute square of the wave function. Otherwise,

<sup>4</sup> The localization length in 1D was found to be of the order of the mean free path. Exact solutions can be found in [213, 214].

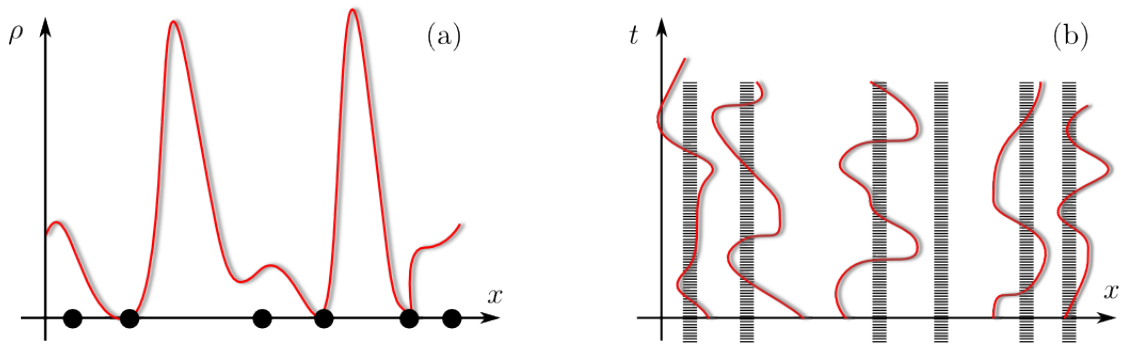


**Figure 6.2:** (a) Illustration of a particle density distribution in a disordered 1D system. Wave functions undergo scattering on impurities (black dots) which results in charge density wave formation. (b) Possible particle trajectories (red line) in space-time. Scattering processes on disorder potentials lead to pinning of the wave functions to impurities confining the possible particle tunneling paths in space. Columns indicate time-independent positions of impurities.

if the wave function remains delocalized,  $|\psi_i|^2$  scales on average inversely proportional to the total site number<sup>5</sup>. In infinitely large systems this results in a vanishing probability for any position  $i$ .

The realization that Anderson localization is purely based on scattering of (matter)waves attracted the attention of wave physicists to disorder phenomena. The interest was increased by the fact that, compared to electronic systems, in photonic samples localization can be experimentally investigated in the absence of interaction effects. In analogy to electronic systems, localization of waves is traced back to interference between multiple scattering paths. In several experiments localization was observed for sound waves [217], microwaves [218, 219] and light waves [220–222].

### Competition between disorder and interactions

Including interactions in disordered systems is a challenging task from the theoretical point of view. If weak interactions are investigated, the electrons can still be considered as well described by the Fermi liquid theory as long as the disorder strength is small and the localization length large. However, this approach breaks down already for intermediate disorder strengths [223–226]. Moreover, contrary to 2D and 3D systems, where interactions larger than a certain critical value are needed to induce a metal-Mott insulator transition, in 1D there exists no limit of weak interactions.

The physics resulting from the simultaneous presence of both effects is not yet fully understood. Although interaction and disorder both lead to metal-insulator transitions, their action is competing. In a repulsively interacting system the potential energy is minimized when particles localize on separate lattice sites, which leads to a uniform density distribution. In contrast, the pinning of particles induced by disorder localizes wave functions to a few randomly distributed lattice sites. Various investigations demonstrated how this interplay affects systems. For a semi-elliptic density of states in high dimensions the presence of both disorder and interaction was found to lead to a disordered metal surrounded by an insulating phase. The latter consisted of Anderson and Mott insulators continuously connected with each other [44, 58]. Since in the first studies of non-interacting, weakly

<sup>5</sup>This behavior follows from the normalization factor  $1/\sqrt{L}$  contained in every extended state.



interacting, as well as strongly interacting 2D systems [62, 63, 216] only insulating regions were found, it was believed for a long time that a metallic phase cannot occur. However, theoretical studies via renormalization group [60, 224] involving  $N$  flavors of electrons predicted the existence of a quantum critical point, at which a metal-insulator transition takes place in 2D. This prediction was confirmed experimentally in silicon metal-oxide-semiconductor field-effect transistors (MOSFET's) [52, 227]. In 1D fermionic systems the situation remains controversial [55, 228].

### Anderson-Hubbard model

A random potential  $V(\mathbf{r})$  introduced by impurities can be written in a good approximation as

$$V(\mathbf{r}) = \sum_i f_i(\mathbf{r} - \mathbf{r}_i).$$

Here, the function  $f_i$  represents the particular potential form of a single impurity and  $\mathbf{r}_i$  its position in the lattice. Commonly, the impurity potential is considered to be short-range such that one can approximate further  $f_i(\mathbf{r} - \mathbf{r}_i) = \varepsilon_i \delta(\mathbf{r} - \mathbf{r}_i)$ . A disorder potential is thus characterized by the potential  $\varepsilon_i$  of a single impurity and the impurity density. The on-site energies  $\varepsilon_i$  are random variables which obey a probability distribution function (PDF)  $\mathcal{P}_{\{\varepsilon_i\}}(\varepsilon_1, \dots, \varepsilon_N)$ . If the single potentials do not depend on each other the disorder is uncorrelated and each single random value  $\varepsilon_i$  possesses the same PDF  $\mathcal{P}_\varepsilon(\varepsilon) \equiv \mathcal{P}(\varepsilon)$ , such that

$$\mathcal{P}_{\{\varepsilon_i\}}(\varepsilon_1, \dots, \varepsilon_N) = [\mathcal{P}(\varepsilon)]^N. \quad (6.14)$$

The strength of a disorder potential, denoted by a new parameter  $D$ , is proportional to the standard deviation of the PDF. It is an important energy scale, whose competition with interaction and tunneling energy may lead to a quantum phase transition. Thus, in the real-space representation correlations between on-site potentials on different sites vanish and

$$\langle V(\mathbf{r})V(\mathbf{r}') \rangle \sim \delta(\mathbf{r} - \mathbf{r}').$$

This is an important theoretical simplification which, however, is not always given in experiments. Especially in ultracold gases, where the system is intrinsically pure, disorder has to be added to the system artificially. Here, the experimentalists have to face the obstacle of creating true randomness in a controllable systematic way, which often leads to finite correlations in realized disorder potentials. Optical potentials with a finite correlation length of several lattice spacings are called quasi-periodic and represent intermediate systems between homogeneous and fully disordered [43, 229]. The best realization of an uncorrelated disorder constitute speckle potentials (see Sec. 6.2.2).

Given the disorder potential  $V(\mathbf{r}) = \sum_i \varepsilon_i \delta(\mathbf{r} - \mathbf{r}_i)$  the field representation of the corresponding Hamiltonian part reads

$$\begin{aligned} \mathcal{H}_{\text{dis}} &= \int d\mathbf{r} \hat{\Psi}^\dagger(\mathbf{r}) V(\mathbf{r}) \hat{\Psi}(\mathbf{r}) = \sum_{k,l} \int d\mathbf{r} \omega^*(\mathbf{r} - \mathbf{r}_k) \hat{c}_k^\dagger V(\mathbf{r}) \omega(\mathbf{r} - \mathbf{r}_l) \hat{c}_l \\ &= \sum_{k,l} V_{kl} \hat{c}_k^\dagger \hat{c}_l. \end{aligned} \quad (6.15)$$

In the derivation we used the fermionic field operators obeying anticommutation relations

$$\{\hat{\Psi}(\mathbf{r}), \hat{\Psi}(\mathbf{r}')\} = 0, \quad \{\hat{\Psi}^\dagger(\mathbf{r}), \hat{\Psi}^\dagger(\mathbf{r}')\} = 0, \quad \{\hat{\Psi}(\mathbf{r}), \hat{\Psi}^\dagger(\mathbf{r}')\} = \delta(\mathbf{r} - \mathbf{r}'),$$

and their Wannier representation in the lowest band approximation (compare with Eq. (3.24))

$$\hat{\Psi}(\mathbf{r}) = \sum_l \omega(\mathbf{r} - \mathbf{r}_l) \hat{c}_l .$$

The parameter  $V_{kl}$  in Eq. (6.15) is

$$\begin{aligned} V_{kl} &= \int d\mathbf{r} \omega^*(\mathbf{r} - \mathbf{r}_k) V(\mathbf{r}) \omega(\mathbf{r} - \mathbf{r}_l) \\ &= \sum_i \int d\mathbf{r} \omega^*(\mathbf{r} - \mathbf{r}_k) \varepsilon_i \delta(\mathbf{r} - \mathbf{r}_i) \omega(\mathbf{r} - \mathbf{r}_l) \\ &= \sum_i \omega^*(\mathbf{r}_i - \mathbf{r}_k) \varepsilon_i \omega(\mathbf{r}_i - \mathbf{r}_l) . \end{aligned}$$

In sufficiently deep lattices the Wannier functions are strongly localized such that the major contribution to the sum comes from the on-site terms  $k = l = i$ . Additionally, since the Wannier functions are normalized  $\int d\mathbf{r} |\omega(\mathbf{r} - \mathbf{r}_i)| = 1$ , in deep lattice potentials we can approximate their form by delta functions such that in the localization center  $|\omega(\mathbf{r}_i)| \approx 1$ . With this assumptions we get

$$\begin{aligned} V_{kl} &= \sum_i \omega^*(\mathbf{r}_i - \mathbf{r}_k) \varepsilon_i \omega(\mathbf{r}_i - \mathbf{r}_l) \\ &\approx \sum_i \varepsilon_i \delta_{kl} . \end{aligned}$$

Finally, the disorder potential part of the Hamiltonian (6.15) becomes

$$\mathcal{H}_{\text{dis}} = \sum_i \varepsilon_i \hat{n}_i .$$

In the special case of random on-site potentials, the homogeneous Fermi-Hubbard Hamiltonian given in Eq. (6.12) combined with  $\mathcal{H}_{\text{dis}}$  is called Anderson-Hubbard Hamiltonian and reads

$$\hat{\mathcal{H}} = - \sum_{\langle ij \rangle, \sigma} t_{ij} (\hat{c}_{i, \sigma}^\dagger \hat{c}_{j, \sigma} + h.c.) + \sum_i U_i \hat{n}_{i, \uparrow} \hat{n}_{i, \downarrow} - \sum_{i, \sigma} (\mu_\sigma - \varepsilon_i) \hat{n}_{i, \sigma} . \quad (6.16)$$

Hopping and interaction matrix elements, i.e.  $t_{ij}$  and  $U_i$ , are lattice dependent. Since the Wannier functions, on which the calculation of  $t_{ij}$  and  $U_i$  is based, depend on the lattice depth and thus on random potential on-site offsets, tunneling and interaction strength become random variables as well, see Fig. 6.3. In this case the system contains *diagonal* ( $\varepsilon_i$  and  $U_i$ ) as well as *off-diagonal* ( $t_{ij}$ ) disorder. Nevertheless, as a first approximation one can assume  $t_{ij} \equiv t$  and  $U_i \equiv U$ . Depending on the particular disorder type, this supposition is a good or a rough approach (see Sec. 6.2.2).

Compared to the homogeneous Hubbard model, the Anderson-Hubbard model is more complex since the translational symmetry is lost due to the randomness. Hence, similarly to the Fermi-Hubbard Hamiltonian, no general analytic exact solution exists so far.

### 6.2.2 Types of disorder

Due to the opportunity to measure in-situ atomic density profiles [116, 118], the control over inter-atomic interactions, the implementation of any spatial dimension and potential

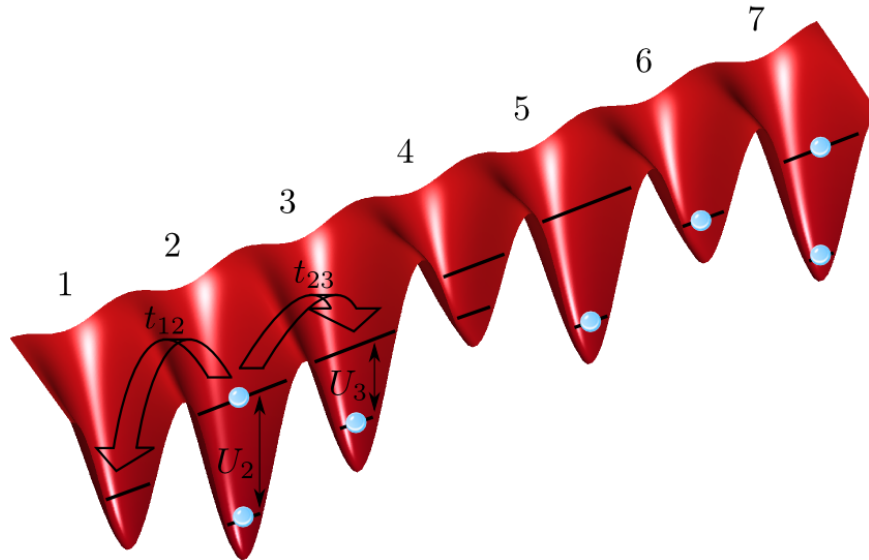


**Figure 6.3:** Tunneling and interaction in a disordered lattice. The potential offsets lead to shifts in the on-site spectra which reduce the tunneling between neighboring sites. Thus, the most probable hopping matrix element  $t_{ij}$  from site 1 to site 2 is smaller than between sites 2 and 3. The steeper the on-site potential the more localized are the Wannier functions. Functional dependence of the interaction matrix element on the Wannier states Eq. (3.57) leads to enhancement in the Coulomb repulsion. Therefore, in the illustration the most likely interaction strength  $U_i$  at site 2 is larger than at site 3.

landscape [117], ultracold quantum gases are well suited to be a toy model for studies on homogeneous Hubbard-type systems. Besides these advantages a unique possibility to design perfectly controlled disordered samples attracted the attention of the atomic gases community to the issue of Anderson localization [40, 230, 231], which can be investigated without accounting for additional effects like phonon processes [55]. In this section we will give a brief overview on the most common disorder types used in theory and/or experiments with ultracold gases. Although an implementation of a precise probability distribution is possible only in tunable optical lattices, different kinds of disorder and corresponding investigations serve as simulators for disordered solid matter, where the exact shape of the impurity potential is not known.

Before we proceed with an introduction of different disorder realizations, we would like to mention the different categories they can be divided into. One classification relies on the values the on-site energy offsets can take on. If their amplitudes are limited to some values or a certain closed energy interval the disorder is called *bounded*. If no such restrictions exist the disorder is *unbounded*. A further distinction concerns the possible offset values. One distinguishes between *continuous* and *discrete* distributions. While in the case of continuous disorder the probability for any value within an energy range is finite, discrete distributions allow only limited fixed values while the probability for the other energies is zero.

Although all kinds of disorder induce localization of matter waves - Anderson localization - in a certain parameter regime depending on the type of the given distribution the predicted phenomena can differ qualitatively.

### Box disorder

The box disorder is the most common used disorder type. It owes its name the constant probability distribution function in a fixed energy interval (see Fig. 6.4 (a)). For this kind of disorder the on-site energies  $\varepsilon_i$  are random variables, each distributed independently according to

$$\mathcal{P}(\varepsilon_i) = \frac{1}{2D} \Theta(D - |\varepsilon_i|), \quad (6.17)$$

where  $\Theta$  is a Heaviside function and  $D$  is the disorder strength. Since the values for  $\varepsilon_i$  are restricted to the range  $[-D; D]$  this disorder is continuous and bounded. In the limit  $D \rightarrow 0$  the homogeneous system is obtained. Up to now the box disorder has not yet been realized in experiments, however, it is widely used in theoretical investigations. It can serve to get a first grasp on disorder physics before specific distributions are applied in order to obtain more quantitative predictions.

The special feature of this disorder model is that offset amplitudes average out:  $\langle \varepsilon_i \rangle = \int d\varepsilon_i \mathcal{P}(\varepsilon_i) \varepsilon_i = 0$ . In this case we can assume site independent  $U$  and  $t$  in the Anderson-Hubbard Hamiltonian (6.16) to represent sample averaged matrix elements. This approximation is most accurate for this disorder type.

### Speckle disorder

A speckle disorder is created by superimposing an optical speckle field onto the homogeneous optical lattice. The speckle field is created by a laser beam which is scattered by a diffusive plate leading to a spatially distributed random intensity pattern. Superposition of a homogeneous potential laser field with a disordered one leads to the formation of a speckle-disordered optical lattice. For the first time a precise control over this kind of disorder was realized in Florence [232]. However, a correlation length of  $10 \mu\text{m}$  was appropriate for investigations of disorder effects in microtraps but too big to be assumed uncorrelated for optical lattices, where the lattice constant is  $532 \text{ nm}$ . A significant enhancement of the disorder length scale up to  $570 \text{ nm}$  was achieved within experiments in the group of DeMarco [233].

A statistical analysis of the scattering processes yields the probability distribution function of the resulting light intensity pattern [234]:  $\mathcal{P}(I) = \frac{1}{\langle I \rangle} \exp(-I/\langle I \rangle) \Theta(I)$ , where  $\Theta(I)$  corresponds to the Heaviside function and  $\langle I \rangle$  is the averaged light intensity. It is important to note that this distribution allows for infinite on-site energy values although their probability is exponentially small. Of course, in experiments the laser intensity is not tunable to infinitely large values, thus, the given analytical expression corresponds to the best approximation of experimental conditions. Since the lattice potential (lattice depth) experienced by an atom is proportional to the laser intensity (see Eq. (2.15)), the PDF describing disordered on-site energies is identical to the resulting distribution  $\mathcal{P}(I)$  in [234] and is given by

$$\mathcal{P}(\varepsilon_i) = \frac{1}{D} \exp\left(-\frac{\varepsilon_i}{D}\right) \Theta(\varepsilon_i). \quad (6.18)$$

$D$  denotes the disorder strength and is proportional to the speckle field strength [235]. Varying the speckle laser intensity, the disorder strength can be tuned to a desired value. The speckle disorder belongs to the class of unbounded continuous disorder, the PDF is shown in Fig. 6.4 (b).

### Quasi-periodic disorder

In experiments this type of disorder is realized by image projection of a randomly structured substrate onto a periodic optical system [236] or follows from a superposition with a

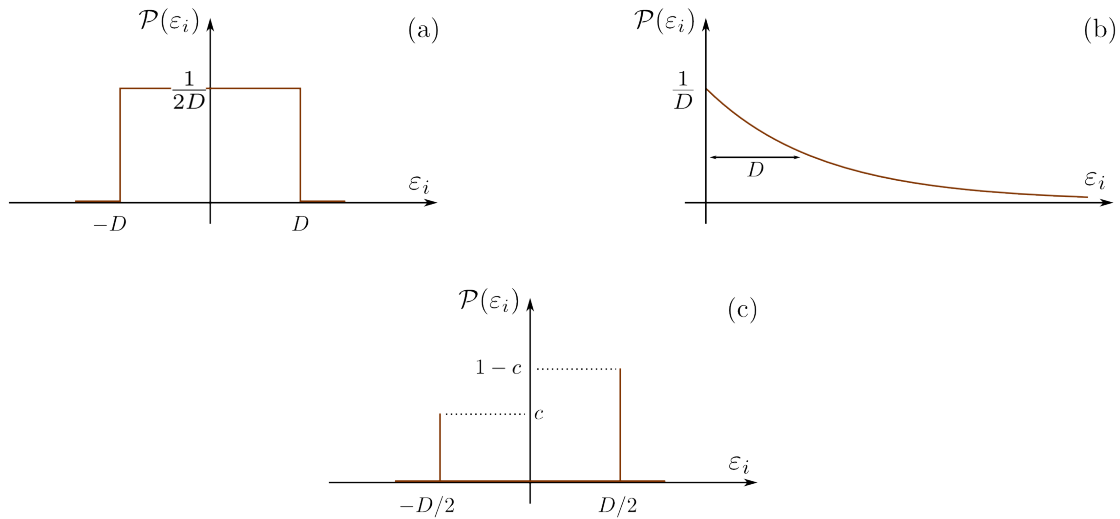


**Figure 6.4:** Probability distribution functions of the on-site energies for different disorder types. (a) In case of a box distribution the random on-site energies are equally probable and restricted to the range  $[-D; D]$ . (b) For speckle-disordered lattices energy shifts can take all (positive) values since this type of disorder is unbounded. The corresponding PDF, however, declines exponentially with increasing  $\varepsilon_i$ . (c) When binary disorder is implemented on-site offsets can take only two possible discrete values. Their occurrence corresponds to the impurity ratio/concentration in the sample.

second weaker lattice with non-commensurate spacing<sup>6</sup> [43, 237, 238]. The resulting lattice potential landscape (compare with Eq. (2.21)) becomes

$$V(\mathbf{r}) = V_{lat,0} \cos^2(\mathbf{k}\mathbf{r}) + V_2 [\cos^2(\mathbf{k}_1\mathbf{r}) + \cos^2(\mathbf{k}_2\mathbf{r})],$$

where  $V_{lat,0}$  and  $V_2$  denote the strength of the original homogeneous and added non-commensurate potentials respectively. Correspondingly, the wave vectors  $\mathbf{k}$  and  $\mathbf{k}_1, \mathbf{k}_2$  refer to the original and supplementary laser beams, whereby  $k_1 = k_2 \neq k$ . The pseudo-randomness is given by the ratio  $k_1/k$ . The on-site energies are calculated from the lattice potential via

$$\varepsilon_i = \int d\mathbf{r} \omega^*(\mathbf{r} - \mathbf{r}_i) V(\mathbf{r}) \omega(\mathbf{r} - \mathbf{r}_i),$$

where  $\omega(\mathbf{r} - \mathbf{r}_i)$  denote the Wannier functions. The strength of the disorder is controlled by the intensity of the second laser and allows continuous disorder amplitudes. Since the maximal energy offset is obtained when the maxima of both standing laser waves are superimposed and the minimal when both lasers interfere destructively, the possible amplitudes are bounded. However, since the realization is experiment-specific no uniform expression for the PDF exists. Nevertheless, a measurement of relative disorder offsets is possible and given as a histogram in [43].

In such quasi-periodic lattices the correlations of disorder potentials at nearby sites are finite. This leads to difficulties in the detection of localization due to compensation effects of inter-particle interactions, which become negligible only in the limit of weak correlations. In case of weak interactions, however, Anderson localization was predicted to appear also in correlated disordered systems [236].

<sup>6</sup>Such lattices are also referred to as bichromatic.

### Binary disorder

Binary disorder is created when additionally to a condensate, which has to be investigated, a second atomic species is loaded into a lattice and its degrees of freedom are subsequently eliminated or reduced such that particles become (almost) trapped on random lattice sites [154, 160]. The main species experiences a random potential mediated by the inter-species interactions. For the mobile species facing spatially varying interactions is equivalent to being in a lattice with distinct randomly distributed on-site potentials. Thus, the disorder strength can be adjusted via Feshbach resonances, which control the scattering length. The corresponding PDF of binary disorder is

$$\mathcal{P}(\varepsilon_i) = c\delta(\varepsilon_i + \frac{D}{2}) + (1 - c)\delta(\varepsilon_i - \frac{D}{2}),$$

where  $c$  represents the fraction of sites occupied by impurities and  $1 - c$  are the empty sites. In analogy, in solid matter the occupation fraction  $c$  corresponds to the impurity concentration. The disorder strength is proportional to the inter-species interaction strength in the weakly interacting regime. Contrary to previously discussed continuous disorder types, here the on-site energy can take only two values representing an impurity atom present at a lattice site  $i$  or not. The distribution is bounded and discrete, the corresponding PDF is shown in Fig. 6.4 (c).

Depending on the properties of added impurities one differs *quenched* and *annealed* disorder types. In case of quenched disorder the parameters characterizing the species, e.g. their positions, are time independent. Thus, each experimental measurement corresponds to a fixed disorder configuration and statistics based on different samples are required. Contrary, for annealed disorder the impurity atoms are allowed to change their position in time on a time scale larger than the dynamics of the original atoms. Consequently, within one experimental setup different configurations are created which implements an intrinsic averaging over various disorder samples. The main challenge in an experimental realization constitutes localization of impurities without simultaneous mobility reduction of the dynamic atoms.

## 6.3 Quantum phases

The Hubbard Hamiltonian was introduced to describe correlated fermionic systems in a lattice. By construction, the model characterizes the system depending on the interaction to tunneling ratio  $U/t$  and the filling. The kinetic term preferring to delocalize fermions over the lattice competes with the interaction term, which localizes fermions to lattice sites. Thus, at zero temperature the ground state displays either properties of delocalized (metallic) phase or of localized (insulating phase) particles. The transition between the two phases is triggered by the strength of the corresponding matrix elements.

In contrast to Bose-Hubbard Model, in the Fermi-Hubbard Hamiltonian the correlations influence the higher dimensional systems<sup>7</sup> less than one-dimensional lattices [239]. The reason is the absence of the long-range order in 1D [240]. In 2 and 3 dimensional systems the interactions have to exceed a critical  $U_c$  to induce a Metal-Mott insulator transition, whereas in 1D the metallic phase appears only at  $U = 0$  [241]. Since an analytic solution of the Hubbard model exists up to now only for 1D systems [215, 241], in higher dimensions only approximative numerical calculations yield the phase diagrams.

<sup>7</sup>Throughout this section higher dimensional systems refer to 2D and 3D.

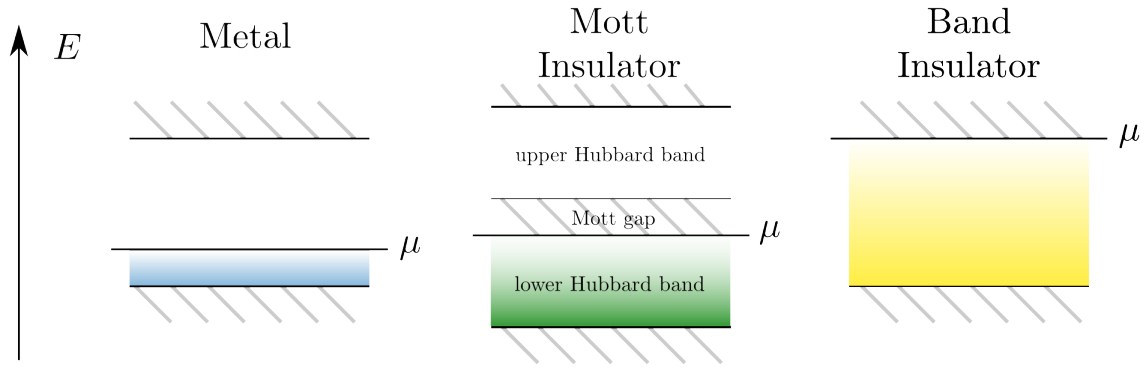


**Figure 6.5:** Classification of metallic and insulating phases based on band filling. If the filling of the highest occupied band is not commensurate (the chemical potential is within the band but not in the center) a material shows metallic properties. If the band is half-filled, i.e. every energy level is singly occupied by a fermion, a Mott insulator is formed in some materials. Here the Mott gap  $\sim U$  appears subdividing the original band into upper and lower Hubbard bands. When the chemical potential reaches or exceeds the top edge of the band a material becomes band insulating.

In this section we would like to give a brief overview over the phases of the homogeneous Fermi-Hubbard model regardless of the dimensionality. In particular, phases such as Metal, Mott insulator and band insulator will be characterized based on experimentally and/or theoretically accessible observables rather than critical parameters at which the transitions take place.

### 6.3.1 Insulators: Mott and band

Based on the non-interacting or weakly interacting electron picture first theoretical distinctions [242–244] between metal and insulator were introduced based on the filling of the bands: the energetically highest band is completely filled up with electrons in insulating materials and only partially in case of metals, see illustration Fig. 6.5. Equivalently, if the chemical potential lies within the band gap a material is in the *band-insulator* phase. Vice versa, if the chemical potential is within the band the systems show metallic properties.

Although the band theory successfully explained many materials, it failed to predict vanishing conductivity in *d*-electron transition-metal oxides [245]. The latter show insulating behavior for a partially filled conduction band which, referring to the previous theories, is supposed to be metallic. In 1937 Peierls was the first to mention that repulsive Coulomb interactions between electrons could prevent them from moving [183]. This idea pointed out the importance of correlation effects and opened the new research field of strongly correlated electrons. The most important theoretical explanations were provided by Mott [212, 246, 247] in whose honor this state is called *Mott insulator*. He explained insulating behavior based on a correlation-induced gap arising in the half-filled conduction band once all states within a band are singly-occupied. To populate the already occupied state with an additional electron the Coulomb repulsion has to be exceeded. This leads to a separation of the conduction band into two bands: a band originating from singly-occupied states and the energetically higher band of doubly populated sites, see Fig. 6.5. If the chemical potential lies in the energy gap between these bands the Mott insulator is created. Further studies of the phase and the phase transition revealed intricate properties. More evolved investigations of charge and spin fluctuations demonstrated mass-divergence and carrier-number-losses occurring at phase transitions which are in detail explained in [184].

### 6.3.2 Spectrum

The different phases are commonly discussed based on the excitation characteristics of a system. A single-particle excitation of a system has its origin in adding or removing a particle with momentum  $q$  and energy  $E(q)$ <sup>8</sup>. This is best described by the *single-particle spectral function*  $\rho(q, \omega)$ , which gives the probability to find an energy level at a frequency  $\omega$  with a momentum  $q$  occupied. It is important to note that only in free-electron systems individual excitations are real electrons, in weakly interacting systems the concept of quasi-particles - such as electrons dressed by fluctuations - is common [250]. The quasi-particles have a well-defined relation between frequency and momentum,  $\omega = E(q)$ , although the interacting dispersion  $E(q)$  is often not known explicitly. A frequently used theoretical approach to obtain electronic band structures is density functional theory (DFT) [251–253]. On the experimental side the angle-resolved photoemission spectroscopy (ARPES) allows the measurement of the band structure of a solid surface. Scattering of electrons via an angle-dependent beam of photons provides information about the energy and momentum distribution of extracted electrons.

Unlike in isolated atoms or molecules, in condensed matter the spectrum is not discrete but continuous, since the overlapping electronic orbitals of lattice ions lead to a band structure in the thermodynamic limit. Thus, a number of states may be available at every energy within a band, which is described by the *density of states* (DOS). In homogeneous systems, a high DOS indicates a large number of states accessible at a given energy, a vanishing DOS signals that no states exist, which marks a band gap.

Since the DOS characterizes the entire lattice, spectral contributions from impurities, lattice defects etc., are averaged. A local spectrum is referred to as *local density of states* and contains effects originating from the hybridization with direct neighbor-sites. Hence, inhomogeneities can lead to the formation of local or spatially limited additional energy states in the thermodynamic limit, which in consequence of the averaging, do not appear in the DOS but are visible in the LDOS [254, 255]. This property of the local spectrum becomes important for the identification of the Anderson localized phase as will be discussed later in this section. In homogeneous systems DOS and LDOS are identical.

### Green's functions

The mathematical definition of the local spectral function is given in terms of the retarded Green's function. In the following we will only give a brief overview of necessary terminology. Details of the Green's functions formalism can be found in [78, 256]. The retarded fermionic Green's function is defined:

$$G_{ij,\sigma}(t) = -i\theta(t)\langle\{\hat{c}_{i,\sigma}(t), \hat{c}_{j,\sigma}^\dagger(0)\}\rangle,$$

where the operator  $\hat{c}_{i,\sigma}(t)$  annihilates a fermion at site  $i$  at time  $t$  which was created by operator  $\hat{c}_{j,\sigma}^\dagger(0)$  at site  $j$  for  $t = 0$  and curly brackets indicate the anticommutator. Here, the expectation value is calculated in the grand canonical ensemble, which for an arbitrary operator  $\hat{A}$  is

$$\langle\hat{A}\rangle = \frac{1}{Z}\text{Tr}[e^{-\beta(\mathcal{H}-\mu\hat{N})}\hat{A}],$$

<sup>8</sup>There exist other excitations such as plasmons or sound excitations, which describe a collective response of the system to a disturbance. However, since this is not the topic of this thesis, we refer to further literature for details [248, 249].



with the Hamiltonian of the interacting system  $\mathcal{H}$ , the grand canonical partition function  $Z = \text{Tr} \exp[-\beta(\mathcal{H} - \mu\hat{N})]$  and the inverse temperature  $\beta = 1/k_B T$ . Evaluating the trace in the complete eigensystem of the grand canonical potential  $\{E_n, |n\rangle\}$  and performing the Fourier transformation leads to the Lehmann representation of the Green's function

$$G_{ij,\sigma}(\omega) = \frac{1}{Z} \sum_{n,m} \langle n | \hat{c}_{i,\sigma} | m \rangle \langle m | \hat{c}_{j,\sigma}^\dagger | n \rangle e^{-\beta E_n} \frac{e^{\beta(E_n - E_m)} + 1}{\omega - (E_n - E_m) + i\eta}, \quad (6.19)$$

where  $\eta = 0^+$ . From this representation it is clear, that the Green's function has poles at the excitation energies of the system. The corresponding local spectral function is defined as

$$\begin{aligned} \rho_{i,\sigma}(\omega) &= -\frac{1}{\pi} \text{Im} G_{ii,\sigma}(\omega) \\ &\stackrel{(6.19)}{=} \lim_{\eta \rightarrow 0} \frac{1}{Z} \sum_{n,m} \langle n | \hat{c}_{i,\sigma} | m \rangle \langle m | \hat{c}_{i,\sigma}^\dagger | n \rangle e^{-\beta E_n} \left( e^{\beta(E_n - E_m)} + 1 \right) \frac{\eta}{(\omega - (E_n - E_m))^2 + \eta^2} \\ &= \frac{1}{Z} \sum_{n,m} \langle n | \hat{c}_{i,\sigma} | m \rangle \langle m | \hat{c}_{i,\sigma}^\dagger | n \rangle e^{-\beta E_n} \left( e^{\beta(E_n - E_m)} + 1 \right) \delta(\omega - (E_n - E_m)). \end{aligned} \quad (6.20)$$

An excitation is possible only if the excitation energy matches an electronic transition. Poles of the spectral function mark such frequencies. Correspondingly, the DOS is obtained as the arithmetic average over the on-site spectra:

$$\langle \rho_{i,\sigma}(\omega) \rangle_a \equiv \rho_{a,\sigma}(\omega) = \frac{1}{L} \sum_i^L \rho_{i,\sigma}(\omega). \quad (6.21)$$

### Localized and delocalized states

Differences between the LDOS and the DOS of the system appear when potential inhomogeneities are present. To analyze the spectral features of a disordered system in more detail we have to draw our attention to the spectral representation of the Green's function Eq. (6.19). Since our further investigations will be concentrated on the zero temperature regime, we perform the following discussion in the  $T = 0$  limit. Using the resolvent operator  $1/(z - \mathcal{H})$  for a system described by a Hamiltonian  $\mathcal{H}$  the local Green's function<sup>9</sup> can be written as

$$G_{ii}(z) = \langle i | \frac{1}{z - \mathcal{H}} | i \rangle, \quad (6.22)$$

where  $z = \omega \pm i\eta$ , depending on whether a retarded or advanced Green's function is required. Given the non-degenerate eigensystem of the Hamiltonian  $\{|n\rangle, E_n\}$ , inserting the unity matrix  $\sum_n |n\rangle\langle n|$  into Eq. (6.22) yields

$$G_{ii}(z) = \sum_n \frac{\langle i | n \rangle \langle n | i \rangle}{z - E_n} \equiv \sum_n \frac{f_n}{z - E_n}. \quad (6.23)$$

Here  $f_n = \langle i | n \rangle \langle n | i \rangle$  represents the absolute square of the overlap of the eigenstate  $|n\rangle$  with the Wannier state  $|i\rangle$ . For simplicity the index  $i$  is dropped from  $f_n$ .

Localized and extended states can strictly only be distinguished in the infinite system, i.e. in the limit  $L \rightarrow \infty$ . The number of states increases linearly with the total number of

<sup>9</sup>The resolvent operator representation is not restricted to local descriptions, the corresponding general Green's function reads  $G_{ij}(z) = \langle i | \frac{1}{z - \mathcal{H}} | j \rangle$ .

lattice sites and hence also the number of summands in the Eq. (6.23). If the eigenstate  $|n\rangle$  is delocalized, there is a finite contribution on every site which decays  $\sim 1/L$  due to the normalization factor of the wave function  $1/\sqrt{L}$ . Thus, as  $L \rightarrow \infty$  the number of summands growth to infinity and the contribution of every new summand, also small, remains finite. On the other hand, if the state  $|n\rangle$  is localized the corresponding wave function decays exponentially away from the localization maximum [39]. Hence,  $f_n \sim \exp\{-2|\mathbf{r}_n - \mathbf{r}_i|/\xi_n\}$  with  $\mathbf{r}_n$  pointing at the site of the localization center of the eigenstate,  $|\mathbf{r}_n - \mathbf{r}_i|$  indicating the distance between the localization maximum and any arbitrary site  $i$  and  $\xi_n$  being the localization length. In the limit  $L \rightarrow \infty$  the factors  $f_n$  tend to well defined values  $f_n^\infty$  since new summands correspond to additional sites situated further away and lead to exponentially small contributions. This differences in the properties of  $f_n$  for  $L \rightarrow \infty$  can be used to distinguish between localized and extended states as we will see next.

The return probability introduced in Sec. 6.2.1, which is defined as the probability to find a particle initially located at site  $i$  at time 0 later at time  $t$  at the same site, is given by [257]

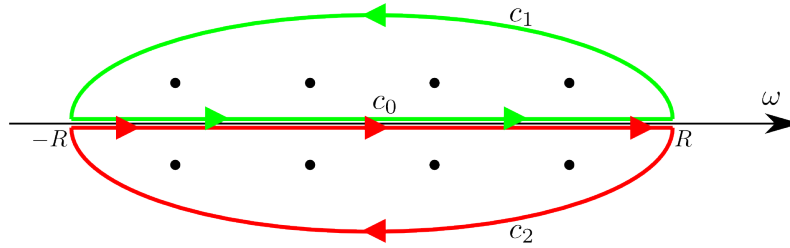
$$\mathcal{P}_{i \rightarrow i}(t) = |\alpha_i(t)|^2 = |G_{ii}(t)|^2, \quad (6.24)$$

where  $|\alpha_i(t)|^2$  is the amplitude of the single-particle wave function at site  $i$  resulting from the wave function expansion in the Wannier basis  $|\psi(t)\rangle = \sum_{j=1}^L \alpha_j(t)|j\rangle$ . Following the derivations in [257] one can show that

$$\lim_{t \rightarrow \infty} \mathcal{P}_{i \rightarrow i}(t) = \lim_{\eta \rightarrow 0} \frac{\eta}{\pi} \int_{-\infty}^{\infty} d\omega G_{ii}(\omega + i\eta) G_{ii}(\omega - i\eta). \quad (6.25)$$

The value of this integral, vanishing or finite, depends on the analytical properties of the Green's functions and distinguishes delocalized from extended states.

The integration along the real axis  $\int d\omega$  in Eq. (6.25) can be expanded to the complex plane  $\int dz$ :



The black dots indicate the singularities of the retarded and advanced Green's functions and green and red lines the two different integration paths, where

$$\int_{c_0} g(z) dz = \lim_{R \rightarrow \infty} \int_{-R}^R dz g(z), \quad (6.26)$$

$$\int_{c_1} g(z) dz = \lim_{R \rightarrow \infty} \int_0^\pi d\phi g(Re^{i\phi}), \quad (6.27)$$

$$\int_{c_2} g(z) dz = \lim_{R \rightarrow \infty} \int_{2\pi}^\pi d\phi g(Re^{i\phi}), \quad (6.28)$$

with  $g$  corresponding to the integrand of the Eq. (6.25). Cauchy's residue theorem [258] states that an integral of a function  $f$ , which is holomorphic in  $\mathbb{C} \setminus \{a_n\}$ , taken along a

closed path  $c$  in the clockwise direction which does not lead through any of the points  $\{a_n\}$  is given by the sum of residua, namely

$$\oint_c f(z)dz = 2\pi i \sum_n \text{Res}(f, a_n), \quad (6.29)$$

whereby the sum is taken only over  $a_n$  enclosed by the path  $c$ . A residue of a function with a simple pole at  $a$  can be calculated as follows:

$$\text{Res}(f, a) = \lim_{z \rightarrow a} (z - a)f(z). \quad (6.30)$$

Applying Cauchy's theorem to the integration over the green and red paths respectively leads to

$$\begin{aligned} 2\pi i \sum_n \text{Res}(g, i\eta + E_n) &\stackrel{(6.29)}{=} \oint_{\text{green}} g(z)dz = \int_{c_0} g(z)dz + \int_{c_1} g(z)dz, \\ -2\pi i \sum_n \text{Res}(g, -i\eta + E_n) &\stackrel{(6.29)}{=} \oint_{\text{red}} g(z)dz = \int_{c_0} g(z)dz + \int_{c_2} g(z)dz. \end{aligned}$$

The minus sign in the last line is due to the anticlockwise integration. The sum over both integrals simplifies to the original integration along the  $\omega$ -axis

$$\begin{aligned} 2\pi i \sum_n \left( \text{Res}(g, i\eta + E_n) - \text{Res}(g, -i\eta + E_n) \right) &= \oint_{\text{green}} g(z)dz + \oint_{\text{red}} g(z)dz \\ &= 2 \int_{c_0} g(z)dz + \int_{c_1} g(z)dz + \int_{c_2} g(z)dz \\ &= 2 \int_{c_0} g(z)dz \equiv 2 \int_{-\infty}^{\infty} g(\omega)d\omega \quad (6.31) \end{aligned}$$

due to the symmetry of the integrand used in the step from the second to the last line

$$\begin{aligned} \int_{c_1} g(z)dz + \int_{c_2} g(z)dz &\stackrel{(6.27),(6.28)}{=} \lim_{R \rightarrow \infty} \left( \int_0^\pi d\phi g(Re^{i\phi}) + \int_{2\pi}^\pi d\phi g(Re^{i\phi}) \right) \\ &= \lim_{R \rightarrow \infty} \left( \int_0^\pi d\phi g(Re^{i\phi}) - \int_\pi^{2\pi} d\phi g(Re^{i\phi}) \right) \\ &= 0. \end{aligned}$$

This means that the value of the integral in Eq. (6.25) and with it the return probability can be traced back to the residua of the Green's functions. The latter are calculated as follows

$$\begin{aligned} \text{Res}(g, i\eta + E_n) &= \lim_{z \rightarrow i\eta + E_n} (z - (i\eta + E_n))g(z) \\ &= \lim_{z \rightarrow i\eta + E_n} (z - (i\eta + E_n))G_{ii}(\omega + i\eta)G_{ii}(\omega - i\eta) \\ &= \frac{f_n^2}{2i\eta} \end{aligned}$$

and

$$\begin{aligned} \text{Res}(g, -i\eta + E_n) &= \lim_{z \rightarrow -i\eta + E_n} (z - (-i\eta + E_n))g(z) \\ &= \lim_{z \rightarrow -i\eta + E_n} (z - (-i\eta + E_n))G_{ii}(\omega + i\eta)G_{ii}(\omega - i\eta) \\ &= -\frac{f_n^2}{2i\eta}. \end{aligned}$$

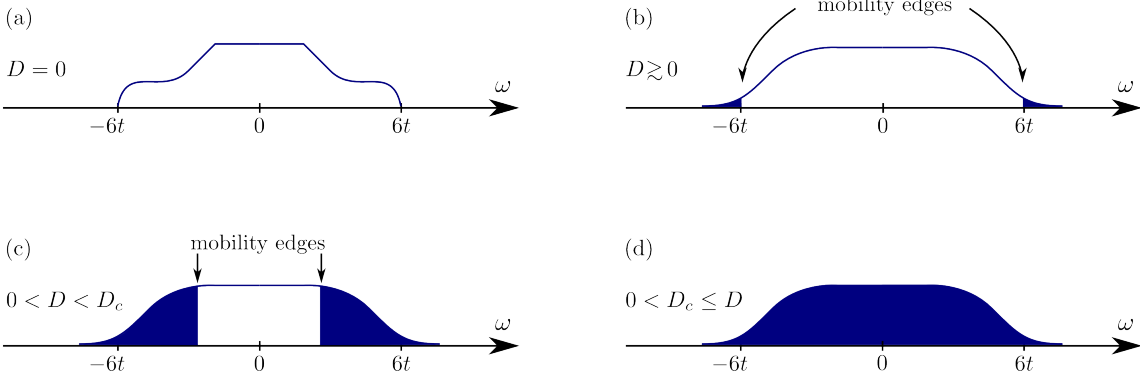


**Figure 6.6:** Effect of disorder on the density of states. (a) A sketched 3d DOS for a homogeneous system. (b) Weak disorder leads to formation of exponentially decaying band tails. The states within this edges are localized (blue area) and well separated from the delocalized (white area). The critical frequency, called mobility edge, indicates the border between the both. (c) Further increase of disorder strength shifts the mobility edges to the center of the band. (d) If  $D$  exceeds the critical disorder strength upper and lower mobility edges meet at the band center and all states become localized. The system is in the Anderson localized phase.

Putting these results into Eq. (6.31) leads the expression for the integral

$$\int_{-\infty}^{\infty} g(\omega) d\omega = \frac{\pi}{\eta} \sum_n f_n^2. \quad (6.32)$$

Finally, inserting Eq. (6.32) into Eq. (6.25) we derived the expression for the return probability based on the definition of the Green's function

$$\lim_{t \rightarrow \infty} \mathcal{P}_{i \rightarrow i}(t) = \lim_{\eta \rightarrow 0} \sum_n f_n^2. \quad (6.33)$$

Now, the importance of  $f_n$  is obvious for the characterization of the state  $|n\rangle$ . For extended states  $f_n \sim 1/L$ , as mentioned before, and consequently the summation vanishes in the thermodynamic limit since

$$\sum_n f_n^2 \sim \sum_n \frac{1}{L^2} = \frac{1}{L} \xrightarrow{L \rightarrow \infty} 0.$$

Thus, when the states are delocalized the return probability vanishes in the limit of infinitely large systems. Contrary to localized states, where  $f_n \xrightarrow{L \rightarrow \infty} f_n^\infty$  whereby  $f_n^\infty$  become exponentially small for new  $|n\rangle$  appearing with increasing system size. With this the sum  $\sum_n f_n$  converges and remains finite in the thermodynamic limit. This result perfectly corresponds to the interpretation given by Anderson (cf. Eq. (6.13)).

At the same time referring to the definition Eq. (6.22), finite values of  $f_n$  correspond to a dense distribution of poles with finite residua classifying the corresponding local Green's function as localized. On the other hand, extended states give rise to a branch cut in  $G_{ii}(\omega)$ .

Contrary to 1D and 2D systems in 3D localized and delocalized states are present for disorder strengths below a critical value. However, in the spectrum the localized states are clearly separated from extended ones by a boundary  $E_c$ , which is called *mobility edge* [259], see Fig. 6.6. In case of a degeneracy of states for any arbitrary energy level  $E_n$

a coexistence of extended and localized states is impossible. The localized state would immediately hybridize with the delocalized one which provokes delocalization. In one of his fundamental publications [260] Lifshitz investigated in detail the structure of the energy spectrum of elementary excitations in systems without spatial periodicity. He found that disorder leads to broadening of the original energy band and that states with energy lower than the band edge of the homogeneous system have to be stabilized by fluctuations. The latter produce an exponential decay in the density of states, see Fig. 6.6. The states associated with these energy levels are localized [255]. With increasing disorder strength also the energetically higher lying states become localized, which shifts the mobility edges towards the band center. Above a critical value, disorder finally localizes all states and the mobility edges merge in the band center.

### 6.3.3 Averaging

Up to now we have introduced the concept of spectral functions and pointed out the features for localized and delocalized states, which appear as a consequence of inhomogeneities in a lattice potential. However, when a problem with a random on-site potential is solved, the result depends on the disorder configuration chosen initially. Since only predictions from realization-independent results are meaningful, observables need to be averaged with respect to the probability distribution of the disorder<sup>10</sup>.

Depending on the method used, this issue is solved in different ways: some methods like R-DMFT (see Sec. 6.5.3) solve the problem for a set of disorder configurations and average over the observables afterwards, which makes sense when the method treats disorder non-perturbatively. Differently to this deterministic approach, an intrinsically statistical treatment is possible where the averaged correlation functions are incorporated from the start and adjusted selfconsistently during simulations<sup>11</sup>, like in the replica method, Keldysh technique or statistical DMFT [53, 261, 262]. Independent of the method of choice, it is obvious that due to randomness of on-site energies all observables become randomly distributed obeying probability distribution functions. Thus, to ensure an accurate description of disordered systems one must account for the corresponding PDFs.

### Probability distribution function

Since the results presented in this thesis concern mainly the spectral properties of a disordered system, we would like to explain the concept of PDF and averaging using the local density of states  $\rho_i(\omega)$  defined in Eq. (6.20). The distribution of LDOS serves to characterize spatial fluctuations in the system.

In non-interacting homogeneous systems a delocalized single-particle eigenstate  $\psi_i^{(0)}$  with an eigenenergy  $\varepsilon_0$  is described by the PDF

$$\text{(homogeneous system):} \quad \mathcal{P}[\rho_i(\varepsilon_0)] = \delta(\rho_i - \rho_0),$$

where  $\rho_0 \equiv \rho_i(\varepsilon_0) = |\psi_i^{(0)}|^2$  denotes the density of states. Since in homogeneous lattices the extended wave function is constantly spread over the entire lattice, the probability to find the local amplitude  $\rho_0$  is equal on every site which leads to a delta-shaped distribution function as shown in Fig. 6.7.

<sup>10</sup>In experiment, a large sizes of systems lead to self-averaging, i.e. the small parts of the system can be assumed as independent. Thus, in many cases, already few disorder realizations are statistically sufficient.

<sup>11</sup>A widely used selfconsistent numerical approach for the PDF of local single-particle Green's functions  $\mathcal{P}[G_{ii}(\omega)]$  was first implemented by Abou-Chacra *et al.* [254] and is referred to as the *local distribution approach*.

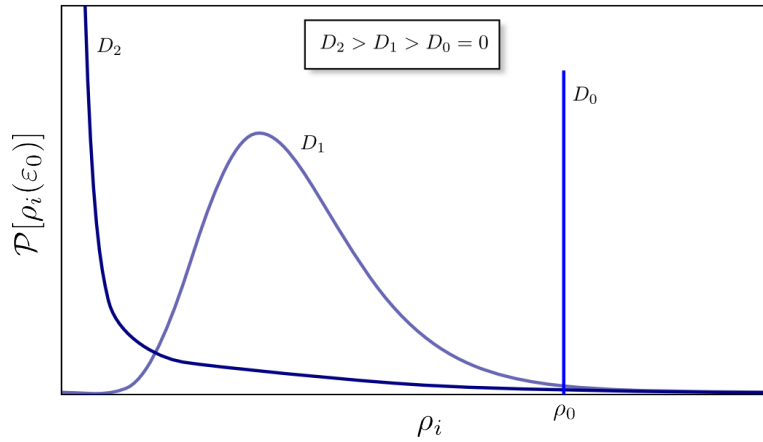


**Figure 6.7:** Illustration of the probability distribution function of the local density of states. A delta-distribution indicates a homogeneous system ( $D_0 = 0$ ) where a state at eigenenergy  $\varepsilon_0$  with the spectral weight  $\rho_0$  is delocalized and the corresponding wave function is homogeneously spread over all lattice sites. With increasing disorder strength the amplitude of the wave function redistributes: scattering processes enhance the probability to find a particle within a certain area. This leads to the emergence of a tail in the distribution, reflecting an increased LDOS on a small finite number of sites. The maximum of the distribution is shifted to values lower than  $\rho_0$  due to lower LDOS on the large number of remaining sites.

When the lattice potential is disordered the on-site energies on each site are shifted with respect to each other leading to a reduced hybridization of states. Correspondingly, the spectral weight of a state is spread unequally over a finite number of states and the PDF broadens: few sites carry more spectral weight (the tail of the distribution) and the majority of sites less spectral weight (the maximum of the distribution, which is shifted to  $\rho_i < \rho_0$ ). Finally, an Anderson localized state has a wave function whose amplitude is maximal on few sites and decays exponentially else. Here, the most spectral weight is distributed among few sites whereby the rest of the lattice contributes only marginally. Thus, when randomly choosing a site, the probability to find exactly the localization center is very low while a small amplitude of the wave function is very likely. The characteristic corresponding probability distribution function has a long tail and a maximum at vanishing  $\rho_i$ , as illustrated in Fig. 6.7. For two- and  $(2 + \varepsilon)$ -dimensional systems, Altshuler *et al.* [225] found that the LDOS distribution is of the Gaussian form with logarithmically decaying asymptotic behavior and develops pure log-normal behavior when the Anderson transition is approached. In 1D chains  $\mathcal{P}[\rho_i(\omega)]$ , was also shown to be of log-normal form [263]

$$\mathcal{P}[\rho_i(\omega)] = \frac{1}{\sqrt{2\pi\sigma^2}} \frac{1}{\rho_i(\omega)} \exp\left(-\frac{(\ln(\rho_i(\omega)) - x_0)^2}{2\sigma^2}\right),$$

where  $x_0$  and  $\sigma$  are the mean and the standard deviation respectively. These analytic predictions have been reproduced in numerical simulations for two- and three-dimensional lattices of different types via the kernel polynomial method. Furthermore, the finite-size scaling behavior of the LDOS's PDF has been shown to reveal the Anderson localization [264].

Due to the asymmetry of the log-normal PDF, the most probable value has to be identified: the *typical* value  $\rho_{\text{typ}}(\omega)$ . This value characterizes the system and recovers the translational invariance also in disordered lattices [48]. Furthermore, with increasing disorder strength the localization rises and the typical value approaches zero, indicating a vanishing spectral

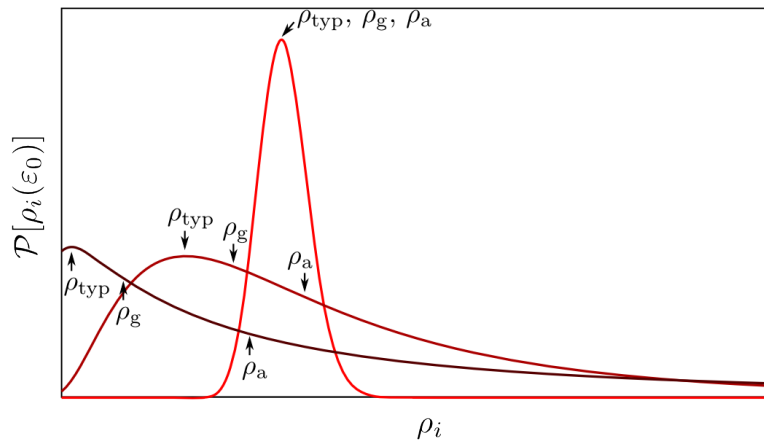


**Figure 6.8:** Illustration of LDOS probability density function characterized by arithmetic and geometric means. The geometric average approximates the typical value of the PDF best while the arithmetic average is displaced further away with increasing asymmetry in the distribution.

weight of a state on most lattice sites. In principle, it is possible to obtain the LDOS PDF via photoemission spectroscopy or by numerical calculations. However, the latter is very demanding if the particles are interacting. Thus, an appropriate parameter is needed to represent a disordered statistical ensemble.

### Arithmetic average

The arithmetic average is commonly used to characterize a statistical distribution. It is defined as

$$\rho_a(\omega) = \langle \rho_i(\omega, \{\varepsilon_1, \dots, \varepsilon_L\}) \rangle_a = \frac{1}{NL} \sum_{j=1}^N \sum_{i=1}^L \mathcal{P}(\varepsilon_i) \rho_i(\omega, \{\varepsilon_1, \dots, \varepsilon_L\}_j), \quad (6.34)$$

for a given set of  $N$  disorder configurations and  $L$  sites. However, a description of a system based on arithmetically averaged values only is meaningful if during the time evolution the full phase space is available to a particle. In such samples the system and corresponding observables are called *self-averaging*. This is not always the case, as for example at the transition to Anderson localization. The long tail of the distribution causes a shift in the arithmetic average away from the most probable value. Since this asymmetry persists with increasing disorder, the arithmetic average does not vanish, contrary to the typical value, and therefore does not represent the properties of disordered ensembles accurately. Here, the most probable value of the PDF does not coincide with the arithmetic mean given by Eq. (6.34), see Fig. 6.8.

Since the arithmetic average describes the total density of states, this result indicates that when the states are extended the LDOS is a continuous function of frequency in infinite systems and so is the DOS. However, for localized states the DOS remains continuous, while the LDOS becomes discrete.

### Geometric average

A more efficient approach than a full PDF calculation, and more reliable than the arithmetic mean, is the typical medium theory (TMT) [54]. Within this method, an appropriate

parameter is defined which best approximates the most probable value  $\rho_{\text{typ}}(\omega)$  and shows the same critical behavior at the Anderson transition as  $\rho_{\text{typ}}(\omega)$  – the geometric average.

The geometric average for one disorder configuration is defined by

$$\begin{aligned} \langle \rho_i(\omega, \{\varepsilon_1, \dots, \varepsilon_L\}) \rangle_{\text{geom}} &= \exp \left( \frac{1}{L} \sum_i^L \mathcal{P}(\varepsilon_i) \ln [\rho_i(\omega, \{\varepsilon_1, \dots, \varepsilon_L\})] \right) \\ &= \left[ \rho_1^{\mathcal{P}(\varepsilon_1)}(\omega, \{\varepsilon_1, \dots, \varepsilon_L\}) \cdots \rho_L^{\mathcal{P}(\varepsilon_L)}(\omega, \{\varepsilon_1, \dots, \varepsilon_L\}) \right]^{1/L}. \end{aligned}$$

In contrast to the arithmetic average, the values to be averaged over are multiplied and an  $L^{\text{th}}$ -order root is taken subsequently. Consequently, this parameter is very sensitive to localization, since as soon as the LDOS  $\rho_i(\omega, \{\varepsilon_1, \dots, \varepsilon_L\})$  vanishes at even one site  $\langle \rho_i \rangle_{\text{geom}}$  becomes zero. On the other hand, the arithmetic average vanishes only when all on-site spectra vanish, which never occurs since every state always possesses finite spectral weight within a system. Disorder simply leads to a redistribution of this weight among the lattice sites. Thus, in order to identify the transition from delocalized to the Anderson localized phase based on the PDF of the LDOS,  $\langle \rho_i \rangle_{\text{geom}}$  is a reliable parameter which represents the typical value, as shown in Fig. 6.8. However, the numerical implementation holds a couple of pitfalls resulting from finite energy resolution, such that a finite-size scaling behavior rather than a proper value of  $\langle \rho_i \rangle_{\text{geom}}$  should be associated with localization. A more detailed description of this problem in non-interacting systems was presented in [265]. The scaling properties of the geometric mean in correlated systems are investigated within this thesis in Sec. 7.

The averaging procedure also has to account for different disorder realizations. In this thesis, the average over different disorder configurations corresponds to the arithmetic average of geometric means, namely

$$\begin{aligned} \rho_g(\omega) &= \frac{1}{N} \sum_j^N \langle \rho_i(\omega, \{\varepsilon_1, \dots, \varepsilon_L\}_j) \rangle_{\text{geom}} \\ &= \frac{1}{N} \sum_j^N \exp \left( \frac{1}{L} \sum_i^L \mathcal{P}(\varepsilon_i) \ln [\rho_i(\omega, \{\varepsilon_1, \dots, \varepsilon_L\}_j)] \right) \\ &= \frac{1}{N} \sum_j^N \left[ \rho_1^{\mathcal{P}(\varepsilon_1)}(\omega, \{\varepsilon_1, \dots, \varepsilon_L\}_j) \cdots \rho_L^{\mathcal{P}(\varepsilon_L)}(\omega, \{\varepsilon_1, \dots, \varepsilon_L\}_j) \right]^{1/L}. \end{aligned} \quad (6.35)$$

In some publications [266], however, the difference between averaging over the system or over the set of configurations is not emphasized and the geometric average is calculated as

$$\text{(not true generally)} \quad \rho_g(\omega) = \exp \left( \frac{1}{LN} \sum_{i=1}^L \sum_{j=1}^N \mathcal{P}(\varepsilon_i) \ln [\rho_i(\omega, \{\varepsilon_1, \dots, \varepsilon_L\}_j)] \right). \quad (6.36)$$

For sufficiently large systems, this difference does not play a role and the results of Eq. (6.35) and (6.36) coincide. However, for small to intermediate systems, the finite energy resolution compensated by artificial spectral broadening masks the localization: when the localization length  $\xi$  exceeds the system size  $L$  or becomes smaller than the broadening, a state appears extended. Hence, only the scaling behavior of the system size can reveal the true nature of a state. In contrast, averaging over disorder realizations only reduces the statistical deviations. The expression (6.36), however, suggests equal



statistical meaning for both parameters, which can be misunderstood in the sense that the number of sites and realizations can compensate each other and therefore can be treated on equal footing. In this case a localized state may be incorrectly classified as delocalized.

### 6.3.4 Charge gap

For  $T = 0$ , the charge gap is defined as the energy difference between a system with an electron added and a system with an electron removed [241]

$$G = E(N + 1) + E(N - 1) - 2E(N), \quad (6.37)$$

where  $E(N)$  is the many-body ground state energy for  $N$  particles. This observable can be directly related to collective particle-hole excitations described by the conductivity if the propagation of the particle is not correlated with that of the hole. Then this excitation can be decomposed into its individual constituents: a particle in an excited state (compared to the original configuration), which is related to a system with an electron added, and a hole in the original ground state, which corresponds to a system with a particle removed. Since, according to the previous discussion, finite conductivity indicates the existence of electron-hole states energetically close to the ground state, the values  $E(N + 1)$ ,  $E(N)$  and  $E(N - 1)$  become equal in metallic phase and the gap vanishes. Vice versa, a finite gap corresponds to a vanishing conductivity in an insulator.

Nevertheless, in this description two-particle processes, like e.g. the formation of a Cooper-pair in a superconductor, are not included and the corresponding contribution to the DC conductivity will be missed. Instead the gap in the one-particle excitation spectrum would be mistakenly assigned to an insulating phase. At the same time, the existence of excited states arbitrarily close to the ground state does not necessarily lead to metallic behavior. As already mentioned in the criteria for a finite conductivity, excited states must be spatially extended to carry charge through the entire system. To tie up to previous discussions on spectra, the DOS has to be finite at the Fermi energy. Randomly distributed but spatially localized states lead to a finite LDOS near the Fermi edge and thus to a vanishing gap, but do not contribute to charge transport. Such systems are called Anderson insulators (see Sec. 6.2.1).

At finite temperatures the definition Eq. (6.37) is no longer valid. However, for  $k_B T < G$  thermal excitations remain below the zero-temperature energy-gap barrier such that the system remains an insulator. At higher temperatures the gap is smeared out or even shifted, as is the case in semi-conductor optics [267].

Despite the discussed obstacles, a charge gap calculation is easy to implement numerically and serves, in combination with supplementary observables, for quantum phase characterization.

### 6.3.5 Conductivity

Another observable used to distinguish a metal from an insulator is the electrical conductivity. Since this observable measures the response of the system to an external field, the characterization happens, strictly speaking, out of equilibrium. However, if small fields are applied they can be treated as a perturbation such that the system can be considered to

be close to thermal equilibrium. By means of linear response theory [268] the corresponding conductivity tensor is derived from an *equilibrium* current-current correlation function  $\langle \hat{n}_i^\dagger(\tau) \hat{n}_j(0) \rangle$ , which describes the propagation of a particle-hole pair in the lattice. For an arbitrarily weak applied field the latter is only possible if close to the Fermi level states exist, which are extended over the system. A vanishing conductivity at  $T = 0$  clearly indicates an insulator and a finite conductivity value is the hallmark of metals [267]. Particularly, for exponentially localized states there is no DC conductivity. Since transport can only occur between states of the same energy in the same neighborhood, for localized states random shifts of energy levels produced by the on-site disorder prevent tunneling.

At finite temperatures thermal excitations lead to current transport even in zero-temperature insulators and a distinction between “metal” and “insulator”, strictly speaking, is no longer possible. Experimentally, both are distinguished when the magnitudes of corresponding conductivities are compared, i.e. metals exceed the conductivity of insulators by orders of magnitude. However, semimetals and semiconductors show comparable DC properties at room temperature and can be classified as metal and insulator respectively only at low temperatures. Thus, only in the limit  $T \rightarrow 0$  this distinction is strictly possible.

A calculation of the current-current correlator, e.g. by means of the Green’s function formalism, is possible but also challenging due to electron-hole interactions. An easier way to analyze the transport properties is based on single-electron excitations.

### 6.3.6 Compressibility

The compressibility is defined as:

$$\kappa = \frac{\partial n}{\partial \mu} \quad (6.38)$$

and gives the variation of the particle density under the variation of the chemical potential. An alternative formulation for  $T = 0$  is based on the ground state energy

$$\frac{1}{n^2 \kappa} = \frac{\partial^2 e_0(n)}{\partial n^2}, \quad (6.39)$$

with the ground state energy density  $e_0(n) = E_0(n)/L$ , total ground state energy  $E_0$  and system size  $L$ . As depicted in Fig. 6.5, in insulating phases (band and Mott) the chemical potential lies within the band gap where no states exist. If no states can be populated changes of  $\mu$  do not lead to a change of the particle number. Thus, a vanishing compressibility indicates an insulating regime. In the metal, however, the compressibility is finite. Special attention must be paid to disorder dominated systems. Since irregular potential offsets on different sites lead to energetically randomly distributed local states, their (de-)population via adjustment of the  $\mu$  is possible, which reflects in a finite compressibility. However, like in the case of charge gap, the spatial confinement of wave functions prevents macroscopic charge transport - one of the criteria for the existence of a true metal. Hence, analyzing e.g. disordered systems via the compressibility alone leads to a wrong classification of the Anderson insulator as a “metal”.

Similar to the charge gap, this observable reflects the single-particle properties of the system and is therefore computationally less demanding to address than higher correlators. In combination with observables clearly indicating the missing properties, such as the wave function localization, the compressibility can be used to distinguish different quantum phases.

### 6.3.7 Participation ratio and inverse participation number

The localization properties of a system can be quantified by means of the participation ratio. Bell and Dean [269] have introduced this quantity for the first time in 1970 for non-interacting systems. For an eigenstate  $|i\rangle$  to an eigenvalue  $\omega_i$  with the wave function in the Wannier representation  $\psi_j(\omega_i)$ , where  $j$  is the site index, the *participation ratio* (PR) is given by

$$P(\omega_i) = \frac{1}{L \sum_{j=1}^L |\psi_j(\omega_i)|^4}. \quad (6.40)$$

Additionally to  $P$ , a related quantity - the *inverse participation number* (IPN), is defined as

$$I(\omega_i) = \sum_{j=1}^L |\psi_j(\omega_i)|^4. \quad (6.41)$$

The meaning of these quantities becomes apparent by a simple example. Suppose the wave function corresponding to an energy level  $|i\rangle$  spreads over  $c$  lattice sites with equal amplitude  $|\psi_j(\omega_i)|^2 = 1/c$  and vanishes elsewhere. Then the defined quantities are

$$\text{localization:} \quad P(\omega_i) = \frac{c}{L} \quad I(\omega_i) = \frac{1}{c}.$$

Thus, it is obvious that  $P(\omega_i)$  gives the ratio of sites contributing to this state, whereas  $I(\omega_i)$  represents the inverse of the number of sites where a given state has a significant amplitude. In the thermodynamic limit  $\lim_{L \rightarrow \infty} P(\omega_i) \sim 1/L$  vanishes and  $I(\omega_i)$  remains constant, since it does not depend on the system size. For a maximally localized state (only on one site) the IPN becomes 1 which is the upper bound for this observable.

Rather than in this simplification, the interference of the particles, which bounds the wave packet to a finite region, leads to an exponentially decreasing amplitude outside of this region characterized by the localization length  $\xi(\omega_i)$ . In this case  $I(\omega_i)$  scales with the system size. For periodic boundary conditions it is

$$\text{exponential localization:} \quad I(\omega_i) = I_\infty(\omega_i) \coth[L/\xi(\omega_i)], \quad (6.42)$$

with  $I_\infty(\omega_i) = 1/\xi(\omega_i)$  (for a detailed calculation see App. G).

In a homogeneous system the single-particle eigenstates are delocalized and described by plane waves  $\psi_j(\omega_i) = \exp(i\mathbf{k}_i \mathbf{r}_j) / \sqrt{L}$  in the Wannier representation, where  $\mathbf{k}_i$  denotes a pseudo-momentum corresponding to the eigenvalue  $\omega_i$ . Using this definition, PR and IPN defined by Eq. (6.40) and (6.41) take on the values

$$\text{delocalization:} \quad P(\omega_i) = 1 \quad I(\omega_i) = \frac{1}{L}.$$

Thus, unlike for localized states, delocalization is indicated by a constant participation ratio  $P(\omega_i)$ , whereas the inverse participation number  $I(\omega_i)$  vanishes as  $1/L$  when the  $L \rightarrow \infty$  limit is considered.

Thus, the scaling behavior with the system size gives insight into localization or delocalization properties driven by disorder or interaction. Since both quantities characterize localization equivalently, it is enough to analyze the system based on one of them. Unfortunately, in the course of time, the naming of the observables has been mixed such that

for a unique identification the reader is encouraged to consider the given mathematical definitions.

In an interacting system the IPN is defined as [59]

$$I(\omega) = \frac{\sum_i^L \rho_i(\omega)^2}{(\sum_i^L \rho_i(\omega))^2}, \quad (6.43)$$

where  $\rho_i(\omega)$  is the local density of states defined in Eq. (6.20). Similarly to the non-interacting case, in the thermodynamic limit the delocalized states are expected to lead to a vanishing IPN, while in the localized phase the IPN remains finite for  $L \rightarrow \infty$ .

As mentioned before, in disordered systems a mobility edge  $\omega_c$  separates extended states from localized ones in the energy spectrum. Generalizing the above example to any dimension  $D$  and taking the thermodynamic limit in a localized phase, one has  $P(\omega) \rightarrow 0$  for  $\omega \rightarrow \omega_c$ . This implies that the single-particle state at  $\omega = \omega_c$  only extends over an infinitesimal fraction of the volume  $L^D$ . However, since at  $\omega_c$  the state  $\psi(\omega_c)$  has to be extended as well, it follows that the wave function has to be fractal. This issue is discussed in more detail by Aoki [270]. The scaling of  $P$  and  $I$  as a function of the energy difference  $\omega - \omega_c$  was calculated by Wegner within the non-linear sigma-model [271].

In non-interacting  $1D$  systems localization is expected to occur at any finite disorder strength [61, 215, 272] and the wave functions for all energies are supposed to be localized in thermodynamic limit. For any finite systems the localization length  $\xi(\omega)$  may exceed the system size. Hence, only for system sizes that are several times larger than the localization length an insulator can be distinguished from a metal. This property makes a careful finite-size scaling of PR and IPN essential. Especially in the presence of interactions a clear separation of interaction effects from finite-size effects is required.

## 6.4 Finite temperatures

The theory of quantum phase transitions is strictly applicable only in the  $T = 0$  limit. Likewise, the characterization of a metal and an insulator based on critical behavior of appropriate observables fails at finite temperatures. For  $T > 0$  thermal excitations lead to a finite DC conductivity, which masks the true nature of the phase explored at  $T = 0$ , and leads to a classification of materials in “good” and “bad” conductors. Instead of the phase transition a crossover is observed [184], see Fig. 6.9.

Within this crossover regime one speaks of semi-metals and semi-conductors. Similarly to a metal, in a semi-metal there exists no gap between the bands. However, the conductivity is based on the conduction and valence band crossing the Fermi level. Therefore the density of states at the Fermi energy is very low and correspondingly the conductivity. In the same way as in metals, the conductivity decreases with increasing temperature due to phonon excitations interacting with tunneling electrons. In semi-conductors the charge-gap separates conduction from the valence band, however the extend of the gap is smaller than in normal insulators. Thus, conduction properties are based upon thermal excitations which leads a thermal behavior different from metals/semi-metals. With increasing temperature the conductivity of semi-conductors increases<sup>12</sup>.

<sup>12</sup>More precise, the conductivity shows a non-monotonic behavior as a function of  $T$  due to activation of different charge carriers, for more details see [77].

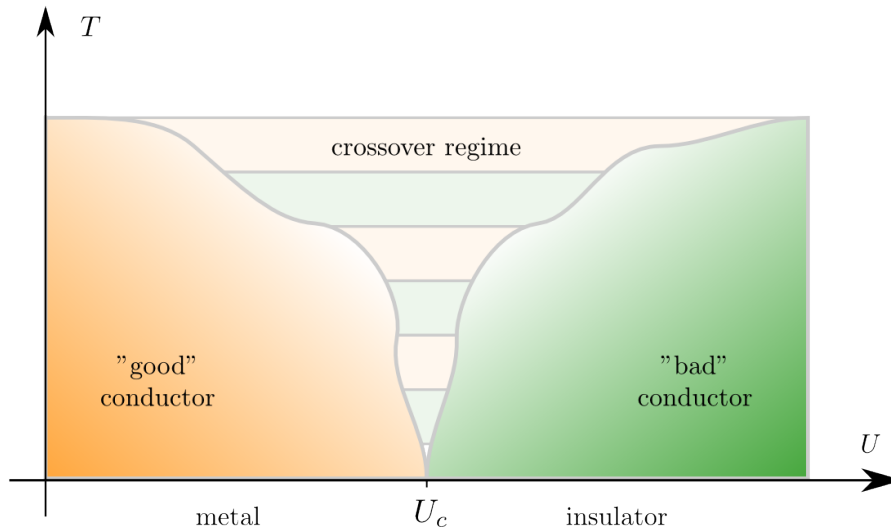


**Figure 6.9:** Illustration of the metal-insulator transition. At zero temperature a true quantum phase transition between metallic and insulating phases is triggered by the interaction. For  $T > 0$  instead of a sharp transition a crossover between “good” and “bad” conductors exists which contains semi-metals and semi-conductors.

## 6.5 Numerical method: DMFT

Although the Fermi-Hubbard model is one of the simplest, due to the approximations and simplifications included, that nonetheless describes the physics for a wide range of systems, it is generally not exactly solvable in 2D and 3D. In one spatial dimension it was solved analytically by E. Lieb and F.-Y. Wu in 1968 [241]. They found that for  $T = 0$  in the thermodynamic limit at half-filling the Mott insulating phase is present at any finite repulsive interaction strength<sup>13</sup>. The investigated homogeneous systems showed metallic properties only in the case of non-interacting particles and away from half-fillings.

In order to obtain and characterize phase diagrams of the fermionic Hubbard Hamiltonian in higher dimensions or for non-homogeneous systems, approximative and exact numerical methods are required. The most common are exact diagonalization (ED), quantum Monte Carlo (QMC), density matrix renormalization group (DMRG) and dynamical mean-field theory (DMFT). Within exact diagonalization, the Fermi-Hubbard Hamiltonian is diagonalized numerically. This procedure, however, holds several restrictions on investigated systems due to computational limitations. Since the dimension of the matrix to be diagonalized scales exponentially with the particle and lattice site number, this method is only applicable to small systems [274–276]. With the QMC technique studies of comparably small system sizes are possible at zero and finite temperatures, however, the method suffers from the so-called sign problem [133, 277–279]. DMRG is based on a matrix product state variational formulation and is a commonly used approach to solve interacting and/or non-homogeneous quantum problems. The disadvantage of this method is, that up to now it is applicable to one dimensional problems only [280]. The method of choice in this thesis is DMFT, which approximates the lattice problem with many degrees of freedom by an effective single-site model with less degrees of freedom. Hereby, the spatial fluctuations are neglected but the local quantum fluctuations are fully taken into account. This tech-

<sup>13</sup> In the extended Fermi-Hubbard model including the next-nearest neighbor hopping a richer phase diagram is obtained [273].

nique allows a non-perturbative treatment of a broad range of parameters and, as every mean-field method, provides qualitatively good results in higher dimensions [208, 281–284].

In this chapter we will give a brief introduction to the DMFT method, sketch the used impurity solver NRG and MPT and present the real-space extension of DMFT, known as R-DMFT.

### 6.5.1 DMFT

We start with the fermionic Hubbard model

$$\hat{\mathcal{H}} = - \sum_{\langle ij \rangle, \sigma} t_{ij} (\hat{c}_{i\sigma}^\dagger \hat{c}_{j\sigma} + h.c.) + U \sum_i \hat{n}_{i\uparrow} \hat{n}_{i\downarrow} - \sum_{i, \sigma} \mu_\sigma \hat{n}_{i\sigma}, \quad (6.44)$$

where  $\sigma \in \uparrow, \downarrow$  labels spin, while  $\hat{c}_{i\sigma}^\dagger$ ,  $\hat{c}_{i\sigma}$  and  $\hat{n}_{i\sigma}$  are the creation, annihilation and particle number operators for an electron on site  $i$  with spin  $\sigma$ . The summation  $\sum_{\langle ij \rangle}$  refers to nearest neighbors.  $U$  is the on-site interaction,  $t_{ij}$  the nearest-neighbor tunneling matrix element and  $\mu_\sigma$  the chemical potential. In the absence of an external magnetic field the chemical potential becomes independent of spin direction<sup>14</sup>, otherwise spin imbalance can be implemented choosing  $\mu_\uparrow \neq \mu_\downarrow$ . For the sake of simplicity we drop the spin index and concentrate on spin balanced cases. The corresponding partition function can be written as a path integral over the Grassmann variables  $c_{i\sigma}$  and their complex conjugates  $c_{i\sigma}^*$

$$Z = \int \prod_{i, \sigma} Dc_{i\sigma}^* Dc_{i\sigma} e^{-S}. \quad (6.45)$$

For details of derivation see [256, 285, 286]. The action  $S$  corresponding to the Hubbard Hamiltonian is given by

$$S = \int_0^\beta d\tau \left( \sum_{i\sigma} c_{i\sigma}^*(\tau) (\partial_\tau - \mu) c_{i\sigma}(\tau) - \sum_{\langle ij \rangle, \sigma} (t_{ij} c_{i\sigma}^*(\tau) c_{j\sigma}(\tau) + c.c.) + U \sum_i n_{i\uparrow}(\tau) n_{i\downarrow}(\tau) \right) \quad (6.46)$$

It is impossible to calculate the action for realistic lattice sizes with appropriate number of degrees of freedom. Therefore, the goal of DMFT is to reduce the lattice problem to a single-site model with an effective self-consistent bath. In the following we derive the selfconsistency equations based on the *cavity method* by explicitly removing a site  $i = 0$ , called *impurity* site, from the lattice, which we refer to as *cavity*. The effective action of the impurity site is defined by integrating out the other degrees of freedom

$$\frac{1}{Z_{\text{eff}}} e^{-S_{\text{eff}}} \equiv \frac{1}{Z} \int \prod_{i \neq 0, \sigma} Dc_{i\sigma}^* Dc_{i\sigma} e^{-S}. \quad (6.47)$$

The effective action is obtained by expanding Eq. (6.47) in a time ordered series. Derivation of the exact form and subsequent limit in infinite dimensions are shown in appendix E. For

<sup>14</sup>In ultracold atomic gases different spin states are realized without external Zeeman fields by loading fermions in different total atomic spin states. The spin imbalance thus corresponds to unequal number of atoms of different spin.

infinite dimensional systems the terms  $\mathcal{O}(1/d)$  or  $\mathcal{O}(1/z)$ , where  $d$  denotes the dimension and  $z = 2d$  the number of nearest neighbors, vanish and the result reads

$$\begin{aligned} S_{\text{eff}} &= \int_0^\beta d\tau \left( \sum_\sigma c_{0\sigma}^*(\tau) (\partial_\tau - \mu) c_{0\sigma}(\tau) + U n_{0\uparrow}(\tau) n_{0\downarrow}(\tau) \right) \\ &\quad + \sum_\sigma \sum_{\substack{\langle i0 \rangle \\ \langle j0 \rangle}} \int_0^\beta \int_0^\beta d\tau_1 d\tau_2 t_{i0} t_{j0} c_{0\sigma}^*(\tau_1) G_{ij,\sigma}^{(0)}(\tau_1, \tau_2) c_{0\sigma}(\tau_2) \\ &= - \sum_\sigma \int_0^\beta \int_0^\beta d\tau_1 d\tau_2 c_{0\sigma}^*(\tau_1) \mathcal{G}_{0,\sigma}^{-1}(\tau_1, \tau_2) c_{0\sigma}(\tau_2) + \int_0^\beta d\tau U n_{0\uparrow}(\tau) n_{0\downarrow}(\tau). \end{aligned} \quad (6.48)$$

In the last step we have defined the *Weiss Green's function*

$$\mathcal{G}_{0,\sigma}^{-1}(\tau_1, \tau_2) = -\delta(\tau_1 - \tau_2) (\partial_{\tau_1} - \mu) - \sum_{\langle i0 \rangle, \langle j0 \rangle} t_{i0} t_{j0} G_{ij,\sigma}^{(0)}(\tau_1, \tau_2)$$

where  $G_{ij,\sigma}^{(0)}(\tau, \tau') = -\langle T_\tau \hat{c}_{i\sigma}^\dagger(\tau) \hat{c}_{j\sigma}(\tau') \rangle^{(0)}$  is the cavity Green's function of the interacting fermions calculated in the system excluding the impurity site, which is emphasized by the index  $(0)$ . In the frequency representation the Weiss Green's function reads

$$\mathcal{G}_{0,\sigma}^{-1}(i\omega_n) = i\omega_n + \mu - \sum_{\langle i0 \rangle, \langle j0 \rangle} t_{i0} t_{j0} G_{ij,\sigma}^{(0)}(i\omega_n) \quad (6.49)$$

with  $\omega_n = (2n + 1)\pi/\beta$  denoting Matsubara frequencies. In the effective model  $\mathcal{G}_{0,\sigma}$  plays the role of a non-interacting Green's function and contains the effects of all sites in the bath including the hybridization of the impurity site with the bath. It should not be confused with the non-interacting local Green's function of the original lattice model. The Weiss Green's function is related to Green's functions of the initial lattice via [11, 281]

$$G_{ij,\sigma}^{(0)} = G_{ij,\sigma} - \frac{G_{i0,\sigma} G_{0j,\sigma}}{G_{00,\sigma}}. \quad (6.50)$$

It is interesting to note that the cavity Green's function corresponds to the lattice Green's function reduced by the paths connecting sites  $i$  and  $j$  through the impurity site 0.

To calculate the Weiss Green's function we insert Eq. (6.50) into Eq. (6.49)

$$\begin{aligned} \mathcal{G}_{0,\sigma}^{-1}(i\omega_n) &= i\omega_n + \mu - \sum_{\langle i0 \rangle, \langle j0 \rangle} t_{i0} t_{j0} \left[ G_{ij,\sigma}(i\omega_n) - \frac{G_{i0,\sigma}(i\omega_n) G_{0j,\sigma}(i\omega_n)}{G_{00,\sigma}(i\omega_n)} \right] \\ &= i\omega_n + \mu - \underbrace{\sum_{\substack{\langle i0 \rangle \\ \langle j0 \rangle}} t_{i0} t_{j0} G_{ij,\sigma}(i\omega_n)}_A + \frac{1}{G_{00,\sigma}(i\omega_n)} \underbrace{\left[ \sum_{\langle i0 \rangle} t_{i0} G_{i0,\sigma}(i\omega_n) \right]^2}_B \end{aligned} \quad (6.51)$$

To proceed we rewrite the Green's functions using the following relations

$$G_{ij,\sigma}(i\omega_n) = \sum_{\mathbf{k}} e^{-i\mathbf{k}(\mathbf{r}_i - \mathbf{r}_j)} G_{\mathbf{k},\sigma}(i\omega_n) \quad (6.52)$$

$$\sum_{\langle i0 \rangle} t_{i0} \exp(i\mathbf{k}\mathbf{r}_i) = \varepsilon(\mathbf{k}) \quad (6.53)$$

$$G_{\mathbf{k},\sigma}(i\omega_n) = \frac{1}{i\omega_n + \mu - \Sigma_\sigma(i\omega_n) - \varepsilon_{\mathbf{k}}} \quad (6.54)$$

$$\sum_{\mathbf{k}} \rightarrow \int_{-\infty}^{\infty} d\varepsilon \rho(\varepsilon) \quad (6.55)$$

Eq. (6.52) is the Fourier transformation of the real space Green's function to momentum space. Eq. (6.53) is the already introduced definition of the non-interacting dispersion relation  $\varepsilon(\mathbf{k})$ , see Sec. 3.1.1. The form of the Green's Fourier transform in Eq. (6.54) is based on the assumption of a purely local selfenergy  $\Sigma_\sigma(i\omega_n)$ , which is true for infinite dimensional systems [281]. And last but not least, the summation over the momenta can be rewritten into an integral over the energy for a known density of states  $\rho(\varepsilon)$  as given in Eq. (6.55). Rewriting the Eq. (6.51) leads

$$A : \sum_{\substack{\langle i0 \rangle \\ \langle j0 \rangle}} t_{i0} t_{j0} G_{ij,\sigma}(i\omega_n) \stackrel{(6.52)}{=} \sum_{\mathbf{k}} \sum_{\langle i0 \rangle} t_{i0} e^{-i\mathbf{k}\mathbf{r}_i} \sum_{\langle j0 \rangle} t_{j0} e^{i\mathbf{k}\mathbf{r}_j} G_{\mathbf{k},\sigma}(i\omega_n)$$

$$\stackrel{(6.53)}{=} \sum_{\mathbf{k}} \varepsilon^2(\mathbf{k}) G_{\mathbf{k},\sigma}(i\omega_n)$$

$$\stackrel{(6.54)}{=} \sum_{\mathbf{k}} \varepsilon^2(\mathbf{k}) \frac{1}{i\omega_n + \mu - \Sigma_\sigma(i\omega_n) - \varepsilon_{\mathbf{k}}}$$

$$\stackrel{(6.55)}{=} \int_{-\infty}^{\infty} d\varepsilon \rho(\varepsilon) \frac{\varepsilon^2}{i\omega_n + \mu - \Sigma_\sigma(i\omega_n) - \varepsilon}$$

$$B : \sum_{\langle i0 \rangle} t_{i0} G_{i0,\sigma}(i\omega_n) \stackrel{(6.52)}{=} \sum_{\mathbf{k}} \sum_{\langle i0 \rangle} t_{i0} e^{-i\mathbf{k}\mathbf{r}_i} G_{\mathbf{k},\sigma}(i\omega_n)$$

$$\stackrel{(6.53)}{=} \sum_{\mathbf{k}} \varepsilon(\mathbf{k}) G_{\mathbf{k},\sigma}(i\omega_n)$$

$$\stackrel{(6.54)}{=} \sum_{\mathbf{k}} \varepsilon(\mathbf{k}) \frac{1}{i\omega_n + \mu - \Sigma_\sigma(i\omega_n) - \varepsilon_{\mathbf{k}}}$$

$$\stackrel{(6.55)}{=} \int_{-\infty}^{\infty} d\varepsilon \rho(\varepsilon) \frac{\varepsilon}{i\omega_n + \mu - \Sigma_\sigma(i\omega_n) - \varepsilon}$$

The transformed expressions  $A$  and  $B$  can now be inserted into Eq. (6.51), where we define  $\vartheta = i\omega_n + \mu - \Sigma_\sigma(i\omega_n)$

$$\begin{aligned} \mathcal{G}_{0,\sigma}^{-1}(i\omega_n) &= i\omega_n + \mu - \int_{-\infty}^{\infty} d\varepsilon \rho(\varepsilon) \frac{\varepsilon^2}{\vartheta - \varepsilon} + \frac{\left[ \int_{-\infty}^{\infty} d\varepsilon \rho(\varepsilon) \frac{\varepsilon}{\vartheta - \varepsilon} \right]^2}{\int_{-\infty}^{\infty} d\varepsilon \rho(\varepsilon) \frac{1}{\vartheta - \varepsilon}} \\ &= \Sigma_\sigma(i\omega_n) + \left[ \int_{-\infty}^{\infty} d\varepsilon \rho(\varepsilon) \frac{1}{i\omega_n + \mu - \Sigma_\sigma(i\omega_n) - \varepsilon} \right]^{-1}. \end{aligned}$$

The details of the derivation can be found in appendix F. Referring to Eq. (6.52), (6.54) and (6.55) we identify the last summand as the local impurity Green's function and the result as the Dyson equation

$$\mathcal{G}_{0,\sigma}^{-1}(i\omega_n) = \Sigma_\sigma(i\omega_n) + G_{00,\sigma}^{-1}(i\omega_n). \quad (6.56)$$

Together with the definition of the lattice on-site Green's function

$$G_{ii,\sigma}(i\omega_n) = \sum_{\mathbf{k}} \frac{1}{i\omega_n + \mu - \Sigma_\sigma(i\omega_n) - \varepsilon_{\mathbf{k}}} \quad (6.57)$$

we finally obtain the set of equations which define selfconsistency. When the on-site Green's function given by Eq. (6.57) coincides with the local Green's function calculated from the effective action via Eq. (6.56), selfconsistency is reached:



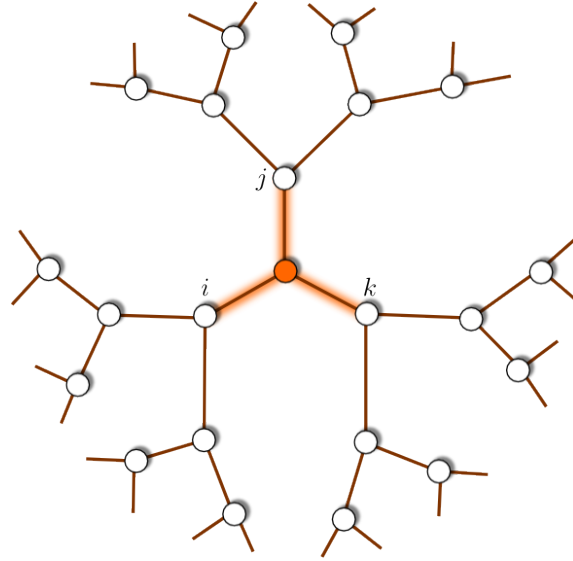


**Figure 6.10:** Illustration of the Bethe lattice with  $z = 3$  nearest neighbors. DMFT calculations on this lattice simplify numerics since the sites  $i$ ,  $j$  and  $k$  are decoupled, when the central site, also called the impurity site, is separated from the system together with the corresponding bonds (highlighted in orange).

$$\text{DMFT selfconsistency loop: } S_{\text{eff}}(\mathcal{G}_{0,\sigma}^{-1}) \rightarrow G_{00,\sigma}^{-1}(S_{\text{eff}}) \rightarrow \mathcal{G}_{0,\sigma}^{-1}(G_{00,\sigma}^{-1})$$

## Bethe lattice

Bethe lattices are cycle-free structures, i.e. any two points are joined by a single path. Each site is connected to  $z$  neighbors and the total number of sites increases exponentially. Such lattice structure is demonstrated in Fig. 6.10 for  $z = 3$ . The Bethe lattice is an artificial lattice which does not possess the translational symmetries of a Bravais lattice, except the  $z = 2$  case, which corresponds to a 1D lattice. Due to its special topology lattice problems simplify or even become exactly solvable [287]. Thus, the mean-field theories derived on a Bethe lattice including correlations between fluctuations at different sites are expected to be more trustworthy than conventional mean-field methods formulated for a non-distorted lattice but neglecting these correlations [288]. Finally, due to the analytic behavior of the semi-elliptic Bethe density of states at the band edges, similarly to 3D cubic lattices [257], the results of Bethe lattice calculations are often used as an approximation of 3D systems. Especially in DMFT the Bethe lattice leads to a simplification of the selfconsistency equations derived above and is therefore frequently used [51, 289–291]. Since within this thesis the results for a square 2D lattice are compared with Bethe lattice results, the features of the latter lattice will be briefly explained.

In DMFT the impurity site of the Bethe lattice, highlighted by the orange color in Fig. 6.10, is identified with the impurity site. Separating the impurity together with the corresponding bonds from the lattice disconnects sites next to the impurity, see Fig. 6.10. Thus, the cavity Green's function  $G_{ij,\sigma}^{(0)}(i\omega_n)$ , which describes propagation of a fermion from impu-

rity's nearest neighbor site  $i$  to  $j$ , becomes zero for  $i \neq j$  since the sites are decoupled and the Weiss Green's function Eq. (6.49) simplifies

$$\begin{aligned} \mathcal{G}_{0,\sigma}^{-1}(i\omega_n) &= i\omega_n + \mu - \sum_{\substack{\langle i0 \rangle \\ \langle j0 \rangle}} t_{i0}t_{j0}G_{ij,\sigma}^{(0)}(i\omega_n)\delta_{ij} \\ &= i\omega_n + \mu - \sum_{\langle i0 \rangle} t_{i0}^2 G_{ii,\sigma}^{(0)}(i\omega_n) \\ &\approx i\omega_n + \mu - zt^2 G_\sigma(i\omega_n). \end{aligned} \quad (6.58)$$

In the last step the approximation was done substituting  $G_{ii,\sigma}^{(0)}(i\omega_n)$  by  $G_{ii,\sigma}(i\omega_n) \equiv G_\sigma(i\omega_n)$ . This approach is reasonable for infinite dimensional systems since it corresponds to ignoring the missing impurity site in the cavity system leading to a vanishing error of order  $1/z$ .

The simplification in Eq. (6.58) has effect only on one step of the selfconsistency: given the interacting Green's function  $G_{00,\sigma}$  the new Weiss Green's function is calculated via the Dyson equation (6.56) or in the case of Bethe lattices via Eq. (6.58). However, the most non-trivial step of the selfconsistency loop is not the determination of the Weiss Green's function but the calculation of the local Green's function given an effective action. This problem can be tackled when a model Hamiltonian can be found which has the same effective action as the one calculated based on the Weiss Green's function.

### Single impurity Anderson model

The effective action defined in Eq. (6.48) has the same form as the action of the single impurity Anderson Model where  $\mathcal{G}_{0,\sigma}$  represents the effective bath of conduction electrons. The Anderson Hamiltonian reads

$$\mathcal{H}_{\text{AM}} = \mathcal{H}_{\text{bath}} + \mathcal{H}_{\text{coupling}} + \mathcal{H}_{\text{imp}}, \quad (6.59)$$

where the individual parts are defined as

$$\mathcal{H}_{\text{bath}} = \sum_{\mathbf{k},\sigma} (\varepsilon_{\mathbf{k},\sigma} - \mu) \hat{n}_{\mathbf{k},\sigma} \quad (6.60)$$

$$\mathcal{H}_{\text{coupling}} = \sum_{\mathbf{k},\sigma} V_{\mathbf{k},\sigma} (\hat{a}_{\mathbf{k},\sigma}^\dagger \hat{c}_{0,\sigma} + h.c.) \quad (6.61)$$

$$\mathcal{H}_{\text{imp}} = -\mu \sum_{\sigma} \hat{n}_{0,\sigma} + U \hat{n}_{0\uparrow} \hat{n}_{0\downarrow}. \quad (6.62)$$

The operators  $\hat{a}_{\mathbf{k},\sigma}^\dagger$  and  $\hat{a}_{\mathbf{k},\sigma}$  are creation and annihilation operators of non-interacting fermions for states of wave vector  $\mathbf{k}$  and spin component  $\sigma$  corresponding to an energy  $\varepsilon_{\mathbf{k},\sigma}$  in the bath. The impurity Hamiltonian represents the interacting local problem, where  $\hat{c}_{0,\sigma}^\dagger$  ( $\hat{c}_{0,\sigma}$ ) is the creation/annihilation operator on the impurity energy level indicated by 0. And last but not least, the tunneling between the impurity and the bath is described by  $\mathcal{H}_{\text{coupling}}$  with  $V_{\mathbf{k},\sigma}$  being the tunneling matrix element. A good discussion of this model can be found in [37].

In analogy to the derivation of the effective action Eq. (6.48) the action of the impurity site of the Anderson model is

$$S_{\text{AM}} = - \sum_{\sigma} \int_0^\beta \int_0^\beta d\tau_1 d\tau_2 c_{0\sigma}^*(\tau_1) \mathcal{G}_{\text{AM},\sigma}^{-1}(\tau_1, \tau_2) c_{0\sigma}(\tau_2) + \int_0^\beta d\tau U n_{0\uparrow}(\tau) n_{0\downarrow}(\tau) \quad (6.63)$$

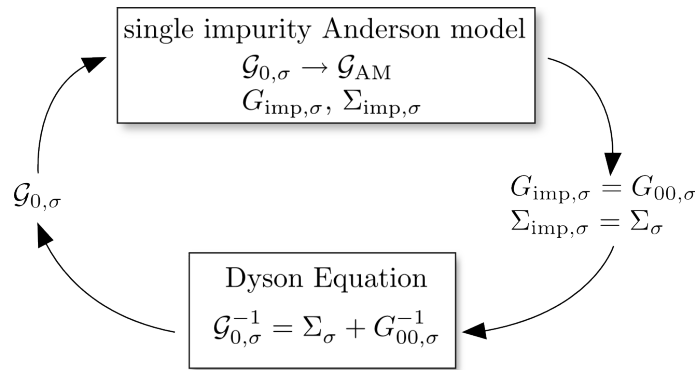
with

$$\mathcal{G}_{\text{AM},\sigma}^{-1}(\tau_1, \tau_2) = -\delta(\tau_1 - \tau_2)(\partial_{\tau_1} - \mu) - \Delta_{\sigma}(\tau_1, \tau_2) \quad (6.64)$$

or Fourier transformed

$$\mathcal{G}_{\text{AM},\sigma}^{-1}(i\omega_n) = i\omega_n + \mu - \Delta_{\sigma}(i\omega_n) \quad (6.65)$$

with the hybridization function  $\Delta_{\sigma}(i\omega_n) = \sum_{\mathbf{k}} V_{\mathbf{k},\sigma}^2 / (i\omega_n - \varepsilon_{\mathbf{k},\sigma} + \mu)$ . It is clear that the parameters  $V_{\mathbf{k},\sigma}$  and  $\varepsilon_{\mathbf{k},\sigma}$  have to be determined such that  $\mathcal{G}_{\text{AM},\sigma} \equiv \mathcal{G}_{0,\sigma}$ , where  $\mathcal{G}_{0,\sigma}$  is an initial Weiss field. When this condition is fulfilled, the single impurity Anderson model has to be solved numerically, which leads to the impurity selfenergy  $\Sigma_{\text{imp},\sigma}$  and Green's function  $G_{\text{imp},\sigma}$ . Following the identity of the Weiss Green's functions, i.e.  $\mathcal{G}_{\text{AM},\sigma} \equiv \mathcal{G}_{0,\sigma}$ , the impurity quantities such as the selfenergy and local Green's function must coincide with the corresponding lattice quantities  $\Sigma_{\sigma}$  and  $G_{00,\sigma}$ , which inserted in Eq. (6.56) (or in Eq. (6.58) in case of Bethe lattices<sup>15</sup>) leads to the new Weiss Green's function  $\mathcal{G}_{0,\sigma}$ . Thus, mapping the lattice problem onto a single-impurity model requires an iterative solution of a coupled problem:



The most challenging and computationally costly step in the iterative solution procedure is the repeated solution of the impurity model, which is a many-body problem. The most common numerical methods are:

(i) *Quantum Monte Carlo* (QMC), e.g. the Hirsch-Fye algorithm, solves the single impurity problem on a discretized imaginary time scale at finite temperature. The interacting Green's function is calculated by stochastic Monte Carlo sampling [289, 290, 292–295]. One of the disadvantages of the method is that the results obtained are in imaginary-time or Matsubara frequencies, which require additional analytical continuations to the real frequency range. The latter is essential for investigations of physical properties via spectral features, which are accessible in experiments. Another important obstacle is the low-temperature regime, which suffers from significant statistical errors and high computational times.

(ii) *Exact Diagonalization* (ED), solves the impurity problem by approximating the bath by a few orbitals, whose number is limited due to exponential increase of the corresponding Hilbert space. The parameters of the bath, i.e. energies and tunneling amplitudes, are chosen according to the model to be solved and incorporate the free choice of possible shapes of the bath [296–298]. A serious limitation of this method is the considered size of the bath leading to a poor frequency resolution. This makes it unfavorable to investigate physics at low energy scales.

<sup>15</sup> The Eq. (6.56) remains still true for Bethe lattices, however, due to the required inversion of the on-site Green's function at every frequency it unnecessarily exaggerates the calculus. This can be avoided by using directly Eq. (6.58).

(iii) *Numerical Renormalization Group* (NRG) discretizes the bath too. However, in contrast to ED, in NRG the discretization is on a logarithmic scale. This enables arbitrarily good resolution near the Fermi level which makes the application of NRG more suitable for low energy physics. Away from the band center only a qualitative description is possible due to less fine frequency resolution. After discretization the bath is mapped onto a semi-infinite chain in which the sites are coupled via effective tunneling elements to each other. The resulting Hamiltonian is diagonalized iteratively [299, 300].

(iv) *Modified Perturbation Theory* (MPT) expands the selfenergy in series up to second order in the Hubbard interaction  $U$  around the Hartree-Fock solution [301, 302]. Compared to the precursor method *Iterative Perturbation Theory* [302, 303] also systems away from half-filling can be handled. Compared to NRG it benefits from easier numerical implementation which reflects in the much lower computational time, however the accuracy around the Fermi level is lowered especially in the strong interaction regime.

Although the methods ED and QMC are in principle numerically exact, they suffer from severe limitations, such that application of approximate methods still remains necessary. In this thesis we used the impurity solvers NRG and MPT, which we are going to describe in more detail in the next subsections.

## 6.5.2 Impurity solver: NRG and MPT

### NRG

The Numerical Renormalization Group (NRG) was invented by Wilson in 1975 [299]. The main idea of a renormalization group is a mapping  $T$  of a Hamiltonian, which is specified by a set of coupling parameters  $\{t_i\}$ , onto another Hamiltonian with a new set of coupling parameters  $\{t'_i\}$ , such that  $T(\{t_i\}) = \{t'_i\}$ . In general the transformation is non-linear and often applied successively to enable scaling from a large to a reduced energy scale. In the following we will briefly derive the NRG equation for the flat-band impurity Anderson model following [304].

Thus, the starting point is the Hamiltonian Eq. (6.59)

$$\mathcal{H}_{\text{AM}} = \mathcal{H}_{\text{imp}} + \sum_{\mathbf{k},\sigma} \tilde{\varepsilon}_{\mathbf{k},\sigma} \hat{a}_{\mathbf{k},\sigma}^\dagger \hat{a}_{\mathbf{k},\sigma} + \sum_{\mathbf{k},\sigma} V_{\mathbf{k},\sigma} (\hat{a}_{\mathbf{k},\sigma}^\dagger \hat{c}_{0,\sigma} + h.c.), \quad (6.66)$$

where we substituted  $\varepsilon_{\mathbf{k},\sigma} - \mu = \tilde{\varepsilon}_{\mathbf{k},\sigma}$  and  $\mathcal{H}_{\text{imp}}$  is defined in Eq. (6.62). The calculations are significantly simplified when the dispersion relation is considered to be isotropic, i.e.  $\tilde{\varepsilon}_{\mathbf{k}} = \tilde{\varepsilon}_{|\mathbf{k}|}$  and correspondingly the coupling between impurity and the bath  $V_{\mathbf{k}} = V_{|\mathbf{k}|}$ . This is equivalent to the impurity coupling only to the  $s$ -wave states of conducting band.

The first step in the derivation of the NRG equations is the transformation from a discrete to a continuous bath energy spectrum. This we do by substituting the sum  $\sum_{\mathbf{k}}$  by an integral  $\int d\varepsilon \rho(\varepsilon)$  and the discrete creation/annihilation operators of the bath by corresponding continuous  $\hat{a}_{\mathbf{k},\sigma}^\dagger \rightarrow \hat{a}_{\varepsilon,\sigma}^\dagger / \sqrt{\rho(\varepsilon)}$ . The resulting Hamiltonian for a continuous conduction band reads

$$\mathcal{H}_{\text{AM}} = \mathcal{H}_{\text{imp}} + \sum_{\sigma} \int_{-D}^D d\varepsilon \left[ \varepsilon \hat{a}_{\varepsilon,\sigma}^\dagger \hat{a}_{\varepsilon,\sigma} + \sqrt{\rho(\varepsilon)} V_{\sigma}(\varepsilon) (\hat{a}_{\varepsilon,\sigma}^\dagger \hat{c}_{0,\sigma} + h.c.) \right],$$

where  $D$  denotes half-bandwidth,  $\rho(\varepsilon)$  is the one-particle density of states per spin and  $V_{\sigma}(\varepsilon)$  results from the transformation to continuous energies, i.e.  $V_{\mathbf{k},\sigma}(\varepsilon_{\mathbf{k},\sigma}) \rightarrow V_{\sigma}(\varepsilon)$ .

Further simplification is achieved when the dispersion relation is expanded in a Taylor series around  $k_F$

$$\varepsilon(k) = \varepsilon_F + (k - k_F) \left. \frac{d\varepsilon(k)}{dk} \right|_{k=k_F} + \mathcal{O}(k^2)$$

and the terms of second and higher orders are neglected. This leads to a flat density of states, when  $\rho(\varepsilon)$  is written as series in  $k$  and all but the leading constant term are dropped

$$\rho(\varepsilon) = \rho = \frac{1}{2D}, \quad -D < \varepsilon < D.$$

Additionally, the coupling can be assumed to be constant  $V_\sigma(\varepsilon) \approx V_\sigma$ . These approximations are accurate around the Fermi energy considered to be in the band center and become arbitrarily inaccurate towards the band edges. Since flat-band NRG is based on this approach, the obtained results are precise for  $\varepsilon \approx 0$  and become more approximative when  $\varepsilon \rightarrow |D|$ <sup>16</sup>. To change into a more convenient notation of energies in units of the bandwidth we rescale  $\kappa = \varepsilon/D$  and  $\hat{\alpha}_{\varepsilon,\sigma}^\dagger \rightarrow \hat{\alpha}_{\kappa,\sigma}^\dagger/\sqrt{D}$ . Together with constant  $\rho$  and  $V_\sigma$  the final Hamiltonian reads

$$\mathcal{H}_{\text{AM}} = D \left[ \frac{1}{D} \mathcal{H}_{\text{imp}} + \sum_{\sigma} \int_{-1}^1 d\kappa \kappa \hat{\alpha}_{\kappa,\sigma}^\dagger \hat{\alpha}_{\kappa,\sigma} + \sum_{\sigma} \sqrt{\frac{\Gamma_{\sigma}}{\pi D}} \int_{-1}^1 d\kappa (\hat{\alpha}_{\kappa,\sigma}^\dagger \hat{c}_{0,\sigma} + h.c.) \right], \quad (6.67)$$

with  $\Gamma_{\sigma} = \pi \rho V_{\sigma}^2$ .

The next step is the logarithmic discretization of the energy scale. The problems which are tackled by renormalization techniques are ones in which there is no characteristic energy scale and every energy contributes. This is e. g. the case in the Kondo problem, which is derived from the single impurity Anderson model via the Schrieffer-Wolff transformation [37]. Originally, to reflect the logarithmic breakdown of the perturbation theory in the Kondo model, Wilson divided the energy scales within the bath such that

$$\Lambda^{-(n+1)} < |\kappa - \kappa_F| < \Lambda^{-n} \quad n = 1, 2, 3, \dots$$

Here,  $\kappa_F = \varepsilon_F/D$  denotes the Fermi energy and  $\Lambda$  is chosen arbitrarily but greater than unity<sup>17</sup>. From there on, this mapping was also used in general studies of the Anderson model. Fig. 6.11 (a) demonstrates the implementation of the logarithmic scale for a half-bandwidth normalized to unity and  $\kappa_F = 0$ . In each energy subinterval a complete set of orthonormal functions can be generated setting up a Fourier series

$$\phi_{np}^{\pm}(\kappa) = \begin{cases} \frac{\Lambda^{n/2}}{\sqrt{1-\Lambda^{-1}}} \exp(\pm i\omega_n p \kappa), & \text{for } \Lambda^{-(n+1)} < \pm\kappa < \Lambda^{-n}, \\ 0, & \text{otherwise,} \end{cases}$$

whereby  $n = 0, 1, 2, \dots$  denotes the interval index and  $p$  the Fourier index which takes on all integer values in the range  $[-\infty; \infty]$ . The Fourier frequency in the  $n$ -th interval  $\omega_n$  is defined

$$\omega_n = \frac{2\pi\Lambda^n}{1 - \Lambda^{-1}}. \quad (6.68)$$

<sup>16</sup> For the use within DMFT the impurity solver can be adjusted to arbitrary forms of the band, which leads to corresponding changes in the derived equations and more accurate results away from the band center. Details can be found in [305].

<sup>17</sup> For  $\Lambda \rightarrow 1$  the continuum limit is obtained, where discretization becomes exact. A more detailed discussion concerning appropriate values of  $\Lambda$  is given at the end of this section.

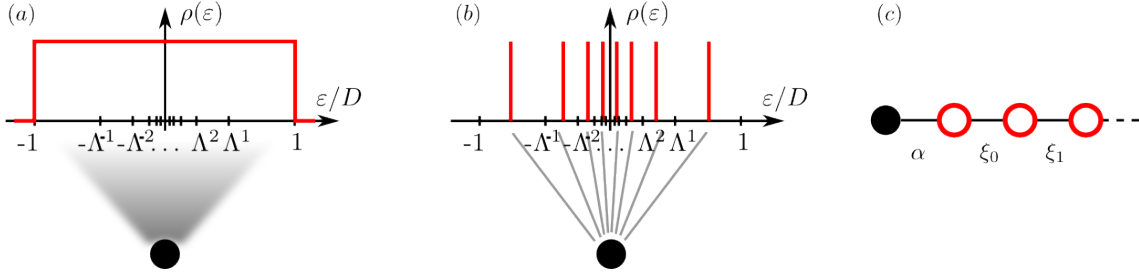


**Figure 6.11:** Schematic structure for the derivation of the NRG equations. (a) Starting from the impurity coupling to a continuous bath with a flat density of states  $\rho(\varepsilon)$ , the logarithmic scaling leads to a discretization and classification of energy sub-intervals in different orders of magnitude. (b) Hereby each sub-interval is approximated to be represented by a single state. (c) Finally in the last transformation the mapping on a semi-infinite chain is performed, where the coupling between different states decays as  $\xi_n \sim \Lambda^{-n/2}$ .

With a new set of discrete operators<sup>18</sup> for positive and negative  $\kappa$  respectively

$$\hat{a}_{np,\sigma}^\dagger = \int_{-1}^1 d\kappa [\phi_{np}^+(\kappa)]^* \hat{\alpha}_{\kappa,\sigma}^\dagger \quad \text{and} \quad \hat{b}_{np,\sigma}^\dagger = \int_{-1}^1 d\kappa [\phi_{np}^-(\kappa)]^* \hat{\alpha}_{\kappa,\sigma}^\dagger$$

the continuous energy creation/annihilation operators can be expressed

$$\hat{\alpha}_{\kappa,\sigma}^\dagger = \sum_{np} \left( \hat{a}_{np,\sigma}^\dagger \phi_{np}^+(\kappa) + \hat{b}_{np,\sigma}^\dagger \phi_{np}^-(\kappa) \right). \quad (6.69)$$

Substituting definition Eq. (6.69) into Hamiltonian Eq. (6.67) reduces the continuous problem to a discrete spectrum again

$$\mathcal{H}_{\text{AM}} = D \left[ \frac{1}{D} \mathcal{H}_{\text{imp}} + \frac{1 + \Lambda^{-1}}{2} \sum_{np,\sigma} \Lambda^{-n} (\hat{a}_{np,\sigma}^\dagger \hat{a}_{np,\sigma} - \hat{b}_{np,\sigma}^\dagger \hat{b}_{np,\sigma}) \right] \quad (6.70)$$

$$+ \frac{1 - \Lambda^{-1}}{2\pi i} \sum_{\substack{\sigma,n \\ p \neq \bar{p}}} \frac{\Lambda^{-n}}{\bar{p} - p} (\hat{a}_{np,\sigma}^\dagger \hat{a}_{n\bar{p},\sigma} - \hat{b}_{np,\sigma}^\dagger \hat{b}_{n\bar{p},\sigma}) e^{i \frac{2\pi(\bar{p}-p)}{1-\Lambda^{-1}}} \quad (6.71)$$

$$+ \sqrt{1 - \Lambda^{-1}} \sum_{n,\sigma} \sqrt{\frac{\Gamma_\sigma}{\pi D}} \Lambda^{-n/2} \left[ (\hat{a}_{n0,\sigma}^\dagger + \hat{b}_{n0,\sigma}^\dagger) \hat{c}_{0,\sigma} + h.c. \right]. \quad (6.72)$$

The crucial simplification of this Hamiltonian concerns neglecting all states  $p \neq 0$  such that each sub-interval is represented by a single state, see Fig. 6.11. The justification for this step is based on the fact, that  $p \neq 0$  states do not couple to the impurity and the only term coupling the operators  $\hat{a}_{np,\sigma}/\hat{b}_{np,\sigma}$  to  $\hat{a}_{n0,\sigma}/\hat{b}_{n0,\sigma}$  is the second summand Eq. (6.71), which becomes vanishingly small for  $\Lambda \rightarrow 1$ <sup>19</sup>. With this assumption the Hamiltonian reads

$$\mathcal{H}_{\text{AM}} = D \left[ \frac{1}{D} \mathcal{H}_{\text{imp}} + \frac{1 + \Lambda^{-1}}{2} \sum_{n,\sigma} \Lambda^{-n} (\hat{a}_{n,\sigma}^\dagger \hat{a}_{n,\sigma} - \hat{b}_{n,\sigma}^\dagger \hat{b}_{n,\sigma}) + \sum_{\sigma} \sqrt{\frac{2\Gamma_\sigma}{\pi D}} \left( \hat{f}_{0,\sigma}^\dagger \hat{c}_{0,\sigma} + h.c. \right) \right]. \quad (6.73)$$

with the new operator representing the conduction field at the impurity site

$$\hat{f}_{0,\sigma}^\dagger = \sqrt{\frac{(1 - \Lambda^{-1})}{2}} \sum_n \Lambda^{-n/2} (\hat{a}_{n,\sigma}^\dagger + \hat{b}_{n,\sigma}^\dagger), \quad (6.74)$$

<sup>18</sup>These operators can be shown to satisfy fermionic commutation relations  $\{\hat{a}_{np,\sigma}; \hat{a}_{n\bar{p},\sigma}^\dagger\} = \delta_{n\bar{n}} \delta_{p\bar{p}} \delta_{\sigma\bar{\sigma}}$

<sup>19</sup>The verification of this approach even for  $\Lambda \leq 3$  can be found in [299].

where we drop the subscript  $p = 0$  for all operators in the expression (6.73) as well as in the following notation.

It is convenient to make a unitary transformation from the set of operators  $\{\hat{a}_{n,\sigma}, \hat{b}_{n,\sigma}\}$  to a new set  $\{\hat{f}_{n,\sigma}\}$ , where Eq. (6.74) still represents  $\hat{f}_{0,\sigma}$ . There are infinitely many possibilities to construct new operator sets, however, all of them lead to coupling between different operators  $\hat{f}_{n,\sigma}$  since the conducting term (second summand of Eq. (6.73)) is already diagonal in  $\{\hat{a}_{n,\sigma}, \hat{b}_{n,\sigma}\}$ . The convention is to take the set where only nearest neighbors  $\hat{f}_{n,\sigma}$  and  $\hat{f}_{n\pm 1,\sigma}$  couple. The resulting Hamiltonian exhibits a form of a semi-infinite chain, see Fig. 6.11 (c) and reads

$$\mathcal{H}_{\text{AM}} = D \left[ \frac{1}{D} \mathcal{H}_{\text{imp}} + \frac{1 + \Lambda^{-1}}{2} \sum_{n,\sigma} \Lambda^{-n/2} \xi_n (\hat{f}_{n,\sigma}^\dagger \hat{f}_{n+1,\sigma} + h.c.) + \sum_{\sigma} \sqrt{\frac{2\Gamma_{\sigma}}{\pi D}} (\hat{f}_{0,\sigma}^\dagger \hat{c}_{0,\sigma} + h.c.) \right] \quad (6.75)$$

with coefficients  $\xi_n$  of order 1 given by

$$\xi_n = \frac{(1 - \Lambda^{-n-1})}{\sqrt{(1 - \Lambda^{-2n-1})} \sqrt{(1 - \Lambda^{-2n-3})}}.$$

The details of the transformation can be found in [304, 305].

In the following step the Hamiltonian Eq. (6.75) is diagonalized iteratively. The Hamiltonian is truncated after  $N$  levels and a sequence of Hamiltonians is defined

$$H_N = \Lambda^{(N-1)/2} \sum_{\sigma} \left[ \frac{1}{D} \tilde{\mathcal{H}}_{\text{imp}} + \sum_{n=0}^{N-1} \Lambda^{-n/2} \xi_n (\hat{f}_{n,\sigma}^\dagger \hat{f}_{n+1,\sigma} + h.c.) + \sqrt{\tilde{\Gamma}_{\sigma}} (\hat{f}_{0,\sigma}^\dagger \hat{c}_{0,\sigma} + h.c.) \right],$$

where

$$\begin{aligned} \tilde{\Gamma}_{\sigma} &= \left( \frac{2}{1 + \Lambda^{-1}} \right)^2 \frac{2\Gamma_{\sigma}}{\pi D} = \left( \frac{2}{1 + \Lambda^{-1}} \right)^2 \frac{2\rho|V_{\sigma}|^2}{D}, \\ \tilde{\mathcal{H}}_{\text{imp}} &= \frac{2}{1 + \Lambda^{-1}} \mathcal{H}_{\text{imp}} \stackrel{(6.62)}{=} -\tilde{\mu} \sum_{\sigma} (\hat{c}_{0,\sigma}^\dagger \hat{c}_{0,\sigma} + h.c.) + \tilde{U} \hat{n}_{0\uparrow} \hat{n}_{0\downarrow}, \\ \tilde{\mu} &= \frac{2}{1 + \Lambda^{-1}} \mu \quad \text{and} \quad \tilde{U} = \frac{2}{1 + \Lambda^{-1}} U. \end{aligned}$$

The original Hamiltonian  $\mathcal{H}_{\text{AM}}$  Eq. (6.75) is recovered in the limit

$$\mathcal{H}_{\text{AM}} = \lim_{N \rightarrow \infty} \frac{1 + \Lambda^{-1}}{2} D \frac{H_N}{\Lambda^{(N-1)/2}}.$$

From the definition of  $H_N$  following recursion relation is derived

$$H_{N+1} = \sqrt{\Lambda} H_N + \xi_n (\hat{f}_{N,\sigma}^\dagger \hat{f}_{N+1,\sigma} + h.c.). \quad (6.76)$$

This relation is the heart of the NRG method: starting with the initial Hamiltonian  $H_0$  involving only operators  $\hat{f}_{0,\sigma}, \hat{c}_{0,\sigma}$  an eigensystem is calculated, from which the repeated use of the recursion Eq. (6.76) leads to desired  $H_N$ .

The diagonalization can be further simplified when symmetries (conserved quantum numbers) are exploited such as spin and fermion number/charge conservation. Given the spin operator

$$\mathbf{S}_N = \frac{1}{2} \sum_{n=0}^N \hat{f}_{n,\sigma}^\dagger \boldsymbol{\sigma}_{\sigma,\sigma'} \hat{f}_{n,\sigma'} + \frac{1}{2} \hat{c}_{0,\sigma}^\dagger \boldsymbol{\sigma}_{\sigma,\sigma'} \hat{c}_{0,\sigma'},$$

where  $\sigma_{\sigma,\sigma'}$  represent Pauli matrices and the summation over repeated spin indices is assumed, and the charge operator

$$Q_N = \sum_{n=0}^N (\hat{f}_{n,\sigma}^\dagger \hat{f}_{n,\sigma} - 1) + (\hat{c}_{0,\sigma}^\dagger \hat{c}_{0,\sigma} - 1),$$

one can verify that the Hamiltonian  $H_N$  commutes with  $Q_N, \mathbf{S}_N^2$  and  $S_N^Z$ . Thus, the eigenstates of the Hamiltonian can be chosen to be simultaneously the eigenstates of these operators. The particularities of the numerical implementation and corresponding simplifications are described in [304, 305].

In practice, calculation of the complete eigensystem of  $H_N$  is impossible for large  $N$  since the number of states grows exponentially  $\sim 2^{2(N+2)}$  and the numerical diagonalization becomes very time consuming. For the calculation of low-temperature and  $T = 0$  properties, which we focus on within this thesis, the low-lying states are essential such that a cut-off of energetically higher states can be applied at every iteration step. This procedure, however, leads to an accumulation of systematic errors, which gets worse for  $\Lambda \rightarrow 1$ . Since the latter determines the accuracy of the logarithmic discretization the choice of  $\Lambda$  represents a middle ground between the high accuracy of the discretization ( $\Lambda \rightarrow 1$ ) and the reduction of cut-off mistakes ( $\Lambda > 1$ ).

Additionally, we would like to emphasize that derived equations are based on the flat-band approximation. This is a serious limitation since the density of states is not flat in general. However, the NRG equations can be adjusted to arbitrary systems approximating  $\rho(\varepsilon)$  by a representative distinct constant value within each interval  $[\Lambda^{-(n+1)}; \Lambda^{-n}]$  separately. Modified derivations can be found in [305, 306]. Nevertheless, the accuracy remains limited due to the successive 0<sup>th</sup>-order approximations of the density of states, which become worse with rougher frequency resolution on the logarithmic scale when band edges are approached. Close to the band center, after all, the method accounting for the band structure provides more precise results.

In DMFT the  $\xi_n$  are not calculated via one of the above equations but determined self-consistently based on the lattice Weiss Green's function. This follows from the mapping of the Hamiltonian on the single impurity Anderson model (see the selfconsistency loop scheme on page 147).

When the diagonalization is completed local observables can be calculated such as impurity magnetic susceptibility, specified heat, impurity spectrum etc., see [300, 304, 305, 307].

## MPT

In 1992 Georges and Kotliar invented the iterative perturbation theory (IPT) to tackle the single impurity Anderson model at half-filling [290]. Although perturbative, this solver has the advantage of high frequency resolution compared to ED, and leads to results on the real frequency axis that are accessible within QMC only after analytical continuation. Particularly, zero- and low-temperature regimes can be attained, which are computationally not feasible or inherently connected to large statistical errors in QMC. The modification implemented by Kajueter and Kotliar [301], known as modified perturbation theory (MPT), enables additionally the use of the model away from half-filling. As already mentioned, MPT is a perturbative method, however, the investigations demonstrated that the series expansion up to second order in  $U$  is sufficient to reproduce the atomic limit behavior



correctly for half-filling [308]. Since the description of weak interactions is implemented by construction, the MPT represents a computationally efficient impurity solver proven to be reliable also in the intermediate correlation regimes [297, 308, 309].

The goal is again to solve approximatively the Anderson model Eq. (6.66). Contrary to NRG, the calculation of the selfenergy here is based on the series representation of  $\Sigma$  in terms of the interaction strength. Similar to IPT, the expansion of the impurity selfenergy up to the second order in  $U$  around the Hartree-Fock term reads [302]

$$\Sigma_{\text{imp},\sigma}(\omega) = U\langle\hat{n}_{0,-\sigma}\rangle + \Sigma_{\text{imp},\sigma}^{(2)}(\omega),$$

with  $\hat{n}_{0,\sigma}$  being the impurity number operator. The second order correction is given by

$$\Sigma_{\text{imp},\sigma}^{(2)}(\omega) = U^2 \int d\varepsilon_1 \int d\varepsilon_2 \int d\varepsilon_3 \left[ \frac{\rho_{\text{imp},\sigma}^{(\text{HF})}(\varepsilon_1)\rho_{\text{imp},-\sigma}^{(\text{HF})}(\varepsilon_2)\rho_{\text{imp},-\sigma}^{(\text{HF})}(\varepsilon_3)}{\omega - \varepsilon_1 + \varepsilon_2 - \varepsilon_3} \right. \\ \left. (f(\varepsilon_1)f(-\varepsilon_2)f(\varepsilon_3) + f(-\varepsilon_1)f(\varepsilon_2)f(-\varepsilon_3)) \right],$$

where  $f(\omega) = [\exp(\omega/k_B T) + 1]^{-1}$  denotes the Fermi function and  $\rho_{\text{imp},\sigma}^{(\text{HF})}(\omega)$  corresponds to the Hartree-Fock impurity spectrum

$$\rho_{\text{imp},\sigma}^{(\text{HF})}(\omega) = -\frac{1}{\pi} \text{Im}G_{\text{imp},\sigma}^{(\text{HF})}(\omega + i\eta), \quad (6.77)$$

with spectral broadening  $\eta \rightarrow 0^+$ . Here, the Hartree-Fock Green's function is defined

$$G_{\text{imp},\sigma}^{(\text{HF})}(\omega + i\eta) = \frac{1}{\omega + i\eta + \tilde{\mu}_\sigma - \Delta_\sigma(\omega + \mu) - U\langle\hat{n}_{0,-\sigma}\rangle},$$

with the hybridization function  $\Delta(\omega + \mu) = \sum_{\mathbf{k}} V_{\mathbf{k}}^2 / (\omega + \mu - \varepsilon_{\mathbf{k}})$ . The parameter  $\tilde{\mu}_\sigma$  is one of the free parameters, which we will set later. Within IPT it is fixed by  $\tilde{\mu}_\sigma \equiv \mu$ .

Unlike in IPT, Following Kajueter and Kotliar [301] the ansatz for the selfenergy within MPT is

$$\Sigma_{\text{imp},\sigma}(\omega) = U\langle\hat{n}_{0,-\sigma}\rangle + \frac{a_\sigma \Sigma_{\text{imp},\sigma}^{(2)}(\omega)}{1 - b_\sigma \Sigma_{\text{imp},\sigma}^{(2)}(\omega)}. \quad (6.78)$$

Additionally to the already introduced  $\tilde{\mu}_\sigma$ ,  $a_\sigma$  and  $b_\sigma$  constitute further free parameters. In MPT they are adjusted such that the shape of the impurity spectral function is best fitted, i.e. the first four moments of the spectrum are reproduced since they fix high-energy behavior of the self-energy<sup>20</sup>. The moments are defined

$$M_0^{(m)} = \int_{-\infty}^{\infty} d\omega \rho_{\text{imp}}(\omega) \omega^m,$$

where  $m = 0, 1, 2, 3, \dots$  indicates the order of the moment. However, the calculation of the moments is challenging, since with increasing  $m$  higher order correlations appear<sup>21</sup>. In their publication [301] Kajueter *et al.* adjusted  $b_\sigma$  to get the correct result for the atomic limit and  $a_\sigma$  to reproduce the  $m = 2$  moment of the resulting spectrum. In contrast,

<sup>20</sup>Due to different parameter choice, within IPT the high-energy properties of the self-energy away from half-filling are not correct.

<sup>21</sup>The explicit expressions for the first three moments are given in [302].

Potthof *et al.* extended the method to account additionally for the  $m = 3$  moment [302]. The authors demonstrated that adjusting the parameters to  $m = 2$  and 3 recovers limiting cases<sup>22</sup>. Especially the consideration of the  $m = 3$  moment was shown to be significant for spontaneous magnetism. Due to the validity in the atomic limit, i.e. for  $U \rightarrow \infty$ , and by construction based on series expansion in the weakly interacting case  $U \rightarrow 0$  MPT is considered to give approximative but reasonable results also in between. Finally, the good agreement with paramagnetic QMC data [309] approves its use as impurity solver within DMFT.

From the  $1/\omega$  expansion of the selfenergy the coefficients are determined:

$$a_\sigma = \frac{\langle n_{0,-\sigma} \rangle (1 - \langle n_{0,-\sigma} \rangle)}{\langle n_{0,-\sigma} \rangle^{(\text{HF})} (1 - \langle n_{0,-\sigma} \rangle^{(\text{HF})})},$$

$$b_\sigma = \frac{B_{0,-\sigma} - \mu - B_{0,-\sigma}^{(\text{HF})} + \tilde{\mu}_\sigma + U(1 - 2\langle n_{0,-\sigma} \rangle)}{U^2 \langle n_{0,-\sigma} \rangle^{(\text{HF})} (1 - \langle n_{0,-\sigma} \rangle^{(\text{HF})})}.$$

The explicit expressions for the expectation values in the Hartree-Fock approximation, indicated by the index (HF), are

$$\langle n_{0,\sigma} \rangle^{(\text{HF})} = \int_{-\infty}^{\infty} d\omega f(\omega) \rho_{\text{imp},\sigma}^{(\text{HF})}(\omega),$$

$$B_{0,\sigma}^{(\text{HF})} = \frac{1}{\langle n_{0,\sigma} \rangle^{(\text{HF})} (1 - \langle n_{0,\sigma} \rangle^{(\text{HF})})} \sum_l V_{l,\sigma} \langle \hat{c}_{l,\sigma}^\dagger c_{0,\sigma} \rangle^{(\text{HF})} (2\langle n_{0,-\sigma} \rangle^{(\text{HF})} - 1)$$

with  $\rho_{\text{imp},\sigma}^{(\text{HF})}(\omega)$  given in Eq. (6.77) and  $f(\omega)$  being the Fermi function.

And last but not least the parameter  $\tilde{\mu}_\sigma$  has to be set. There exist three different possibilities to determine  $\tilde{\mu}_\sigma$  which all ensure correct behavior for weak and strong coupling limits [302]:

- (1)  $\tilde{\mu}_\sigma = \mu,$
- (2)  $\langle \hat{n}_{0,\sigma} \rangle^{(\text{HF})} = \langle \hat{n}_{0,\sigma} \rangle,$
- (3)  $\mu = \mu_{U \rightarrow 0} + \Sigma_\sigma(\omega = 0).$

Together with  $a_\sigma = 1$  and  $b_\sigma = 0$  the first condition recovers IPT with corresponding limitations. Otherwise, for choices of  $a_\sigma$  and  $b_\sigma$  oriented on higher spectral moments this possibility to fix  $\tilde{\mu}_\sigma$  is equivalent to (2) and (3). The second condition compensates the energetic shift of the Hartree-Fock Green's function for constant  $\Delta_\sigma$  implicating  $\tilde{\mu}_\sigma = \mu_{U \rightarrow 0} + U \langle \hat{n}_{0,-\sigma} \rangle$ . The third condition is restricted to zero temperature regimes, since it implies that  $\text{Im}\Sigma_\sigma(\omega = 0) = 0$  which is only true for  $T = 0$  [311], and is equivalent to the Luttinger theorem [312]. The results presented in this thesis are based on the constraint (2). Further peculiarities of this impurity solver and its numerical implementation can be found in [301, 302, 313].

### 6.5.3 RDMFT

The method DMFT derived in the foregoing chapters, was explained to map the many-body lattice problem on an impurity-site coupling to a bath. So far this impurity site was

<sup>22</sup> The method MPT reproduces the correct selfenergy in atomic limit, limit of infinite dimensions, where the exact expressions are known [78, 310], and in the weak coupling regime  $U \rightarrow 0$ , which guarantees correct description of the Fermi-liquid.

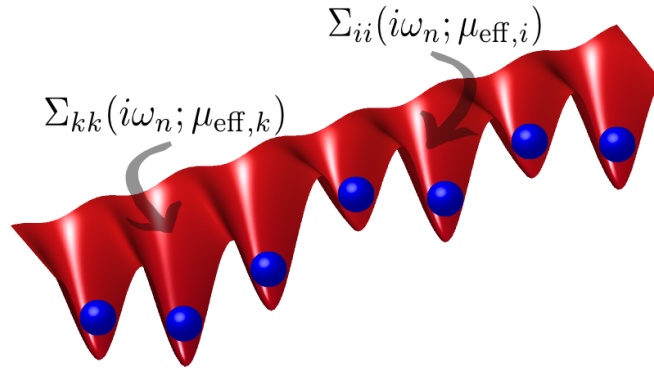


**Figure 6.12:** Implementation of the position space resolution in the real space DMFT extension (RDMFT). Each site is described by a distinct selfenergy which remains local but varies within a lattice when the potential is inhomogeneous.

considered to represent any arbitrary site of the lattice, which is justified in homogeneous systems. From here it follows, that without further amendment this approach is not applicable to inhomogeneous lattices as is the case in most experiments in which the atoms are trapped in the lattice via an external potential or potential disorder is present. For studies of such systems the DMFT was extended to the so-called *RDMFT*. In this extension the real space resolution is incorporated by means of local but site-dependent self-energies, i.e.  $\Sigma_{ij,\sigma}(i\omega_n) = \Sigma_{\sigma}(i\omega_n)$  (DMFT) becomes  $\Sigma_{ij,\sigma}(i\omega_n) = \Sigma_{ii,\sigma}(i\omega_n, \mu_{\text{eff},i})$  in RDMFT, see Fig. (6.12), [208, 281, 314]. Neglecting the momentum dependence and consequently non-local correlations is still exact only in infinite dimensions [298, 310], however, due to intrinsic coupling between the sites the method is still capable of treating all kinds of inhomogeneous potentials exactly. This enables the desired real space differentiation and with it a description of trapped systems, different types of disorder and magnetic ordering [17, 51, 146, 228, 284, 315]. In this chapter we will give a brief derivation of the RDMFT method.

Interacting fermions in an inhomogeneous lattice are described by the introduced Fermi-Hubbard Hamiltonian<sup>23</sup> (see Eq. (6.44))

$$\hat{\mathcal{H}} = -t \sum_{\langle ij \rangle, \sigma} (\hat{c}_{i,\sigma}^\dagger \hat{c}_{j,\sigma} + h.c.) + U \sum_i \hat{n}_{i\uparrow} \hat{n}_{i\downarrow} + \sum_{i,\sigma} (\varepsilon_i - \mu) \hat{n}_{i\sigma},$$

where  $\sigma \in \{\uparrow, \downarrow\}$  labels spin, while  $\hat{c}_{i\sigma}^\dagger$ ,  $\hat{c}_{i\sigma}$  and  $\hat{n}_{i\sigma}$  are the creation, annihilation and particle number operators for an electron on site  $i$  with spin  $\sigma$ . The on-site energy  $\varepsilon_i$  represents the inhomogeneous on-site potential, i.e. trapping potential, disorder potential etc., superimposed on the homogeneous lattice potential.  $U$  is the on-site interaction and  $t$  is the nearest-neighbor hopping matrix element. Both parameters are considered homogeneous despite potential differences between neighboring sites, which is a valid construct when the potential differences are small and an approximation otherwise. We will consider the case of site dependent  $U_i$  and  $t_{ij}$  later in Sec. 8. Since the sites differ one from another, distinct from DMFT [281] **each** lattice site  $i$  is mapped onto a single-impurity

<sup>23</sup>In case of a randomly disordered potential landscape the Hamiltonian is called *Anderson Hamiltonian* in honor of the P. W. Anderson who first analyzed the properties of disordered systems such as Anderson localization [39].

Anderson Hamiltonian within RDMFT. This leads to a set of impurity problems (compare to Eq. (6.59))

$$\hat{\mathcal{H}}_{\text{AM}}^{(i)} = \sum_{l\sigma} \epsilon_{i,l\sigma} \hat{a}_{l\sigma}^\dagger \hat{a}_{l\sigma} + \sum_{l\sigma} V_{i,l\sigma} (\hat{a}_{l\sigma}^\dagger \hat{c}_{0\sigma} + \text{h.c.}) - \mu_{\text{eff},i} \sum_{\sigma} \hat{c}_{0\sigma}^\dagger \hat{c}_{0\sigma} + U \hat{n}_{0\uparrow} \hat{n}_{0\downarrow},$$

where  $\hat{a}_{l\sigma}^\dagger$  ( $\hat{c}_{0\sigma}^\dagger$ ) and  $\hat{a}_{l\sigma}$  ( $\hat{c}_{0\sigma}$ ) are fermionic creation and annihilation operators in the bath (on the impurity),  $\sigma$  represents the spin index and  $\mu_{\text{eff},i} = \mu - \epsilon_i$  the effective on-site chemical potential. The parameters  $\epsilon_{i,l\sigma}$  and  $V_{i,l\sigma}$  determine the particular hybridization function at site  $i$

$$\Delta_{i\sigma}(\omega) = \sum_l V_{i,l\sigma}^2 \delta(\omega - \epsilon_{i,l\sigma}). \quad (6.79)$$

The selfconsistency of the inhomogeneous lattice is reached when a set of Weiss Green's functions is found  $\{\mathcal{G}_{0,\sigma}^{(i)}\}$  which satisfies the system parameters and is reproduced when iteratively used within RDMFT routine<sup>24</sup>.

In particular, the selfconsistency loop within RDMFT is organized as follows (see Fig. 6.12): starting with a set of Weiss Green's functions  $\{\mathcal{G}_{0,\sigma}^{(i)}\}$  every site is mapped on a distinct single-impurity Anderson model which is subsequently solved by means of an impurity solver. The calculated local spectra are used to obtain a set of selfenergies  $\{\Sigma_{ii,\sigma}\}$ . Based on the identity of the Weiss Green's function and the local Green's function, the new set of Weiss fields is determined from local Dyson equations

$$\mathcal{G}_{0,\sigma}^{(i)}(i\omega_n)^{-1} = \Sigma_{ii,\sigma}(i\omega_n) + G_{ii,\sigma}(i\omega_n)^{-1}, \quad (6.80)$$

where  $G_{ii,\sigma}(i\omega_n)$  denotes the interacting local Green's function<sup>25</sup> for site  $i$ . To obtain the latter we need an intermediate step: given the non-interacting lattice Green's matrix  $\mathbf{G}_\sigma^0(i\omega_n)$  in real-space representation

$$\mathbf{G}_\sigma^0(i\omega_n)^{-1} = (\mu + i\omega_n)\mathbb{1} - \mathbf{J} - \mathbf{V}, \quad (6.81)$$

where  $\mathbb{1}$  is the unity matrix,  $\mathbf{J}$  is the matrix of hopping amplitudes,  $\mathbf{V} = \epsilon_i \delta_{ij}$  represents the matrix of on-site potentials, and real-space Dyson equation

$$\mathbf{G}_\sigma^{-1}(i\omega_n) = \mathbf{G}_\sigma^0(i\omega_n)^{-1} - \Sigma_\sigma(i\omega_n) \quad (6.82)$$

inverting Eq. (6.82) for each frequency leads the interacting lattice Green's matrix  $\mathbf{G}_\sigma(i\omega_n)$  with diagonal matrix elements  $G_{ii,\sigma}(i\omega_n)$ . Inserting  $G_{ii,\sigma}(i\omega_n)$  into Eq. (6.80) completes the RDMFT loop. Fig. 6.13 illustrates the individual steps of the RDMFT selfconsistency loop in the right order.

The advantage of RDMFT compared to DMFT is the real-space resolution, however, this extension suffers from longer computational time since the time consuming impurity solver is called  $L$ -times in an  $L$ -sites lattice, if no spatial symmetries are present, and the real-space Green's matrix to be inverted scales  $\sim L^{3/2}$ . An additional bottle neck in the inversion of the lattice Green's matrix Eq. (6.82) is the limited computational memory available. Within this thesis the computational effort could be considerably reduced<sup>26</sup>

<sup>24</sup>Within DMFT only single impurity problem had to be solved which consequently required a consistent solution with respect to a single Weiss field.

<sup>25</sup>For homogeneous lattices the interacting local Green's functions are identical and the lattice problem reduces to a single-site problem where  $G_{ii,\sigma} \equiv G_{00,\sigma}$  corresponding to DMFT notation.

<sup>26</sup>Calculations on  $N$  nodes reduce the CPU time approximately by a factor  $1/N$  when impurity solvers of different sites are calculated in parallel and by an additional factor of  $1/N$  when matrix inversion is parallelized for different frequencies.

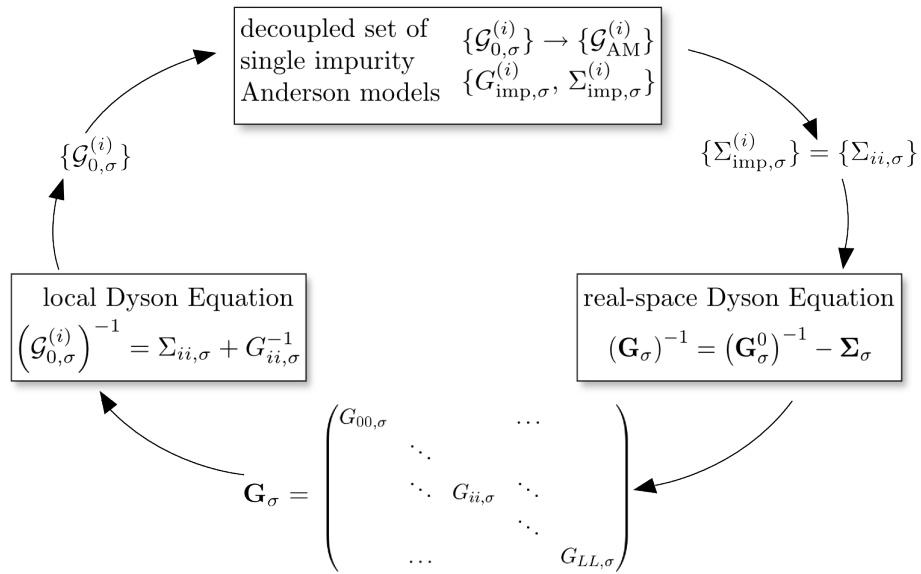


**Figure 6.13:** Illustration of the RDMFT selfconsistency loop for an  $L$ -sites lattice. Explanations to single steps can be found in text.

by parallelizing impurity calculations on distinct sites and matrix inversions for different frequencies. Additional enhancement can be achieved when the sparse form of the matrix  $\mathbf{G}_\sigma^{-1}$  is exploited.



# 7. Phase diagram of fermionic 1D Hubbard model with box disorder

## 7.1 Peculiarities of 1D fermionic systems

One dimensional systems play a special role in condensed and ultracold gases systems. In order to describe the unique effect interactions induce in 1D, analogous to the Fermi liquid theory in 2 and 3D, the Luttinger liquid was invented. One dimensional systems, theoretically explored since 1950's, gained also experimental relevance nearly 20 years later as a consequence of material progress on organic compounds. Later on, realizations of 1D systems on nanoscales followed such as quantum nanotubes, Josephson junction arrays etc. And last but not least, the development of ultracold systems since 1997 enables not only a high-precision realization of any dimension but also the tuning of system parameters opening a new possibility of experimental quantum simulations.

The exceptional position of 1D systems can be illustrated in the following Gedankenexperiment, see illustration Fig. 7.1. Considering interacting particles in free space, in higher dimensions a nearly free propagation of a particle is possible. Contrary, in 1D in order to propagate a particle has to push other particles such that an individual motion becomes 'collective'. From this simple illustration one can already deduce that effects of interactions are at their strongest in one dimension. Accounting for interactions via perturbation theory leads to singularities in 1D [223]. This indicates that even weak interactions in low-dimensional systems yield drastic consequences compared to higher dimensions.

Additional challenge constitutes the presence of the disorder. As already introduced in foregoing sections, disorder can give rise to Anderson localization. Following the exact solutions, in 1D the localization length is of the order of the mean free path itself [213, 214]. It means that in contrast to higher dimensional systems, where localization is due to interference effects, in one dimension the forward and backward scattering from impurities is sufficient to stop the transport.

The physics resulting from the simultaneous presence of both effects is not yet fully understood, due to a competition arising between disorder and interaction. Both forces may induce metal-insulator transition, however, via different mechanisms. In repulsively interacting systems localization of particle wave functions at different sites minimizes the potential energy. Consequently, interactions favor a homogeneous density distribution.

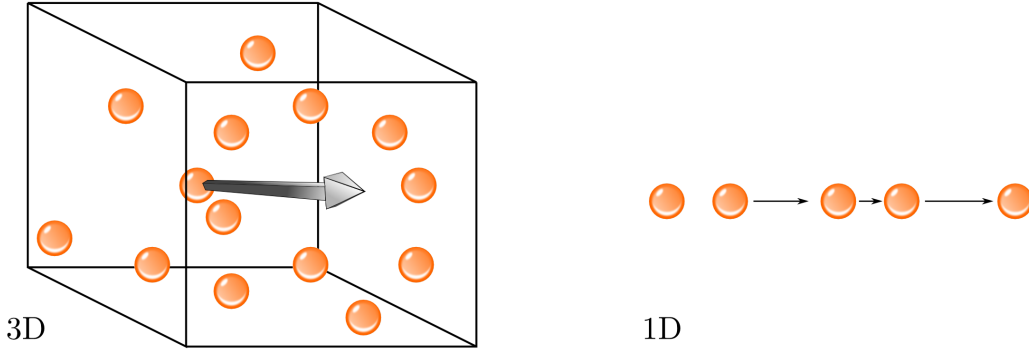


**Figure 7.1:** Illustration of particle propagation in different dimensions in free space. In 3D there may be a path such that an interacting particle can propagate almost freely through the system as indicated by the arrow. In 1D no single-particle motion exists because each fermion obstructs a passage of the other. The interactions, even weak, induce collective effects.

Contrary, scattering from impurities binds particles to a few lattice sites inducing random distribution.

Investigation of interacting spinful fermions in a box disordered 1D lattice at half filling is one of the aims of this dissertation [228]. The ground state phase diagram is obtained by means of the real-space dynamical mean-field theory (R-DMFT) and compared to calculations via the exact density matrix renormalization group (DMRG) done by Georg Harder. The phases are characterized and distinguished using the following physical observables: a) the geometric average of the local density of states, representing its typical value, and its scaling behavior with the system size, b) the charge gap in the thermodynamic limit, c) the inverse participation ratio and its dependence on the system size.

## 7.2 Model and methods

Strongly correlated disordered fermions on a lattice are described by the Anderson-Hubbard Hamiltonian

$$\begin{aligned} \mathcal{H} = & -t \sum_{i,\sigma} (\hat{c}_{i,\sigma}^\dagger \hat{c}_{i+1,\sigma} + \hat{c}_{i+1,\sigma}^\dagger \hat{c}_{i,\sigma}) + U \sum_i \hat{n}_{i\uparrow} \hat{n}_{i\downarrow} \\ & + \sum_{i,\sigma} (\varepsilon_i - \mu) \hat{n}_{i\sigma}, \end{aligned} \quad (7.1)$$

where  $\sigma \in \{\uparrow, \downarrow\}$  labels spin, while  $\hat{c}_{i\sigma}^\dagger$ ,  $\hat{c}_{i\sigma}$  and  $\hat{n}_{i\sigma}$  are the creation, annihilation and particle number operators for an electron on site  $i$  with spin  $\sigma$ .  $U$  is the on-site interaction and  $t$  is the nearest-neighbor hopping matrix element. The on-site energies  $\varepsilon_i$  are random variables, each distributed independently according to  $\mathcal{P}(\varepsilon_i) = \Theta(D - |\varepsilon_i|) \cdot 1/2D$ . Here  $\Theta$  is a Heaviside function and  $D$  is the disorder strength. We consider a 1D bipartite lattice with commensurate filling  $\langle n_i \rangle = \langle n_{i\uparrow} + n_{i\downarrow} \rangle = 1$ . In the homogeneous case, i.e. for  $D = 0$ , this Hamiltonian can be solved exactly by means of the Bethe ansatz [241]. However, advanced numerical methods are required when the on-site energies are random.

Commonly used approaches to solve interacting quantum problems in one spatial dimension are the perturbative renormalization group (RG), the density matrix renormalization



group (DMRG) and quantum Monte-Carlo (QMC). The RG is able to capture localization and delocalization effects for repulsive as well as for attractive interactions. However, it describes the system accurately only for small disorder strength [55, 316]. Since we would like to study both strong disorder and strong interactions regimes our method of choice is the real-space dynamical mean-field theory (RDMFT) [208, 298, 314] combined with numerical renormalization group (NRG) impurity solver. Besides the description of the Mott-Hubbard metal-insulator transition and magnetic ordering it is capable of treating spatial inhomogeneities such as disorder. Similar to DMFT, this extension is non-perturbative and takes local quantum fluctuations full into account, whereby all non-local contributions are neglected. Particularly, the selfenergy within RDMFT is assumed a local but site dependent quantity. The details to this technique are given in Sec. 6.5.3.

Although leading to qualitatively correct predictions in 3D, non-local selfenergy terms have been shown to influence the metal-insulator transition [317]. Therefore, in order to benchmark the results of RDMFT in low dimensions a quantitative comparison to exact DMRG calculations is presented. DMRG is an exact method and allows for a determination of the phase diagram in a broad parameter range [318–320], similar to QMC.

## 7.3 Results

### 7.3.1 Local density of states

In order to describe the transition from delocalized to localized states it is useful to characterize the spectral properties of the system by the local density of states (LDOS), which measures the local amplitude of the wave function at a given site  $i$

$$\rho_{i\sigma}(\omega) = -\frac{1}{\pi} \text{Im} G_{ii\sigma}(\omega).$$

The calculation of the on-site Green's function  $G_{ii\sigma}(\omega)$  is based on the local spectrum for a particular disorder realization  $\{\varepsilon_1, \varepsilon_2, \dots, \varepsilon_L\}$ . In this work we focus on the paramagnetic solution and drop the spin index  $\sigma$  for readability. To gain realization-independent information, arithmetic and geometric averaging over the spectral functions is performed

$$\begin{aligned} \rho_a(\omega) &= \frac{1}{NL} \sum_j^N \sum_i^L \rho_i(\omega, \{\varepsilon_1, \dots, \varepsilon_L\}_j) \\ \rho_g(\omega) &= \frac{1}{N} \sum_j^N \exp\left(\frac{1}{L} \sum_i^L \ln \left[\rho_i(\omega, \{\varepsilon_1, \dots, \varepsilon_L\}_j)\right]\right) \end{aligned}$$

given  $N$  disorder realizations and  $L$  sites. In this work averages over 50–100 configurations were performed for each  $(U, D)$  parameter set. The geometric average is a good approximation of the typical value of the probability distribution function for the LDOS.[54] Thus, the geometrically averaged spectral function is critical at the Anderson transition, i.e. it is finite in the delocalized regime and vanishes in the localized phase and therefore can be interpreted as an order parameter.[39, 53, 54, 266] The arithmetic average remains finite in the Anderson-localized regime and corresponds to the global density of states (DOS).

This classification is, however, only reliable in the thermodynamic limit  $L \rightarrow \infty$ . In finite systems a careful analysis of finite-size effects has to be performed. In a system of length  $L$

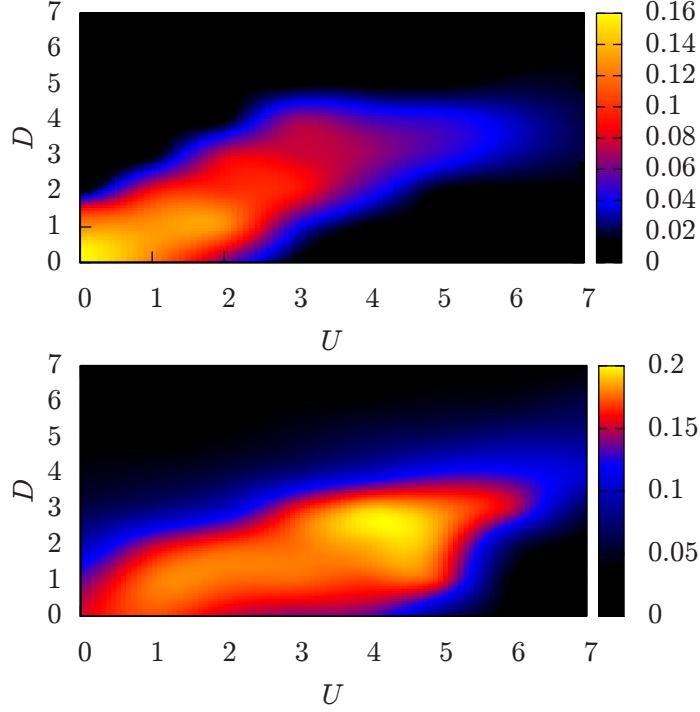


**Figure 7.2:**  $\rho_g(0)$  calculated by means of DMRG (upper panel) and RDMFT (lower panel). The Mott phase is located in the lower right area and the Anderson-Mott phase in the upper left area. They are separated by a region with finite typical LDOS, which indicates a delocalization tendency.

the spectrum is discrete and the non-interacting energy level spacing in the DOS scales as  $1/L$ . This discrete level structure due to the finite size can be smoothed by a broadening of each level to reconstruct the DOS in the thermodynamic limit. Unfortunately, spectral broadening with a width  $\eta$ , which is necessary due to the finite system size, limits the spectral resolution of our calculations. The interaction-driven metal-insulator transition can therefore only be detected when the gap exceeds  $\eta$ . Similarly, the effect of the disorder strength is underestimated. Disorder increases the energy level spacing in the LDOS, which leads to localization. Due to broadening this discretization is smeared out and Anderson localization is observed at a larger value of  $D$  than in the thermodynamic limit. A further finite-size effect is the competition between the system size  $L$  and the localization length  $\xi$ . When localization sets in with increasing disorder, the localization length is larger than the system size and even exponentially localized states contribute spectral weight at all lattice sites in finite-size systems. Accordingly, disorder-driven localization can only be identified for  $L \gg \xi$ . Due to these limitations, the goal of our work is to reveal the localization/delocalization trends in the system rather than to determine sharp phase boundaries.

To investigate a possible emergence of a metallic phase,  $\rho_g(\omega)$  is analyzed at the Fermi level  $\omega = 0$  using RDMFT with  $L = 128$ ,  $\eta = 0.05$  and 10-50 disorder configurations, and using DMRG with  $L = 64$ ,  $\eta = 0.2$  and 16 disorder configurations, where the results are additionally deconvolved<sup>1</sup>. The results are presented in Fig. 7.2.

<sup>1</sup>Further explanations and details about DMRG parameter can be found in the publication [228]

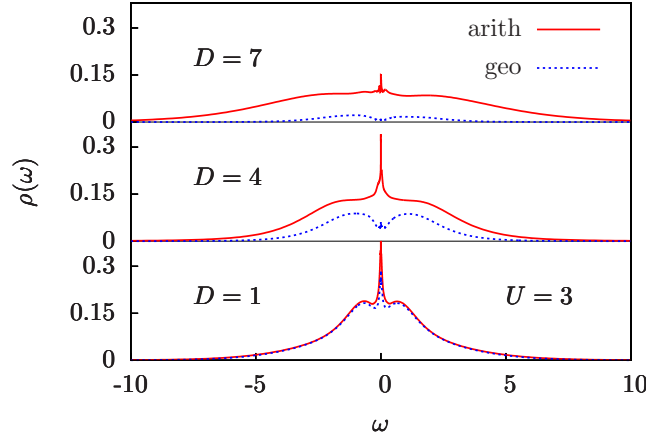


**Figure 7.3:** Comparison between geometrically (dashed line) and arithmetically averaged (solid line) LDOS for  $U = 3$  calculated within RDMFT. With increasing disorder strength the geometrically averaged density of states gradually vanishes, starting from the band edges.

Three different regimes are found in the system: The Anderson-Mott insulating regime at large  $D$ , the Mott-insulator at large  $U$  and a delocalization (metallic) tendency for intermediate disorder and interaction strength.

(i) **Anderson-Mott Insulator (AMI):** As the spectrum of the localized system consists of a dense distribution of poles,[255] the geometrically averaged LDOS vanishes at all frequencies while the arithmetical average remains finite. The formation of AMI proceeds from the edges of the band towards the band center with increasing disorder strength (see Fig. 7.3). As soon as the geometrically averaged LDOS  $\rho_g(\omega)$  vanishes at the Fermi level  $\omega = 0$  the system becomes fully localized. We first analyze our results along the  $D$  axis at  $U = 0$ . Exact calculations predict the non-interacting system to undergo an Anderson metal-insulator transition in the thermodynamic limit  $L \rightarrow \infty$  at any finite disorder strength.[241] However, we obtain clear signatures of localization at  $U = 0$  only for  $D \gtrsim 2$  (DMRG) or  $D \gtrsim 3$  (RDMFT). This can be traced back to the finite size of the investigated system. The localization length in this case is larger than the system size, such that the states remain quasi-extended and are only localized for very large system sizes.[321] A careful analysis of the scaling behavior with system size was performed in RDMFT for  $U = 0$  and  $D = 3$  and is displayed in Fig. 7.4a. The decay of  $\rho_g(0)$  with increasing system size confirms localization (see a detailed discussion of the finite-size scaling below).

(ii) **Mott Insulator (MI):** Here for  $D = 0$  and  $U > 0$  the LDOS  $\rho(\omega)$  vanishes at the Fermi level  $\omega = 0$  due to the appearance of a Mott gap. In the deconvolved DMRG results  $\rho$  decreases monotonously with increasing interaction and a MI appears for  $U \gtrsim 3$ . Within RDMFT the Luttinger theorem ensures pinning of the spectral weight at the Fermi level.[322] Thus,  $\rho_g(\omega = 0)$  remains finite and constant up to  $U = 4$  and the gap is first formed at  $U \gtrsim 5$  (see Fig. 7.2). DMRG as well as RDMFT results for finite system size disagree with exact calculations for a homogeneous system in thermodynamic limit, where a Mott insulator is predicted to appear at any finite interaction strength.[215] In RDMFT, as in every other DMFT extension, the finite metallic phase in 1D is due to the approximation of a local selfenergy, which becomes exact only in infinite dimensions. In DMRG this discrepancy in the detection of the Mott gap is a consequence of the unavoidable spectral broadening  $\eta$ . Due to this broadening the Mott-gap is smeared out and the resulting crit-

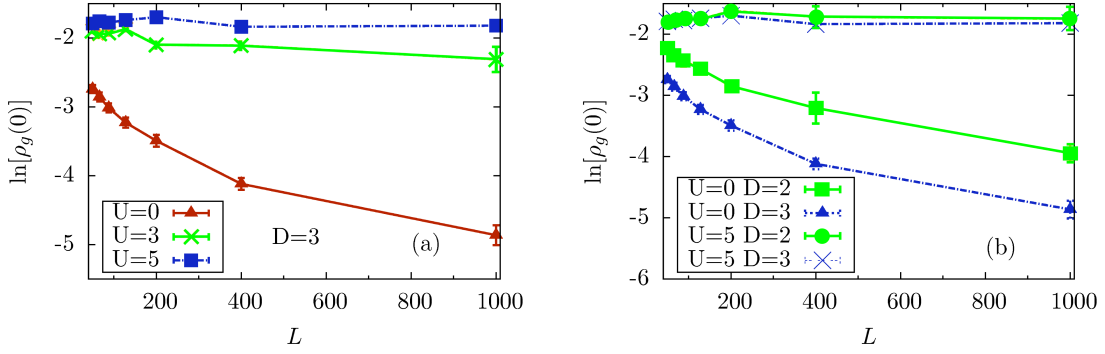


**Figure 7.4:** Finite-size scaling for the geometrically averaged LDOS at the Fermi-level calculated within RDMFT. The results are averaged over 10-50 configurations. (a) The decay with system size at  $D = 3$  and  $U = 0$  indicates Anderson localization while for  $D = 3$  and  $U = 3$  and  $5$  the vanishing size dependence denotes delocalization. (b) Similarly, states which are Anderson-localized at  $U = 0$  become delocalized for  $U = 5$ . Finite interaction shifts  $\rho_g(0)$  to higher values and reduces the dependence on the system size.

ical  $U$  represents an upper bound at which the Mott-insulator is formed. In DMRG, the broadening effects are partially corrected by applying a deconvolution to the spectra. A careful analysis of the finite-size effects in the gap formation is presented in section 7.3.2.

(iii) **Delocalization:** For low to intermediate disorder and interaction, the geometrically averaged spectral density  $\rho_g(\omega)$  is finite at the Fermi level  $\omega = 0$ . The non-black area in both phase diagrams in Fig. 7.2 indicates this delocalization regime. Due to the deconvolution procedure within DMRG the spectral weights are lower than those obtained by RDMFT.

In the absence of disorder and interaction ( $U = D = 0$ ) the system is metallic and satisfies Luttinger's theorem[312] in agreement with our findings. Additionally, a delocalization region is observed for intermediate interaction and disorder strengths. The latter, however, may in principle be due to overestimated spectral weights in finite systems for localization length  $\xi > L$  and finite spectral broadening.

To decide whether true delocalization is observed, a careful finite-size scaling analysis of the RDMFT results was performed for the intermediate  $U$  and  $D$  regimes. The scaling behavior of  $\rho_g(0)$  characterizes the phase of the system: in the non-interacting case if the states are Anderson-localized and the localization length  $\xi \ll L$ , the geometrically averaged LDOS scales as  $\exp[-L/\xi]$  for periodic boundary conditions. If  $\xi > L$  the decay of  $\rho_g(0)$  with system size is algebraic.[323] In systems with finite interactions the functional dependence of  $\rho_g(0)$  on system size is not known, however, the geometrically averaged spectral weight is still expected to decay to zero with increasing system size for localized states and to remain finite for delocalized ones in the limit  $L \rightarrow \infty$ .

In Fig. 7.4a we observe the delocalizing effect of interactions. For  $D = 3$  and  $U = 0$  the geometrically averaged LDOS decays with increasing system size, which indicates the Anderson localized phase. Thus, the final spectral weight visible in the phase diagram in Fig. 7.2 (lower panel) for this parameter set is a finite-size effect for the  $L = 128$  lattice. Upon increasing the interaction strength to  $U = 3$  and  $U = 5$  no clear localization signature could be observed anymore within accessible system sizes.

In Fig. 7.4b the effects of increasing disorder strength and interactions on the localization properties of the system are compared. A geometric average which decays with increasing

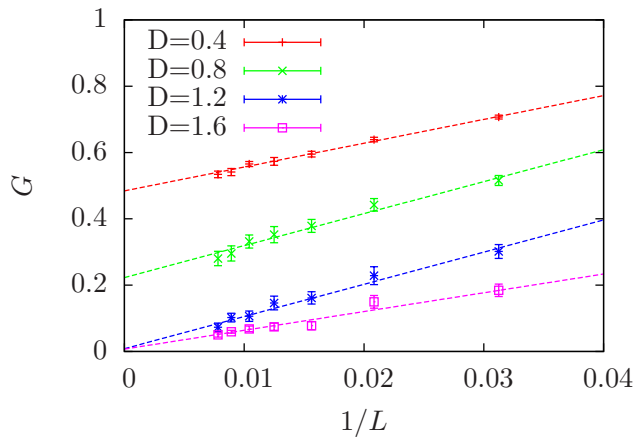


**Figure 7.5:** Charge gap versus inverse system size for  $U = 3$  calculated within DMRG. For disorder strength  $D \gtrsim 1.5$  the disappearance of the gap in the thermodynamic limit  $1/L \rightarrow 0$  indicates the transition from the gapped Mott insulating to a gapless delocalized phase.

system size  $L$  for  $U = 0$  and  $D = 2$  and  $3$  indicates the Anderson localized phase. Again, the delocalization trend observed in Fig. 7.2 (lower panel) for this parameter set turns out to be a finite-size effect for the  $L = 128$  lattice. The redistribution of spectral weight due to increased disorder strength leads to a well pronounced shift of  $\rho_g(0)$  towards lower values for  $D = 3$  compared to  $D = 2$  in the non-interacting case. Strong interaction  $U = 5$  shifts the geometric average upwards and the dependence on the system sizes studied here vanishes which indicates delocalization.

### 7.3.2 Charge gap

In the homogeneous 1D Hubbard model at half-filling a metallic phase exists only at  $U = 0$ . At any finite interaction strength a charge gap in the density of states is predicted to appear and the system becomes Mott insulating. Thus, starting in the MI phase, the additional influence of disorder can be detected via a vanishing gap. Georg Harder performed the calculation of the charge gap by means of DMRG as  $G = [E(N+1) + E(N-1) - 2E(N)]$ , where  $E(N)$  is the ground state energy for  $N$  particles. It is important to note that the computation of the energy  $E(N)$  is not based on the spectrum and is therefore not affected by the artificial broadening  $\eta$ . Thus, the calculated charge gap is exact for a given system size. System sizes up to  $L = 128$  sites are used and averages over 16 disorder realizations are done.

The finite-size scaling for the charge gap at  $U = 3$  and various disorder strengths is presented in Fig. 7.5. In the thermodynamic limit  $1/L \rightarrow 0$  the charge gap closes with increasing disorder and vanishes at  $D \approx 1.5$ . The scaling of the charge gap with system size was fitted by the function  $G(L) = G_\infty + \frac{g}{L}$ . This finite-size analysis confirms the delocalization in Fig. 7.2 (upper panel) for  $U = 3$  and  $D \gtrsim 1.5$ . In contrast, the finite spectral weight at smaller disorder strength was found to be a finite-size effect.

The extrapolated gaps for various disorder and interaction strengths normalized with respect to the extrapolated gaps of the corresponding homogeneous systems are presented in Fig. 7.6 for different interaction strength. The indicated error bars are the asymptotic standard errors of the fitting routine. For intermediate interaction strength the critical

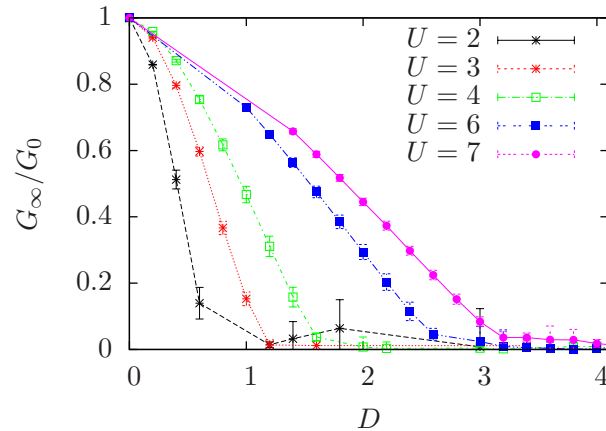


**Figure 7.6:** Scaling of the gap normalized to the non-disordered values  $G_0$  in the thermodynamic limit, calculated within DMRG. The gap effectively vanishes for disorder strength  $D \approx U/2$ . The error bars correspond to the statistical errors of the fitting routine.

disorder needed to destroy the gap was found to be  $\approx U/2$ . This tendency becomes less clear for  $U \leq 2$  as the limited resolution of the exponentially small gap complicates our analysis. The remaining gapless region covers the delocalized as well as the Anderson-Mott localized regime. For a quantitative analysis of this region we calculate the inverse participation ratio as described in the following section.

### 7.3.3 Inverse participation ratio

An alternative characterization of the localization properties can be carried out by means of the inverse participation ratio  $I(\omega)$  (IPR). This observable corresponds to the inverse of the number of sites over which a state is extended<sup>2</sup>. In the non-interacting homogeneous case it is defined as  $I(\omega) = \sum_i^L |\psi_i(\omega)|^4$ , where  $\psi(\omega)$  is a single particle wave function. If a state at frequency  $\omega$  is exponentially localized with corresponding localization length  $\xi(\omega)$  then  $I(\omega)$  scales as  $I_\infty(\omega) \coth[L/\xi(\omega)]$  with the system size for periodic boundary conditions and  $\lim_{L \rightarrow \infty} I(\omega) = I_\infty(\omega) = 1/\xi(\omega)$ . In the case of a purely delocalized state, i.e. for a wave function homogeneously extended over the whole system, the IPR vanishes as  $1/L$  with increasing system size.

In an interacting system the IPR is [59]

$$I(\omega) = \frac{\sum_i^L \rho_i(\omega)^2}{(\sum_i^L \rho_i(\omega))^2}. \quad (7.2)$$

According to the non-interacting case, in the thermodynamic limit IPR vanishes for the delocalized states and remains finite in the localized system. Thus, the scaling behavior with system size gives insight into localization or delocalization driven by disorder or interaction. In Fig. 7.7 the IPR at  $\omega = 0$  is plotted as a function of system size. As expected, for  $U = 0$  and  $D = 3$  the system is Anderson localized and the IPR saturates for  $L \rightarrow \infty$ . Moreover, fitting the data by  $I(0) = I_\infty \coth[L/\xi(\omega)]$  shows that the scaling behavior also

<sup>2</sup>For the sake of consistency with our publication [228] the most common name of this observable is used in this section rather than the historic title. Therefore, the here mentioned IPR is identical to the IPN introduced in Sec. 6.3.7.

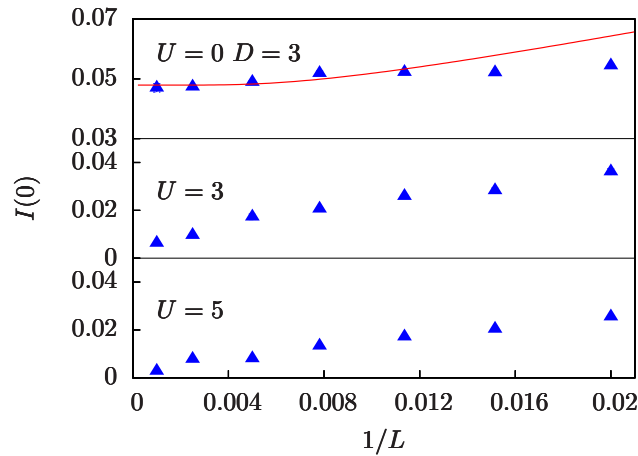


**Figure 7.7:** (Color online) Finite-size scaling of the IPR, calculated within RDMFT. The  $U = 0$ ,  $D = 3$  data are fitted by  $I(0) = I_{\infty}(\omega) \coth[L/\xi(\omega)]$  which corresponds to the characteristic scaling in the localized regime. The decay of  $I(0)$  for  $D = 3$  and  $U = 3$  and  $5$  with increasing system size indicates delocalization.

holds for open boundary conditions at larger system sizes. For finite interaction strength  $U = 3$  and  $U = 5$ , however,  $I(0)$  decays with system size (note the differing scales on the y axis). The vanishing IPR highlights the delocalizing effect of the repulsive interaction. These results confirm our findings in Fig. 7.4.

## 7.4 Discussion and conclusion

By means of real-space dynamical mean-field theory (R-DMFT) and the density matrix renormalization group (DMRG) we investigated the 1D Anderson-Hubbard model at half filling with box-disorder. By varying the disorder and interaction strengths, Anderson- and Mott-insulating regimes are found. Additionally, for intermediate interaction and disorder strength a strong indication of a metallic phase was observed within accessible system sizes. These phases are characterized and distinguished by qualitatively different scaling behavior of the local density of states, the energy gap in the excitation spectrum and the inverse participation number.

In 1D up to now only next-neighbor interacting disordered spinless fermions have been studied exactly via DMRG [324] where, based on the phase sensitivity, a delocalized phase for intermediate attractive interaction and disorder strength was found. Our results constitute the first clue for delocalization in the ground state phase diagram of spinful fermions with on-site interactions. Although DMRG as well as RDMFT agreed in their observations, a further studies of finite-size scaling by means of an exact method are required to prove the existence of the metal unequivocally.





## 8. Strongly correlated fermions in speckle-disordered lattices

In this chapter the effects of an unbounded disorder type will be investigated: the speckle disorder. In experiments with ultracold atoms, the speckle potential is created by a coherent laser beam which is scattered by a diffusor plate [40, 41, 231–233]. As mentioned in Sec. 6.2.2, the corresponding probability distribution function (PDF) decays exponentially. Thus, obtained on-site energies are bounded from below, whereby the lowest value  $\varepsilon_i = 0$  is the most likely one. The salient property of this disorder type is, that infinitely large energetic offsets are theoretically possible albeit being unlikely. This unbounded character is the main difference to the previously studied box disorder. As will be shown in the results section in this chapter, this particular feature leads to substantial changes in the ground state phase diagram. At the same time, it must be mentioned that unbounded disorder is implemented only in optical lattices and does not exist in solids. However, since an implementation of box disorder, which is more condensed matter relevant, is not achieved in ultracold systems yet, the investigation of speckle disorder still contributes substantially to an understanding of disorder physics.

Due to the specific statistical nature of this kind of disorder, a more accurate description of system parameters is required than discussed in the previous chapter. Additionally to arbitrary on-site energies, also termed diagonal disorder, the randomness in hopping amplitudes has to be considered here. This off-diagonal disorder is induced by energetic shifts between neighboring lattice sites, which affect the tunneling probability. The incorporation of both diagonal and off-diagonal disorder constitutes a complete description of particles in a disordered lattice in a single particle picture.

The simultaneous presence of strong repulsion and speckle disorder has been realized recently in a 3D bosonic optical system [233]. In this experiment a disorder-induced insulating state was observed. On the theoretical side, studies on speckle-disordered bosonic systems have been done [46, 325]. However, no comparable investigations have been provided for fermions so far. This missing link will be given in the following chapter, where a description of interacting fermions in a speckle-disordered optical lattice is elaborated.

## 8.1 Joint probability distribution functions

A speckle disorder distribution of on-site energies  $\varepsilon_i$  is given by

$$\mathcal{P}_\varepsilon(\varepsilon_i) = \frac{1}{D} e^{-\varepsilon_i/D} \Theta(\varepsilon_i),$$

where  $D$  denotes the disorder strength and  $\Theta(\varepsilon_i)$  the Heaviside function. As explained in Sec. 6.2.2, this PDF is derived from the light intensity pattern distribution of the laser [234]. Correspondingly, the disorder strength  $D$  is proportional to the tunable speckle field strength  $s_D$ . The proportionality constant depends on the ratio of the speckle field autocorrelation length to the typical spatial extend of the Wannier function and is therefore experiment specific. In the setup implemented by White *et al.* the relation  $D = 0.97s_D$  was found [233]. We assume that the on-site energies of all lattice sites are independently and identically distributed.

The random energy distribution yields statistically distributed tunneling matrix elements. Particularly, the hopping coefficient  $t_{ij}$  at a neighboring pair of sites is correlated with the difference in the on-site energies  $\Delta\varepsilon_{ij} = \varepsilon_i - \varepsilon_j$ . Hence, the distribution for  $t_{ij}$  cannot be sampled independent from  $\Delta\varepsilon_{ij}$  but is rather described by a joint PDF [235]

$$\mathcal{P}_{\varepsilon,t}(\Delta\varepsilon_{ij}, t_{ij}) \neq \mathcal{P}_\varepsilon(\Delta\varepsilon_{ij})\mathcal{P}_t(t_{ij}). \quad (8.1)$$

In our calculations this dependence is accounted by a conditional PDF  $\mathcal{P}_t(t_{ij}|\Delta\varepsilon_{ij})$ , which we construct for a given fixed distribution of  $\varepsilon_{ij}$  values. The details of the derivation are given in the Appendix H.

Additionally, shifts in the on-site potentials influence the Wannier functions. Since the local interaction matrix element is proportional to the fourth power of the Wannier function the on-site interaction strength becomes a random variable. The corresponding distribution of on-site coefficients  $U_i$  obeys a joint PDF

$$\mathcal{P}_{\varepsilon,U}(\varepsilon_i, U_i) \neq \mathcal{P}_\varepsilon(\varepsilon_i)\mathcal{P}_U(U_i),$$

which also needs to be taken into account. Similar to the joint PDF of the difference in the nearest neighbor energies and the hopping amplitudes, the joint PDF  $\mathcal{P}_{\varepsilon,U}(\varepsilon_i, U_i)$  is accounted for by the conditional PDF  $\mathcal{P}_U(U_i|\varepsilon_i)$ . The methodical details are explained in Appendix H.

The parameters  $\varepsilon_i, U_i, t_{ij}$  corresponding to experimentally realized systems, e.g. as in the experiment by White *et al.* [233], were calculated by S. Q. Zhou and D. M. Ceperley [235] for the fixed disorder strength  $s_D = 1E_R$  and lattice depth  $s = 14$ . Their computation of the Hubbard parameters was based on the imaginary time evolution of a 3D  $6 \times 6 \times 6$  lattice for 1222 disorder realizations. The resulting statistics are adjusted appropriately to the parameter regimes used in this thesis to obtain the desired conditional PDFs in the way described in Appendix H.

## 8.2 Phase diagram

To obtain the ground state phase diagram of a speckle-disordered lattice the Anderson-Hubbard Hamiltonian

$$\mathcal{H} = - \sum_{ij,\sigma} t_{ij} \hat{c}_{i,\sigma}^\dagger \hat{c}_{j,\sigma} + \sum_i U_i \hat{n}_{i\uparrow} \hat{n}_{i\downarrow} + \sum_{i,\sigma} (\varepsilon_i - \mu) \hat{n}_{i\sigma}$$

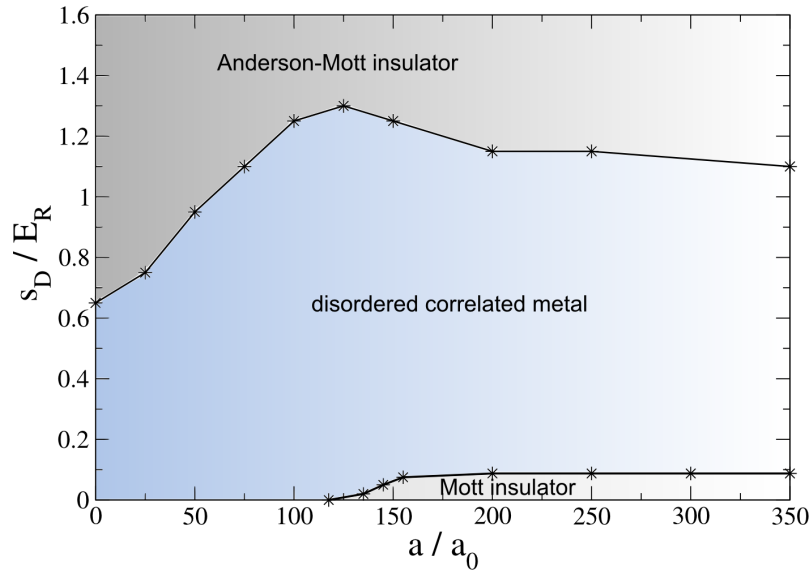


**Figure 8.1:** Paramagnetic ground state phase diagram for half-filled speckle-disordered optical lattice at lattice depth  $s = 10$ . The speckle field strength  $s_D$ , which is proportional to the disorder strength, is given in units of the recoil energy. The  $s$ -wave scattering length  $a$ , which defines the interaction strength, is given in units of the Bohr radius  $a_0$ .

was solved via statistical dynamical mean-field theory (statDMFT) by D. Semmler. This method constitutes an extension to DMFT that allows for an explicit calculation of the full PDFs of local observables [53, 313, 314]. This method is purely local and incorporates by construction stochastic processes on a Bethe lattice, which is characterized by the connectivity  $K$ . This procedure differs conceptually from the introduced RDMFT, where a certain lattice structure and a fixed disorder configuration was simulated. In statDMFT the system is represented by an ensemble of local Green's functions  $\{G_{ii}(\omega)\}$  obeying a corresponding PDF. Using these Green's functions, a set of selfenergies is calculated and new local Green's functions are obtained. Based on this new ensemble  $\{G_{ii}(\omega)\}$  the new PDF is constructed, which closes the selfconsistency loop. A more detailed description is given in [51, 313].

Our calculations are done for ultracold  $^{40}\text{K}$  atoms in an optical lattice generated by a laser with a wavelength  $\lambda = 738$  nm. The lattice depth in the units of recoil energy is  $s = 10$ . The system is adjusted to be half-filled, i.e.  $\sum_{i,\sigma} \langle \hat{n}_{i\sigma} \rangle = 1$ . The lattice connectivity was set to  $K = 6$ . Throughout this chapter the energy is given in units of the non-interacting bandwidth of the homogeneous system. For the following phase diagram for a Bethe lattice it is  $W_0 = 4t\sqrt{K}$ , where  $t$  is extracted from the band structure calculation for  $s = 10$  [75].

The obtained phase diagram is presented in Fig. 8.1 and consists of the following phases: I) *Mott insulator*, identified by a gapped spectrum. The corresponding DOS vanishes at the Fermi level, i.e.  $\rho_a(\omega = 0) = 0$  (for definition of the arithmetic average see Eq. (6.34)). In particular, in the absence of disorder ( $s_D = 0$ ) a metal-Mott insulator transition is found at the critical scattering length  $a_c = 117.5a_0$ . For finite but small disorder strength the Mott insulator is stable for scattering lengths  $a > a_c$ , see arithmetically and geometrically averaged spectra in Fig. 8.2 (a).

II) *Anderson-Mott insulator*, characterized by a point-like spectrum. The corresponding single-particle excitations described by the LDOS are localized at the Fermi level. In

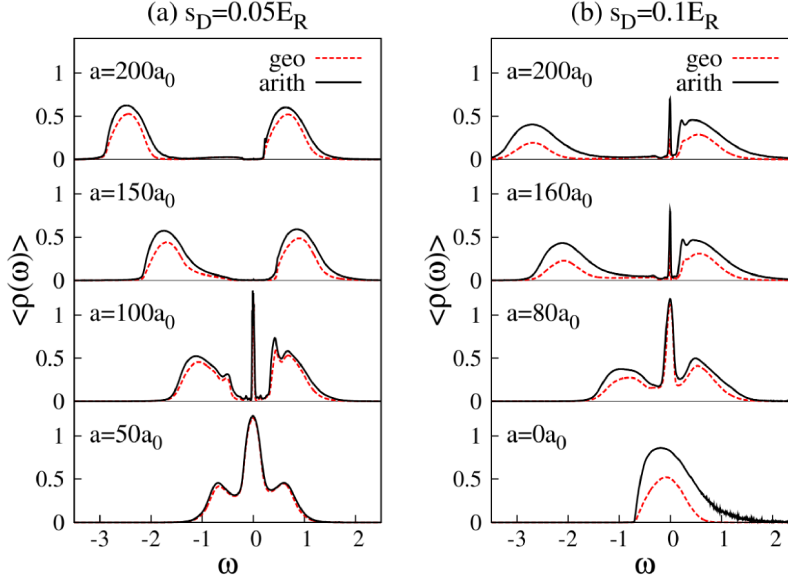


**Figure 8.2:** Averaged arithmetic (black solid) and geometric (red dashed) spectral functions for various scattering and disorder strengths. (a) At  $s_D = 0.05E_R$  a charge gap is formed with increasing scattering length. (b) At  $s_D = 0.1E_R$  the disorder stabilizes a metallic phase such that the spectral weight at the Fermi level  $\omega = 0$  remains finite.

the non-interacting case ( $a = 0$ ) the system is observed to undergo the metal-Anderson insulator transition for  $s_D = 0.65$ .

III) *Metal*, distinguished by a finite averaged LDOS at the Fermi level. This means that the state at  $\omega = 0$  is delocalized and can contribute to the charge transport. Remarkably, for intermediate speckle field strengths the metallic phase is stabilized by disorder such that no metal-insulator transition was obtained for the investigated scattering length up to  $a = 350a_0$ , see Fig. 8.2 (b). This behavior occurs as a consequence of a spectral redistribution caused by disorder. Due to the unbounded nature of the speckle disorder, states with high energy are occupied for every disorder strength  $D$ . Although their number is exponentially suppressed in  $1/D$ , these states fill up the spectral gap leading to a stabilization of a metal even for strong interactions. This means that the Mott transition at finite disorder strength, which is observed in the Fig. 8.1, might even be an artifact of the statDMFT, since due to the computational effort only finite ensemble sizes  $\{G_{ii}(\omega)\}$  are feasible.

Intriguingly, the phase diagram obtained by statDMFT investigations for speckle-disordered systems differs quantitatively from the results presented for a bounded box disorder computed by means of DMFT [44, 58, 326]. A metallic phase was obtained at intermediate disorder and interaction strengths for box disorder, however, in contrast to our results its extent was finite. Consequently, the Mott and Anderson-Mott insulators were found to be continuously connected [44]. The differences in obtained phase diagrams can be referred to the differences in disorder types: the unbounded speckle disorder allows for large disorder offsets at every disorder strength, which influences the competition between interaction and disorder strength in a subtle way.

Furthermore, it is interesting to compare the fermionic results obtained here with a corresponding bosonic phase diagram for speckle disorder. In the latter case, the excitation gap of the Mott insulator is destroyed by an arbitrarily weak speckle field. Thus, a Mott insulating phase in bosonic systems is obtained only in homogeneous cases, whereas for fermions a Mott insulator may exist at  $D > 0$ .

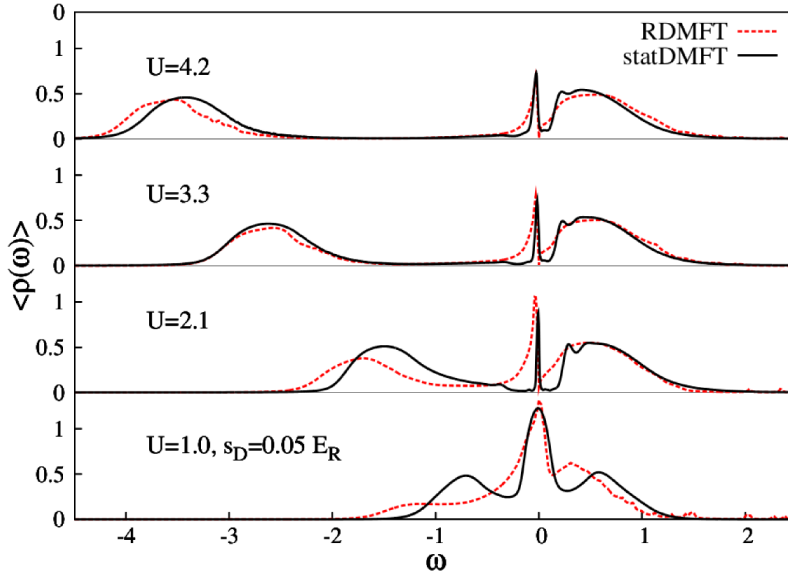


**Figure 8.3:** Comparison of the arithmetically averaged spectral function obtained via RDMFT (red dashed) and statDMFT (black solid). For a fixed speckle field strength  $s_D = 0.05E_R$  the agreement of both methods improves with increasing interaction strength  $U$ . RDMFT results are performed on a  $24 \times 24$  lattice.

### 8.3 Comparison with RDMFT

The use of Bethe lattices is popular when condensed matter problems are simulated via DMFT, since for this lattice structure the corresponding equations defining the hybridization function simplify, see Sec. 6.5.1. Although the obtained results are known to be accurate for higher dimensional systems, in two dimensions stronger deviations from results gained for realistic square lattices might be possible. In order to crosscheck the statDMFT outcome and to benchmark the range of validity of Bethe lattices, a complementary investigation of a two-dimensional square lattice by means of RDMFT is performed.

The bandwidth in a non-interacting homogeneous square lattice is given by  $W_0 = 4td$ , where  $d$  is the dimension of the system. Thus, in a two-dimensional square lattice the bandwidth constitutes  $W_0 = 8t$ . In order to present a quantitative comparison of two numerical methods, the connectivity  $K = 4$  was chosen in statDMFT to obtain the same bandwidth. Throughout the following results the interaction strength  $U$  denotes the most probable value of the respective marginal PDF  $\mathcal{P}_U(U_i) = \int d\varepsilon_i \mathcal{P}_{\varepsilon,U}(\varepsilon_i, U_i)$ .

An exemplary comparison of the arithmetically averaged LDOS resulting from both methods for identical parameters is presented in Fig. 8.3. The results obtained via statDMFT for a semi-elliptical DOS agree qualitatively with the results gained for a square lattice via RDMFT. Interestingly, the deviations are most pronounced for weaker interactions when the kinetic energy dominates the system. Due to a connection between the kinetic energy and the lattice structure, the differences become most evident for a low and intermediate interaction strength (Fig. 8.3  $U = 1.0$  and  $U = 2.1$ ). For stronger interactions,  $U = 3.3$  and  $U = 4.2$ , the agreement improves.

Similar to statDMFT, a delocalized phase is observed within RDMFT for finite disorder and interaction regimes. In Fig. 8.4 arithmetically and geometrically averaged LDOS for  $s_D = 0.01E_R$  and  $s_D = 0.05E_R$  are displayed. For a weak disorder  $s_D = 0.01E_R$  increasing the interaction strength  $U$  leads to a metal-Mott insulator transition, analogously

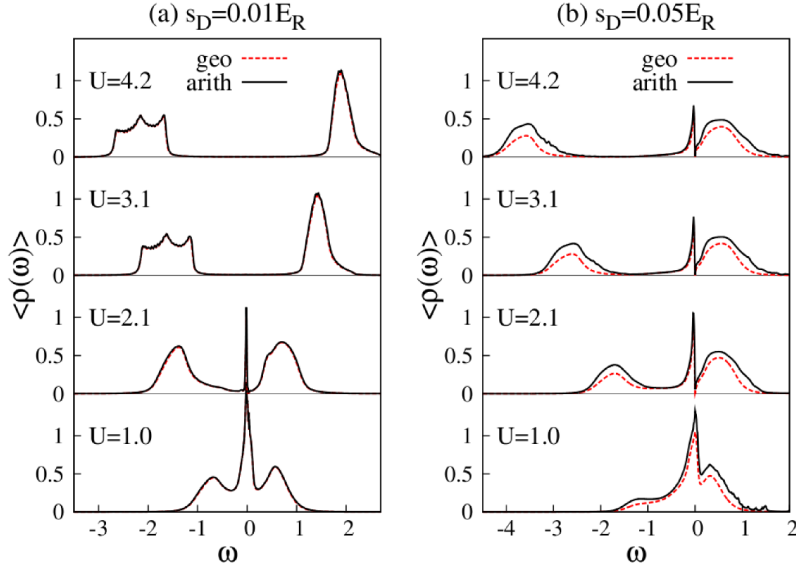


**Figure 8.4:** Geometrically (red dashed) and arithmetically (black solid) averaged LDOS for various disorder and interaction strengths obtained via RDMFT. (a) An increasing interaction strength  $U$  leads to a metal-Mott insulator transition for the speckle field strength  $s_D = 0.01E_R$ . (b) For a higher disorder strength  $s_D = 0.05E_R$  the metallic phase remains stable when  $U$  is increased.

to statDMFT. However, already for  $s_D = 0.05E_R$  the spectral weight at the Fermi level  $\omega = 0$  is stabilized by disorder. This differs from the behavior predicted by statDMFT in Fig. 8.2 (a).

The peaked structure of the lower Hubbard band in Fig. 8.4 is a feature obtained only within RDMFT. This can be partially referred to a finite spectral resolution of a finite size system, since this structure is not fully recovered for other lattice sizes.

The advantage of RDMFT, compared to other DMFT extensions, is the real-space resolution. Owing to this feature, spectral particularities of different phases can be visualized. In Fig. 8.5 color coded LDOS  $\rho_i(\omega)$  obtained for every site of a  $24 \times 24$  lattice are presented. Extended single particle excitations are indicated by finite spectral weights on every site while localized states appear as unconnected points or areas in the diagram. Thus, at  $U = 1.0$  and  $s_D = 0.01E_R$  in Fig. 8.5 (a) the system is metallic, since the spectral weight at the Fermi level  $\omega = 0$  is finite at every lattice site. For  $U = 3.1$  and  $s_D = 0.01E_R$  the systems is in the Mott insulating phase, see Fig. 8.5 (b). This phase is indicated by a spectral gap proportional to the interaction strength  $U$  and the formation of Hubbard bands. At the high speckle field strength  $s_D = 0.4E_R$  the system is expected to be Anderson-Mott insulating for all interaction strengths. Indeed, all states are localized leading to randomly distributed point-like local spectral weights, as exemplified for  $U = 1.0$  in Fig. 8.5 (c).

In conclusion, the main results obtained for higher dimensional speckle-disordered Bethe systems have been proven to hold also in two-dimensional square lattices. In particular, the phases such as metal, Mott insulator and Anderson-Mott insulator are also obtained within RDMFT even though for slightly different parameter regimes.

Despite the observations which support or refine the statDMFT results, RDMFT calculations reveal an additional common feature of two-dimensional correlated disordered systems known as *zero-bias anomaly*.

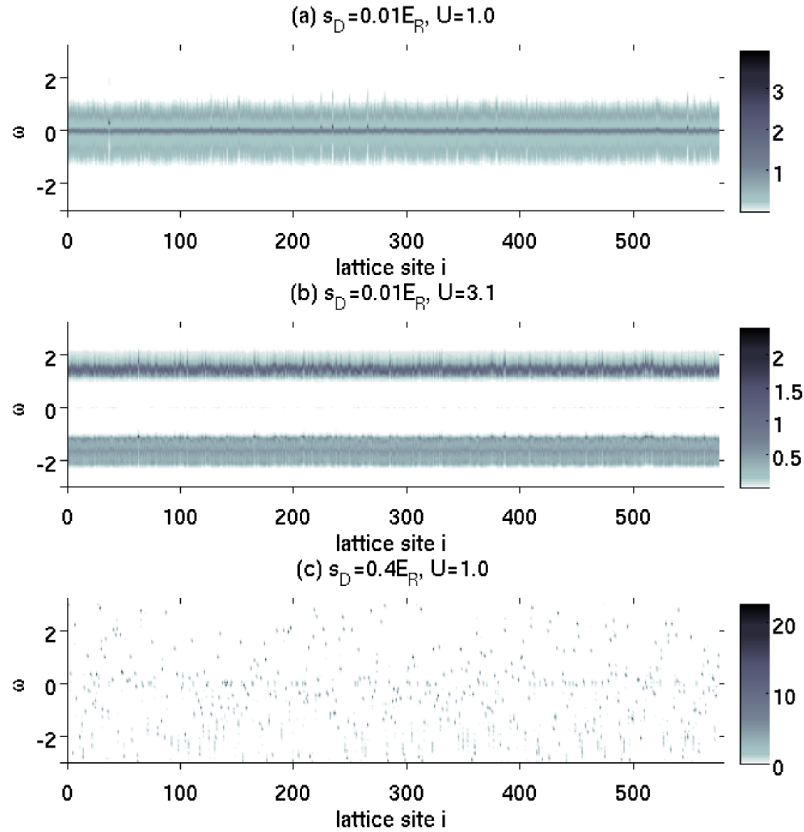


**Figure 8.5:** Color coded LDOS  $\rho_i(\omega)$  as a function of frequency  $\omega$  and lattice site index  $i$  for three different parameter sets. The three regimes correspond to (a) metallic, (b) Mott-insulating and (c) Anderson-Mott insulating phases, respectively.

## 8.4 Zero-bias anomaly

“Pseudogaps”, or zero-bias anomalies (ZBAs), were observed in the early investigations on the metal-insulator transition and studies of the disorder effects. In weakly disordered metals, Altshuler and Aronov demonstrated a suppression of the spectral density at the chemical potential by means of perturbation theory [327]. In the atomic limit of completely localized particles, Efros and Shklovskii have shown the emergence of the Coulomb gap at the chemical potential resulting from unscreened Coulomb potential and disorder [328]. Both effects are based on non-local interactions and the corresponding energy scale is given by interaction strength  $U$  or magnetic exchange  $t^2/U$ , respectively.

This predictions, however, are in contradiction to the ZBA observed recently via exact diagonalization and quantum Monte Carlo calculations for strongly interacting and strongly disordered systems described by the Anderson-Hubbard Hamiltonian [329, 330]. The appearing soft gap was found to be insensitive upon variation of filling, disorder and interaction strengths. The resistivity of the ZBA against doping concentration changes has been observed also experimentally [331]. Particularly, the independence of  $U$  and  $D$  in the strongly interacting and strongly disordered regime indicates that the tunneling  $t$  constitutes the relevant energy scale. Suggestions have been provided to explain the formation of anomalies with an energy scale  $\sim t$  based on non-local selfenergy terms [329, 332, 333], however a conclusive general theory has not been presented yet.

Although DMFT is a theoretical approach that retains only the local self-energy, a pseudogap at the Fermi level was observed in our calculations. In particular, the suppression of

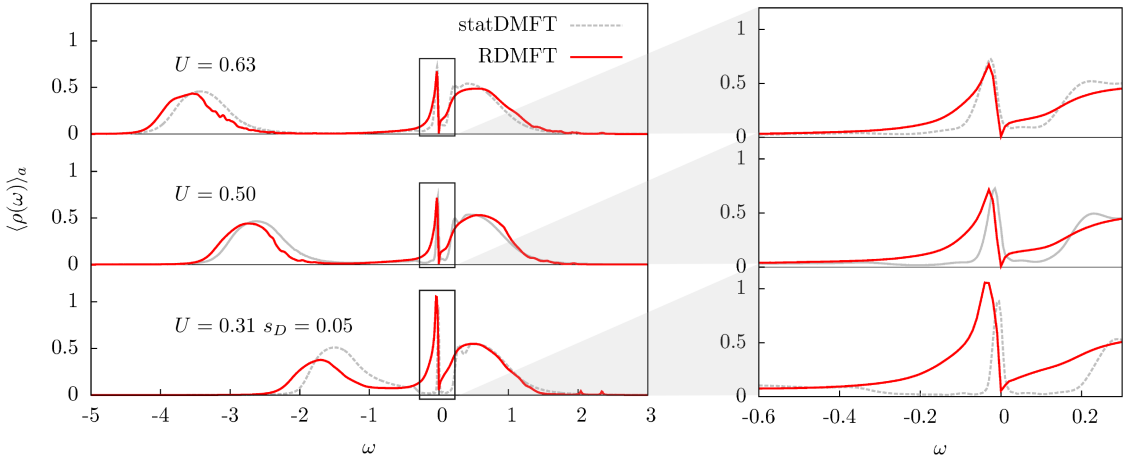


**Figure 8.6:** Density of states obtained via RDMFT and statDMFT. (left) Within the Mott gap, which is expected for given most probable interaction strengths  $U = 0.31, 0.50$  and  $0.63$  at  $s_D = 0$ , finite disorder  $s_D = 0.05$  leads to a formation of the spectral peak at the Fermi level. However, a more quantitative comparison (right) reveals a pseudogap in RDMFT results appearing at  $\omega = 0$ . The speckle field and interaction energies are given in units of the recoil energy.

the DOS at the Fermi level was found only within RDMFT, as shown in the comparison between RDMFT and statDMFT results in Fig. 8.6. For the sake of comparability, within this section all energy scales will be given in units of the recoil energy.  $U$  denotes the most likely interaction strength of the corresponding marginal distribution  $\mathcal{P}_U(U_i) = \int d\varepsilon_i \mathcal{P}_{\varepsilon,U}(\varepsilon_i, U_i)$ . For finite speckle field strength and interaction strength exceeding the critical value for metal-Mott insulator transition the spectral redistribution of the states induced by disorder leads to the formation of a peak in the DOS at the Fermi level in both methods. However, contrary to statDMFT results presented here and DMFT predictions given in [59], in RDMFT the spectral weight is drastically reduced at  $\omega = 0$ , see Fig. 8.6 (right). This indicates that the ZBA is connected to the particular lattice structure as well as to the reduced dimensionality. The unsymmetrical v-shape of the pseudogap observed here is due to the spectral properties of the speckle disorder.

We begin the investigations of the parameter dependence of the observed anomaly analyzing the influence of the speckle field strength. In the homogeneous half-filled case ( $s_D = 0$ ) the system is Mott insulating and shows a spectral gap in the DOS for  $U = 0.5E_R$ , see Fig. 8.7 (a). However, on increasing  $s_D$ , for  $s_D < U$ , the gap becomes partially filled. Due to the spectral redistribution induced by disorder it is expected that the observed gradual filling would continue with increasing disorder strength and finally lead to a complete disappearance of the ZBA at large enough disorder  $s_D > U$ . This continuity, however, is not obtained within our calculations. In contrast, the pseudogap becomes independent of disorder for sufficiently strong speckle fields. Figs. 8.7 (b) and (c) demonstrate this property for  $U = 0.63E_R, 0.44E_R$  and various disorder strengths. These observations agree qualitatively with QMC results for box-disordered 2D lattices [329]. However, a more quantitative comparison reveals different energy scales at which speckle disorder ceases affecting the ZBA. For  $U = 0.63E_R$  and  $0.44E_R$  the pseudogap remains stable against variation of the disorder strength already at values  $s_D < U$ , which is in contrast to observed critical strength  $\Delta = U$  in [329]. On the other hand, sufficiently large disorder is observed to destroy the ZBA, i.e. for  $U = 0.63E_R$  the pseudogap is smeared out at



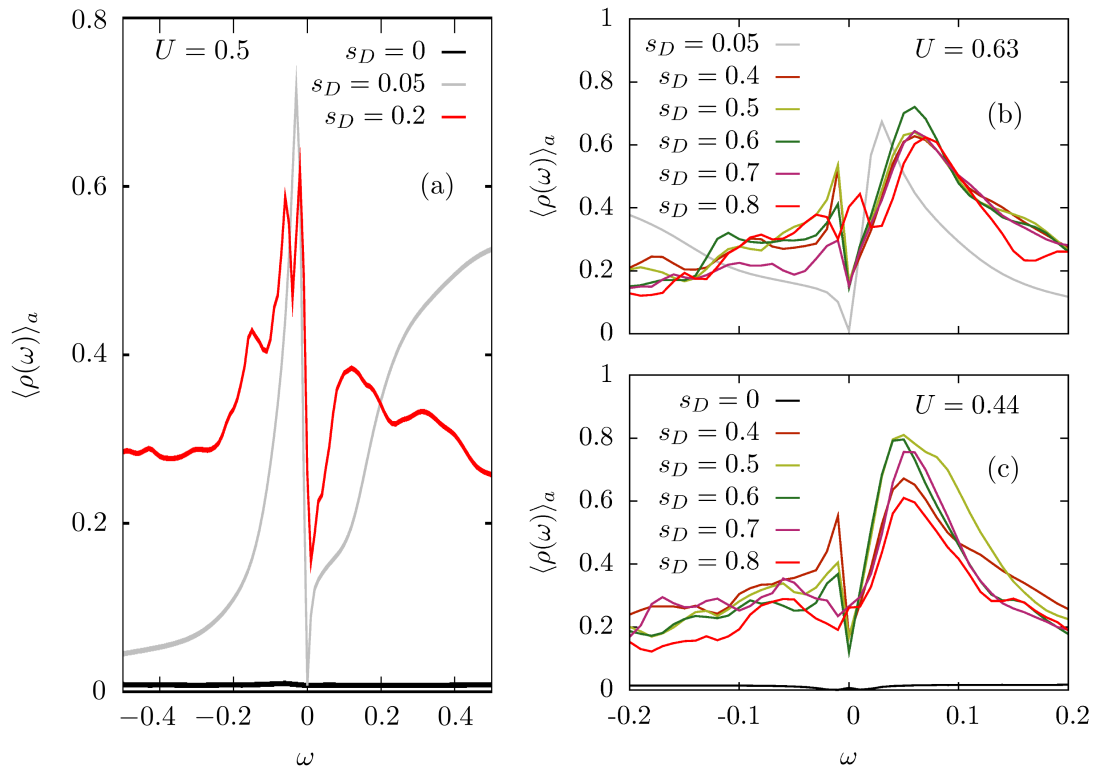


**Figure 8.7:** Evolution of the pseudogap as a function of speckle field strength. (a) The Mott gap obtained at  $s_D = 0$  and  $U = 0.5$  is gradually filled in with increasing  $s_D$ . The pseudogap appearing at the Fermi level shifts towards higher spectral values with increasing disorder strength. (b) The ZBA appearing at the small disorder strength  $s_D = 0.05$  for  $U = 0.63$  saturates for  $s_D = 0.4 - 0.7$ . At  $s_D = 0.8$  the pseudogap is filled. (c) For  $U = 0.44$  similar stabilization of the pseudogap is observed for  $s_D = 0.4 - 0.6$ . Speckle field strengths  $s_D \geq 0.7$  lead to a disappearance of the ZBA. The speckle field and interaction energies are given in units of the recoil energy.

$s_D = 0.8E_R$  and for  $U = 0.44E_R$  at  $s_D = 0.7E_R$ , whereas in box-disordered systems even for  $\Delta/U = 2$  no influence was detected. This differences can be partially traced back to the speckle field PDF, which allows high disorder values with a non-vanishing probability for small speckle field strengths. In particular, for strong  $s_D$  the likelihood of dramatically big offsets becomes significant and may be responsible for the observed disappearance of the pseudogap.

The evolution of the density of states for various interaction strengths and a fixed speckle field is demonstrated in Fig. 8.8. The form and the position of the pseudogap is found to remain unaffected by  $U$ . In particular no effects are found neither in the limit of weak speckle field strengths  $s_D \ll U$  (Fig. 8.8 (a)) nor for large disorder  $s_D \approx U$  (Fig. 8.8 (c)). This is surprising, since if the effect of disorder is only to compete with interaction by redistributing the spectral weight, a change of DOS would be expected when  $U$  is varied at a fixed disorder speckle field strength. In contrast, the disorder is observed to stabilize the ZBA already on the scale where  $s_D < U$ . A stable pseudogap irrespective of the interaction strength  $U \geq \Delta$  was reported for a box-disordered lattice away from half filling [329]. The differences in the interaction to disorder fraction, for which the reported features are observed, originate in the distinct disorder types. Our results confirm that in speckle

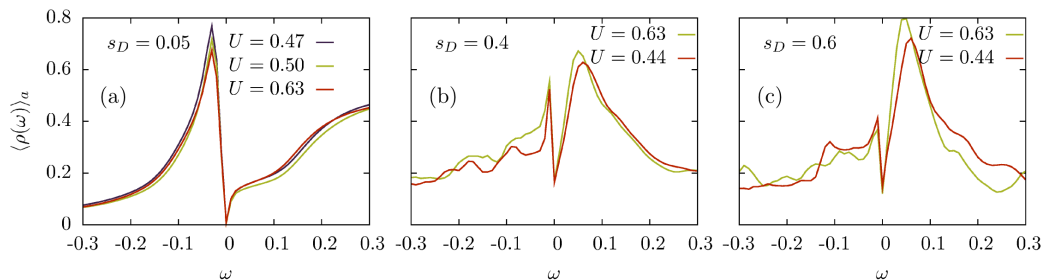


**Figure 8.8:** Influence of the interaction strength on the pseudogap. The variation of the interaction strength leaves the ZBA unaffected (a) for  $s_D \ll U$ , (b) in the regime of intermediate disorder strengths and (c) for  $s_D \approx U$ .

fields the dominant energy scale can not be deduced from the ratio  $s_D/U$  as in the case of bounded disorder types.

Although the spectral anomaly was observed within RDMFT calculations, it is important to keep in mind that only local correlations are treated exactly within this method. This numerical property influences the accuracy of the width and depth of the observed pseudogap. A more quantitative discussion about ZBA and particular influence of unbounded disorder type requires a further characterization of effects induced by tunneling scaling and filling variation. Of a particular interest is also the investigation of the proper form of the selfenergy entering the simulations. As stated in [334], DMFT with purely local selfenergy is not expected to generate a pseudogap, which stands in contrast to our results. However, Song *et al.* used the analytic Hubbard I approximation for the selfenergy, which is the simplest improvement over the Hartree-Fock approximation. In contrast to that, in our simulations a proper impurity solver MPT is applied, which reproduces higher momenta of the spectral function (see Sec. 6.5.2). This suggests that the accuracy of the selfenergy rather than its locality is responsible for the observation of ZBA. Further insights into this peculiarities are essential to clarify the yet unexplained origin of the observed gap anomalies [329, 330, 332].

## 9. Summary and outlook

This dissertation aims at giving a theoretical description of various applications of ultracold gases. A particular focus is cast upon the dynamical evolution of bosonic condensates in non-equilibrium by means of the time-dependent Gutzwiller method. Ground state properties of strongly interacting fermionic atoms in box and speckle disordered lattices are investigated via real-space dynamical mean-field theory.

The first part of this thesis is focused on bosons and heteronuclear bosonic mixtures. The main motivation for the first project was the recent experiment by J. Catani *et al.* [20] where, for the first time, a superfluid mixture of two bosonic species,  $^{87}\text{Rb}$  and  $^{41}\text{K}$ , in a three-dimensional optical lattice was successfully produced. Their experimental findings raised new questions on the reduction of phase coherence in rubidium which was induced by the presence of potassium. In particular, they observed oscillations in the visibility depending of the lattice ramping profile and time, which were not understood to date. We address these questions in our investigations of interacting Rb-K mixture, simulating equilibrium properties and dynamics of this system by means of the Gutzwiller mean-field method. For the sake of numerical efficiency, a two-dimensional system was studied in the regime of experimentally relevant parameters. We explicitly take into account that a heteronuclear mixture breaks the rotational symmetry of the trap, because the centers of mass of the two species are shifted with respect to each other due to the gravitational sag.

We reproduce and explain the experimentally observed oscillations in the visibility by relating them to the lack of of adiabaticity [29]. In particular, we demonstrate that adiabaticity with respect to the many-body states in the lowest band is essential and not guaranteed in recent experiments, since the ramp-up of the optical lattice occurs on a time scale comparable to the tunneling time of the bosons. This violation of adiabaticity leads to undesirable effects in intermediate and deep lattice regimes. The ground state of the system at large lattice depths typically contains a Mott insulating plateau with integer filling in the center. However, the particle density obtained after the ramp is non-integer, unlike in the MI phase, and at the same time has vanishing superfluid order, in contrast to the SF phase, for which reason we refer to it as a *frozen* superfluid. The corresponding visibility is lower than in an equilibrium situation. Moreover, by systematically tracing out the visibility as a function of the ramp-up time, we show that in deep lattices fast ramps induce collective excitations in the Rb-cloud, in particular the breathing mode of the system. The criterion for adiabaticity which we deduce from this is the saturation of

the visibility as a function of ramp-up time. In this regime the superfluid fraction reaches its equilibrium value and the ramp-up is sufficiently slow, so that no collective modes are excited. The maximum of the visibility, which is sometimes used as an experimental criterion, turns out not to be a good indication of adiabaticity.

A further non-equilibrium system studied in this thesis is the spreading of a strongly interacting bosonic cloud. A non-adiabatic switch-off of the initial confinement initiates particle expansion. Analogous investigations on fermionic atoms already revealed new transport properties influenced by interactions. In the non-interacting regime free fermions were observed to expand ballistically [168, 170], in accordance with theoretical results on continuous quantum walks [169], while interactions surprisingly did not lead to the expected simple diffusive behavior. Instead, a coexistence of a diffusive core and ballistic outer region of the cloud were found. The features of an expanding bosonic cloud were addressed only for the limiting cases of hard-core bosons or for anisotropic expansion up to now [33, 34, 134]. One of the goals of this thesis was to present a detailed study of different correlation regimes for experimentally relevant isotropic systems.

In the non-interacting case the cloud is found to change its shape for long expansion times. While for shallow confinement the condensate remains rotational symmetric, reflecting the initial symmetry of the trapping potential, more strongly trapped systems develop quadratic density profiles, corresponding to the symmetry of the reciprocal lattice. The non-interacting cloud radius grows linearly in time, as expected for a quantum random walk. In the interacting case a qualitatively different behavior is observed. A system, initially prepared to consist of a Mott insulating core surrounded by a tiny superfluid ring, always obtains a four-fold rotational symmetry ( $C_4$  symmetry) during the expansion. Here, the formation of a “spiked” structure becomes more evident with increasing interaction strength. The origin of pronounced population along the diagonals is explained based on analytical arguments. Even more remarkable is the obtained emergence of the coherence. During the melting of the Mott insulator, the condensate fraction is shown to approach unity at an exponential rate as a function of time, while simultaneously the occupation of finite momenta increases. This behavior stands in contrast to homogeneous equilibrium condensates characterized by exclusive macroscopic population of the  $\mathbf{k} = (0,0)$  state. Additional investigation of effects of the superfluid outer ring on the evolution of the inner Mott insulating core leads to unexpected new insights into non-equilibrium dynamics. Density and momentum distributions are found to depend on the initial number of particles in the Mott insulator rather than on the particular interaction or tunneling strength in certain parameter regimes. This is remarkable, since the independence of the insulating core expansion from the surrounding superfluid dynamics indicates that the obtained mean-field results are characteristic for the real many-body dynamics.

The second part of this thesis focuses on the investigation of correlated fermions in disordered optical lattices. Two types of disorder, namely continuous unbounded speckle disorder and continuous bounded box disorder, are considered in particular. The effects of both disorder types are analyzed respectively in one and two dimensional lattices.

The method used to treat disordered correlated fermionic problems in this thesis is the real-space dynamical mean-field theory (RDMFT). This technique is deduced from dynamical mean-field theory (DMFT). Within DMFT, the self-energy is approximated to be purely local, which is only exact in infinite dimensions but is known to lead to a qualitatively accurate description of a metal-insulator transition in 3D. In combination with the geometric disorder average of the local density of states, this method allows to detect

Anderson localization [44, 49, 54, 326, 335]. On the other hand, its real-space extension treats the single-particle problem - including disorder - exactly in any spatial dimension, while the local self-energy becomes site-dependent [208, 284, 314]. For this reason RDMFT is expected to be superior to single-site DMFT in low dimensions, a hypothesis which is investigated in this thesis.

One of the most challenging tasks in theoretical physics is the non-perturbative investigation of systems with disorder and interactions present simultaneously. While in higher dimensional systems this question has been addressed and the presence of a disordered metallic phase confirmed by different numerical methods [44, 50, 51, 55–60, 224, 336, 337] and experimental observations [52, 227], the situation in one dimensional lattices remains controversial. In 1D bosonic systems a Mott insulator, a Bose glass and a superfluid phase were found [9, 338–341], of which the latter is analogous to the metallic phase in fermionic systems. However, for repulsively interacting fermions in 1D perturbative RG calculations predict a random antiferromagnet, where the fermions localize individually around randomly distributed sites [55]. Nevertheless, perturbative treatments of disorder can not be expected to capture the physics in the full range of couplings. A non-perturbative investigation of a spin- $\frac{1}{2}$  one dimensional fermionic system with box disorder via RDMFT is presented in this thesis [228].

Since RDMFT neglects all non-local correlations, to assure the correctness we quantitatively compare our results with DMRG, which is a numerically exact method and tackles strong disorder and strong interactions simultaneously in 1D. We have studied the occurrence of delocalization, Anderson- and Mott-insulating phases for interacting disordered spinful fermions on a 1D lattice at commensurate filling. The phases are characterized by means of the local density of states, the scaling of the inverse participation ratio and the charge gap. Both numerical techniques, DMRG and RDMFT, agree in their predictions for parameter regimes well within the Anderson and Mott phases. However, RDMFT was found to be more affected by finite-size effects than DMRG, which is reflected in a larger delocalization trend for a fixed lattice size. As our main result, we present the first non-perturbative calculations indicating a delocalized phase of spinful fermions in 1D due to the interplay of disorder and interaction of intermediate strength, similar to the bosonic case. This trend, observed via DMRG by Georg Harder as well as via RDMFT within this thesis, persisted in finite-size scaling within RDMFT and is observed for the first time within this work.

Investigations based on box disordered systems accounting only for on-site energy offsets are important and serve to obtain a first impression of phenomena. However, box disorder has not yet been realized in experiments. A more relevant case constitutes e.g. speckle disorder, which has been realized recently in optical lattices using optical speckle field [233]. Additionally, the precision of the theoretical description can be improved by implementing joint probability densities for model parameters, since random on-site energies and energy differences between neighboring sites lead to stochastically distributed but correlated on-site interaction and tunneling strengths. Thus, a further aim of this thesis was the description of a speckle disordered fermionic system with diagonal and off-diagonal disorder, i.e. random on-site and hopping energies.

The model was investigated using two related approaches: statistical DMFT and RDMFT. Both methods constitute extensions to DMFT and take into account local correlations only. However, by construction they differ in the conceptual implementation of disorder. While the first technique incorporates probability distribution functions within selfconsistency equations, the second technique solves a problem for a fixed disorder realization. Sec-

only, statistical DMFT is typically operating on an infinite Bethe lattice while RDMFT takes into account the density of states corresponding to a given finite lattice structure. Although a semi-elliptic density of states is a purely mathematical construct it is widely used in theoretical investigations. The physics obtained in three dimensional lattices is qualitatively similar to that on a Bethe lattice, however, in lower dimensions qualitative differences may arise. In order to account for peculiarities of a two dimensional lattice structure, the statistical DMFT results obtained by D. Semmler are compared to RDMFT findings presented in this thesis.

The main outcome of this comparison is the paramagnetic ground state phase diagram. Here, the unbounded nature of speckle disorder is found to lead to qualitatively distinct effects. While for a purely diagonal box disordered system typical medium theory predicts that the Mott and Anderson insulators are connected [44, 58, 326, 335] this is not the case for speckle disordered lattices where a continuous metallic phase separates both insulating regimes. The comparison of results obtained for a Bethe lattice (statistical DMFT) and for a two dimensional square lattice (RDMFT) shows qualitatively similar behavior: for weak disorder a metal-insulator transition is induced by increasing the interaction strength, while stronger disorder is found to stabilize the metallic phase. Quantitative differences are, however, obtained for weak correlations, where the kinetic energy, which is related to the lattice structure, sets the energy scale [51]. Interestingly, a pseudo-gap at the Fermi level in the local density of states on the square lattice is found within RDMFT. This pseudo-gap arises for intermediate and strong interactions in the presence of disorder and remains stable under variation of the system size.

In total, the results of this thesis demonstrate the multitude of questions which can be addressed with ultracold gases. In particular, various non-equilibrium and static disorder phenomena for bosonic and fermionic particles were investigated in this manuscript. However, the control over matter waves achieved within the last years opens up new possibilities for investigations of a combination of both effects. For fermions, a sudden expansion of interacting two-component mixture is found to lead to quantum distillation in homogeneous 1D lattices [342]. In particular, during the expansion doublons are observed to separate dynamically from the rest of the system and to group together into a metastable state. Since 1D lattices are particularly sensitive to interactions, similar investigations in higher dimensions might reveal new features. Moreover, considering the subtle competition between disorder and interactions in certain parameter regimes [44, 50, 51, 58, 228, 326], the expansion dynamics of fermionic doublons in disordered lattices might give new insights into the non-equilibrium physics of disordered fermions which has not been studied yet. Additionally, intriguing effects of condensate formation due to melting of a bosonic Mott insulator, obtained within the framework of this thesis, are promising to yield further fascinating features in a disordered lattice. However, with the methods currently available long-time non-equilibrium fermionic many-body dynamics is not accessible in 2D and 3D. Similarly, the current numerics lacks appropriate schemes to treat dynamic bosonic disordered systems. Thus, recent developments in the field of interacting and disordered ultracold gases clearly require computational progress. For the moment, time dependent Gutzwiller remains the most efficient method for studies of non-equilibrium bosonic interacting lattice systems in higher dimensions, as well as real-space DMFT for research on fermionic static strongly correlated disordered systems, as presented in this thesis.

## 10. Zusammenfassung

Bei genügend tiefen Temperaturen wird der Grundzustand eines bosonischen Systems makroskopisch besetzt. Dieses Phänomen wird als Bose-Einstein-Kondensation (BEC) bezeichnet, zu Ehren der Vorarbeiten von S. Bose im Jahr 1920 [1] und der tatsächlichen Vorhersage von A. Einstein im Jahre 1925 [2]. Doch nach der Vorhersage dauerte es noch lange bis die experimentelle Realisierung kondensierter bosonischer Materie erreicht worden ist. Das Hauptproblem war dabei die extrem niedrige kritische Temperatur, die für die Bildung von Kondensaten erforderlich ist. Den ersten Meilenstein bezüglich der Kontrolle über die Teilchen setzten S. Chu, C. Cohen-Tannoudji und W. D. Phillips. Ihre Erfindung der atomaren Fallen und der Laserkühlung, die eine Temperaturreduktion auf  $\sim 10^{-5}$  K ermöglichte, wurde mit einem Nobelpreis 1997 gefeiert. In 1995 erreichten die Gruppen von E. A. Cornell, C. E. Wieman [3] und W. Ketterle [4] einen neuen Temperaturrekord mit  $\sim 10^{-8}$  K durch zusätzliche Verdampfungskühlung. Für diese Errungenschaft wurde Ihnen 2001 ein Nobelpreis verliehen.

Fermionische Quantengase bilden das Gegenstück zum BEC und werden durch die Fermi-Dirac-Statistik charakterisiert, die E. Fermi und P. Dirac unabhängig von einander entwickelten [5, 6]. Wegen dem verschwindend geringen Streuquerschnitt können niedrige Temperaturen bei Fermionen allerdings nur durch sympathetische Kühlung unter dem Einsatz anderer Atomsorten erreicht werden. Diese Vorgehensweise ermöglichte die erste Realisierung eines ultrakalten fermionischen Gases 1999 [7].

Seit dieser Zeit hat die Forschung an entarteten Quantengasen ein neues Niveau erreicht. Die Herstellung von Kondensaten in verschiedenen Dimensionalitäten, das Einfangen der Teilchen in optischen Gittern verschiedener Symmetrien und schließlich die präzise Einstellung der Tunnelwahrscheinlichkeit und der Wechselwirkungsstärke ermöglichen perfekte Kontrolle über die Systemparameter. Diese Fortschritte führten dazu, dass ultrakalte Atome sich zu einem leistungsstarken Werkzeug für die Untersuchungen stark korrelierter Vielteilchensysteme entwickelt haben, die bis jetzt nur dem Bereich der kondensierten Materie vorbehalten waren.

Da die ultrakalten Systeme präzise einstellbare Quantensimulatoren darstellen, eröffneten sie den Zugang zur Physik am absoluten Nullpunkt, die durch das Bose- und das Fermi-Hubbard Modell beschrieben wird [8, 9]. Während thermische Fluktuationen bei  $T = 0$  einfrieren, bleiben Quantenfluktuationen bestehen und induzieren Phasenübergänge,

die makroskopische Veränderungen im Vielteilchen-Grundzustand mit sich bringen. Der Phasenübergang von einem schwach zu einem stark korrelierten Regime wurde sowohl für Bosonen (superfluid-Mott-Isolator Übergang) [9, 10] and auch für Fermionen (Metall-Mott-Isolator Übergang) [8, 11] theoretisch vorhergesagt und später in ultrakalten Gasen von M. Greiner *et al.* [12], R. Jördens *et al.* [13] und U. Schneider *et al.* [14] beobachtet.

Eine weitere theoretische Vorhersage betrifft langreichweitig geordnete Phasen wie z.B. Quantenmagnetismus und Supersolidität [15–18] in mehratomigen Mischungen. Diese experimentell zu zeigen ist heute eines der wichtigsten Ziele im Bereich der ultrakalten Gase. Ihre Realisierung erfordert jedoch weitaus niedrigere Temperaturen und damit die Kontrolle über weitere Prozesse die zur Erwärmung des Systems führen. Insbesondere wurde bis jetzt der Effekt der Erhöhung des Gitterpotentials unterschätzt, obwohl das Einstellen der Gittertiefe zum Anstieg der Temperatur und der Entropie führen kann. Insbesondere wurden, abhängig von der Gittereinschaltzeit, Oszillationen der Visibilität beobachtet, die nicht erklärt werden konnten [20]. Die Fragen nach den Ursachen der Oszillationen und wie diese vermieden werden können, werden in der vorliegenden Doktorarbeit untersucht. Ihre Klärung trägt dazu bei die Präzision und Zuverlässigkeit von zukünftigen Experimenten zu verbessern.

Die oben genannten Aspekte werden im Rahmen unserer Untersuchungen an wechselwirkenden bosonischen Rb-K Mischungen aufgegriffen. Die Gleichgewichtseigenschaften sowie Dynamik werden mittels Gutzwiller Methode simuliert. Zwecks höherer numerischer Effizienz werden zwei-dimensionale Gitter in experimentell relevanten Parameterregimes untersucht. Dabei wird explizit berücksichtigt, dass mehratomige Mischungen die Rotationssymmetrie der Falle brechen, weil die Schwerpunkte beider Atomarten aufgrund der Gravitationskraft gegeneinander verschoben sind.

Wir reproduzieren und erklären die experimentell beobachteten Oszillationen der Visibilität basierend auf der fehlenden Adiabaticität [29]. Im Einzelnen demonstrieren wir, dass Adiabaticität in Bezug auf die Vielteilchenzustände im niedrigsten Band essentiell ist, jedoch in aktuellen Experimenten nicht gewährleistet wird. Der Grund dafür ist, dass die Einstellzeit einer gewünschten Gittertiefe auf der Zeitskala der bosonischen Tunnelprozesse stattfindet. Das Verletzen der Adiabaticität führt zu unerwünschten Effekten in mitteltiefen bis tiefen Gittern. Der Grundzustand des Systems für große Gittertiefen besteht typischerweise aus einem Mott-isolierenden Plateau mit ganzzahliger Teilchenzahl. Die errechnete Teilchendichte, die das dynamische Einstellen einer entsprechenden Gittertiefe zur Folge hat, ist im Gegensatz zur Mott-isolierenden Phase nicht ganzzahlig und weist gleichzeitig verschwindende superfluide Ordnung auf, im Gegensatz zur superfluiden Phase. Aus diesem Grund bezeichnen wir diesen dynamisch erzeugten Zustand als "gefrorenes" Superfluid. Die resultierende Visibilität ist niedriger als im Gleichgewichtszustand bei der selben Gittertiefe. Darüber hinaus zeigen wir durch eine systematische Untersuchung der Visibilität als Funktion der Einschaltzeit, dass in tiefen Gittern schnelles Einschalten zu kollektiven Anregungen der Rubidiumwolke führt. Als Kriterium für die Adiabaticität, die wir daraus ableiten wollen, gilt die Sättigung der Visibilität als Funktion der Einstellzeit. In diesem Regime erreicht der superfluide Anteil seinen Gleichgewichtswert bei gleichzeitig langsamer Gittertiefeinstellung, sodass keine kollektiven Moden angeregt werden. Das Maximum der Visibilität, was in Experimenten des Öfftens als Indiz für Adiabaticität verwendet wird, stellt sich als ein unzureichendes Kriterium heraus.

Obwohl ein Gleichgewichtszustand das Ziel der meisten Experimente ist, kann Nichtgleichgewicht gezielt hervorgerufen werden. Die damit stimulierte Vielteilchendynamik offenbart nicht nur viele spannende Phänomene sondern kann auch als neue experimentelle



Messmethode etabliert werden [30, 31]. In jüngsten Arbeiten [32] wurde gezeigt, dass starke atomare Wechselwirkungen dramatischen Einfluss auf die Thermodynamik des Systems haben, selbst wenn die Änderungen am System adiabatisch durchgeführt werden. Weitere experimentelle Untersuchungen expandierender fermionischer Atome in isotropen optischen Gittern haben ergeben, dass freie Teilchen ballistisch expandieren und wechselwirkende dagegen ein kompliziertes diffusives Verhalten aufweisen. Beim letzteren wurde eine Koexistenz vom diffusiven Kern und ballistischer Umgebung demonstriert [168–170].

Ein weiteres Nichtgleichgewichtssystem, das in dieser Dissertation analysiert wird, ist das Expandieren einer stark wechselwirkenden bosonischen Wolke in experimentell relevanten isotropen Systemen. Ein nichtadiabatischer Abschaltvorgang der anfänglichen Teilchenfalle initiiert eine Ausbreitung der Atomwolke und führt zur Veränderung physikalischer Eigenschaften des Systems wie der Geometrie und der Kohärenz.

Im nichtwechselwirkenden Fall haben die Simulationen ergeben, dass die Wolke ihre Form bei langen Expansionszeiten verändern kann. Während nach dem Abstellen eines flachen Fallenpotentials die sich ausbreitenden Kondensate die ursprüngliche Rotationssymmetrie der Falle beibehalten, führt starke örtliche Anfangsbegrenzung zu quadratischen Dichteprofilen, entsprechend der Symmetrie des reziproken Gitters. Der Radius der nichtwechselwirkenden Wolke wächst linear in der Zeit, wie für einen quantenmechanischen Random-Walk erwartet [168, 170]. Für endliche Wechselwirkungen wird ein qualitativ anderes Verhalten beobachtet. Ein System, bestehend aus einem Mott-isolierenden Kern umgeben von einem superfluiden Ring, entwickelt während der Expansion immer eine vierfache Rotationssymmetrie ( $C_4$  Symmetrie) mit ausgeprägter Besetzung entlang der Diagonalen. Die Ausbildung dieser Spike-Struktur wird deutlicher mit zunehmender Wechselwirkungsstärke und wird durch analytische Betrachtungen in dieser Arbeit erklärt. Umso bemerkenswerter ist die Entstehung der Kohärenz. Während des Schmelzens des Mott Isolators erreicht der ursprünglich verschwindende Kondensatanteil als Funktion der Zeit exponentiell den Maximalwert bei gleichzeitiger Besetzung endlicher Impulszustände. Dieses Verhalten steht im Gegensatz zu homogenen Kondensaten im Gleichgewicht, die durch exklusive makroskopische Bevölkerung des Zustands  $\mathbf{k} = (0, 0)$  charakterisiert werden. Zusätzliche Analyse des Einflusses des superfluiden Rings auf den inneren Mott-isolierenden Kern ergab neue Einsichten in die Nichtgleichgewichtsdynamik. Es wurde festgestellt, dass in bestimmten Parameterbereichen die resultierenden Dichte- und Impulsverteilungen vielmehr von der ursprünglichen Anzahl der Mott-isolierenden Teilchen abhängen als von der Wechselwirkungs- oder Tunnelstärke. Die Unabhängigkeit der Ausdehnung des isolierenden Inneren von der superfluiden Umgebung suggeriert, dass die Phänomene, die mittels der Molekularfeldnäherungsmethode Gutzwiller beobachtet wurden, charakteristisch für reale Vielteilchen Physik sind.

Der hohe Grad an Kontrolle und Einstellbarkeit der optischen Gitterpotentiale erlaubt eine weitere Anwendung von ultrakalten Systemen: Die Erforschung der Unordnungsphysik. Verunreinigungsatome, die von Natur aus oder künstlich bedingt in Festkörpern auftreten, zeigten starken Einfluss auf die Transporteigenschaften von Elektronen. Phänomene wie z. B. die unerwartete Erhöhung der Leitfähigkeit, bekannt als Kondo Effekt [36, 38], oder die Lokalisierung der elektronischen Eigenzustände ab einer kritischen Konzentration der Verunreinigungen [39] – die Anderson Lokalisierung – werden seit mehreren Jahrzehnten studiert. Die experimentelle Analyse von Unordnung in Festkörpern ist jedoch schwer, weil die Justierung der Systemparameter eingeschränkt ist, anders als in ultrakalten Gasen. Die zunehmende Regulierbarkeit von optischen Gittern hat die experimentelle Realisierung von Unordnungspotentialen mit unterschiedlicher Stärke und auch mit verschiedenen Typen

von Unordnung ermöglicht. In bosonischen Systemen mit Speckle-Unordnung wurde die Anderson Lokalisierung bereits nachgewiesen [40–43]. Fermionische ungeordnete Systeme sind dagegen bis jetzt nur wenig experimentell erforscht worden [52]. Doch die jüngsten Fortschritte in der Erweiterung der nichtperturbativen Berechnungsmethoden auf ungeordnete Systeme, wie z. B. dynamische Molekularfeldtheorie (DMFT) [53, 54], ermöglichen quantitative theoretische Vorhersagen für angehende Experimente.

Deshalb befasst sich der zweite Teil dieser Dissertation mit der Charakterisierung der Unordnungseffekte in ein- und zweidimensionalen korrelierten fermionischen Systemen mittels ortsaufgelöster Molekularfeldtheorie (RDMFT) [208, 281, 314]. Zwei Arten der Unordnungsfelder werden einzeln untersucht: Das kontinuierliche unbeschränkte Speckle-Feld und die kontinuierliche begrenzte Box-Unordnung. Von besonderem Interesse ist hierbei die gleichzeitige Präsenz von Unordnung und Korrelationen. Obwohl diese beide Wechselwirkungen einen Metall-Isolator Übergang induzieren ist ihre Wirkung konträr: die abstoßende Elektron-Elektron Wechselwirkung begünstigt eine gleichmäßige Verteilung der Partikel, die Unordnung dagegen lokalisiert elektronische Wellenfunktionen auf wenigen zufällig verteilten Gitterplätzen. Den neuesten Studien zufolge führt das Zusammenspiel der beiden Wechselwirkungen zur Ausbildung einer metallischen Phase in höherdimensionalen [44, 58] und sogar in zweidimensionalen [44, 55, 58, 60] Gittern, entgegen der langjährigen Annahme, dass in 2D keine Phasenübergänge existieren [61–63].

Die Situation in eindimensionalen Systemen bleibt jedoch kontrovers. Anders als in perturbativen Rechnungen mittels der Renormierungsgruppe [55] zeigen nichtperturbative Simulationen durchgeführt im Rahmen dieser Doktorarbeit mittels RDMFT starke Indizien für Delokalisierung [228]. Die Ergebnisse unserer Untersuchungen für eindimensionale wechselwirkende fermionische Spin- $\frac{1}{2}$ -Systeme mit Box-Unordnung sind in dieser Dissertation präsentiert. Da RDMFT nichtlokale Fluktuationen vernachlässigt, wird die Richtigkeit der Ergebnisse durch einen quantitativen Vergleich mit numerisch exakten Resultaten der Dichtematrix Renormalisierungsgruppe (DMRG) gewährleistet. Im Rahmen unserer Arbeit wurden delokalisierte, Anderson- und Mott-lokalisierte Phasen für Halbfüllung gefunden. Die Charakterisierung der Phasen basierte auf der Analyse lokaler Zustandsdichten, der Skalierung der invertierten Besetzungszahl und der spektralen Lücke. Beide numerische Methoden, RDMFT und DMRG, stimmten in ihren Vorhersagen für Parameterbereiche innerhalb der Anderson und Mott Phasen überein. Allerdings zeigte RDMFT stärkere Finite-Size Effekte als DMRG, was sich in größeren Delokalisierungstendenzen bei fester Gittergröße spiegelte. Als ein Hauptergebnis präsentieren wir nichtperturbative Rechnungen, die eine delokalisierte Phase aufweisen. Diese entsteht infolge des Zusammenspiels der mittelstarken Unordnung und Wechselwirkung. Diese Phase bildet das Analogon zu Boseglas, das in eindimensionalen ungeordneten bosonischen Systemen gefunden wurde [9, 338–341]. Dieser Effekt, untersucht mittels DMRG bei Georg Harder als auch mittels RDMFT im Rahmen dieser Dissertation, zeigte Stabilität gegenüber Finite-Size Skalierung in RDMFT und wurde das erste Mal im Rahmen dieser Arbeit nachgewiesen.

Eine Implementierung der Box-verteilten Unordnungsfelder dient dazu einen ersten Überblick über die Physik zu gewinnen. Allerdings, wurde die Box-Unordnung bisher noch nicht experimentell realisiert, während die Speckle-Unordnung mittels optischer Streufelder in optischen Gittern erzeugt werden kann [233]. Zusätzlich zu der Implementierung der Speckle-Unordnung kann die Präzision der theoretischen Beschreibung erhöht werden indem gemeinsame Wahrscheinlichkeiten für Modellparameter eingesetzt werden. Diese beschreib-

en stochastisch verteilte korrelierte Wechselwirkungs- und Tunnelstärken, die infolge lokaler Energien und Energiedifferenzen zwischen benachbarten Gitterplätzen entstehen.

Somit liegt ein weiterer Fokus dieser Arbeit auf der Beschreibung von Speckle-Feldern in fermionischen Gittern unter der Berücksichtigung der diagonalen und off-diagonalen Unordnung, also den zufälligen Wechselwirkungsstärken und Tunnelwahrscheinlichkeiten. Das Modell wurde unter Verwendung von zwei verwandten Ansätzen diskutiert: statistische DMFT (statDMFT) und orts aufgelöste DMFT (RDMFT). Beide Methoden stellen Erweiterungen zu DMFT dar und berücksichtigen nur die lokalen Fluktuationen. Allerdings, unterscheiden sie sich per Konstruktion in der Implementierung der Unordnung. Während die erste Methode die Wahrscheinlichkeitsverteilungen in die Selbstkonsistenzgleichungen auf unendlichen Bethe Gittern integriert, löst die zweite das physikalische Problem für jeweils eine feste Unordnungskonfiguration unter Berücksichtigung der Zustandsdichte einer beliebigen gegebenen endlichen Gitterstruktur. Obwohl die semi-elliptische Zustandsdichte des Bethe Gitters ein rein mathematisches Konstrukt ist, ist sie in theoretischen Simulationen weit verbreitet. Die Physik der dreidimensionalen Systeme entspricht qualitativ den Ergebnissen auf dem Bethe Gitter, allerdings können in niedrigeren Dimensionen Abweichungen entstehen. Zum Zwecke der Untersuchung möglicher Anomalien in 2D wurden die Ergebnisse der statDMFT, erzielt durch Denis Semmler, mit den Resultaten der RDMFT in dieser Dissertation verglichen.

Der markanteste Unterschied zwischen den beiden Methoden wurde am Fermi Niveau der lokalen Zustandsdichte festgestellt. RDMFT Rechnungen zeigen eine Pseudo-Lücke im Spektrum quadratischer Gitter. Diese Pseudo-Lücke bildet sich bei mittleren und starken Wechselwirkungen in Gegenwart von Unordnung und bleibt unter Variation der Größe des Systems stabil. Resultate der statDMFT wiesen keine solche Eigenschaften auf. Die gewonnenen Ergebnisse für das paramagnetische Grundzustandsphasendiagramm im Bethe Gitter stimmen qualitativ mit den Resultaten für ein zweidimensionales quadratisches Gitter (RDMFT) überein: für schwache Unordnung wird ein Metall-Isolator Übergang durch eine Erhöhung der Wechselwirkungsstärke induziert, indes führt stärkere Unordnung zur Stabilisierung der metallischen Phase. Quantitative Unterschiede wurden jedoch bei schwachen Korrelationen entdeckt, wenn die kinetische Energie, die in Relation zur Gitterstruktur steht, die führende Energieskala darstellt [51]. Ein Vergleich mit den existierenden Ergebnissen für Box-Unordnung zeigt, dass die spektralen Eigenschaften der Speckle-Unordnung zu qualitativ anderen Effekten führen. Während in einem rein diagonalen Box-ungeordneten System die Mott und Anderson Isolatoren verbunden sind [44, 58, 326, 335], weist ein Speckle-ungeordnetes Gitter eine kontinuierliche metallische Phase auf, die beide isolierenden Regimes trennt.

Insgesamt zeigen die Ergebnisse dieser Arbeit, dass eine Vielzahl von Fragen mit ultrakalten Gasen behandelt werden kann. Insbesondere werden in dieser Dissertation verschiedene Nichtgleichgewichtseffekte und statische Unordnungsphänomene für bosonische und fermionische Partikel untersucht. Die Kontrolle über Materiewellen ist in den letzten Jahren stark verbessert worden und eröffnet neue Möglichkeiten für die experimentelle Realisierung von Kombinationen aus beiden Effekten. In fermionischen 1D Kondensaten führte eine plötzlich initiierte Expansion einer zwei-atomigen Mischung zu Quantendestillation [342]. Hierin wurde während der Ausbreitung eine Abseparation der Doublonen vom Rest des Systems beobachtet, wobei sich diese zu einem metastabilen Zustand gruppierten. Da 1D Gitter eine besondere Sensitivität gegenüber Wechselwirkungen aufweisen, könnten ähnliche Untersuchungen in höheren Dimensionen zu neuen Erkenntnissen verhelfen. Angesichts des subtilen Wettbewerbs zwischen Unordnung und Wechsel-

wirkung in bestimmten Parameterregimes [44, 50, 51, 58, 228, 326], könnte die Expansionsdynamik fermionischer Doublonen in verunreinigten Gittern neue Einblicke in die Nichtgleichgewichtsphysik ungeordneter Fermionen gewähren, die bisher noch nicht untersucht wurde. Darüber hinaus versprechen die im Rahmen dieser Arbeit untersuchten überraschenden Effekte des schmelzenden bosonischen Mott Isolators, weitere faszinierende Ergebnisse in ungeordneten Gittern. Doch mit den derzeit verfügbaren numerischen Methoden sind Langzeit-Nichtgleichgewichtsstudien der Vielteilchendynamik in 2D und 3D nicht zugänglich. Ebenso mangelt es an numerischen Techniken zur Behandlung dynamischer ungeordneter bosonischer Systeme. Die jüngsten Entwicklungen im Bereich der wechselwirkenden und ungeordneter ultrakalten Gase machen also die Notwendigkeit eines numerischen Fortschritts deutlich. Zu diesem Zeitpunkt bleibt jedoch der zeitabhängige Gutzwiller die effizienteste Methode zur Behandlung wechselwirkender bosonischer Nichtgleichgewichtssysteme, und die orts aufgelöste DMFT die effektivste Methode zur Lösung statischer wechselwirkender ungeordneter fermionischer Probleme.

## A. Bose-Hubbard parameters

In this appendix we calculate the repulsive interspecies interaction  $U_{ab}$  when two different species  $a$  and  $b$  are simultaneously present in the lattice. The Schrödinger equation describing two different interacting particles corresponds to Eq. (3.45) with the reduced mass corrected with respect to the mass of the particles involved  $m_{\text{red}} = \frac{m_a m_b}{m_a + m_b}$ . Following the derivation Eq. (3.46)-(3.48) the resulting short-range pseudo-potential reads

$$V_p(\tilde{\mathbf{r}}) = g_{ab}\delta(\tilde{\mathbf{r}}), \quad (\text{A.1})$$

with

$$g_{ab} = \frac{2\pi\hbar^2 a_{s,ab}}{m_{\text{red}}}.$$

The scattering length between two different species is, in general, different to the scattering length between the same atomic species which we accounted for by substituting  $a_s$  with  $a_{s,ab}$ . Thus, the interaction Hamiltonian in field operator representation is

$$\begin{aligned} \mathcal{H}_{\text{int},ab} &= \frac{1}{2} \int d\mathbf{r} \int d\mathbf{r}' \hat{\Psi}_a^\dagger(\mathbf{r}) \hat{\Psi}_b^\dagger(\mathbf{r}') V_p(\mathbf{r} - \mathbf{r}') \hat{\Psi}_b(\mathbf{r}') \hat{\Psi}_a(\mathbf{r}) \\ &\stackrel{(\text{A.1})}{=} \frac{g_{ab}}{2} \left( \int dx \int dx' \hat{\Psi}_a^\dagger(x) \hat{\Psi}_b^\dagger(x') \delta(x - x') \hat{\Psi}_b(x') \hat{\Psi}_a(x) \right)^3 \\ &= \frac{g_{ab}}{2} \sum_{\substack{i,j, \\ l,n}} \left( \int dx \int dx' w_a^*(x - x_i) w_b^*(x' - x_j) \delta(x - x') w_b(x' - x_l) w_a(x - x_n) \right)^3 \\ &\quad \times \hat{b}_{a,i}^\dagger \hat{b}_{b,j}^\dagger \hat{b}_{b,l} \hat{b}_{a,n} \\ &= \frac{g_{ab}}{2} \sum_{\substack{i,j, \\ l,n}} \left( \int dx w_a^*(x - x_i) w_b^*(x - x_j) w_b(x - x_l) w_a(x - x_n) \right)^3 \hat{b}_{a,i}^\dagger \hat{b}_{b,j}^\dagger \hat{b}_{b,l} \hat{b}_{a,n} \end{aligned} \quad (\text{A.2})$$

From the second to the third line we expressed the creation/annihilation field operators in the Wannier basis (see Eq. (3.24)). The indices  $a$  and  $b$  should emphasize that the shapes of the Wannier functions depend on the species. This might seem surprising as the Wannier functions are connected via a Fourier transform to Bloch states, which are

the eigenstates of a periodic potential regardless of the species being trapped. However, the intensity of the laser and thus the depth of the optical lattice potential depends on the detuning between the laser frequency and the addressed atomic transition Eq. (2.15). Therefore, each species experiences a different lattice depth,  $s_a$  and  $s_b$ , which affects the degree of localization. Thus, the Wannier function  $w_a(x - x_i)$  equals the Wannier function  $w_b(x - x_i)$  only if  $s_a = s_b$ .

Taking only the leading term of the sum into account, namely  $i = j = l = n$  where the overlap of the Wannier functions is maximal and consequently the integral of Eq. (A.2) becomes

$$\begin{aligned}
\mathcal{H}_{\text{int},ab} &= \frac{g_{ab}}{2} \left[ \int dx |w_a(x)|^2 |w_b(x)|^2 \right]^3 \sum_{i,j,l,n} \delta_{ij} \delta_{jl} \delta_{ln} \hat{b}_{a,i}^\dagger \hat{b}_{b,j}^\dagger \hat{b}_{b,l} \hat{b}_{a,n} \\
&= \frac{g_{ab}}{2} \left[ \int dx |w_a(x)|^2 |w_b(x)|^2 \right]^3 \sum_i \hat{n}_{a,i} \hat{n}_{b,i} \\
&= \frac{U_{ab}}{2} \sum_i \hat{n}_{a,i} \hat{n}_{b,i}
\end{aligned} \tag{A.3}$$

From the first to the second line we used the fact that the creation/annihilation operators of different species commute. Moreover, in translationally invariant potentials the equivalence of the Wannier states at different lattice sites holds such that  $w_{a/b}(x - x_i) = w_{a/b}(x)$ . The resulting interaction Hamiltonian Eq. (A.3) describes the on-site interaction between different species.

The interaction matrix element

$$U_{ab} = g_{ab} \left[ \int dx |w_a(x)|^2 |w_b(x)|^2 \right]^3 .$$

can be calculated exactly via a band calculation leading to Bloch states followed by a Fourier transformation to the Wannier states, or alternatively approximated in the deep lattice regime. For the latter we replace the Wannier functions by Gaussians

$$w_{a(b)}(x) = \frac{1}{\sqrt{\sigma_{a(b)}} \pi^{1/4}} \exp \left\{ -\frac{x^2}{2\sigma_{a(b)}^2} \right\} \quad \text{with} \quad \sigma_{a(b)} = \frac{a}{\pi s_{a(b)}^{1/4}} \tag{A.4}$$

where  $a = \lambda/2$  is the lattice constant,  $s_{a(b)} = V_{0,a(b)}/E_{r,a(b)}$  the lattice depth of species a and b respectively,  $E_{r,a(b)} = \hbar^2 k^2 / 2m_{a(b)}$  the species dependent recoil energy and  $k = 2\pi/\lambda$  the laser momentum. In deep lattices the interaction matrix element takes the form

$$\begin{aligned}
U_{ab} &= g_{ab} \left[ \int dx |w_a(x)|^2 |w_b(x)|^2 \right]^3 \\
&= g_{ab} \frac{1}{(\sigma_a \sigma_b \pi)^3} \left[ \int dx \exp \left\{ -\frac{x^2}{\sigma_a^2} - \frac{x^2}{\sigma_b^2} \right\} \right]^3 \\
&= g_{ab} \frac{1}{(\sigma_a \sigma_b \pi)^3} \left[ \frac{\sigma_a \sigma_b}{\sqrt{2(\sigma_a^2 + \sigma_b^2)}} \sqrt{2\pi} \right]^3 \\
&= \frac{2\pi \hbar^2 a_{ab}}{m_{\text{red}}} \frac{1}{\sqrt{\pi(\sigma_a^2 + \sigma_b^2)}^3} \\
&= \frac{2\pi \hbar^2 a_{ab} \pi^3}{\sqrt{\pi} m_{\text{red}} d^3} \frac{1}{\left(1 + \sqrt{\frac{E_{r,b} V_{0,a}}{E_{r,a} V_{0,b}}}\right)^{3/2}} \left(\frac{V_{0,a}}{E_{r,a}}\right)^{3/4} \\
&= 4\sqrt{\pi} k a_{ab} E_{r,a} \frac{(1 + m_a/m_b)}{\left(1 + \sqrt{\frac{m_a V_{0,a}}{m_b V_{0,b}}}\right)^{3/2}} s_a^{3/4} \tag{A.5}
\end{aligned}$$

or equivalently

$$= 4\sqrt{\pi} k a_{ab} E_{r,b} \frac{(1 + m_b/m_a)}{\left(1 + \sqrt{\frac{m_b V_{0,b}}{m_a V_{0,a}}}\right)^{3/2}} s_b^{3/4}. \tag{A.6}$$





## B. Particle number violation for parallel updates

In this appendix we discuss the possible particle number violation due to the updating procedure. As discussed in Sec. 3.5, the mean-field Hamiltonian of the system decouples into a direct product of single-site Hamiltonians and hence the time evolution of the lattice decomposes into time evolutions of each site. This suggests different possibilities how the time steps  $t \rightarrow t + \Delta$  can be calculated: either the sites are updated sequentially or in parallel. In a *parallel update* the state  $|\Psi(t + \Delta t)\rangle_i$  at site  $i$  is calculated independently of other sites based on nearest-neighbor SF-parameters  $\{\langle \hat{b}_j(t) \rangle\}$ . Once the mean-field many-body state  $|\Psi(t + \Delta t)\rangle_1 \cdot \dots \cdot |\Psi(t + \Delta t)\rangle_L$  is evaluated at time  $t + \Delta t$ , the next time step is calculated analogously based on SF-parameters  $\{\langle \hat{b}_j(t + \Delta t) \rangle\} = \{ \langle \Psi(t + \Delta t) | \hat{b}_j | \Psi(t + \Delta t) \rangle \}$ . In the *sequential updating* procedure, each site is updated after one another, e. g. from top left to right bottom, whereby when updating site  $i$  to time  $t + \Delta t$  the updated  $\{\langle \hat{b}_j(t + \Delta t) \rangle\}$  as well as the  $\{\langle \hat{b}_j(t) \rangle\}$  SF-parameters which have not yet been updated, are taken into account according to the actual single-site states of the neighbors. These methods are not equivalent as we will show next. For the sake of simplicity in the following discussion we concentrate on homogeneous systems, whereby the results can be easily extended to inhomogeneous lattices which validates our conclusions in general. The derivation follows unpublished results by M. Snoek.

The time evolution of the many-body Gutzwiller state decouples into unitary single-site time evolutions (see Sec. 3.5) as

$$|\Psi(t + \Delta t)\rangle_i = \hat{U}_i(\Delta t) |\Psi(t)\rangle_i \quad \text{with} \quad \hat{U}_i(\Delta t) = e^{-i\hat{\mathcal{H}}_{MF,i}(t)\Delta t}, \quad (\text{B.1})$$

where  $\hat{\mathcal{H}}_{MF,i}(t)$  corresponds to the on-site mean-field Hamiltonian

$$\hat{\mathcal{H}}_{MF,i}(t) = -J(\hat{b}_i^\dagger \eta_i(t) + h.c.) - \mu \hat{n}_i + \frac{U}{2} \hat{n}_i(\hat{n}_i - 1) \quad (\text{B.2})$$

with  $\eta_i$  being the sum over nearest neighbors SF-parameters.

For the sake of readability we make use of the following abbreviations

$$\hat{U}_i \equiv \hat{U}_i(\Delta t), \quad \hat{\mathcal{H}}_{MF,i} \equiv \hat{\mathcal{H}}_{MF,i}(t) \quad \text{and} \quad \langle \hat{A}_i(t) \rangle = {}_i\langle \Psi(t) | \hat{A}_i | \Psi(t) \rangle_i \equiv \langle \hat{A}_i \rangle_t,$$

where  $\hat{A}_i$  denotes an arbitrary operator on site  $i$ . In this notation, the particle number at time  $t$  and  $t + \Delta t$  on site  $i$  reads

$$\begin{aligned} n_i(t) &= \langle \hat{n}_i(t) \rangle = \langle \hat{n}_i \rangle_t, \\ n_i(t + \Delta t) &= \langle \hat{n}_i(t + \Delta t) \rangle = {}_i \langle \Psi(t + \Delta t) | \hat{n}_i | \Psi(t + \Delta t) \rangle_i = {}_i \langle \Psi(t) | \hat{U}_i^\dagger \hat{n}_i \hat{U}_i | \Psi(t) \rangle_i = \langle \hat{U}_i^\dagger \hat{n}_i \hat{U}_i \rangle_t. \end{aligned}$$

The deviation in particle number as a consequence of any general update results in

$$\begin{aligned} \delta n_i &= n_i(t + \Delta t) - n_i(t) = \langle \hat{U}_i^\dagger \hat{n}_i \hat{U}_i - \hat{n}_i \rangle_t \\ &= \langle \hat{U}_i^\dagger \hat{n}_i \hat{U}_i - \hat{U}_i^\dagger \hat{U}_i \hat{n}_i \rangle_t \\ &= \langle \hat{U}_i^\dagger [\hat{n}_i, \hat{U}_i] \rangle_t. \end{aligned} \quad (\text{B.3})$$

Next we use the Taylor series expansion of the unitary time evolution operator

$$\hat{U}_i = \sum_{k=0}^{\infty} \frac{(-i\hat{\mathcal{H}}_{MF,i}\Delta t)^k}{k!} \quad \hat{U}_i^\dagger = \sum_{l=0}^{\infty} \frac{(i\hat{\mathcal{H}}_{MF,i}\Delta t)^l}{l!} \quad (\text{B.4})$$

to discuss particle deviation in orders of  $\Delta t$ . The derivation then becomes

$$\delta n_i = \frac{1}{2} \sum_{k,l} \left\langle \frac{(-1)^{k+l} \Delta t^{k+l}}{k!l!} \left( \hat{\mathcal{H}}_{MF,i}^l [\hat{n}_i, \hat{\mathcal{H}}_{MF,i}^k] + [\hat{\mathcal{H}}_{MF,i}^l, \hat{n}_i] \hat{\mathcal{H}}_{MF,i}^k \right) \right\rangle_t. \quad (\text{B.5})$$

The size of the time step considered is chosen small in order to justify the approximation of the integral in Eq. (3.140). Therefore, the major contributions to  $\delta n_i$  are given by low order terms in  $\Delta t$  which are discussed below.

To first order in  $\Delta t$  only the summands  $\{k = 0, l = 1\}$  and  $\{k = 1, l = 0\}$  contribute

$$\begin{aligned} \delta n_i^{(1)} &= \frac{1}{2} \langle i\Delta t [\hat{\mathcal{H}}_{MF,i}, \hat{n}_i] - i\Delta t [\hat{n}_i, \hat{\mathcal{H}}_{MF,i}] \rangle_t \\ &= i\Delta t \langle [\hat{\mathcal{H}}_{MF,i}, \hat{n}_i] \rangle_t \\ &\stackrel{\text{Eq. (3.125)}}{=} Ji\Delta t \langle (\eta_i \hat{b}_i^\dagger - \eta_i^* \hat{b}_i) \rangle_t, \end{aligned} \quad (\text{B.6})$$

where  $\eta_i = \sum_{j \text{ n.n. } i} \langle \hat{b}_j \rangle_{\{t\}}$  is the sum over mean-field parameters evaluated at times  $\{t\}$ . It is important to note that, depending on the updating procedure, the sites may be updated at the same time (parallel update) or successive (sequential update) which, as we will discuss later, significantly influences the results.

The second order corrections contain contributions from summands  $\{k = 0, l = 2\}$ ,  $\{k = 1, l = 1\}$  and  $\{k = 2, l = 0\}$ , thus

$$\begin{aligned} \delta n_i^{(2)} &= \frac{i^2 \Delta t^2}{2} \left\langle \frac{1}{2!} [\hat{n}_i, \hat{\mathcal{H}}_{MF,i}^2] - \hat{\mathcal{H}}_{MF,i} [\hat{n}_i, \hat{\mathcal{H}}_{MF,i}] - [\hat{\mathcal{H}}_{MF,i}, \hat{n}_i] \hat{\mathcal{H}}_{MF,i} + \frac{1}{2!} [\hat{\mathcal{H}}_{MF,i}^2, \hat{n}_i] \right\rangle_t \\ &= \frac{\Delta t^2}{2} \langle [\hat{\mathcal{H}}_{MF,i}, [\hat{n}_i, \hat{\mathcal{H}}_{MF,i}]] \rangle_t \\ &\stackrel{\text{Eq. (3.125)}}{=} \frac{\Delta t^2}{2} \langle [\hat{\mathcal{H}}_{MF,i}, J (\eta_i \hat{b}_i^\dagger - \eta_i^* \hat{b}_i)] \rangle_t \\ &= \frac{J\Delta t^2}{2} \left( \underbrace{\eta_i \langle [\hat{\mathcal{H}}_{MF,i}, \hat{b}_i^\dagger] \rangle_t}_A - \eta_i^* \langle [\hat{\mathcal{H}}_{MF,i}, \hat{b}_i] \rangle_t \right). \end{aligned} \quad (\text{B.7})$$

Since  $[\hat{\mathcal{H}}_{MF,i}, \hat{b}_i^\dagger]^\dagger = -[\hat{\mathcal{H}}_{MF,i}, \hat{b}_i]$  we can obtain the full expression  $B$  from evaluated commutator relation  $A$ . Given the mean-field Hamiltonian Eq. (B.2) for homogeneous systems the term  $A$  results

$$\begin{aligned} A: \quad [\hat{\mathcal{H}}_{MF,i}, \hat{b}_i^\dagger] &= -J\eta_i^*[\hat{b}_i, \hat{b}_i^\dagger] - (\mu + \frac{U}{2})[\hat{n}_i, \hat{b}_i^\dagger] + \frac{U}{2}[\hat{n}_i^2, \hat{b}_i^\dagger] \\ &= -J\eta_i^* - (\mu + \frac{U}{2})\hat{b}_i^\dagger + \frac{U}{2}(\hat{n}_i\hat{b}_i^\dagger + \hat{b}_i^\dagger\hat{n}_i), \end{aligned} \quad (\text{B.8})$$

where we used commutation relations

$$[\hat{b}_i, \hat{b}_i^\dagger] = 1, \quad [\hat{n}_i, \hat{b}_i^\dagger] = \hat{b}_i^\dagger, \quad [\hat{n}_i^2, \hat{b}_i^\dagger] = \hat{n}_i\hat{b}_i^\dagger + \hat{b}_i^\dagger\hat{n}_i.$$

From here it follows that

$$B: \quad [\hat{\mathcal{H}}_{MF,i}, \hat{b}_i] = J\eta_i + (\mu + \frac{U}{2})\hat{b}_i - \frac{U}{2}(\hat{b}_i\hat{n}_i + \hat{n}_i\hat{b}_i). \quad (\text{B.9})$$

Substituting  $A$  and  $B$  in Eq. (B.7) by full expressions (B.8) and (B.9) and simplifying the resulting expression gives

$$\begin{aligned} \delta n_i^{(2)} &= \frac{J\Delta t^2}{2} \left( -2J|\eta_i|^2 - (\mu + \frac{U}{2})(\langle \hat{b}_i^\dagger \rangle \eta_i - \langle \hat{b}_i \rangle \eta_i^*) \right. \\ &\quad \left. + \frac{U}{2}(2\eta_i \langle \hat{b}_i^\dagger \hat{n}_i \rangle + 2\eta_i^* \langle \hat{b}_i \hat{n}_i \rangle + \eta_i \langle \hat{b}_i^\dagger \rangle - \eta_i^* \langle \hat{b}_i \rangle) \right). \end{aligned} \quad (\text{B.10})$$

Corrections to  $\delta n_i$  for higher orders of  $\Delta t$  are considered to be vanishingly small and are therefore neglected in the following discussion.

### Parallel updates

As already mentioned at the beginning of the appendix, when all sites are updated simultaneously all SF-fields  $\eta_i$  are calculated based on  $\{\langle \hat{b}_j \rangle_t\}$ , which are identical in a homogeneous system:

$$\eta_i = \sum_{j \text{ n.n. } i} \langle \hat{b}_j \rangle_{\{t\}} = z \langle \hat{b} \rangle_t \equiv \eta, \quad (\text{B.11})$$

where  $z$  denotes the number of nearest neighbors. With this the first order particle number deviation Eq. (B.6) vanishes

$$\begin{aligned} \delta n^{(1)} &= Ji\Delta t \langle (\eta \hat{b}^\dagger - \eta^* \hat{b}) \rangle_t \\ &\stackrel{\text{Eq. (B.11)}}{=} Ji\Delta tz \left( \langle \hat{b} \rangle_t \langle \hat{b}^\dagger \rangle_t - \langle \hat{b} \rangle_t^* \langle \hat{b} \rangle_t \right) \\ &= 0. \end{aligned}$$

However, the second order contribution Eq. (B.10) remains, in general, finite

$$\begin{aligned} \delta n^{(2)} &= \frac{J\Delta t^2}{2} \left( -2J|\langle \hat{b} \rangle_t|^2 - (\mu + \frac{U}{2})(\langle \hat{b}^\dagger \rangle_t \langle \hat{b} \rangle_t - \langle \hat{b} \rangle_t \langle \hat{b}^\dagger \rangle_t^*) \right. \\ &\quad \left. + \frac{U}{2}(2\langle \hat{b} \rangle_t \langle \hat{b}^\dagger \hat{n} \rangle_t + 2\langle \hat{b} \rangle_t^* \langle \hat{b} \hat{n} \rangle_t + \langle \hat{b} \rangle_t \langle \hat{b}^\dagger \rangle_t - \langle \hat{b} \rangle_t^* \langle \hat{b} \rangle_t) \right) \\ &= J\Delta t^2 \left( -J|\langle \hat{b} \rangle_t|^2 + \frac{U}{2}(\langle \hat{b} \rangle_t \langle \hat{b}^\dagger \hat{n} \rangle_t + \langle \hat{b} \rangle_t^* \langle \hat{b} \hat{n} \rangle_t) \right) \end{aligned}$$

This means that in homogeneous systems the particle number changes due to the choice of update scheme in the second order in  $\Delta t$

$$\delta n = \delta n^{(1)} + \delta n^{(2)} + \mathcal{O}(\Delta t^3) = J\Delta t^2 \left( -J|\langle \hat{b} \rangle_t|^2 + \frac{U}{2} (\langle \hat{b} \rangle_t \langle \hat{b}^\dagger \hat{n} \rangle_t + \langle \hat{b} \rangle_t^* \langle \hat{b} \hat{n} \rangle_t) \right) + \mathcal{O}(\Delta t^3).$$

Extending the above discussion to inhomogeneous lattices generalizes this conclusion: parallel updates violate the particle number conservation in the second order in  $\Delta t$  by construction for any lattice structure.

### Sequential updates

When the sites are updated sequentially, the SF-field  $\eta_i$  consists of newer and older mean-field parameters. Hence, the number of refreshed and not-refreshed  $\langle \hat{b}_i \rangle$  depends on the position of the currently updated site<sup>1</sup>. In case of a 2D system, alternating the updating direction between “top left to bottom right” and “bottom right to top left” every time step corrects for possible current flows and on average each site can be assumed to have  $z/2$  old and  $z/2$  new SF-parameter values. Indicating the older SF-parameter by an index  $t$  and the newer by  $t + \Delta t$ , the SF-field  $\eta_i$  reads

$$\eta_i = \sum_{j \text{ n.n. } i} \langle \hat{b}_j \rangle_{\{t\}} = \frac{z}{2} \langle \hat{b}_j \rangle_t + \frac{z}{2} \langle \hat{b}_j \rangle_{t+\Delta t}. \quad (\text{B.12})$$

Since every site in a homogeneous lattice has on average the same SF-field we can drop the site index. The particle number deviation Eq. (B.6) to first order then reads

$$\begin{aligned} \delta n^{(1)} &= Ji\Delta t \langle (\eta \hat{b}^\dagger - \eta^* \hat{b}) \rangle_t \\ &\stackrel{\text{Eq. (B.12)}}{=} Ji\Delta t \langle (\frac{z}{2} \langle \hat{b} \rangle_t + \frac{z}{2} \langle \hat{b} \rangle_{t+\Delta t}) \hat{b}^\dagger - (\frac{z}{2} \langle \hat{b} \rangle_t + \frac{z}{2} \langle \hat{b} \rangle_{t+\Delta t})^* \hat{b} \rangle_t \\ &= Ji\Delta t \left( \frac{z}{2} \langle \hat{b} \rangle_{t+\Delta t} \langle \hat{b}^\dagger \rangle_t - \frac{z}{2} \langle \hat{b} \rangle_{t+\Delta t}^* \langle \hat{b} \rangle_t \right). \end{aligned} \quad (\text{B.13})$$

To proceed we expand  $\langle \hat{b} \rangle_{t+\Delta t}$  in orders of  $\Delta t$

$$\begin{aligned} \langle \hat{b} \rangle_{t+\Delta t} &= \langle \hat{U}^\dagger \hat{b} \hat{U} \rangle_t \\ &= \sum_{k,l} \frac{(-1)^k i^{k+l} \Delta t^{k+l}}{k!l!} \langle \hat{\mathcal{H}}_{MF}^l \hat{b} \hat{\mathcal{H}}_{MF}^k \rangle_t \\ &= \langle \hat{b} \rangle_t + i\Delta t \langle [\hat{\mathcal{H}}_{MF}, \hat{b}] \rangle_t - i\Delta t \langle \hat{b} [\hat{\mathcal{H}}_{MF}] \rangle_t + \mathcal{O}(\Delta t^2) \\ &\approx \langle \hat{b} \rangle_t + i\Delta t \langle [\hat{\mathcal{H}}_{MF}, \hat{b}] \rangle_t \end{aligned} \quad (\text{B.14})$$

Inserting this result into Eq. (B.13) we find

$$\begin{aligned} \delta n^{(1)} &= Ji\Delta t \frac{z}{2} \left( \langle \hat{b} \rangle_t \langle \hat{b}^\dagger \rangle_t - \langle \hat{b}^\dagger \rangle_t \langle \hat{b} \rangle_t \right) \\ &\quad + Ji\Delta t \frac{z}{2} \left( i\Delta t \langle [\hat{\mathcal{H}}_{MF}, \hat{b}] \rangle_t \langle \hat{b}^\dagger \rangle_t - i\Delta t \langle [\hat{\mathcal{H}}_{MF}, \hat{b}^\dagger] \rangle_t \langle \hat{b} \rangle_t \right) \\ &= -J\Delta t^2 \frac{z}{2} \left( \langle [\hat{\mathcal{H}}_{MF}, \hat{b}] \rangle_t \langle \hat{b}^\dagger \rangle_t - \langle [\hat{\mathcal{H}}_{MF}, \hat{b}^\dagger] \rangle_t \langle \hat{b} \rangle_t \right). \end{aligned} \quad (\text{B.15})$$

<sup>1</sup>Some boundary sites have either 1 updated and  $z - 1$  not updated sites or vice versa, depending on the direction of the sequential calculations within a lattice. Moreover, the first and the last site have 0 or all new  $\langle \hat{b}_i \rangle$  values.

The  $\mathcal{O}(\Delta t)$  summand in the first line vanishes. Strictly speaking, due to its  $\Delta t^2$  dependency the remaining term represents an additional contribution to  $\delta n^{(2)}$  rather than to the first order term. However, we proceed with previous notation and keep this in mind when evaluating second order term. Analogously, the second order particle number deviation Eq. (B.7) reads

$$\begin{aligned}
\delta n^{(2)} &= \frac{J\Delta t^2}{2} \left( \eta \langle [\hat{\mathcal{H}}_{MF}, \hat{b}^\dagger] \rangle_t - \eta^* \langle [\hat{\mathcal{H}}_{MF}, \hat{b}] \rangle_t \right) \\
&\stackrel{\text{Eq. (B.12)}}{=} \frac{J\Delta t^2}{2} \frac{z}{2} \left( (\langle \hat{b} \rangle_t + \langle \hat{b} \rangle_{t+\Delta t}) \langle [\hat{\mathcal{H}}_{MF}, \hat{b}^\dagger] \rangle_t - (\langle \hat{b} \rangle_t + \langle \hat{b} \rangle_{t+\Delta t})^* \langle [\hat{\mathcal{H}}_{MF}, \hat{b}] \rangle_t \right) \\
&\stackrel{\text{Eq. (B.14)}}{=} J\Delta t^2 \frac{z}{2} \left( \langle \hat{b} \rangle_t^* \langle [\hat{\mathcal{H}}_{MF}, \hat{b}] \rangle_t - \langle \hat{b} \rangle_t \langle [\hat{\mathcal{H}}_{MF}, \hat{b}^\dagger] \rangle_t \right) + \mathcal{O}(\Delta t^3).
\end{aligned}$$

This contribution exactly cancels the result in Eq. (B.15), such that

$$\delta n = \delta n^{(1)} + \delta n^{(2)} + \mathcal{O}(\Delta t^3) = 0 + \mathcal{O}(\Delta t^3). \quad (\text{B.16})$$

Hence, the sequential time evolution of single lattice sites conserves the particle number up to order  $\mathcal{O}(\Delta t^3)$ . A similar relation holds for inhomogeneous lattices.



## C. Efficient calculation of time evolution within Gutzwiller

The derivation of Eq. (3.141) is based on the Taylor expansion of an analytic function  $f$  applied to an arbitrary operator  $\mathbf{B}$ :  $f(\mathbf{B}) = \sum_{k=0}^{\infty} \frac{f^{(k)}(0)}{k!} \mathbf{B}^k$ . From here one can easily show that

$$f(\mathbf{B}) = \mathbf{U}f(\mathbf{U}^\dagger\mathbf{B}\mathbf{U})\mathbf{U}^\dagger \quad (\text{C.1})$$

namely

$$\begin{aligned} \mathbf{U}f(\mathbf{U}^\dagger\mathbf{B}\mathbf{U})\mathbf{U}^\dagger &= \mathbf{U} \sum_{k=0}^{\infty} \frac{f^{(k)}(0)}{k!} (\mathbf{U}^\dagger\mathbf{B}\mathbf{U})^k \mathbf{U}^\dagger \\ &= \mathbf{U}\mathbf{U}^\dagger \sum_{k=0}^{\infty} \frac{f^{(k)}(0)}{k!} \mathbf{B}^k \mathbf{U}\mathbf{U}^\dagger \\ &= \sum_{k=0}^{\infty} \frac{f^{(k)}(0)}{k!} \mathbf{B}^k \quad \text{q.e.d.} \end{aligned} \quad (\text{C.2})$$

From the first to the second line we used the fact that  $\mathbf{U}^\dagger\mathbf{U} = \mathbf{U}\mathbf{U}^\dagger = 1$  and consequently  $(\mathbf{U}^\dagger\mathbf{B}\mathbf{U})^n = \underbrace{\mathbf{U}^\dagger\mathbf{B}\mathbf{U}\mathbf{U}^\dagger\mathbf{B}\mathbf{U}\dots\mathbf{U}^\dagger\mathbf{B}\mathbf{U}}_n = \mathbf{U}^\dagger \underbrace{\mathbf{B}\dots\mathbf{B}}_n \mathbf{U} = \mathbf{U}^\dagger\mathbf{B}^n\mathbf{U}$ .

Now, back to Eq. (3.141). Since the derivation is not specific for any time or lattice site we drop the corresponding indices in the following explanation. As the exponential function is an analytic function we can make use of Eq. (3.141) and write

$$Ae^{-\frac{i}{\hbar}\mathcal{H}}A^\dagger = AA^\dagger e^{-\frac{i}{\hbar}A\mathcal{H}A^\dagger}AA^\dagger = e^{-\frac{i}{\hbar}\mathbf{E}}. \quad (\text{C.3})$$

The last step is based on the fact that for a unitary operator  $A$  consisting of eigenvectors the transformation  $A\mathcal{H}A^\dagger$  brings the mean-field Hamiltonian to diagonal form with its eigenvalues ordered along the diagonal

$$A\mathcal{H}A^\dagger = \mathbf{E} = \begin{pmatrix} E^{(0)} & 0 & \dots \\ 0 & E^{(1)} & \dots \\ \vdots & \vdots & \ddots \end{pmatrix}.$$

The next step will be to show that for any diagonal matrix  $C = \alpha_i \delta_{ij}$  the relation  $f(C) = f(\alpha_i) \delta_{ij}$  holds for any analytic function  $f$ . A single matrix element  $ij$  of the Taylor series expansion  $f(C) = \sum_{k=0}^{\infty} \frac{f^{(k)}}{k!}(0) C^k$  is

$$\begin{aligned}
[f(C)]_{ij} &= \sum_{k=0}^{\infty} \frac{f^{(k)}}{k!}(0) [C^k]_{ij} \\
&= \sum_{k=0}^{\infty} \frac{f^{(k)}}{k!}(0) C_{iq_1} \cdot C_{q_1 q_2} \cdot \dots \cdot C_{q_{k-1} j} \\
&= \sum_{k=0}^{\infty} \frac{f^{(k)}}{k!}(0) \alpha_{q_1} \delta_{iq_1} \cdot \alpha_{q_2} \delta_{q_1 q_2} \cdot \dots \cdot \alpha_j \delta_{q_{k-1} j} \\
&= \sum_{k=0}^{\infty} \frac{f^{(k)}}{k!}(0) \alpha_j^k \delta_{ij} \\
&= \begin{pmatrix} f(\alpha_1) & 0 & \dots \\ 0 & f(\alpha_2) & \dots \\ \vdots & \vdots & \ddots \end{pmatrix} \quad \text{q.e.d.}
\end{aligned}$$

Applying this identity to the Eq. (C.3) leads to the simplification  $e^{-\frac{i}{\hbar} \mathbf{E}} = \mathbf{D}$ , with

$$\mathbf{D} = \begin{pmatrix} e^{-\frac{i}{\hbar} E^{(0)}} & 0 & \dots \\ 0 & e^{-\frac{i}{\hbar} E^{(1)}} & \dots \\ \vdots & \vdots & \ddots \end{pmatrix}.$$

as is given in Eq. (3.141).



## D. Temperature estimation in a weak lattice

The ramp-up in our work starts at the lattice depth  $s = 5$  and not at  $s = 0$ , as in the experiment, due to the required tight-binding regime of the Hubbard Model. Therefore, starting from  $s = 5$  we have to recalculate the temperature based on the initial experimental temperature 73 nK [20] before the ramp. It can be shown by the following argument that the ramp-up of the optical lattice cools the system down. As a first estimate, let us assume that the lattice is ramped up adiabatically from  $s = 0$  to  $s = 5$  and that the particles are non-interacting. The initial slow ramp of an exponential or any other ramping profile realizes the first condition. The second condition is strictly satisfied only in shallow lattices. For  $s = 5$ , where  $U_{Rb} \sim J_{Rb}$ , it can be assumed to be roughly satisfied and leads to the right temperature range.

In the case of an adiabatic lattice ramp the entropy of the system

$$S = -k_B \sum_k \left( \ln[1 + n_k](1 + n_k) - n_k \ln n_k \right)$$

remains constant. As the experiments start from  $s = 0$ , the initial dispersion corresponds to the free particle dispersion  $\varepsilon_k^i = \hbar^2 \vec{k}^2 / 2m$ . The final situation is of the tight-binding limit and the particle density is evaluated with the dispersion  $\varepsilon_k^f = -2J(\cos(k_x a) + \cos(k_y a))$ , where  $a$  is the lattice constant. As the non-interacting condensate is located around  $\vec{k} = (0, 0)$  the tight-binding dispersion can be approximated by a Taylor series as  $\varepsilon_k^f \approx J(\vec{k}a)^2$ . The initial and final particle densities  $n_k^{i,f} = (e^{\beta \varepsilon_k^{i,f}} - 1)^{-1}$  have the same functional dependence on momentum  $k$ . The sum over functions with the same functional  $k$ -dependence in entropies can only remain constant when these functions are identical. This is realized when the particle density  $n_k$  for the initial lattice depth corresponds to the final density. From the equality of initial and final particle densities the criterion for the final temperature follows:  $T^f / T^i = \varepsilon_k^f / \varepsilon_k^i$ . From here the final temperature can be estimated  $T^f = T^i J \lambda^2 m / 2 \hbar^2$ , where  $\lambda$  is the laser wavelength and  $J$  is the hopping amplitude at the final lattice depth [343].

For a lattice ramp to  $s = 5$  the initial temperature of 73 nK is halved. For this lattice depth the system is in the SF regime, and so the thermal energy competes with the

hopping energy  $J$ . At this point the dimensionality of the experiment has to be taken into account. As the hopping scales with the number of the neighbors  $z$  the ratio  $T^f/zJ$  for our 2D system studied here should correspond to the ratio of the experimental 3D system. This lowers the calculated temperature by an additional factor  $2/3$ , providing the effective temperature  $T^f = 24$  nK such that our 2D system is equivalent to the 3D experimental system.

## E. Calculation of DMFT effective action

Given the action of the complete lattice

$$S = \int_0^\beta d\tau \left( \sum_{i\sigma} c_{i\sigma}^*(\tau) (\partial_\tau - \mu) c_{i\sigma}(\tau) - \sum_{\langle ij \rangle, \sigma} t_{ij} (c_{i\sigma}^*(\tau) c_{j\sigma}(\tau) + c.c.) + U \sum_i n_{i\uparrow}(\tau) n_{i\downarrow}(\tau) \right), \quad (\text{E.1})$$

where  $c_{i\sigma}$  and its complex conjugate denote the Grassmann variables describing fermions and  $\mu$ ,  $U$  and  $t$  are the chemical potential, Hubbard interaction and tunneling strength respectively, we can make following decomposition

$$S = S_0 + \Delta S + S^{(0)}. \quad (\text{E.2})$$

Here, the three summands indicate the impurity action ( $S_0$ ), the action describing the coupling of the impurity to the bath ( $\Delta S$ ) and the cavity action characterizing the bath with impurity removed ( $S^{(0)}$ ). They are defined by

$$\begin{aligned} S_0 &= \int_0^\beta d\tau \left( \sum_\sigma c_{0\sigma}^*(\tau) (\partial_\tau - \mu) c_{0\sigma}(\tau) + U n_{0\uparrow}(\tau) n_{0\downarrow}(\tau) \right) \\ \Delta S &= - \int_0^\beta d\tau \sum_{\langle i0 \rangle, \sigma} t_{i0} \left( c_{i\sigma}^*(\tau) c_{0\sigma}(\tau) + c.c. \right) \\ S^{(0)} &= \int_0^\beta d\tau \left( - \sum_{\langle ij \rangle^{(0)}, \sigma} t_{ij} \left( c_{i\sigma}^*(\tau) c_{j\sigma}(\tau) + c.c. \right) + \sum_{i \neq 0} U n_{i\uparrow}(\tau) n_{i\downarrow}(\tau) \right). \end{aligned}$$

Here,  $\sum_{\langle i0 \rangle, \sigma}$  addresses only the nearest neighbors of the impurity site, and  $\sum_{\langle ij \rangle^{(0)}, \sigma}$  indicates the summation over pairs of sites excluding impurity. Using this decomposition the definition of the effective action Eq. (6.48) takes on the form

$$\frac{1}{Z_{\text{eff}}} e^{-S_{\text{eff}}} = \frac{1}{Z} \int \prod_{i \neq 0, \sigma} Dc_{i\sigma}^* Dc_{i\sigma} e^{-S_0} e^{-\Delta S} e^{-S^{(0)}} \quad (\text{E.3})$$

$$= \frac{e^{-S_0}}{Z} \int \prod_{i \neq 0, \sigma} Dc_{i\sigma}^* Dc_{i\sigma} e^{-S^{(0)}} e^{-\Delta S}. \quad (\text{E.4})$$

Expanding the last exponential function in a Taylor series leads to

$$\frac{1}{Z_{\text{eff}}} e^{-S_{\text{eff}}} = \frac{e^{-S^0}}{Z} \int \prod_{i \neq 0, \sigma} Dc_{i\sigma}^* Dc_{i\sigma} e^{-S^{(0)}} \sum_{k=0}^{\infty} \frac{(-\Delta S)^k}{k!}. \quad (\text{E.5})$$

Identifying the cavity expectation values with

$$\langle O \rangle^{(0)} = \frac{1}{Z^{(0)}} \int \prod_{i \neq 0, \sigma} Dc_{i\sigma}^* Dc_{i\sigma} e^{-S^{(0)}} O \quad (\text{E.6})$$

the equation Eq. (E.5) can be rewritten,

$$\begin{aligned} \frac{1}{Z_{\text{eff}}} e^{-S_{\text{eff}}} &= \frac{e^{-S^0}}{Z} Z^{(0)} \sum_{k=0}^{\infty} \frac{\langle (-\Delta S)^k \rangle^{(0)}}{k!} \\ &= \frac{e^{-S^0}}{Z} Z^{(0)} \left( 1 - \langle \Delta S \rangle^{(0)} + \frac{1}{2} \langle (\Delta S)^2 \rangle^{(0)} + \dots \right) \\ &= \frac{e^{-S^0}}{Z} Z^{(0)} \left( 1 + \int_0^\beta d\tau \sum_{\langle i0 \rangle, \sigma} t_{i0} \underbrace{\langle c_{i\sigma}^*(\tau) c_{0\sigma}(\tau) + h.c. \rangle^{(0)}}_A + \right. \\ &\quad \left. \frac{1}{2} \int_0^\beta \int_0^\beta d\tau d\tau' \sum_{\langle j0 \rangle} \sum_{\langle i0 \rangle, \sigma} t_{i0} t_{j0} \underbrace{\langle T_\tau \left( c_{i\sigma}^*(\tau) c_{0\sigma}(\tau) + h.c. \right) \left( c_{j\sigma}^*(\tau') c_{0\sigma}(\tau') + h.c. \right) \rangle^{(0)}}_B + \dots \right) \end{aligned} \quad (\text{E.7})$$

where  $T_\tau$  is the imaginary time ordering operator. Since the cavity expectation value does not include the impurity site we can separate this term:

$$A : \langle c_{i\sigma}^*(\tau) c_{0\sigma}(\tau) + c.c. \rangle^{(0)} = \langle \hat{c}_{i\sigma}^\dagger(\tau) \rangle^{(0)} c_{0\sigma}(\tau) + c.c.$$

In the case of bosons this term corresponds to the Gutzwiller approximation, see Sec. 3.3, for fermions the expectation value vanishes<sup>1</sup> and with it the total term  $A$ . Further in the Taylor series we find

$$\begin{aligned} B : \langle T_\tau \left( c_{i\sigma}^*(\tau) c_{0\sigma}(\tau) + c.c. \right) \left( c_{j\sigma}^*(\tau') c_{0\sigma}(\tau') + c.c. \right) \rangle^{(0)} &= c_{0\sigma}^*(\tau) c_{0\sigma}(\tau') \langle T_\tau \hat{c}_{i\sigma}^\dagger(\tau) \hat{c}_{j\sigma}(\tau') \rangle^{(0)} + c.c. \\ &= -c_{0\sigma}^*(\tau) c_{0\sigma}(\tau') G_{ij,\sigma}^{(0)}(\tau - \tau') + c.c. \end{aligned}$$

In the last step we have introduced the fermionic Green's function in the cavity system  $G_{ij,\sigma}^{(0)}(\tau, \tau') = -\langle T_\tau \hat{c}_{i\sigma}^\dagger(\tau) \hat{c}_{j\sigma}(\tau') \rangle^{(0)}$ .

Thus, in bosonic DMFT the terms  $A$  and  $B$  are kept which corresponds to the first order correction to the Gutzwiller method, whereby appropriate scaling to the hopping amplitude in the term  $B$  has to be done [17, 344].

In order to obtain the effective action, we identify the exponential terms of the right hand side of Eq. (E.7). For fermions one can show that

$$\begin{aligned} S_{\text{eff}} &= S_0 + \sum_{n=1}^{\infty} \sum_{\sigma} \sum_{\substack{i_1 \dots i_n \\ j_1 \dots j_n}} \int_0^\beta d\tau_{i_1} \dots \int_0^\beta d\tau_{j_n} t_{i_1} \dots t_{i_n} t_{j_1} \dots t_{j_n} c_{0\sigma}^*(\tau_{i_1}) \dots c_{0\sigma}^*(\tau_{i_n}) \\ &\quad G_{i_1 \dots i_n j_1 \dots j_n, \sigma}^{(0)}(\tau_{i_1} \dots \tau_{i_n} \tau_{j_1} \dots \tau_{j_n}) c_{0\sigma}(\tau_{j_1}) \dots c_{0\sigma}(\tau_{j_n}), \end{aligned} \quad (\text{E.8})$$

<sup>1</sup>To be more precise, in the case of fermions all odd terms vanish, which is not true for bosons [17, 139].

where for the sake of readability the notation was simplified, i.e.  $t_i \equiv t_{i0}$  and  $\sum_i \equiv \sum_{\langle i0 \rangle}$ .

Before we proceed with expansion to infinite dimensions we first consider the scaling of kinetic and interaction energies. The interaction energy scales linear with system size, but it does not depend on dimensionality of the system due to the simply summation of on-site terms

$$E_{\text{pot}} = \sum_i U \langle \hat{n}_{i\uparrow} \hat{n}_{i\downarrow} \rangle. \quad (\text{E.9})$$

In contrast, the kinetic term scales as

$$E_{\text{kin}} = - \sum_{\langle ij \rangle, \sigma} t_{ij} \langle (\hat{c}_{i\sigma}^\dagger \hat{c}_{j\sigma} + h.c.) \rangle \sim z \cdot \frac{1}{\sqrt{z}}. \quad (\text{E.10})$$

The reason for the difference in scaling is, that with increasing dimension the number of neighbors  $z$  increases. This influences the sum over the neighboring sites  $\sum_{\langle ij \rangle}$  but also the probability for a particle to tunnel from site  $i$  to site  $j$ , namely  $|\langle \hat{c}_{i\sigma}^\dagger \hat{c}_{j\sigma} \rangle|^2 \sim 1/z \sim 1/2d$  [281, 310]. Thus the linear scaling of the sum is modified by the scaling of the correlation function. Taking the limit of infinite dimensions at this stage would lead to a system completely dominated by the tunneling term. To guarantee equal scaling of kinetic and interaction contributions, the tunneling matrix element must be rescaled

$$t_{ij} = \frac{t_{ij}^*}{\sqrt{2d}}. \quad (\text{E.11})$$

With this scaling the limit of infinite dimensions  $d \rightarrow \infty$  can be taken, which leads to a simplification of Eq. (E.8). Namely, based on scaling of the sums over the sites, the hopping parameters and the Green's functions with  $d$ , only the first term remains finite [281]. The effective action in infinite dimension then reads

$$\begin{aligned} S_{\text{eff}} &= S_0 + \sum_{\sigma} \sum_{\substack{\langle i0 \rangle \\ \langle j0 \rangle}} \int_0^{\beta} d\tau_1 \int_0^{\beta} d\tau_2 t_{i0} t_{j0} c_{0\sigma}^*(\tau_1) G_{ij,\sigma}^{(0)}(\tau_1, \tau_2) c_{0\sigma}(\tau_2) \\ &= \int_0^{\beta} d\tau \left( \sum_{\sigma} c_{0\sigma}^*(\tau) (\partial_{\tau} - \mu) c_{0\sigma}(\tau) + U n_{0\uparrow}(\tau) n_{0\downarrow}(\tau) \right) \\ &\quad + \sum_{\sigma} \sum_{\substack{\langle i0 \rangle \\ \langle j0 \rangle}} \int_0^{\beta} d\tau_1 \int_0^{\beta} d\tau_2 t_{i0} t_{j0} c_{0\sigma}^*(\tau_1) G_{ij,\sigma}^{(0)}(\tau_1, \tau_2) c_{0\sigma}(\tau_2). \end{aligned}$$

Neglecting terms of order  $1/d$  (or  $1/z$ ) determines the accuracy of the approximation when used in finite dimensions. In 3d cubic lattices DMFT calculations are in very good agreement with exact QMC results and experiments [278, 345].



## F. Derivation of the Weiss Green's function

The simplification of the expression

$$\mathcal{G}_{0,\sigma}^{-1}(i\omega_n) = i\omega_n + \mu - \int_{-\infty}^{\infty} d\varepsilon \rho(\varepsilon) \frac{\varepsilon^2}{\vartheta - \varepsilon} + \frac{\left[ \int_{-\infty}^{\infty} d\varepsilon \rho(\varepsilon) \frac{\varepsilon}{\vartheta - \varepsilon} \right]^2}{\int_{-\infty}^{\infty} d\varepsilon \rho(\varepsilon) \frac{1}{\vartheta - \varepsilon}} \quad (\text{F.1})$$

is based on transformations concerning the integrals. Beginning with a variable transformation  $\vartheta - \varepsilon = x$  the integrals are rewritten in the following way

$$\begin{aligned} \int_{-\infty}^{\infty} d\varepsilon \rho(\varepsilon) \frac{\varepsilon^2}{\vartheta - \varepsilon} &= \int_{-\infty}^{\infty} dx \rho(\vartheta - x) \frac{(\vartheta - x)^2}{x} = \int_{-\infty}^{\infty} dx \rho(\vartheta - x) \frac{(\vartheta^2 - 2\vartheta x + x^2)}{x} \\ &= \vartheta^2 \int_{-\infty}^{\infty} dx \rho(\vartheta - x) \frac{1}{x} - 2\vartheta \int_{-\infty}^{\infty} dx \rho(\vartheta - x) + \int_{-\infty}^{\infty} dx \rho(\vartheta - x) x \\ &= \vartheta^2 a - 2\vartheta + \vartheta = \vartheta^2 a - \vartheta, \end{aligned}$$

where we introduced the new variable  $a = \int_{-\infty}^{\infty} dx \rho(\vartheta - x)/x$ . In the last step we used the fact that the density of states is normalized and consequently  $\int_{-\infty}^{\infty} dx \rho(\vartheta - x) = \int_{-\infty}^{\infty} d\varepsilon \rho(\varepsilon) = 1$ . Additionally, the value of the third integral is obtained performing the inverse transformation and making use of the integration properties of a point-symmetric function  $\int dx \rho(\vartheta - x)x = \int d\varepsilon \rho(\varepsilon)(\vartheta - \varepsilon) = \vartheta$ . Analogously,

$$\int_{-\infty}^{\infty} d\varepsilon \rho(\varepsilon) \frac{\varepsilon}{\vartheta - \varepsilon} = \int_{-\infty}^{\infty} dx \rho(\vartheta - x) \frac{\vartheta - x}{x} = \vartheta a - 1.$$

and

$$\int_{-\infty}^{\infty} d\varepsilon \rho(\varepsilon) \frac{1}{\vartheta - \varepsilon} = \int_{-\infty}^{\infty} dx \rho(\vartheta - x) \frac{1}{x} = a.$$

Substituting the integrals in Eq. (F.1) using these identities leads to

$$\begin{aligned}
 \mathcal{G}_{0,\sigma}^{-1}(i\omega_n) &= i\omega_n + \mu - \vartheta^2 a + \vartheta + \frac{(\vartheta a - 1)^2}{a} \\
 &= i\omega_n + \mu - \vartheta^2 a + \vartheta + \vartheta^2 a - 2\vartheta + \frac{1}{a} \\
 &= i\omega_n + \mu - \vartheta + \frac{1}{a} \\
 &= \Sigma_\sigma(i\omega_n) + \left[ \int_{-\infty}^{\infty} dx \rho(\vartheta - x) \frac{1}{x} \right]^{-1},
 \end{aligned}$$

where, in the last step, we inserted the definition  $\vartheta = i\omega_n + \mu - \Sigma_\sigma(i\omega_n)$  (see Sec. 6.5.1). The inverse transformation  $x \rightarrow \varepsilon$  leads to the desired result

$$\mathcal{G}_{0,\sigma}^{-1}(i\omega_n) = \Sigma_\sigma(i\omega_n) + \left[ \int_{-\infty}^{\infty} d\varepsilon \rho(\varepsilon) \frac{1}{i\omega_n + \mu - \Sigma_\sigma(i\omega_n) - \varepsilon} \right]^{-1}.$$



## G. Properties of a localized state

The goal of this appendix is the calculation of the inverse participation ratio (IPR) of a localized state for infinite and finite non-interacting systems. The scaling of  $I(\omega)$  with the system size will be also derived.

To begin we start with the description of a wave function  $\psi(\mathbf{r})$  corresponding to a localized state. In a perfect periodic system we know that the eigenstates can be plane, running or standing waves with a fixed wavenumber, but as soon as disorder is introduced into the system the situation changes. The degeneracy vanishes and eigenstates become real and exponentially localized<sup>1</sup>. Without loss of generality we consider a wave function of a state belonging to an energy  $\omega$  localized at site  $\mathbf{r}_0$  in the origin. The amplitude of this wave function is expected to be maximal at position  $\mathbf{r}_0$ , where the particle is bound to, and to fall off exponentially away from this site characterized by localization length  $\xi(\omega)$  (for better readability we drop the explicit dependence of  $\omega$  in the following):

$$|\psi(\mathbf{r})|^2 = \frac{1}{\xi} e^{-\frac{2|\mathbf{r}-\mathbf{r}_0|}{\xi}}. \quad (\text{G.1})$$

Our goal is to calculate the IPR in a non-interacting system given the definition (see Sec. 6.3.7)

$$I = \sum_i |\psi_i|^4 = \int d^D \mathbf{r} |\psi(\mathbf{r})|^4, \quad (\text{G.2})$$

whereby we substitute the summation over the lattice sites by the integration leaving the dimensionality of the system unspecified. For the sake of simplicity we would like to consider 1D systems in the following derivations, however, since higher dimensional problems are solved analogously, an extension to  $D$  dimensions can be easily done by the reader.

---

<sup>1</sup>This is true for any finite disorder strength in 1D and 2D systems and for a sufficiently large disorder exceeding a critical value in 3D.

First we verify that the amplitude of the wave function Eq. (G.1) is normalized in an infinite system

$$\begin{aligned} \int_{-\infty}^{\infty} dx |\psi(x)|^2 &= \frac{1}{\xi} \int_{-\infty}^{\infty} dx e^{-\frac{2|x|}{\xi}} = \frac{1}{\xi} \left[ \int_{-\infty}^0 dx e^{\frac{2x}{\xi}} + \int_0^{\infty} dx e^{-\frac{2x}{\xi}} \right] \\ &= \frac{1}{\xi} \frac{\xi}{2} \left[ e^{\frac{2x}{\xi}} \Big|_{-\infty}^0 - e^{-\frac{2x}{\xi}} \Big|_{-\infty}^0 \right] = \frac{1}{2} [1 + 1] = 1 \quad \text{q.e.d.} \end{aligned}$$

From here the inverse participation ratio in infinite systems results in

$$I_{\infty} = \int_{-\infty}^{\infty} |\psi(x)|^4 dx = \frac{1}{\xi^2} \int_{-\infty}^{\infty} e^{-\frac{4|x|}{\xi}} dx = \frac{1}{2\xi}. \quad (\text{G.3})$$

As expected from the interpretation, IPR gives the inverse number of sites the state is spread over, which is proportional to the localization length  $\xi$ .

For finite systems the calculations have to be corrected since the integrated probability density must be 1 within a given system size  $L$ . Particularly, the normalization condition requires

$$\begin{aligned} \frac{1}{A_L} \int_{-L}^L dx |\psi(x)|^2 &= \frac{1}{A_L} \frac{1}{\xi} \int_{-L}^L dx e^{-\frac{2|x|}{\xi}} = \frac{1}{A_L} (1 - e^{-2\frac{L}{\xi}}) \stackrel{!}{=} 1 \\ \Leftrightarrow A_L &= 1 - e^{-2\frac{L}{\xi}}. \end{aligned}$$

With the normalized finite size wave function amplitude  $|\psi_L(x)|^2 = |\psi(x)|^2/A_L$  the IPR in finite systems is

$$\begin{aligned} I_L &= \int_{-L}^L |\psi_L(x)|^4 dx \\ &= \frac{1}{A_L^2} \frac{1}{\xi^2} \int_{-L}^L dx e^{-\frac{4|x|}{\xi}} \\ &= \frac{1}{2\xi} \frac{1 + e^{-2L/\xi}}{1 - e^{-2L/\xi}} \\ &= \frac{1}{2\xi} \coth\left(\frac{L}{\xi}\right). \end{aligned} \quad (\text{G.4})$$

Consequently, in the thermodynamic limit IPR tends to  $\lim_{L \rightarrow \infty} I_L = I_{\infty} = 1/2\xi$ , which perfectly agrees with Eq. (G.3) and corresponds to the given result in the Sec. 6.3.7. The functional dependency on the lattice size is given by  $\coth(L/\xi)$ . It is important to note that in this derivation periodic boundary conditions were assumed. Hence, in finite systems the effects of open boundary condition may lead to deviations from  $L$ -dependency derived above for small  $L$ .

## H. Sampling of the Hubbard parameter distributions

To realistically model experimental setups, the Hubbard parameter  $t_{ij}$  and  $U_i$  have to be carefully estimated. We perform our calculations for  $^{40}\text{K}$ , as this is one of the commonly used fermionic species in ultracold experiments. For our PDF we take data calculated by Zhou and Ceperley [235], which was determined from a comparable experiment on  $^{87}\text{Rb}$ , and appropriately modify it. Since the hopping and interaction parameters depend only on the single particle states and are independent of bosonic or fermionic statistics, the data obtained for bosonic species can be rescaled corresponding to the setup investigated here: laser wavelength  $\lambda = 738$  nm and lattice depth (in units of recoil energy)  $s = 10$ .

In particular, for a given lattice depth the hopping and interaction strength following from band calculations [75] are used. The extracted  $U$  is rescaled based on the functional dependency Eq. (3.57) for laser wavelength  $\lambda = 738$  nm and possible scattering lengths for  $^{40}\text{K}$ . This interaction strength determines the most probable value of the distribution  $\mathcal{P}_{\varepsilon,U}(\varepsilon_i, U_i)$ . The variation of the distribution should be proportional to the  $s_D$  chosen. Thus, the distribution extracted from the data of Zhou and Ceperley is rescaled to account for these requirements. Afterwards, given  $\varepsilon_i$  the local interaction strength  $U_i$  is sampled from the conditional PDF  $\mathcal{P}_U(U_i|\varepsilon_i)$ .

Similarly to the interaction, the hopping amplitude is extracted from calculated parameters [75]. As  $t$  depends only on the lattice depth (see Eq. (3.39)) it does not need to be rescaled and constitutes the most probable value of the conditional PDF, which will be constructed next. In contrast to the interaction, the tunneling amplitude depends on the energy difference between two neighboring sites  $\Delta\varepsilon_{ij} = \varepsilon_i - \varepsilon_j$  rather than on the respective on-site energy. For this reason, a conditional PDF was obtained from the data in [235]: For 200 discrete values of  $\Delta\varepsilon$  a histogram approximating  $\mathcal{P}_t(t_{ij}|\Delta\varepsilon_{ij})$  was extracted. Integration of this distribution with respect to  $t_{ij}$  yields the conditional cumulative  $F_t(t_{ij}|\Delta\varepsilon_{ij})$ , which has to be normalized according to the condition  $\lim_{t \rightarrow \infty} F_t(t_{ij}|\Delta\varepsilon_{ij}) = 1$ . The cumulative inverted with respect to  $t_{ij}$  constitutes the desired PDF  $\mathcal{P}_t(t_{ij}|\Delta\varepsilon_{ij})$ . Based on this, a hopping amplitude  $t_{ij}$  is obtained for a fixed  $\Delta\varepsilon_{ij}$ .

The appropriate numerical routines were implemented by U. Bissbort.



# Bibliography

- [1] S. N. Bose, “Plancks Gesetz und Lichtquantenhypothese,” Z. Phys., vol. 26, pp. 178–181, 1924.
- [2] Quantentheorie des einatomigen idealen Gases. Sitzungsber. Preuss. Akad. Wiss, 1925.
- [3] M. H. Anderson, J. R. Ensher, M. R. Matthews, C. E. Wieman, and E. A. Cornell, “Observation of Bose-Einstein condensation in a dilute atomic vapor,” Science, vol. 269, p. 198, 1995.
- [4] K. B. Davis, M. O. Mewes, M. R. Andrews, N. J. van Druten, D. S. Durfee, D. M. Kurn, and W. Ketterle, “Bose-Einstein condensation in a gas of sodium atoms,” Phys. Rev. Lett., vol. 75, pp. 3969–3973, Nov 1995.
- [5] E. Fermi, “Sulla quantizzazione del gas perfetto monoatomico,” Rendiconti Lincei, vol. 3, 1926.
- [6] P. A. M. Dirac, “On the theory of quantum mechanics,” Proc. Phys. Soc. London. Series A, vol. 112, no. 762, pp. 661–677, 1926.
- [7] B. DeMarco and D. S. Jin, “Onset of Fermi degeneracy in a trapped atomic gas,” Science, vol. 285, no. 5434, pp. 1703–1706, 1999.
- [8] Hubbard J., “Electron correlations in narrow energy bands,” P. Roy. Soc. Lond. A Mat., vol. 276, p. 238, 1963.
- [9] M. P. A. Fisher, P. B. Weichman, G. Grinstein, and D. S. Fisher, “Boson localization and the superfluid-insulator transition,” Phys. Rev. B, vol. 40, pp. 546–570, Jul 1989.
- [10] D. Jaksch, C. Bruder, J. I. Cirac, C. W. Gardiner, and P. Zoller, “Cold bosonic atoms in optical lattices,” Phys. Rev. Lett., vol. 81, pp. 3108–3111, Oct 1998.
- [11] J. Hubbard, “Electron correlations in narrow energy bands. III. an improved solution,” P. Roy. Soc. Lond. A Mat., vol. 281, p. 401, 1964.
- [12] M. Greiner, O. Mandel, T. Esslinger, T. W. Hänsch, and I. Bloch, “Quantum phase transition from a superfluid to a Mott insulator in a gas of ultracold atoms,” Nature, vol. 415, 2002.
- [13] R. Jördens, N. Strohmaier, K. Günter, H. Moritz, and T. Esslinger, “A Mott insulator of fermionic atoms in an optical lattice,” Nature, vol. 455, p. 204, 2008.
- [14] U. Schneider, L. Hackermüller, S. Will, T. Best, I. Bloch, T. A. Costi, R. W. Helmes, D. Rasch, and A. Rosch, “Metallic and insulating phases of repulsively interacting Fermions in a 3d optical lattice,” Science, vol. 322, no. 5907, pp. 1520–1525, 2008.

- [15] I. Titvinidze, M. Snoek, and W. Hofstetter, “Supersolid Bose-Fermi mixtures in optical lattices,” *Phys. Rev. Lett.*, vol. 100, no. 10, p. 100401, 2008.
- [16] H. P. Büchler and G. Blatter, “Supersolid versus phase separation in atomic Bose-Fermi mixtures,” *Phys. Rev. Lett.*, vol. 91, p. 130404, Sep 2003.
- [17] A. Hubener, M. Snoek, and W. Hofstetter, “Magnetic phases of two-component ultracold bosons in an optical lattice,” *Phys. Rev. B*, vol. 80, p. 245109, Dec 2009.
- [18] S. G. Soyler, B. Capogrosso-Sansone, N. V. Prokof’ev, and B. V. Svistunov, “Sign-alternating interaction mediated by strongly-correlated lattice bosons,” *New J. Phys.*, vol. 11, no. 7, p. 073036, 2009.
- [19] S. Trotzky, P. Cheinet, S. Fölling, M. Feld, U. Schnorrberger, A. M. Rey, A. Polkovnikov, E. A. Demler, M. D. Lukin, and I. Bloch, “Time-resolved observation and control of superexchange interactions with ultracold atoms in optical lattices,” *Science*, vol. 319, no. 5861, pp. 295–299, 2008.
- [20] J. Catani, L. D. Sarlo, G. Barontini, F. Minardi, and M. Inguscio, “Degenerate Bose-Bose mixture in a three-dimensional optical lattice,” *Phys. Rev. A*, vol. 77, 2008.
- [21] T.-L. Ho and Q. Zhou, “Intrinsic heating and cooling in adiabatic processes for bosons in optical lattices,” *Phys. Rev. Lett.*, vol. 99, p. 120404, Sep 2007.
- [22] B. L. Tolra, K. M. O’Hara, J. H. Huckans, W. D. Phillips, S. L. Rolston, and J. V. Porto, “Observation of reduced three-body recombination in a correlated 1d degenerate Bose gas,” *Phys. Rev. Lett.*, vol. 92, p. 190401, May 2004.
- [23] P. R. Johnson, E. Tiesinga, J. V. Porto, and C. J. Williams, “Effective three-body interactions of neutral bosons in optical lattices,” *New J. Phys.*, vol. 11, no. 9, p. 093022, 2009.
- [24] T. Best, S. Will, U. Schneider, L. Hackermüller, D. van Oosten, I. Bloch, and D.-S. Lühmann, “Role of interactions in  $^{87}\text{Rb}$ - $^{40}\text{K}$  Bose-Fermi mixtures in a 3d optical lattice,” *Phys. Rev. Lett.*, vol. 102, no. 3, p. 030408, 2009.
- [25] A. J. Daley, J. M. Taylor, S. Diehl, M. Baranov, and P. Zoller, “Atomic three-body loss as a dynamical three-body interaction,” *Phys. Rev. Lett.*, vol. 102, p. 040402, Jan 2009.
- [26] J. Zakrzewski, “Mean-field dynamics of the superfluid-insulator phase transition in a gas of ultracold atoms,” *Phys. Rev. A*, vol. 71, p. 043601, Apr 2005.
- [27] P. Buonsante, S. M. Giampaolo, F. Illuminati, V. Penna, and A. Vezzani, “Mixtures of strongly interacting bosons in optical lattices,” *Phys. Rev. Lett.*, vol. 100, no. 24, p. 240402, 2008.
- [28] J. Zakrzewski and D. Delande, “Breakdown of adiabaticity when loading ultracold atoms in optical lattices,” *Phys. Rev. A*, vol. 80, p. 013602, Jul 2009.
- [29] J. Wernsdorfer, M. Snoek, and W. Hofstetter, “Lattice-ramp-induced dynamics in an interacting Bose-Bose mixture,” *Phys. Rev. A*, vol. 81, p. 043620, Apr 2010.
- [30] T. Stöferle, H. Moritz, C. Schori, M. Köhl, and T. Esslinger, “Transition from a strongly interacting 1d superfluid to a Mott insulator,” *Phys. Rev. Lett.*, vol. 92, p. 130403, Mar 2004.

- [31] C. Kollath, A. Iucci, T. Giamarchi, W. Hofstetter, and U. Schollwöck, “Spectroscopy of ultracold atoms by periodic lattice modulations,” *Phys. Rev. Lett.*, vol. 97, p. 050402, Jul 2006.
- [32] L. Hackermüller, U. Schneider, M. Moreno-Cardoner, T. Kitagawa, T. Best, S. Will, E. Demler, E. Altman, I. Bloch, and B. Paredes, “Anomalous expansion of attractively interacting fermionic atoms in an optical lattice,” *Science*, vol. 327, no. 5973, pp. 1621–1624, 2010.
- [33] M. Rigol and A. Muramatsu, “Emergence of quasicondensates of hard-core bosons at finite momentum,” *Phys. Rev. Lett.*, vol. 93, p. 230404, Dec 2004.
- [34] M. Rigol and A. Muramatsu, “Free expansion of impenetrable bosons on one-dimensional optical lattices,” *Mod. Phys. Lett. B*, vol. 19, no. 18, pp. 861–881, 2005.
- [35] I. Hen and M. Rigol, “Strongly interacting atom lasers in three-dimensional optical lattices,” *Phys. Rev. Lett.*, vol. 105, p. 180401, Oct 2010.
- [36] W. de Haas, J. de Boer, and G. van den Berg, “The electrical resistance of gold, copper and lead at low temperatures,” *Physica*, vol. 1, no. 7–12, pp. 1115 – 1124, 1934.
- [37] A. C. Hewson, *The Kondo problem to heavy Fermions*. Cambridge university press, 2 ed., 1997.
- [38] J. Kondo, “Resistance minimum in dilute magnetic alloys,” *Prog. Theoret. Phys.*, vol. 32, no. 1, pp. 37–49, 1964.
- [39] P. W. Anderson, “Absence of diffusion in certain random lattices,” *Phys. Rev.*, vol. 109, pp. 1492–1505, Mar 1958.
- [40] J. Billy, V. Josse, Z. Zuo, A. Bernard, B. Hambrecht, P. Lugan, D. Clement, L. S. Palencia, P. Bouyer, and A. Aspect, “Direct observation of Anderson localization of matter waves in a controlled disorder,” *Nature*, vol. 453, p. 891, 2008.
- [41] G. Roati, C. D’Errico, L. Fallani, M. Fattori, C. Fort, M. Zaccanti, G. Modugno, M. Modugno, and M. Inguscio, “Anderson localization of a non-interacting Bose-Einstein condensate,” *Nature*, vol. 453, pp. 895–898, 2008.
- [42] S. R. White, “Density matrix renormalization group algorithms with a single center site,” *Phys. Rev. B*, vol. 72, p. 180403, Nov 2005.
- [43] L. Fallani, J. E. Lye, V. Guarrera, C. Fort, and M. Inguscio, “Ultracold atoms in a disordered crystal of light: Towards a Bose glass,” *Phys. Rev. Lett.*, vol. 98, p. 130404, Mar 2007.
- [44] K. Byczuk, W. Hofstetter, and D. Vollhardt, “Mott-Hubbard transition versus Anderson localization in correlated electron systems with disorder,” *Phys. Rev. Lett.*, vol. 94, p. 056404, Feb 2005.
- [45] G. Roux, T. Barthel, I. P. McCulloch, C. Kollath, U. Schollwöck, and T. Giamarchi, “Quasiperiodic Bose-Hubbard model and localization in one-dimensional cold atomic gases,” *Phys. Rev. A*, vol. 78, p. 023628, Aug 2008.

- [46] U. Bissbort, R. Thomale, and W. Hofstetter, “Stochastic mean-field theory: Method and application to the disordered Bose-Hubbard model at finite temperature and speckle disorder,” Phys. Rev. A, vol. 81, p. 063643, Jun 2010.
- [47] L. Pollet, N. V. Prokof’ev, B. V. Svistunov, and M. Troyer, “Absence of a direct superfluid to Mott insulator transition in disordered Bose systems,” Phys. Rev. Lett., vol. 103, p. 140402, Sep 2009.
- [48] K. Byczuk, W. Hofstetter, U. Yu, and D. Vollhardt, “Correlated electrons in the presence of disorder,” Eur. Phys. J. Special Topics, vol. 180, pp. 135–151, 2009.
- [49] K. Byczuk, W. Hofstetter, and D. Vollhardt, “Competition between Anderson localization and antiferromagnetism in correlated lattice Fermion systems with disorder,” Phys. Rev. Lett., vol. 102, p. 146403, Apr 2009.
- [50] D. Semmler, K. Byczuk, and W. Hofstetter, “Mott-Hubbard and Anderson metal-insulator transitions in correlated lattice fermions with binary disorder,” Phys. Rev. B, vol. 81, p. 115111, Mar 2010.
- [51] D. Semmler, J. Wernsdorfer, U. Bissbort, K. Byczuk, and W. Hofstetter, “Localization of correlated fermions in optical lattices with speckle disorder,” Phys. Rev. B, vol. 82, p. 235115, Dec 2010.
- [52] S. Anissimova, S. V. Kravchenko, A. Punnoose, A. M. Finkel’stein, and T. M. Klapwijk, “Flow diagram of the metal–insulator transition in two dimensions,” Nat. Phys., vol. 3, pp. 707 – 710, 2007.
- [53] V. Dobrosavljević and G. Kotliar, “Mean field theory of the Mott-Anderson transition,” Phys. Rev. Lett., vol. 78, pp. 3943–3946, May 1997.
- [54] V. Dobrosavljević, A. A. Pastor, and B. K. Nikolić, “Typical medium theory of Anderson localization: A local order parameter approach to strong-disorder effects,” Europhys. Lett., vol. 62, pp. 76–82, 2003.
- [55] T. Giamarchi and H. J. Schulz, “Anderson localization and interactions in one-dimensional metals,” Phys. Rev. B, vol. 37, pp. 325–340, Jan 1988.
- [56] H. Pang, S. Liang, and J. F. Annett, “Effect of randomness on the Mott state,” Phys. Rev. Lett., vol. 71, pp. 4377–4380, Dec 1993.
- [57] D. J. Schwab and S. Chakravarty, “Glassy states in fermionic systems with strong disorder and interactions,” Phys. Rev. B, vol. 79, p. 125102, Mar 2009.
- [58] M. C. O. Aguiar, V. Dobrosavljević, E. Abrahams, and G. Kotliar, “Critical behavior at the Mott-Anderson transition: A typical-medium theory perspective,” Phys. Rev. Lett., vol. 102, no. 15, p. 156402, 2009.
- [59] Y. Song, R. Wortis, and W. A. Atkinson, “Dynamical mean field study of the two-dimensional disordered Hubbard model,” prb, vol. 77, no. 5, p. 054202, 2008.
- [60] A. Punnoose and A. M. Finkel’stein, “Metal-insulator transition in disordered two-dimensional electron systems,” Science, vol. 310, no. 5746, pp. 289–291, 2005.
- [61] E. Abrahams, P. W. Anderson, D. C. Licciardello, and T. V. Ramakrishnan, “Scaling theory of localization: Absence of quantum diffusion in two dimensions,” Phys. Rev. Lett., vol. 42, pp. 673–676, Mar 1979.



- [62] B. L. Altshuler, A. G. Aronov, and P. A. Lee, "Interaction effects in disordered Fermi systems in two dimensions," Phys. Rev. Lett., vol. 44, pp. 1288–1291, May 1980.
- [63] B. Tanatar and D. M. Ceperley, "Ground state of the two-dimensional electron gas," Phys. Rev. B, vol. 39, pp. 5005–5016, Mar 1989.
- [64] R. Grimm, M. Weidemüller, and Y. B. Ovchinnikov, "Optical dipole traps for neutral atoms," Adv. Atom. Mol. Phys., vol. 42, p. 95.
- [65] H. J. Metcalf and P. van der Straten, "Laser cooling and trapping of atoms," J. Opt. Soc. Am. B, vol. 20, pp. 887–908, May.
- [66] D. E. Pritchard, E. L. Raab, V. Bagnato, C. E. Wieman, and R. N. Watts, "Light traps using spontaneous forces," Phys. Rev. Lett., vol. 57, pp. 310–313, Jul 1986.
- [67] E. L. Raab, M. Prentiss, A. Cable, S. Chu, and D. E. Pritchard, "Trapping of neutral sodium atoms with radiation pressure," Phys. Rev. Lett., vol. 59, pp. 2631–2634, Dec 1987.
- [68] A. L. Migdall, J. V. Prodan, W. D. Phillips, T. H. Bergeman, and H. J. Metcalf, "First observation of magnetically trapped neutral atoms," Phys. Rev. Lett., vol. 54, pp. 2596–2599, Jun 1985.
- [69] T. Bergeman, G. Erez, and H. J. Metcalf, "Magnetostatic trapping fields for neutral atoms," Phys. Rev. A, vol. 35, pp. 1535–1546, Feb 1987.
- [70] J. D. Jackson, Classical electrodynamics (3rd edition). Wiley, New York, 1998.
- [71] J. D. Miller, R. A. Cline, and D. J. Heinzen, "Photoassociation spectrum of ultracold Rb atoms," Phys. Rev. Lett., vol. 71, pp. 2204–2207, Oct 1993.
- [72] J. D. Miller, R. A. Cline, and D. J. Heinzen, "Far-off-resonance optical trapping of atoms," Phys. Rev. A, vol. 47, pp. R4567–R4570, Jun 1993.
- [73] Z. Hadzibabic, S. Stock, B. Battelier, V. Bretin, and J. Dalibard, "Interference of an array of independent Bose-Einstein condensates," Phys. Rev. Lett., vol. 93, p. 180403, Oct 2004.
- [74] S. Peil, J. V. Porto, B. L. Tolra, J. M. Obrecht, B. E. King, M. Subbotin, S. L. Rolston, and W. D. Phillips, "Patterned loading of a Bose-Einstein condensate into an optical lattice," Phys. Rev. A, vol. 67, p. 051603, May 2003.
- [75] M. Greiner, Ultracold quantum gases in three-dimensional optical lattice potentials. PhD thesis, Ludwig-Maximilians-Universität München, 2003.
- [76] I. Bloch and M. Greiner, "Exploring quantum matter with ultracold atoms in optical lattices," Adv. At. Mol. Phys., vol. 52, pp. 1–47, 2005.
- [77] N. W. Ashcroft and N. D. Mermin, Solid state physics. Holt, Rinehardt and Winston, 1976.
- [78] W. Nolting, Grundkurs Theoretische Physik 7.: Viel-Teilchen-Theorie. Springer Verlag, 2002.
- [79] R. Bong, ed., Fundamentals and new frontiers of Bose-Einstein condensation. World Scientific Publishing Co. Pte. Ltdl, 2010.

- [80] D.-S. Lühmann, K. Bongs, K. Sengstock, and D. Pfannkuche, “Self-trapping of bosons and fermions in optical lattices,” Phys. Rev. Lett., vol. 101, p. 050402, Jul 2008.
- [81] R. M. Lutchyn, S. Tewari, and S. Das Sarma, “Loss of superfluidity by fermions in the boson Hubbard model on an optical lattice,” Phys. Rev. A, vol. 79, p. 011606, Jan 2009.
- [82] W. Zwerger, “Mott–Hubbard transition of cold atoms in optical lattices,” J. Opt. B.-Quantum S. O., vol. 5, no. 2, p. S9, 2003.
- [83] J. C. Slater, “A soluble problem in energy bands,” Phys. Rev., vol. 87, pp. 807–835, Sep 1952.
- [84] M. Abramowitz and I. A. Stegun, Handbook of mathematical functions. United States department of commerce, 1972.
- [85] E. Chalbaud, J.-P. Gallinar, , and G. Mata, “The quantum harmonic oscillator on a lattice,” J. Phys. A, vol. 19, p. L385, 1986.
- [86] J. Gallinar and E. Chalbaud, “Harmonic oscillator on a lattice in a constant force field and associated bloch oscillations,” Phys. Rev. B, vol. 43, p. 2322, 1991.
- [87] C. Hooley and J. Quintanilla, “Single-atom density of states of an optical lattice,” Phys. Rev. Lett., vol. 93, p. 080404, Aug 2004.
- [88] G. F. Gribakin and V. V. Flambaum, “Calculation of the scattering length in atomic collisions using the semiclassical approximation,” Phys. Rev. A, vol. 48, pp. 546–553, Jul 1993.
- [89] H. Feshbach, “Unified theory of nuclear reactions,” Ann. Phys.-New York, vol. 5, no. 4, pp. 357–390, 1958.
- [90] J. M. Blatt and V. F. Weisskopf, Theoretical nuclear physics. John Wiley and Sons, Inc., New York, 1952.
- [91] K. Huang and C. N. Yang, “Quantum-mechanical many-body problem with hard-sphere interaction,” Phys. Rev., vol. 105, pp. 767–775, Feb 1957.
- [92] S. Will, T. Best, U. Schneider, L. Hackermüller, D. S. Lühmann, and I. Bloch, “Time-resolved observation of coherent multi-body interactions in quantum phase revivals,” Nature, vol. 465, pp. 197 – 201, 2010.
- [93] T. Krämer, M. Mark, P. Waldburger, J. G. Danzl, C. Chin, B. Engeser, A. D. Lange, K. Pilch, A. Jaakkola, H.-C. Nägerl, and R. Grimm, “Evidence for efimov quantum states in an ultracold gas of caesium atoms,” Nature, vol. 440, pp. 31–318, 2006.
- [94] S. Knoop, F. Ferlaino, M. Mark, M. Berninger, H. Schöbel, H.-C. Nägerl, and R. Grimm, “Observation of an efimov-like trimer resonance in ultracold atom-dimer scattering,” Nat. Phys., vol. 5, pp. 227 – 230, 2009.
- [95] M. Zaccanti, B. Deissler, C. D’Errico, M. Fattori, M. Jona-Lasinio, S. MÃijller, G. Roati, M. Inguscio, and G. Modugno, “Observation of an efimov spectrum in an atomic system,” Nat. Phys., vol. 5, pp. 586–591, 2009.

- [96] J. Li, Y. Yu, A. M. Dudarev, and Q. Niu, "Interaction broadening of wannier functions and Mott transitions in atomic bec," *New J. Phys.*, vol. 8, no. 8, p. 154, 2006.
- [97] M. Greiner, O. Mandel, T. W. Hänsch, and I. Bloch, "Collapse and revival of the matter wave field of a Bose-Einstein condensate," *Nature*, vol. 419, pp. 51–54, 2002.
- [98] D.-S. Luehmann, O. Juergensen, and K. Sengstock, "Multi-orbital and density-induced tunneling of bosons in optical lattices," 2011.
- [99] T. Müller, S. Fölling, A. Widera, and I. Bloch, "State preparation and dynamics of ultracold atoms in higher lattice orbitals," *Phys. Rev. Lett.*, vol. 99, p. 200405, Nov 2007.
- [100] L.-M. Duan, E. Demler, and M. D. Lukin, "Controlling spin exchange interactions of ultracold atoms in optical lattices," *Phys. Rev. Lett.*, vol. 91, p. 090402, Aug 2003.
- [101] E. Altman, W. Hofstetter, E. Demler, and M. D. Lukin, "Phase diagram of two-component bosons on an optical lattice," *New J. Phys.*, vol. 5, no. 1, pp. 113–113, 2003.
- [102] A. Isacsson, M.-C. Cha, K. Sengupta, and S. M. Girvin, "Superfluid-insulator transitions of two-species bosons in an optical lattice," *Phys. Rev. B*, vol. 72, p. 184507, Nov 2005.
- [103] V. W. Scarola and S. Das Sarma, "Quantum phases of the extended Bose-Hubbard Hamiltonian: Possibility of a supersolid state of cold atoms in optical lattices," *Phys. Rev. Lett.*, vol. 95, p. 033003, Jul 2005.
- [104] C. Bruder, R. Fazio, and G. Schön, "Superconductor–Mott-insulator transition in Bose systems with finite-range interactions," *Phys. Rev. B*, vol. 47, pp. 342–347, Jan 1993.
- [105] A. van Otterlo and K.-H. Wagenblast, "Coexistence of diagonal and off-diagonal long-range order: A Monte Carlo study," *Phys. Rev. Lett.*, vol. 72, pp. 3598–3601, May 1994.
- [106] G. G. Batrouni, R. T. Scalettar, G. T. Zimanyi, and A. P. Kampf, "Supersolids in the Bose-Hubbard Hamiltonian," *Phys. Rev. Lett.*, vol. 74, pp. 2527–2530, Mar 1995.
- [107] K. Góral, L. Santos, and M. Lewenstein, "Quantum phases of dipolar bosons in optical lattices," *Phys. Rev. Lett.*, vol. 88, p. 170406, Apr 2002.
- [108] I. Bloch, J. Dalibard, and W. Zwerger, "Many body physics with ultracold atoms," *Rev. Mod. Phys.*, vol. 80, 2008.
- [109] X. Lu and Y. Yu, "Finite-temperature effects on the number fluctuation of ultracold atoms across the superfluid–to–Mott-insulator transition," *Phys. Rev. A*, vol. 74, p. 063615, Dec 2006.
- [110] G. Pupillo, C. J. Williams, and N. V. Prokof'ev, "Effects of finite temperature on the Mott-insulator state," *Phys. Rev. A*, vol. 73, p. 013408, Jan 2006.
- [111] S. Trotzky, L. Pollet, F. Gerbier, U. Schnorrberger, I. Bloch, N. V. Prokof'ev, B. Svistunov, and M. Troyer, "Suppression of the critical temperature for superfluidity near the Mott transition," *Nat. Phys.*, vol. 6, pp. 998–1004, 2010.

- [112] Superfluids I: Macroscopic theory of superconductivity. Wiley, New York, 1950.
- [113] Superfluids II: Macroscopic theory of superfluid helium. Wiley, New York, 1954.
- [114] N. H. T. M. P. Minguzzi, A. March, “Superfluidity with and without a condensate in interacting Bose fluids,” Phys. Chem. Liq., vol. 41, pp. 323–335, 2003.
- [115] A. J. Leggett, “Superfluidity,” Rev. Mod. Phys., vol. 71, pp. S318–S323, Mar 1999.
- [116] W. S. Bakr, J. I. Gillen, A. Peng, S. Fölling, and M. Greiner, “A quantum gas microscope for detecting single atoms in a Hubbard-regime optical lattice,” Nature, vol. 462, pp. 74–77, 2009.
- [117] W. S. Bakr, A. Peng, M. E. Tai, R. Ma, J. Simon, J. I. Gillen, S. Fölling, L. Pollet, and M. Greiner, “Probing the superfluid–Mott insulator transition at the single-atom level,” Science, 2010.
- [118] J. F. Sherson, C. Weitenberg, M. Endres, M. Cheneau, I. Bloch, and S. Kuhr, “Single-atom-resolved fluorescence imaging of an atomic Mott insulator,” Nature, vol. 467, pp. 68–72, 2010.
- [119] O. Penrose and L. Onsager, “Bose-Einstein condensation and liquid helium,” Phys. Rev., vol. 104(3), pp. 576–584, 1956.
- [120] A. J. Leggett, “Bose-Einstein condensation in the alkali gases: Some fundamental concepts,” Rev. Mod. Phys., vol. 73, pp. 307–356, Apr 2001.
- [121] A. Lenard, “Momentum distribution in the ground state of the one-dimensional system of impenetrable bosons,” J. Math. Phys., vol. 5, p. 930, 1964.
- [122] A. Lenard, “One-dimensional impenetrable bosons in thermal equilibrium,” J. Math. Phys., vol. 7, p. 1268, 1966.
- [123] H. G. Vaidya and C. A. Tracy Phys. Rev. Lett., vol. 47, p. 1840, 1981.
- [124] K. Sheshadri, H. R. Krishnamurthy, R. Pandit, and T. V. Ramakrishnan, “Superfluid and insulating phases in an interacting-boson model: Mean-field theory and the RPA,” Europhys. Lett., vol. 22, no. 4, p. 257, 1993.
- [125] B. Capogrosso-Sansone, N. V. Prokof’ev, and B. V. Svistunov, “Phase diagram and thermodynamics of the three-dimensional Bose-Hubbard model,” Phys. Rev. B, vol. 75, p. 134302, Apr 2007.
- [126] V. A. Kashurnikov, N. V. Prokof’ev, and B. V. Svistunov, “Revealing the superfluid–Mott-insulator transition in an optical lattice,” Phys. Rev. A, vol. 66, p. 031601, Sep 2002.
- [127] E. Toth, A. M. Rey, and P. B. Blakie, “Theory of correlations between ultracold bosons released from an optical lattice,” Phys. Rev. A, vol. 78, p. 013627, Jul 2008.
- [128] E. Altman, E. Demler, and M. D. Lukin, “Probing many-body states of ultracold atoms via noise correlations,” Phys. Rev. A, vol. 70, p. 013603, Jul 2004.
- [129] S. Fölling, F. Gerbier, A. Widera, O. Mandel, T. Gericke, and I. Bloch, “Spatial quantum noise interferometry in expanding ultracold atom clouds,” Nature, vol. 434, pp. 481–484, 2005.

- [130] T. Rom, T. Best, D. van Oosten, U. Schneider, S. Fölling, B. Paredes, and I. Bloch, “Free fermion antibunching in a degenerate atomic Fermi gas released from an optical lattice,” *Nature*, vol. 444, pp. 733–736, 2006.
- [131] S. Wessel, F. Alet, M. Troyer, and G. G. Batrouni, “Quantum Monte Carlo simulations of confined bosonic atoms in optical lattices,” *Phys. Rev. A*, vol. 70, p. 053615, Nov 2004.
- [132] F. Gerbier, S. Trotzky, S. Fölling, U. Schnorrberger, J. D. Thompson, A. Widera, I. Bloch, L. Pollet, M. Troyer, B. Capogrosso-Sansone, N. V. Prokof’ev, and B. V. Svistunov, “Expansion of a quantum gas released from an optical lattice,” *Phys. Rev. Lett.*, vol. 101, p. 155303, Oct 2008.
- [133] D. M. Ceperley and B. J. Alder, “Ground state of the electron gas by a stochastic method,” *Phys. Rev. Lett.*, vol. 45, pp. 566–569, Aug 1980.
- [134] I. Hen and M. Rigol, “Strongly interacting atom lasers in three-dimensional optical lattices,” *Phys. Rev. Lett.*, vol. 105, p. 180401, Oct 2010.
- [135] J. K. Freericks and H. Monien, “Strong-coupling expansions for the pure and disordered Bose-Hubbard model,” *Phys. Rev. B*, vol. 53, pp. 2691–2700, Feb 1996.
- [136] M. C. Gutzwiller, “Effect of correlation on the ferromagnetism of transition metals,” *Phys. Rev. Lett.*, vol. 10, pp. 159–162, Mar 1963.
- [137] D. S. Rokhsar and B. G. Kotliar, “Gutzwiller projection for bosons,” *Phys. Rev. B*, vol. 44, pp. 10328–10332, Nov 1991.
- [138] W. H. Press, S. A. Teukolsky, W. T. Vetterling, and B. P. Flannery, *Numerical recipes in C, the art of scientific computing*. Cambridge University Press, 1992.
- [139] K. Byczuk and D. Vollhardt, “Correlated bosons on a lattice: Dynamical mean-field theory for Bose-Einstein condensed and normal phases,” *Phys. Rev. B*, vol. 77, no. 23, p. 235106, 2008.
- [140] A. L. Fetter and J. D. Walecka, *Quantum theory of many-particle systems*. McGraw-Hill, 1971.
- [141] V. L. Ginzburg and L. D. Landau, “On the theory of superconductors,” *Zh. Eksp. Teor. Fiz. (Sov. Phys. JETP)*, vol. 20, pp. 1064–1082, 1950.
- [142] D. van Oosten, P. van der Straten, and H. T. C. Stoof, “Quantum phases in an optical lattice,” *Phys. Rev. A*, vol. 63, p. 053601, Apr 2001.
- [143] G. G. Batrouni, R. T. Scalettar, and G. T. Zimanyi, “Quantum critical phenomena in one-dimensional Bose systems,” *Phys. Rev. Lett.*, vol. 65, pp. 1765–1768, Oct 1990.
- [144] W. Krauth, N. Trivedi, and D. Ceperley, “Superfluid-insulator transition in disordered boson systems,” *Phys. Rev. Lett.*, vol. 67, pp. 2307–2310, Oct 1991.
- [145] D. Jaksch, V. Venturi, J. I. Cirac, C. J. Williams, and P. Zoller, “Creation of a molecular condensate by dynamically melting a Mott insulator,” *Phys. Rev. Lett.*, vol. 89, p. 040402, Jul 2002.

- [146] M. Snoek, “Rigorous mean-field dynamics of lattice bosons: Quenches from the Mott insulator,” *Europhys. Lett.*, vol. 95, no. 3, p. 30006, 2011.
- [147] D. van Oosten, P. van der Straten, and H. T. C. Stoof, “Mott insulators in an optical lattice with high filling factors,” *Phys. Rev. A*, vol. 67, p. 033606, Mar 2003.
- [148] L. E. Sadler, J. M. Higbie, S. R. Leslie, M. Vengalattore, and D. M. Stamper-Kurn, “Spontaneous symmetry breaking in a quenched ferromagnetic spinor Bose–Einstein condensate,” *Nature*, vol. 443, p. 312, 2006.
- [149] T. W. Toshiya Kinoshita and D. S. Weiss, “A quantum Newton’s cradle,” *Nature*, vol. 440, pp. 900–903, 2006.
- [150] M. Eckstein and M. Kollar, “Nonthermal steady states after an interaction quench in the Falicov-Kimball model,” *Phys. Rev. Lett.*, vol. 100, p. 120404, Mar 2008.
- [151] D. F. Schwabl, *Statistical mechanics*. Springer-Verlag Berlin Heidelberg, 2006.
- [152] P. A. M. Dirac, “The physical interpretation of the quantum dynamics,” *Proceedings of the Royal Society of London A*, 1926.
- [153] T. Banks, L. Susskind, and M. E. Peskin, “Difficulties for the evolution of pure states into mixed states,” *Nucl. Phys. B*, vol. 244, pp. 125–134, 1984.
- [154] K. Günter, T. Stöferle, H. Moritz, M. Köhl, and T. Esslinger, “Bose-Fermi mixtures in a three-dimensional optical lattice,” *Phys. Rev. Lett.*, vol. 96, no. 18, p. 180402, 2006.
- [155] G. Roati, F. Riboli, G. Modugno, and M. Inguscio, “Fermi-Bose quantum degenerate  $^{40}\text{K}$ – $^{87}\text{Rb}$  mixture with attractive interaction,” *Phys. Rev. Lett.*, vol. 89, p. 150403, Sep 2002.
- [156] M. Taglieber, A.-C. Voigt, T. Aoki, T. W. Hänsch, and K. Dieckmann, “Quantum degenerate two-species Fermi-Fermi mixture coexisting with a Bose-Einstein condensate,” *Phys. Rev. Lett.*, vol. 100, no. 1, p. 010401, 2008.
- [157] R. Jördens, N. Strohmaier, K. Günter, H. Moritz, and T. Esslinger, “A Mott insulator of fermionic atoms in an optical lattice,” *Nature*, vol. 405, p. 204, 2008.
- [158] A.-C. Voigt, M. Taglieber, L. Costa, T. Aoki, W. Wieser, T. W. Hänsch, and K. Dieckmann, “Ultracold heteronuclear Fermi-Fermi molecules,” *Phys. Rev. Lett.*, vol. 102, no. 2, p. 020405, 2009.
- [159] D. M. Weld, P. Medley, H. Miyake, D. Hucul, D. E. Pritchard, and W. Ketterle, “Spin gradient thermometry for ultracold atoms in optical lattices,” *Phys. Rev. Lett.*, vol. 103, p. 245301, Dec 2009.
- [160] S. Ospelkaus, C. Ospelkaus, O. Wille, M. Succo, P. Ernst, K. Sengstock, and K. Bongs, “Localization of bosonic atoms by fermionic impurities in a three-dimensional optical lattice,” *Phys. Rev. Lett.*, vol. 96, no. 18, p. 180403, 2006.
- [161] B. Damski, L. Santos, E. Tiemann, M. Lewenstein, S. Kotochigova, P. Julienne, and P. Zoller, “Creation of a dipolar superfluid in optical lattices,” *Phys. Rev. Lett.*, vol. 90, p. 110401, Mar 2003.

- [162] A. B. Kuklov and B. V. Svistunov, “Counterflow superfluidity of two-species ultracold atoms in a commensurate optical lattice,” Phys. Rev. Lett., vol. 90, p. 100401, Mar 2003.
- [163] T. Gericke, F. Gerbier, A. Widera, S. Fölling, O. Mandel, and I. Bloch, “Adiabatic loading of a Bose-Einstein condensate in a 3d optical lattice,” J. Mod. Opt., vol. 54, no. 5, pp. 735–743, 2007.
- [164] L. Pezzè, L. Pitaevskii, A. Smerzi, S. Stringari, G. Modugno, E. de Mirandes, F. Ferlaino, H. Ott, G. Roati, and M. Inguscio, “Insulating behavior of a trapped ideal Fermi gas,” Phys. Rev. Lett., vol. 93, p. 120401, Sep 2004.
- [165] N. Strohmaier, Y. Takasu, K. Günter, R. Jördens, M. Köhl, H. Moritz, and T. Esslinger, “Interaction-controlled transport of an ultracold Fermi gas,” Phys. Rev. Lett., vol. 99, p. 220601, Nov 2007.
- [166] M. Snoek and W. Hofstetter, “Two-dimensional dynamics of ultracold atoms in optical lattices,” Phys. Rev. A, vol. 76, no. 5, p. 051603, 2007.
- [167] H. Ott, E. de Mirandes, F. Ferlaino, G. Roati, G. Modugno, and M. Inguscio, “Collisionally induced transport in periodic potentials,” Phys. Rev. Lett., vol. 92, p. 160601, Apr 2004.
- [168] U. Schneider, L. Hackermüller, J. P. Ronzheimer, S. Will, S. Braun, T. Best, I. Bloch, E. Demler, S. Mandt, D. Rasch, and A. Rosch, “Breakdown of diffusion: From collisional hydrodynamics to a continuous quantum walk in a homogeneous Hubbard model.” arXiv:1005.3545v1.
- [169] Y. Aharonov, L. Davidovich, and N. Zagury, “Quantum random walks,” Phys. Rev. A, vol. 48, pp. 1687–1690, Aug 1993.
- [170] M. Karski, L. Förster, J.-M. Choi, A. Steffen, W. Alt, D. Meschede, and A. Widera, “Quantum walk in position space with single optically trapped atoms,” Science, vol. 325, no. 5937, pp. 174–177, 2009.
- [171] U. Schneider, Interacting fermionic atoms in optical lattices - A quantum simulator for condensed matter physics. PhD thesis, Johannes Gutenberg-Universität, Mainz, 2010.
- [172] R. A. Bari, “Effects of short-range interactions on electron-charge ordering and lattice distortions in the localized state,” Phys. Rev. B, vol. 3, pp. 2662–2670, Apr 1971.
- [173] J. Sòlyom, “The Fermi gas model of one-dimensional conductors,” Adv. Phys., vol. 28, no. 2, pp. 201–303, 1979.
- [174] U. Wolff, “Saddle point mean field calculation in the Hubbard model,” Nuclear Physics B, vol. 225, no. 3, pp. 391 – 408, 1983.
- [175] P. G. J. van Dongen, “Extended Hubbard model at strong coupling,” Phys. Rev. B, vol. 49, pp. 7904–7915, Mar 1994.
- [176] J. Spalek, “t-j model then and now: A personal perspective from the pioneering times,”

- [177] W. Pauli, "Über den zusammenhang des abschlusses der elektronengruppen im atom mit der komplexstruktur der spektren," Z. Phys. A, vol. 31, pp. 765–783, 1925.
- [178] G. E. Uhlenbeck and S. Goudsmit, "Spinning electrons and the structure of spectra," Nature, vol. 117, pp. 264–265, 1926.
- [179] W. Nolting, Grundkurs Theoretische Physik 6: Statistische Physik. Springer Verlag, 2007.
- [180] A. Altland and B. Simons, Condensed matter field theory. Cambridge University Press, 2006.
- [181] A. G. Truscott, K. E. Strecker, W. I. McAlexander, G. B. Partridge, and R. G. Hulet, "Observation of Fermi pressure in a gas of trapped atoms," Science, no. 291, p. 2570.
- [182] J. Kanamori, "Superexchange interaction and symmetry properties of electron orbitals," J. Phys. Chem. Solids, vol. 10, no. 2-3, pp. 87–98, 1959.
- [183] R. Peierls Proc. Phys. Soc. London, Ser. A, vol. 47, p. 57, 1937.
- [184] M. Imada, A. Fujimori, and Y. Tokura, "Metal-insulator transitions," Rev. Mod. Phys., vol. 70, pp. 1039–1263, Oct 1998.
- [185] C. W. Searle and S. T. Wang, "Studies of the ionic ferromagnet (LaPb)MnO<sub>3</sub> III. ferromagnetic resonance studies," Can. J. Phys., vol. 47, no. 23, pp. 2703–2708, 1969.
- [186] C. Zener, "Interaction between the *d*-shells in the transition metals. II. ferromagnetic compounds of manganese with perovskite structure," Phys. Rev., vol. 82, pp. 403–405, May 1951.
- [187] K. Kubo and N. Ohata, "A quantum theory of double exchange. I," J. Phys. Soc. Jpn., vol. 33, no. 1, pp. 21–32, 1972.
- [188] J. Zaanen, G. A. Sawatzky, and J. W. Allen, "Band gaps and electronic structure of transition-metal compounds," Phys. Rev. Lett., vol. 55, pp. 418–421, Jul 1985.
- [189] J. G. Bednorz and K. A. Müller, "Possible high  $T_c$  superconductivity in the Ba-La-Cu-O system," Z. Phys. B, vol. 64, pp. 189–193, 1986.
- [190] F. Werner, O. Parcollet, A. Georges, and S. R. Hassan, "Interaction-induced adiabatic cooling and antiferromagnetism of cold Fermions in optical lattices," Phys. Rev. Lett., vol. 95, p. 056401, Jul 2005.
- [191] J. Honig, Metallic and non-metallic states of matter. Taylor & Francis, London, 1985.
- [192] N. F. Mott, Metal-insulator transitions. Taylor & Francis, London and New York, 1974.
- [193] S. Falke, H. Knöckel, J. Friebe, M. Riedmann, E. Tiemann, and C. Lisdat, "Potassium ground-state scattering parameters and Born-Oppenheimer potentials from molecular spectroscopy," Phys. Rev. A, vol. 78, p. 012503, Jul 2008.
- [194] K. M. Jones, E. Tiesinga, P. D. Lett, and P. S. Julienne, "Ultracold photoassociation spectroscopy: Long-range molecules and atomic scattering," Rev. Mod. Phys., vol. 78, pp. 483–535, May 2006.



- [195] C. Chin, R. Grimm, P. Julienne, and E. Tiesinga, “Feshbach resonances in ultracold gases,” *Rev. Mod. Phys.*, vol. 82, pp. 1225–1286, Apr 2010.
- [196] K.-K. Ni, S. Ospelkaus, M. H. G. de Miranda, A. Pe’er, B. Neyenhuis, J. J. Zirbel, S. Kotochigova, P. S. Julienne, D. S. Jin, and J. Ye, “A high phase-space-density gas of polar molecules,” *Science*, vol. 322, no. 5899, pp. 231–235, 2008.
- [197] M. A. Baranov, L. Dobrek, and M. Lewenstein, “Superfluidity of trapped dipolar Fermi gases,” *Phys. Rev. Lett.*, vol. 92, p. 250403, Jun 2004.
- [198] G. M. Bruun and E. Taylor, “Quantum phases of a two-dimensional dipolar Fermi gas,” *Phys. Rev. Lett.*, vol. 101, p. 245301, Dec 2008.
- [199] A. R. P. Lima and A. Pelster, “Dipolar Fermi gases in anisotropic traps,” *Phys. Rev. A*, vol. 81, p. 063629, Jun 2010.
- [200] Y. Endo, T. Miyakawa, and T. Nikuni, “Equilibrium properties of trapped dipolar Fermi gases at finite temperatures,” *Phys. Rev. A*, vol. 81, p. 063624, Jun 2010.
- [201] C. Wu and J. E. Hirsch, “Mixed triplet and singlet pairing in ultracold multicomponent fermion systems with dipolar interactions,” *Phys. Rev. B*, vol. 81, p. 020508, Jan 2010.
- [202] K. Mielson and J. K. Freericks, “Density-wave patterns for fermionic dipolar molecules on a square optical lattice: Mean-field-theory analysis,” *Phys. Rev. A*, vol. 83, p. 043609, Apr 2011.
- [203] L. He and W. Hofstetter, “Supersolid phase of cold fermionic polar molecules in two-dimensional optical lattices,” *Phys. Rev. A*, vol. 83, p. 053629, May 2011.
- [204] B. I. Shraiman and E. D. Siggia, “Spiral phase of a doped quantum antiferromagnet,” *Phys. Rev. Lett.*, vol. 62, pp. 1564–1567, Mar 1989.
- [205] H. J. Schulz, “Incommensurate antiferromagnetism in the two-dimensional Hubbard model,” *Phys. Rev. Lett.*, vol. 64, pp. 1445–1448, Mar 1990.
- [206] J. K. Freericks and M. Jarrell, “Magnetic phase diagram of the Hubbard model,” *Phys. Rev. Lett.*, vol. 74, pp. 186–189, Jan 1995.
- [207] B. M. Andersen and G. M. Bruun, “Magnetic and superfluid phases of confined fermions in two-dimensional optical lattices,” *Phys. Rev. A*, vol. 76, p. 041602, Oct 2007.
- [208] M. Snoek, I. Titvinidze, C. Toke, K. Byczuk, and W. Hofstetter, “Antiferromagnetic order of strongly interacting fermions in a trap: real-space dynamical mean-field analysis,” *New J. Phys.*, vol. 10, p. 093008, 2008.
- [209] M. W. Zwierlein, A. Schirotzek, C. H. Schunck, and W. Ketterle, “Fermionic superfluidity with imbalanced spin populations,” *Science*, vol. 311, no. 5760, pp. 492–496, 2006.
- [210] G. B. Partridge, W. Li, R. I. Kamar, Y.-a. Liao, and R. G. Hulet, “Pairing and phase separation in a polarized Fermi gas,” *Science*, vol. 311, no. 5760, pp. 503–505, 2006.

- [211] Y.-i. Shin, C. H. Schunck, A. Schirotzek, and W. Ketterle, “Phase diagram of a two-component Fermi gas with resonant interactions,” *Nature*, vol. 451, pp. 689–693, feb 2008.
- [212] N. F. Mott *Philos. Mag.*, vol. 6, p. 287, 1961.
- [213] V. L. Berezinskii, “Kinetics of a quantum particle in a one-dimensional random potential,” *Sov. Phys. JETP*, vol. 38, p. 620, 1974.
- [214] A. Abrikosov and I. Ryzhkin, “Conductivity of quasi-one-dimensional metal systems,” *Adv. Phys.*, vol. 27, no. 2, pp. 147–230, 1978.
- [215] E. H. Lieb and F. Y. Wu, “The one-dimensional Hubbard model: A reminiscence,” *Physica A*, vol. 321, p. 1, 2003.
- [216] E. Abrahams, ed., *50 years of Anderson localization*. World Scientific Publishing Co. Pte. Ltd., 2008.
- [217] R. Weaver, “Anderson localization of ultrasound,” *Wave Motion*, vol. 12, no. 2, pp. 129 – 142, 1990.
- [218] R. Dalichaouch, J. P. Armstrong, S. Schultz, P. M. Platzman, and S. L. McCall, “Microwave localization by two-dimensional random scattering,” *Nature*, vol. 354, pp. 53–55, 1991.
- [219] A. Z. G. A. A. Chabanov, M. Stoytchev, “Statistical signatures of photon localization,” *Nature*, vol. 404, pp. 850–853, 2000.
- [220] D. S. Wiersma, P. Bartolini, A. Lagendijk, and R. Righini, “Localization of light in a disordered medium,” *Nature*, vol. 390, pp. 671–673, 1997.
- [221] M. Störzer, P. Gross, C. M. Aegerter, and G. Maret, “Observation of the critical regime near Anderson localization of light,” *Phys. Rev. Lett.*, vol. 96, p. 063904, Feb 2006.
- [222] Y. Lahini, A. Avidan, F. Pozzi, M. Sorel, R. Morandotti, D. N. Christodoulides, and Y. Silberberg, “Anderson localization and nonlinearity in one-dimensional disordered photonic lattices,” *Phys. Rev. Lett.*, vol. 100, p. 013906, Jan 2008.
- [223] T. Giamarchi, *Quantum physics in one dimension*. Clarendon Press, Oxford, 2006.
- [224] A. M. Finkel’stein, “Weak localization and coulomb interaction in disordered systems,” *Z. Phys. B*, vol. 56, p. 189, 1984.
- [225] B. L. Altshuler, P. A. Lee, and R. A. Webb, eds., *Mesoscopic phenomena in solids*. North Holland, Amsterdam, 1991.
- [226] P. A. Lee and T. V. Ramakrishnan, “Disordered electronic systems,” *Rev. Mod. Phys.*, vol. 57, pp. 287–337, Apr 1985.
- [227] S. V. Kravchenko, W. E. Mason, G. E. Bowker, J. E. Furneaux, V. M. Pudalov, and M. D’Iorio, “Scaling of an anomalous metal-insulator transition in a two-dimensional system in silicon at  $B = 0$ ,” *Phys. Rev. B*, vol. 51, pp. 7038–7045, Mar 1995.

- [228] J. Wernsdorfer, G. Harder, and W. H. U. Schollwöck, “Signatures of delocalization in the fermionic 1d Hubbard model with box disorder: Comparative study with DMRG and R-DMFT.” arXiv:1108.6057v1.
- [229] E. B. Kolomeisky, “Universal jumps of conductance at the metal-insulator transition in one dimension,” Phys. Rev. B, vol. 47, pp. 6193–6196, Mar 1993.
- [230] D. Clément, A. F. Varón, M. Hugbart, J. A. Retter, P. Bouyer, L. Sanchez-Palencia, D. M. Gangardt, G. V. Shlyapnikov, and A. Aspect, “Suppression of transport of an interacting elongated Bose-Einstein condensate in a random potential,” Phys. Rev. Lett., vol. 95, p. 170409, Oct 2005.
- [231] D. Clément, A. F. Varón, J. A. Retter, L. Sanchez-Palencia, A. Aspect, and P. Bouyer, “Experimental study of the transport of coherent interacting matter-waves in a 1d random potential induced by laser speckle,” New J. Phys., vol. 8, p. 165, 2006.
- [232] J. E. Lye, L. Fallani, M. Modugno, D. S. Wiersma, C. Fort, and M. Inguscio, “Bose-Einstein condensate in a random potential,” Phys. Rev. Lett., vol. 95, p. 070401, Aug 2005.
- [233] M. White, M. Pasienski, D. McKay, S. Q. Zhou, D. Ceperley, and B. DeMarco, “Strongly interacting bosons in a disordered optical lattice,” Phys. Rev. Lett., vol. 102, p. 055301, Feb 2009.
- [234] J. W. Goodman, Speckle phenomena in optics: Theory and applications. Roberts and Company Publishers, 2007.
- [235] S. Q. Zhou and D. M. Ceperley, “Construction of localized wave functions for a disordered optical lattice and analysis of the resulting Hubbard model parameters,” Phys. Rev. A, vol. 81, p. 013402, Jan 2010.
- [236] T. Schulte, S. Drenkelforth, J. Kruse, W. Ertmer, J. Arlt, K. Sacha, J. Zakrzewski, and M. Lewenstein, “Routes towards Anderson-like localization of Bose-Einstein condensates in disordered optical lattices,” Phys. Rev. Lett., vol. 95, p. 170411, Oct 2005.
- [237] B. Damski, J. Zakrzewski, L. Santos, P. Zoller, and M. Lewenstein, “Atomic Bose and Anderson glasses in optical lattices,” Phys. Rev. Lett., vol. 91, p. 080403, Aug 2003.
- [238] R. Roth and K. Burnett, “Phase diagram of bosonic atoms in two-color superlattices,” Phys. Rev. A, vol. 68, p. 023604, Aug 2003.
- [239] J. M. Ziman, Principles of the theory of solids. Cambridge University Press, Cambridge, 1972.
- [240] L. D. Landau and E. M. Lifshits, Statistical physics. Pergamon, New York, 1993.
- [241] E. H. Lieb and F. Y. Wu, “Absence of Mott transition in an exact solution of the short-range, one-band model in one dimension,” Phys. Rev. Lett., vol. 20, pp. 1445–1448, Jun 1968.
- [242] H. Bethe, “Theorie der Beugung von Elektronen an Kristallen,” Ann. Phys., vol. 87, p. 55.

- [243] A. Sommerfeld, “Zur Elektronentheorie der Metalle auf Grund der Fermischen Statistik,” Z. Phys. A, vol. 47, pp. 1–32, 1928.
- [244] F. Bloch, “Über die Quantenmechanik der Elektronen in Kristallgittern,” Z. Phys., vol. 52, pp. 555–600, 1929.
- [245] J. H. de Boer and E. J. W. Verwey, “Semi-conductors with partially and with completely filled 3 d -lattice bands,” Proc. Phys. Soc. London, Ser. A, vol. 49, no. 4S, p. 59, 1937.
- [246] N. F. Mott Proc. Phys. Soc. London, Ser. A, vol. 49, p. 72, 1937.
- [247] N. F. Mott Proc. Phys. Soc. London, Ser. A, vol. 62, p. 416, 1949.
- [248] A. A. Abrikosov, L. P. Gorkov, and I. E. Dzyaloshinski, Methods of quantum field theory in statistical physics. Dover, New York, 1963.
- [249] D. Pines and P. Nozières, The theory of quantum liquids. Benjamin, New York, 1966.
- [250] G. D. Mahan, Many particle physics. Plenum, New York, 1981.
- [251] P. Hohenberg and W. Kohn, “Inhomogeneous electron gas,” Phys. Rev., vol. 136, pp. B864–B871, Nov 1964.
- [252] W. Kohn and L. J. Sham, “Self-consistent equations including exchange and correlation effects,” Phys. Rev., vol. 140, pp. A1133–A1138, Nov 1965.
- [253] L. J. Sham and W. Kohn, “One-particle properties of an inhomogeneous interacting electron gas,” Phys. Rev., vol. 145, pp. 561–567, May 1966.
- [254] R. Abou-Chacra, D. J. Thouless, and P. W. Anderson, “A selfconsistent theory of localization,” J. Phys. C, vol. 6, no. 10, p. 1734, 1973.
- [255] D. J. Thouless, “Electrons in disordered systems and the theory of localization,” Phys. Rep., vol. 13, no. 3, pp. 93 – 142, 1974.
- [256] J. Negele and H. Orland, Quantum many-particle systems. Westview Press, 1 ed., 1998.
- [257] E. N. Economou, Green’s functions in quantum physics. Springer, 3 ed., 2006.
- [258] Theory of functions, parts I and II. Dover, New York, 1996.
- [259] E. N. Economou, S. Kirkpatrick, M. H. Cohen, and T. P. Eggarter, “Localization in disordered materials: Binary alloys,” Phys. Rev. Lett., vol. 25, pp. 520–524, Aug 1970.
- [260] I. Lifshitz, “The energy spectrum of disordered systems,” Adv. Phys., vol. 13, no. 52, pp. 483–536, 1964.
- [261] S. F. Edwards and P. W. Anderson, “Theory of spin glasses,” J. Phys. F, vol. 5, no. 5, p. 965, 1975.
- [262] L. V. Keldysh, “Diagram technique for nonequilibrium processes,” Zh. Eksp. Teor. Fiz., vol. 47, pp. 1515 – 1527, 1964.

- [263] B. L. Altshuler and V. N. Prigodin Zh. Eksp. Teor. Fiz. (Sov. Phys. JETP), vol. 95, p. 348, 1989.
- [264] G. Schubert, J. Schleede, K. Byczuk, H. Fehske, and D. Vollhardt, “Distribution of the local density of states as a criterion for Anderson localization: Numerically exact results for various lattices in two and three dimensions,” Phys. Rev. B, vol. 81, p. 155106, Apr 2010.
- [265] Y. Song, W. A. Atkinson, and R. Wortis, “Geometrically averaged density of states as a measure of localization,” Phys. Rev. B, vol. 76, p. 045105, Jul 2007.
- [266] G. Schubert, A. Weisse, G. Wellein, and H. Fehske, “Comparative numerical study of Anderson localization in disordered electron systems,” High Performance Computing in Science and Engineering Garching 2004, p. 237, 2005.
- [267] F. Gebhard, The Mott metal-insulator transition. Springer, Berlin, 2008.
- [268] R. Kubo, “Statistical mechanical theory of irreversible processes I,” J. Phys. Soc. Jpn., vol. 12, pp. 570–586, 1957.
- [269] R. J. Bell and P. Dean, “Atomic vibrations in vitreous silica,” Discuss. Faraday Soc., vol. 50, 1970.
- [270] H. Aoki, “Fractal dimensionality of wave functions at the mobility edge: Quantum fractal in the Landau levels,” Phys. Rev. B, vol. 33, pp. 7310–7313, May 1986.
- [271] F. Wegner, “Inverse participation ratio in  $2+\epsilon$  dimensions,” Z. Physik B, vol. 36, pp. 209–214, 1980.
- [272] A. Gogolin, “Electron localization near the band edge and dielectric constant of TCNQ salts with strong structural disorder,” Solid State Commun., vol. 45, no. 4, pp. 361 – 365, 1983.
- [273] S. Nishimoto, K. Sano, and Y. Ohta, “Phase diagram of the one-dimensional Hubbard model with next-nearest-neighbor hopping,” Phys. Rev. B, vol. 77, p. 085119, Feb 2008.
- [274] R. Eder, K. Seki, and Y. Ohta, “Self-energy and Fermi surface of the two-dimensional Hubbard model,” Phys. Rev. B, vol. 83, p. 205137, May 2011.
- [275] Y. Ohta, K. Tsutsui, W. Koshibae, and S. Maekawa, “Exact-diagonalization study of the Hubbard model with nearest-neighbor repulsion,” Phys. Rev. B, vol. 50, pp. 13594–13602, Nov 1994.
- [276] A. Liebsch and T. A. Costi, “Non-Fermi-liquid phases in the two-band Hubbard model: Finite-temperature exact diagonalization study of Hund’s rule coupling,” Eur. Phys. J. B, vol. 51, pp. 523–536, 2006.
- [277] F. F. Assaad, R. Preuss, A. Muramatsu, and W. Hanke, “Quantum Monte Carlo simulations of Hubbard type models,” Jour. of Low Temp. Physics, vol. 95, pp. 251–255, 1994. 10.1007/BF00754940.
- [278] R. Staudt, M. Dzierzawa, and A. Muramatsu, “Phase diagram of the three-dimensional Hubbard model at half filling,” Euro. Phys. Jour. B, vol. 17, pp. 411–415, 2000. 10.1007/s100510070120.

- [279] M. Rigol and A. Muramatsu, “Quantum Monte Carlo study of confined fermions in one-dimensional optical lattices,” Phys. Rev. A, vol. 69, p. 053612, May 2004.
- [280] T. Giamarchi, “Mott transition in one dimension,” Physica B, vol. 230, pp. 975–980, 1997.
- [281] A. Georges, G. Kotliar, W. Krauth, and M. J. Rozenberg, “Dynamical mean-field theory of strongly correlated fermion systems and the limit of infinite dimensions,” Rev. Mod. Phys., vol. 68, p. 13, Jan 1996.
- [282] O. Parcollet, G. Biroli, and G. Kotliar, “Cluster dynamical mean field analysis of the Mott transition,” Phys. Rev. Lett., vol. 92, p. 226402, Jun 2004.
- [283] G. Kotliar, S. Y. Savrasov, K. Haule, V. S. Oudovenko, O. Parcollet, and C. A. Marianetti, “Electronic structure calculations with dynamical mean-field theory,” Rev. Mod. Phys., vol. 78, pp. 865–951, Aug 2006.
- [284] R. W. Helmes, T. A. Costi, and A. Rosch, “Mott transition of fermionic atoms in a three-dimensional optical trap,” Phys. Rev. Lett., vol. 100, p. 056403, Feb 2008.
- [285] F. Wegner, “Graßmann - Variable.” lecture notes, 1998.
- [286] H. T. C. Stoof, K. B. Gubbel, and D. B. M. Dickerscheid, Ultracold quantum fields. Springer, 2008.
- [287] R. J. Baxter, Exactly solved models in statistical mechanics. Academic Press, 1982.
- [288] P. D. Gujrati, “Bethe or Bethe-like lattice calculations are more reliable than conventional mean-field calculations,” Phys. Rev. Lett., vol. 74, pp. 809–812, Jan 1995.
- [289] A. Georges and W. Krauth, “Numerical solution of the  $d = \infty$  Hubbard model: Evidence for a Mott transition,” Phys. Rev. Lett., vol. 69, pp. 1240–1243, Aug 1992.
- [290] A. Georges and G. Kotliar, “Hubbard model in infinite dimensions,” Phys. Rev. B, vol. 45, pp. 6479–6483, Mar 1992.
- [291] M. J. Rozenberg, R. Chitra, and G. Kotliar, “Finite temperature Mott transition in the Hubbard model in infinite dimensions,” Phys. Rev. Lett., vol. 83, pp. 3498–3501, Oct 1999.
- [292] R. M. Fye, “New results on Trotter-like approximations,” Phys. Rev. B, vol. 33, pp. 6271–6280, May 1986.
- [293] M. Jarrell, “Hubbard model in infinite dimensions: A quantum Monte Carlo study,” Phys. Rev. Lett., vol. 69, pp. 168–171, Jul 1992.
- [294] M. J. Rozenberg, X. Y. Zhang, and G. Kotliar, “Mott-Hubbard transition in infinite dimensions,” Phys. Rev. Lett., vol. 69, pp. 1236–1239, Aug 1992.
- [295] Q. Si, M. J. Rozenberg, G. Kotliar, and A. E. Ruckenstein, “Correlation induced insulator to metal transitions,” Phys. Rev. Lett., vol. 72, pp. 2761–2764, Apr 1994.
- [296] M. Caffarel and W. Krauth, “Exact diagonalization approach to correlated fermions in infinite dimensions: Mott transition and superconductivity,” Phys. Rev. Lett., vol. 72, pp. 1545–1548, Mar 1994.

- [297] M. J. Rozenberg, G. Moeller, and G. Kotliar, “The metal–insulator transition in the hubbard model at zero temperature II,” Mod. Phys. Lett. B, vol. 8, p. 535, 1994.
- [298] A. Georges, G. Kotliar, W. Krauth, and M. J. Rozenberg, “Dynamical mean-field theory of strongly correlated fermion systems and the limit of infinite dimensions,” Rev. Mod. Phys., vol. 68, pp. 13–125, Jan 1996.
- [299] K. G. Wilson, “The renormalization group: Critical phenomena and the Kondo problem,” Rev. Mod. Phys., vol. 47, pp. 773–840, Oct 1975.
- [300] R. Bulla, T. A. Costi, and T. Pruschke, “Numerical renormalization group method for quantum impurity systems,” Rev. Mod. Phys., vol. 80, pp. 395–450, Apr 2008.
- [301] H. Kajueter and G. Kotliar, “New iterative perturbation scheme for lattice models with arbitrary filling,” Phys. Rev. Lett., vol. 77, p. 131, 1996.
- [302] M. Potthoff, T. Wegner, and W. Nolting, “Interpolating self-energy of the infinite-dimensional Hubbard model: Modifying the iterative perturbation theory,” Phys. Rev. B, vol. 55, pp. 16132–16142, Jun 1997.
- [303] E. Müller-Hartmann, “The Hubbard model at high dimensions: some exact results and weak coupling theory,” Z. Phys. B, vol. 76, pp. 211–217, 1989.
- [304] H. R. Krishnamurthy, J. W. Wilkins, and K. G. Wilson, “Renormalization-group approach to the Anderson model of dilute magnetic alloys. I. Static properties for the symmetric case,” Phys. Rev. B, vol. 21, pp. 1003–1043, Feb 1980.
- [305] W. Hofstetter, Renormalization group methods for quantum impurity systems. PhD thesis, Universität Augsburg, 2000.
- [306] I. Titvinidze, Dynamical mean-field theory approach for ultracold atomic gases. PhD thesis, Goethe-Universität, Frankfurt am Main, 2009.
- [307] R. Bulla, A. C. Hewson, and T. Pruschke, “Numerical renormalization group calculations for the self-energy of the impurity Anderson model,” J. Phys. Cond. Matt., vol. 10, no. 37, p. 8365, 1998.
- [308] X. Y. Zhang, M. J. Rozenberg, and G. Kotliar, “Mott transition in the  $d = \infty$  Hubbard model at zero temperature,” Phys. Rev. Lett., vol. 70, pp. 1666–1669, Mar 1993.
- [309] A. Georges and W. Krauth, “Physical properties of the half-filled Hubbard model in infinite dimensions,” Phys. Rev. B, vol. 48, pp. 7167–7182, Sep 1993.
- [310] W. Metzner and D. Vollhardt, “Correlated lattice Fermions in  $d = \infty$  dimensions,” Phys. Rev. Lett., vol. 62, pp. 324–327, Jan 1989.
- [311] J. Schmalian, M. Langer, S. Grabowski, and K. H. Bennemann, “Theory for dynamical short-range order and Fermi surface volume in strongly correlated systems,” Phys. Rev. B, vol. 54, pp. 4336–4340, Aug 1996.
- [312] J. M. Luttinger, “An exactly soluble model of a many-Fermion system,” J. Math. Phys., vol. 4, p. 1154, 1963.
- [313] D. Semmler, Strongly Correlated Ultracold Gases in Disordered Optical Lattices. PhD thesis, Johann Wolfgang Goethe-Universität, Frankfurt am Main, 2011.

- [314] V. Dobrosavljević and G. Kotliar, “Dynamical mean-field studies of metal-insulator transitions,” Philos. Trans. R. Soc. London, Ser. A, vol. 356, p. 57, 1998.
- [315] E. V. Gorelik, I. Titvinidze, W. Hofstetter, M. Snoek, and N. Blümer, “Néel transition of lattice Fermions in a harmonic trap: A real-space dynamic mean-field study,” Phys. Rev. Lett., vol. 105, p. 065301, Aug 2010.
- [316] T. Giamarchi, P. Le Doussal, and E. Orignac, “Competition of random and periodic potentials in interacting fermionic systems and classical equivalents: The Mott glass,” Phys. Rev. B, vol. 64, p. 245119, Dec 2001.
- [317] Y. Z. Zhang and M. Imada, “Pseudogap and Mott transition studied by cellular dynamical mean-field theory,” Phys. Rev. B, vol. 76, p. 045108, Jul 2007.
- [318] S. R. White, “Density matrix formulation for quantum renormalization groups,” Phys. Rev. Lett., vol. 69, pp. 2863–2866, Nov 1992.
- [319] S. R. White, “Density-matrix algorithms for quantum renormalization groups,” Phys. Rev. B, vol. 48, pp. 10345–10356, Oct 1993.
- [320] U. Schollwöck, “The density-matrix renormalization group,” Rev. Mod. Phys., vol. 77, pp. 259–315, Apr 2005.
- [321] A. Lagendijk, B. van Tiggelen, and D. S. Wiersma, “Fifty years of Anderson localization,” Phys. Today, vol. 62, no. 8, pp. 24–29, 2009.
- [322] J. M. Luttinger, “Analytic properties of single-particle propagators for many-Fermion systems,” Phys. Rev., vol. 121, no. 4, pp. 942–949, 1961.
- [323] M. Janssen, “Statistics and scaling in disordered mesoscopic electron systems,” Phys. Rep., vol. 295, no. 1-2, pp. 1 – 91, 1998.
- [324] P. Schmitteckert, T. Schulze, C. Schuster, P. Schwab, and U. Eckern, “Anderson localization versus delocalization of interacting Fermions in one dimension,” Phys. Rev. Lett., vol. 80, pp. 560–563, Jan 1998.
- [325] F. Krüger, J. Wu, and P. Phillips, “Anomalous suppression of the Bose glass at commensurate fillings in the disordered Bose-Hubbard model,” Phys. Rev. B, vol. 80, p. 094526, Sep 2009.
- [326] K. Byczuk, W. Hofstetter, and D. Vollhardt, “Anderson localization vs. Mott–Hubbard metal–insulator transition in disordered, interacting lattice fermion systems,” Int. J. Mod. Phys. B, vol. 24, p. 1727, 2010.
- [327] B. Altshuler and A. Aronov, “Zero bias anomaly in tunnel resistance and electron-electron interaction,” Solid State Commun., vol. 30, no. 3, pp. 115 – 117, 1979.
- [328] A. L. Efros and B. I. Shklovskii, “Coulomb gap and low temperature conductivity of disordered systems,” J. Phys. C, vol. 8, no. 4, p. L49, 1975.
- [329] S. Chiesa, P. B. Chakraborty, W. E. Pickett, and R. T. Scalettar, “Disorder-induced stabilization of the pseudogap in strongly correlated systems,” Phys. Rev. Lett., vol. 101, p. 086401, Aug 2008.
- [330] H. Shinaoka and M. Imada, “Soft Hubbard gaps in disordered itinerant models with short-range interaction,” Phys. Rev. Lett., vol. 102, p. 016404, Jan 2009.



- [331] S. H. Naqib, J. R. Cooper, R. S. Islam, and J. L. Tallon, “Anomalous pseudogap and superconducting-state properties of heavily disordered  $Y_{1-x}Ca_xBa_2(Cu_{1-y}Zn_y)_3O_{7-\delta}$ ,” Phys. Rev. B, vol. 71, p. 184510, May 2005.
- [332] R. Wortis and W. A. Atkinson, “Physical mechanism for a kinetic energy driven zero-bias anomaly in the anderson-hubbard model,” Phys. Rev. B, vol. 82, p. 073107, Aug 2010.
- [333] H.-Y. Chen, R. Wortis, and W. A. Atkinson, “Disorder-induced zero-bias anomaly in the Anderson-Hubbard model: Numerical and analytical calculations,” Phys. Rev. B, vol. 84, p. 045113, Jul 2011.
- [334] Y. Song, S. Bulut, R. Wortis, and W. A. Atkinson, “Effects of strong correlations on the disorder-induced zero-bias anomaly in the extended Anderson–Hubbard model,” J. Phys. Cond. Matt., vol. 21, no. 38, p. 385601, 2009.
- [335] V. Dobrosavljević, “Typical-medium theory of Mott–Anderson localization,” Int. J. Mod. Phys. B, vol. 24, p. 1680, 2010.
- [336] R. Mélin and F. Iglói, “Strongly disordered Hubbard model in one dimension: Spin and orbital infinite randomness and griffiths phases,” Phys. Rev. B, vol. 74, p. 155104, Oct 2006.
- [337] M. Tezuka and A. M. García-García, “Stability of the superfluid state in a disordered one-dimensional ultracold fermionic gas,” Phys. Rev. A, vol. 82, p. 043613, 2010.
- [338] N. Prokof’ev and B. Svistunov, “Superfluid-insulator transition in commensurate disordered bosonic systems: Large-scale worm algorithm simulations,” Phys. Rev. Lett., vol. 92, no. 1, p. 015703, 2004.
- [339] R. T. Scalettar, G. G. Batrouni, and G. T. Zimanyi, “Localization in interacting, disordered, bose systems,” Phys. Rev. Lett., vol. 66, no. 24, pp. 3144–3147, 1991.
- [340] N. V. Prokof’ev and B. V. Svistunov, “Comment on “one-dimensional disordered bosonic Hubbard model: A density-matrix renormalization group study”,” Phys. Rev. Lett., vol. 80, no. 19, p. 4355, 1998.
- [341] S. Rapsch, U. Schollwöck, and W. Zwerger, “Density matrix renormalization group for disordered bosons in one dimension,” Europhys. Lett., vol. 46, no. 5, pp. 559–564, 1999.
- [342] F. Heidrich-Meisner, S. R. Manmana, M. Rigol, A. Muramatsu, A. E. Feiguin, and E. Dagotto, “Quantum distillation: Dynamical generation of low-entropy states of strongly correlated fermions in an optical lattice,” Phys. Rev. A, vol. 80, p. 041603, Oct 2009.
- [343] P. B. Blakie and J. V. Porto, “Adiabatic loading of bosons into optical lattices,” Phys. Rev. A, vol. 69, p. 013603, Jan 2004.
- [344] M. Snoek and W. Hofstetter, Non-equilibrium quantum gases at finite temperatures, ch. Bosonic Dynamical Mean-Field Theory. World Scientific Press, 2011.
- [345] P. Limelette, P. Wzietek, S. Florens, A. Georges, T. A. Costi, C. Pasquier, D. Jérôme, C. Mézière, and P. Batail, “Mott transition and transport crossovers in the organic compound  $\kappa$ -(BEDT-TTF) $_2$ Cu[N(CN) $_2$ ]Cl,” Phys. Rev. Lett., vol. 91, p. 016401, Jul 2003.



# Danksagung

An erster Stelle möchte ich mich bei meinem Betreuer Prof. Dr. Walter Hofstetter ganz herzlich bedanken, dass er mich in seine Gruppe aufgenommen und meine Promotion begleitet hat. Insbesondere danke ich für die Rücksichtnahme und Förderung während der Abschlußphase.

Ein herzliches Dankeschön auch an Prof. Roser Valenti für Ihre direkte und indirekte Unterstützung und vor allem für Ihre Anteilnahme und Aufrichtigkeit, die mir in den anstrengenden Zeiten der Promotion sehr geholfen haben.

Außerordentlich bereichernd war stets die Zusammenarbeit mit Dr. Michiel Snoek. Er hat sich immer Zeit für ausführliche Diskussionen genommen und mich an seinem unerschöpflichen Wissensschatz teilhaben lassen. Er hat stets an mich geglaubt und mich unterstützt über die Grenzen seiner Anstellung in Frankfurt hinaus. Damit hat er mir den besten Einstieg in die Promotion ermöglicht, den ich mir nur hätte vorstellen können. Für das und alles andere, was ich aus Platzgründen hier nicht aufzählen vermag, kann ich gar nicht genug danken.

Ich möchte mich auch bei der gesamten Arbeitsgruppe bedanken, ohne deren Unterstützung und Hilfe ich sicherlich nicht so weit gekommen wäre. Auch in der Wissenschaft trägt zum Erfolg einzelner das ganze Team bei.

Ich bedanke mich bei David Roosen, durch den ich überhaupt zu der Gruppe kam und der mir durch bedingungslose Computerhilfen das Arbeiten ermöglicht hat.

Ein besonderer Dank gebührt auch Ulf Bissbort, der mir am Institut und außerhalb beigestanden ist und ein echter Freund geworden ist. Ihm verdanke ich nicht nur einige physikalische Kenntnisse sondern auch Fahrradreparatur-Bastel-Koch-Buch-Film-Politik-Weisheit, die ich während meiner Promotion erlangt habe.

Ich danke auch Denis Semmler für die vielen physikalischen und sozial-politischen Diskussionen und Einsichten, zu denen er mir verholfen hat. Ich habe die Zusammenarbeit und seine Ehrlichkeit sehr geschätzt.

Ich möchte mich auch bei Irakli Titvinidze bedanken, von dessen DMFT-Knowhow ich so oft profitiert habe. Seine offene, ehrliche und uneigennützig Art hat stets für Freude gesorgt. Sein Wechsel in eine andere Gruppe hat eine unschließbare Lücke hinterlassen.

Ganz besonders danke ich Ulrike Bornheimer. Es war mir eine große Bereicherung sie während ihrer Bachelorarbeit begleiten zu dürfen. Ich danke ihr für ihre Geduld und die unzähligen leckeren Kuchen.

Auch bei den Gruppenmitgliedern, die gegen Ende meiner Promotionszeit dazu gekommen sind, möchte ich mich bedanken. Insbesondere bei Daniel Cocks für seine unermüdliche

Unterstützung bei allen Englisch-Fragen und den damit verbundenen zeitraubenden Korrekturen. Und um weiter beim Thema zu bleiben, danke ich hier für das Durchlesen und Korrigieren meiner Dissertation: Michiel Snoek, Daniel Cocks, Ulf Bissbort, Irakli Titvinidze, Denis Semmler, Bernd Schmidt, Andrii Sotnikov, Tobias Wernsdorfer, Karin Goß, Viola Priesemann, Frank Deuretzbacher und Liang He.

Einen ganz besonderen Dank möchte ich auch denen aussprechen, die mir stets den Rücken gestärkt und mich ermutigt haben: Friederike Sziekat, Daniela Wirth-Pagano, Karin Goß, Christina Grimm, Viola Priesemann und Alina Serebrinnikova.

Und zum Schluss möchte ich noch den wichtigsten Menschen in meinem Leben danken. Ich danke meinem Mann Tobias Wernsdorfer, der mich nicht nur verbal sondern auch tatkräftig unterstützt hat, insbesondere in den letzten superanstrengenden Wochen vor der Abgabe. Seine Liebe, Zuversicht und Wertschätzung haben mich immer ermuntert, erheitert und getragen. Meinen lieben Eltern, Tatjana und Vladimir Sabelin, danke ich für die bedienungslose Liebe und grenzenlose Unterstützung, die mir schon mein ganzes Leben lang Halt gegeben haben. Und ein großer Dank meinem kleinen Sonnenschein, der das Abschließen der Dissertation mit Freude erfüllt und beschleunigt hat.



# Curriculum Vitae

<b>Personal Data</b>	
Name	Julia Wernsdorfer
Date of birth	9. July 1982
Place of birth	Krementchug, Ukraine
Nationality	German, Ukrainian
Address	Oppenheimer Str. 51 60594 Frankfurt am Main
E-mail	wernsdorfer@itp.uni-frankfurt.de
<b>Scientific Positions</b>	
2011-2007	<p><b>PhD student</b> Johann-Wolfgang-Goethe University, Frankfurt am Main Thesis: "<i>Interacting Ultracold Gases in Optical Lattices: Non-Equilibrium and Disorder Properties</i>" Supervisor: Prof. Dr. W. Hofstetter</p> <p><b>Close collaborations</b> - LENS ( Florence, Italy) - ITFA (Amsterdam, Netherlands)</p>
2009	<p><b>Head of the organisation team</b> of the female physicist conference (Approx. 300 participants from Germany, France and Switzerland) <a href="http://www.physikerinnentagung.de">www.physikerinnentagung.de</a> - Finance: recruiting of sponsors, control of expenses and income - Program: schedule of the conference, support of invited guests - Social: organisation of conference dinner and further activities</p>
2006-2004	<p><b>Scientific Assistant</b> at Neue Materialien Würzburg GmbH Measurements and analysis of electro-rheological fluids</p>
<b>Education</b>	
2007-2002	<p><b>Diploma in physics</b> Average mark 1.06 (On a scale of 1 to 6, 1 being highest grade attainable) Julius-Maximilians-University, Würzburg Diploma thesis: "<i>Kondo Effect in Superconducting environment</i>" Supervisor: Prof. Dr. Fagher F. Assaad</p>

- 2002-1998 **Diploma from German secondary school**  
Average mark 1.7  
(On a scale of 1 to 6, 1 being highest grade attainable)  
Matthias-Grünewald-Gymnasium, Würzburg
- 1998-1997 **Mönchberg-Hauptschule**, Würzburg  
School for foreigners
- 1996-1988 **Secondary school**, Kremenchug (Ukraine)
- 1995-1989 **Diploma from music school**  
Average mark 5.0  
(On a scale of 5 to 1, 5 being highest grade attainable)  
Music school Tchaikovsky, Kremenchug (Ukraine)

### Languages

**German:** native language  
**English:** fluently  
**Russian:** native language  
**Ukrainian:** native language  
**Spanish:** 3 years school education  
1 month intensive course, Barcelona (Spain)  
1 month intensive course in University, Würzburg

### Publications

- in preparation **Expansion of bosonic condensates in optical lattices**  
Julia Wernsdorfer, Ulrike Bornheimer, Ulrich Schneider, Walter Hofstetter
- 2011 **Phase Diagram of Fermionic 1D Hubbard Model with Box Disorder: Comparative Study with DMRG and RDMFT**  
Julia Wernsdorfer, Georg Harder, Ulrich Schollwöck, Walter Hofstetter  
Preprint, arXiv:1108.6057
- 2010 **Strongly Correlated Fermions in a Speckle Disordered Optical Lattice**  
Denis Semmler, Julia Wernsdorfer, Ulf Bissbort, Walter Hofstetter  
Phys. Rev. B 82, 235115 (2010)
- 2010 **Lattice-Ramp Induced Dynamics in an Interacting Bose-Bose Mixture**  
Julia Wernsdorfer, Michiel Snoek, Walter Hofstetter  
Phys. Rev. A 81, 043620 (2010)

### Invited Talks

- 2012 *"Disordered Strongly Correlated Fermions"*  
International workshop  
"Theory of Quantum Gases and Quantum Coherence" (Lyon, France)
- 2011 *"Strongly Correlated Ultracold Fermions in Disordered Optical Lattices"*  
Institute seminar, ITFA (Amsterdam, Netherlands)
- 2009 *"Dynamics of Interacting Bose-Bose Mixtures in Optical Lattices"*  
Institute seminar, LENS (Florence, Italy)

---